Università degli Studi di Messina

Dipartimento di Scienze Matematiche e Informatiche, Scienze Fisiche e Scienze della Terra

DOCTORAL THESIS

Ion Acceleration by High Intensity Pulsed Laser: Transport, Diagnostics and Theoretical Modelling

A thesis submitted for the degree of Doctor of Philosophy

in

PHYSICS

Candidate:
Giuseppe Costa

Supervisor:
Prof. L. Torrisi

Head of PhD School:
Prof. L. Torrisi

S.S.D. FIS/01
Cycle XXXII
PhD in Physics
from 2016 to 2019

Graduate Year 2019

ABSTRACT

Laser at intensity above of 10^{10} W/cm^2 that interacts with a solid target generate photons, electrons, and ion beams, emitted from a plasma which expands in vacuum. The electron and ion energies depend strongly on the laser parameters, on the irradiation conditions, and on the target properties.

This work was performed at the University of Messina, using a Nd:YAG laser, with 3 ns pulse duration, and 1064 nm wavelength, at an intensity of 10^{10} W/cm^2 to generate a plasma by means of different targets. Ion emissions occur mainly along the normal to the target surface and can be detected using the Time–of–Flight technique, through Ion Collector, when the ion current is high enough, or Secondary Electron Multiplier, when the current is less than 10 μA. To increase the current, magnetic fields with cylindrical symmetry can be applied along the axis of ion emission, to obtain a focusing effect for the charged particle beam emerging out of the plasma. The formation of electronic traps, due to the magnetic field's force lines, drives the ions' acceleration by improving their kinetic energy.

The application of a magnetic field generated by a coil, or an electric field generated by semi–cylindrical electrodes, directed orthogonally to the ions beam produces a deflections of charged particles, according to their mass–to–charge ratio and their velocity or energy, respectively. Ion accelerations of the order of hundreds of eV per charge state, plasma temperatures of the order of tens of eV, and Boltzmann energy distributions have been obtained for the different irradiated targets.

At higher intensities, such as those investigated at the INFN–LNS in Catania (10^{12} W/cm^2 with a post–acceleration system up to 30 kV), and at the PALS Laboratory in Prague (10^{16} W/cm^2), a compact Thomson Parabola Spectrometer, designed at the University of Messina, was employed. It allows to detect particles emitted by hot plasmas and do fast analysis of the charge state, kinetic energy and mass–to–charge ratio. The spectrometer consists of a double input pinhole, for alignment, a permanent magnet ($0.004 \div 4$ kG) and an electric field ($0.05 \div 5$ kV/cm) parallel to each other and orthogonal to the direction of the beam. It can be equipped with different types of planar detectors such as phosphor screen, Gafchromic, PM–355 and others.

Further measurements were conducted at the IPPLM of Warsaw, using a Ti:Sapphire laser, with 45 fs pulse duration and intensity of about $\sim 10^{19}$ W/cm^2, to irradiate an advanced target based on a thin film of Graphene oxide covered with metal layers, in order to investigate the acceleration in forward direction, in the Target Normal Sheath Acceleration regime. The Time–of–Flight technique was employed, using semiconductor detectors based on silicon carbide. By optimizing the focusing conditions, a maximum energy for protons of 2.85 MeV was measured, using a gold metallization of 200 nm.

Finally, the experimental data obtained are compared with the simulations performed using the Particle-in-Cell (PIC) method. PIC provides the electronic densities as a function of time and space, and allows to evaluate the electric field developed in the rear surface of the irradiated foil. The simulation indicates that carbon ions are subject to a lower acceleration than protons, depending on the charge–to–mass ratio. Thus, carbon ions are not affected by the maximum electric field due to its fast time decay. Considering the angular emission distribution of protons and the six charge states of carbon, and their Boltzmann energy with a fixed cut–off, the data obtained are in agreement with the experimental measurements.

These measurements, analyses and simulations, collected and performed during my PhD years, are discussed and presented in the following chapters of this thesis.

LIST OF PUBLICATIONS

The work of this thesis is based on the following publications, which the author has carried out during the three years of PhD school in physics:

[I] G. Costa, L. Torrisi and G. Ceccio, "Axial Magnetic Fields applied to Laser–generated Plasma to enhance the ion yield and energy emission" *Activity Report del Dottorato di Ricerca in Fisica, Università degli Studi di Messina*, ISSN: 2038–5889 (2016).

[II] L. Torrisi, G. Costa and G. Ceccio, "Magnetic fields applied to laser–generated plasma to enhance the ion yield acceleration" *5th Workshop: Plasmi, Sorgenti, Biofisica ed Applicazioni*, 112–117 (2017).

[III] L. Torrisi, M. Cutroneo, G. Ceccio, A. Cannavò, N. Restuccia, G. Costa, L. Calcagno, I. Paterniti, C. Marchetta and A. Torrisi, "Nanoparticles by laser and their applications in Nuclear Physics" *LNS Activity Report*, 231–234 (2017).

[IV] L. Torrisi and G. Costa, "Magnetic focusing of emitted ions from laser–generated plasma: enhancement of yield and energy" *Laser and particle Beams*, **35**(2), 202–209 (2017).

[V] G. Costa and L. Torrisi, "Design of an Electromagnet for Laser-generated Plasma diagnostics" *Activity Report del Dottorato di Ricerca in Fisica, Università degli Studi di Messina*, ISSN: 2038–5889 (2017).

[VI] G. Costa and L. Torrisi, "Diagnostics of Particles emitted from a Laser generated Plasma: Experimental Data and Simulations" *The European Physics Journal: Web of Conferences*, **167**, 04005(1–6) (2018).

[VII] L. Torrisi, G. Costa, G. Ceccio, A. Cannavò, N. Restuccia and M. Cutroneo, "Magnetic and electric deflector spectrometers for ion emission analysis from laser generated plasma" *The European Physics Journal: Web of Conferences*, **167**, 03011(1–7) (2018).

[VIII] L. Torrisi and G. Costa, "Simple Magnetic Spectrometer for ions emitted from Laser–generated Plasma at 10^{10} W/cm^2 intensity" *Laser and Particle Beams*, **36**(2), 163–170 (2018).

[IX] G. Costa and L. Torrisi, "Electrical and magnetic spectrometry of ions emitted from laser–generated plasma at 10^{10} W/cm^2 intensity" *45th EPS Conference on Plasma Physics (EPS2018)*, (2018).

[X] G. Costa and L. Torrisi, "Vacuum Chamber upgrade for a better study of Laser–generated Plasmas" *Activity Report del Dottorato di Ricerca in Fisica, Università degli Studi di Messina*, ISSN: 2038–5889 (2018).

[XI] L. Torrisi, M. Cutroneo, A. Torrisi, L. Silipigni, G. Costa, M. Rosinski, J. Badziak, J. Wołowski, A. Zaraś–Szydłowska and P. Parys, "Protons accelerated in the target normal sheath acceleration regime by a femtosecond laser" *Physical Review Accelerators and Beams*, **22**(2), 021302(1–7) (2019).

[XII] L. Torrisi and G. Costa, "Compact Thomson Parabola Spectrometer for fast diagnostics of different intensity Laser–generated Plasmas, *Physical Review Accelerators and Beams*, **22**(4), 042902(1–9) (2019).

[XIII] L. Torrisi and G. Costa, "Ion acceleration by *fs* laser in TNSA regime and comparison of TOF spectra with PIC simulations, *Physical Review Accelerators and Beams*, Submitted, (2019).

[XIV] G. Costa and L. Torrisi, "Particle–in–Cell simulation for experimental ion acceleration by fs laser–generated plasma, *Radiation Effects and Defects in Solids*, Submitted, (2019).

[XV] L. Torrisi and G. Costa, "Magnetic Field to focalize and Accelerate ions produced by ns Laser–generated plasmas, *Japanese Journal of Applied Physics*, Submitted, (2019).

The author research activity, carried out during the three years of doctorate, concerns the transport, diagnostics and theoretical modelling of ions accelerated by plasmas generated by high intensity pulsed lasers.
The author of this PhD thesis has actively participated in the drafting, data analysis and results' interpretation of the reports listed above [I–III,V,X]. He also dealt with the design and/or adaptation of the experimental apparatus, the collection of measurements, their data analysis, computational calculation, and in part with the drafting of the scientific works mentioned in the list [IV,VI–IX]. In articles [XI–XII], the author of this doctoral thesis did not take part in the measurements, but mainly dealt with the data analysis, by fit of the obtained spectra, or overlapping of the data with numerical calculation methods. Finally, in the scientific articles [XIII–XV], this thesis author did not take part in the experimental measures, but dealt with the comparison of these with numerical simulation approaches and the comparison with the experimental data.

Contents

Introduction

Since the invention of the laser, about six decades ago, coherent light emission focused on solid (or gaseous) materials has been used to evaporate and transform them into a plasma. Plasma is a hot gas in which the thermal energy of its constituents dominates the electrostatic forces that ordinarily bind electrons to the nuclei. Basically, they are an ensemble of charged particles and the fields generated by them, which are characterized by high temperature, density, electrical conductivity and responses to applied external electromagnetic fields. Although less common in our daily experience, it constitutes a large part of the universe, and is considered as the *fourth state of matter*.

In May 1960, T.H. Maiman switched on the first laser based on ruby crystal that emitted light of 694 *nm* wavelength, in red region spectrum. Since then, the laser has become one of the most powerful tools in fundamental research, due to the multitude of applications with a high scientific, technological, industrial and social impact. In the evolution of laser technology, from its advent on earth to the present, we can discriminate two eras distinct from the invention of the *Chirped Pulse Amplification* (CPA) technique, in 1985.

Before the introduction of the CPA technique, lasers were characterized by that which today is referred as "long" pulses, i.e. all those laser pulses that exceed the duration of nanoseconds. The laser light focused for these devices may range between 10^9 and 10^{15} W/cm^2, and has been the object of many experimental campaigns since the early 1960s. Although the basics laser–matter interaction are well known, there is still a lot of physics to be explored in such regime. Long pulses interact with the electrons of matter, forcing them to quiver. While electron–electron collisions contribute only for thermalization, ion–ion collisions take place in a long time, electron–ion collisions become important for evaluating the absorbed energy. The hot plasma electrons temperature generated by long laser pulses is less than *keV* units.

With the advent of CPA technology, the power of a laser pulse has increased significantly. The power is concatenated to the pulse energy and its duration, by definition. Modern lasers are able to achieve pulse durations in the order of picoseconds (short pulses) or even femtoseconds (ultra–short pulses). Thanks to the implementation of the CPA technique, the ultra–short pulse is stretched in time using diffractive elements, reaching time scales of many orders of magnitude higher, up to nanosecond. The pulse energy is then increased, ensuring that the intensity of the amplified beam is below to a critical value that would seriously damage the device (due to non–linear optical effects, such as self–focusing). After amplification, it is recompressed at times comparable to ultra–short pulses.

Short and ultra–short pulses when focused with spot size of tens of microns, may approach 10^{20} W/cm^2. At these intensities, the electrons, heated by the incident electromagnetic wave, quickly reaches relativistic energy in the order of hundreds of MeV, or approaching GeV. Their free mean path can become much larger than the target size (if less than tens of microns), and the system can be schematized as collision–free or collisionless plasma. The most popular ultra–short pulsed laser devices is the Titanium–Sapphire laser (Ti:Sapphire), which is pumped by smaller lasers, such as Nd:YAG systems; Ti:Sapphire laser has typical pulse lengths of the order of tens of femtoseconds. Currently many laboratories around the world have promised intensities above 10^{21} W/cm^2 for the upcoming future, such as the European project namely *Extreme Light Infrastructure* (ELI).

In this work, the main topic is the ion acceleration by means of laser–generated plasmas, with intensities from 10^{10} to 10^{19} W/cm^2, and long to ultra–short pulses. The laser field is not able to accelerate directly the plasma ions to these intensities, however the electrons mediate between the laser beam and the ion acceleration. The electric field generated as a result of the separation of charge between electrons, accelerated by the incident electromagnetic wave, and the positive ions of the target, drives the acceleration of the latter. The maximum energy and properties of the ion beam depend on the accelerating electric field, which may reach values of the order of TV/m. The maximum energies, for protons, range from hundreds of eV, for long pulses and relatively low intensities of 10^{10} W/cm^2, to hundreds of MeV for lasers with intensities of the order of 10^{20} W/cm^2 and ultra–short pulses.

In this scenario, the diagnosis of the ions emitted by the laser–generated plasma depends on the particle energy that has to be detected, and therefore directly on the intensity of the laser used in the interaction. When the ion energies are less than hundreds of keV per charge state, which can be obtained with lasers of an intensity of less than 10^{15} W/cm^2, a suitable analysis of them can be made by means of electrical or magnetic deflections as a result of their passage in proper spectrometers. These devices are usually coupled with the Time–of–Flight (TOF) technique, which consists in evaluating the time necessary for a particle to travel a known distance.

However, at intensities above 10^{15} W/cm^2, ions acquire energies of the order of MeV or higher, and the diagnostics of these become more complex. The electric and magnetic fields of deflection can be combined in a single device, maintaining the values of the fields in the range widely available to any laboratory. An example is the Thomson Parabola Spectrometer (TPS), which employs a magnetic and an electrical field parallel to each other and orthogonal to the direction of the beam, suitably collimated, to deflect the particles, according to the mass–to–charge ratio. The TOF technique, which certainly remains a useful diagnostic tool, presents some difficulties when the laser intensities become high, for example high electromagnetic noise, overlapping of the signal with the photopeak, difficulty in separating the various ions detected, low sensitivity for hot electrons and protons. To overcome these lacks, the semiconductor devices based on silicon carbide clearly improve the signal obtained compared to that detected with Ion Collectors.

The great interest that motivates research of several groups throughout the world is related to the large number of applications arising from the pulsed laser–generated plasmas. From long to ultra–short pulses, all are used in a wide range of scientific, technological or industrial fields. Some of these are, for example, the use of laser plasmas as an ion source to be injected into large accelerators, ion implantation within substrates for the development of advanced materials, nuclear reactions in plasmas, the use of ion beams in medicine or astrophysics, and others. In order to implement several of these applications, the beam must be transported and selected in energy. These operations can be performed by devices such as quadrupoles, sextupoles and magnetic or electrical lenses.
Simulation software such as COMSOL Multiphysics can be used to model correctly the transport of the beam, or the deflection through electric and/or magnetic fields. A comparison between these kind of simulations and the experimental data allows to obtain important information on the main parameters of the charged particle beams, such as energy, acceleration voltage, emittance, angular distribution, charge distribution, and so on. In many others applications, however, it is necessary to know the range of charged particles into the material where they move; in this case one of the best simulation codes, widely adopted by the scientific community, is SRIM, which is able to calculate the ion beams stopping power within the irradiated medium. Finally, for a clear understanding of the interaction dynamics between high intensity lasers and plasmas, the most suitable simulation method is the Particle-in-Cell (PIC) approach. In recent decades, PIC codes have become a unique tool in many areas of plasma physics, and have allowed a more accurate understanding of the phenomena of interaction between high–intensity lasers and plasmas.

Chapter 1

Pulsed Laser–induced non equilibrium Plasmas

For long time, laser–driven ion acceleration, has been proposed in a large number of experiments by nanoseconds duration pulse. Since 1990s, thanks to the advent of Chirped Pulsed Amplification (CPA), picoseconds and femtoseconds laser are developed, reaching ultra–high laser intensity that allowed to accelerate protons up to order of tens of MeV energy. In this first chapter, author wants to introduce the interaction dynamics of long pulses (ns-class lasers) and of short or ultra–short pulses (ps–fs class laser) with matter. The main phenomena responsible for target ionization will be illustrated, such us Multi-photon Ionization (MPI), Barrier Suppression Ionization (BSI) and so on. Since interaction between incoming electromagnetic wave and plasma just formed, while the first propagates, can occurs phenomena like Relativistic Self–focusing, Skin effect, Brunel Mechanism, and so on. Finally, three ion acceleration regimes are introduced. The first, called Backward Plasma Acceleration (BPA), mostly relates to the interaction of long pulses by thick targets, produces ion beam with energy distribution like Boltzmann ones, and cut–off value not higher than tens of keV per charge–state. The second is Target Normal Sheath Acceleration (TNSA), concerning the interaction of short pulses with thin targets, that produces acceleration of (light) plasma ions up to tens of MeV per charge–state. The last discussed, and the most promising, is Radiation Pressure Acceleration (RPA), where an ultra–short pulse interacts with targets in different regimes, and the radiation pressure drive the acceleration. Here the energy of the protons could reach hundreds of MeV per charge–state.

1.1 Laser–Matter Interaction

When high intensity laser is focused onto matter, a large number of free electron is created by photoelectric effect directly, or depending on wavelength and target's material, by multi-photon processes. If the number of electrons is enough, the formation of a dense and highly ionized plasma is more efficient by electron-neutrals and electron-ions collisions. Plasma's duration has a time comparable to that of laser pulse, before the particles expand or recombine if it is in vacuum, air or in liquid respectively [1, 2].

In recent years, the study of plasmas generated by laser pulses has become very topical and important due to the large number of applications that derive from it, such as ions source, pulsed laser deposition, implantation processes, nuclear reaction, proton-therapy and many other [3–6].

1.1.1 Laser Ablation Threshold

Laser ablation consists in the removal of particles, atoms, molecules, clusters and so on, from the target irradiated by laser pulse. The ablation process shows that under a value limit of energy is not possible remove particles from the target; this limit value is called *ablation threshold*.

Laser ablation threshold is a value that depends mainly on the laser fluence and target material. When the laser fluence increases the ablation rate also increases, up to a saturation value. *Torrisi et al.* [7] evaluate the laser ablation rate as function of laser fluence at different wavelenght in polymethylmethacrylate (PMMA), as shown in below figure.

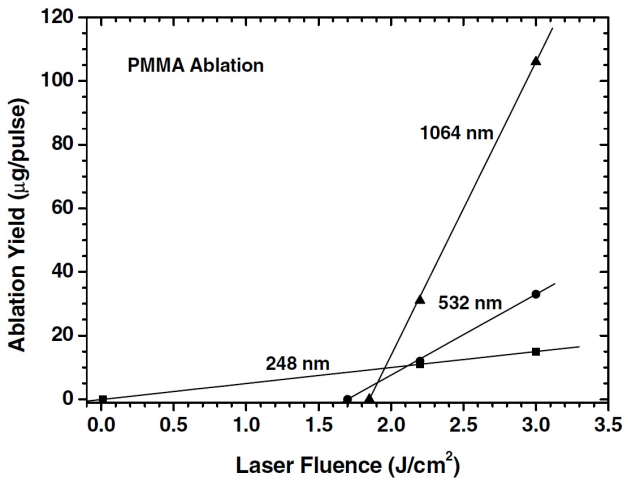

Figure 1.1: *Ablation Yield vs Laser fluence in PMMA at different wavelenght, image from ref [7].*

If we take into account the Figure 1.1, for a Nd:YAG laser with fundamental wavelength 1064 *nm* the ablation threshold is about 1.9 J/cm^2; so if the laser have a pulse duration of a few nanosecond, the minimum laser intensity that ablate a target of PMMA is $\sim 10^9$ W/cm^2. On the other hands, in conducting materials the ablation threshold, in terms of laser intensity, is lower by orders of magnitude [8].

The difference can be found in the internal band structure, and in the number of free electrons present in the different materials.

In fact, in classical treatment of Drude model for metal [9], many electrons can be considered "free" to move in the solid conduction band. An excited electron in conduction band is in contact by a large number of free others electrons. The collision electron–electron can occur in a time of the order 10^{-14} s, while collision electron–phonon time is in the order of 10^{-12} s [10]; these two timescale are far less than the time necessary for an electron–hole recombination with radiative emission [11]. Thus, the non-radiative processes are more likely than the radiative ones, and when the material is hit by an electromagnetic wave, the

electrons interacts through collisional processes that determine an increase in temperature of the irradiated medium and its vaporization. This is called *Thermal Model*.
Thermal model assumes that the threshold fluence represents the energy density necessary to evaporate in vacuum the irradiated mass of target [7]:

$$F_{thr}^{Th} = \frac{E_{heat} + E_{fus} + E_{sub}}{S} = \frac{V\rho}{S}\frac{(c_s\Delta T + \lambda_f + \lambda_e)}{1-R} \tag{1.1}$$

where E_{heat}, E_{fus} and E_{sub} are the heating energy from room to fusion temperature, the fusion energy and the evaporation energy respectively, while S is the spot size of the laser. By a simplification it is possible to rewrite the Equation 1.1 as shown, where V is the ablated volume, ρ is the density of the target, ΔT is the temperature variation, λ_f and λ_e are the fusion and vaporization latent heat respectively and R is the target reflectivity.
On the other hand, if the number of absorbed photon, n_{phot} is larger than atomic density of the medium, n_{at}, and if the photon energy is larger than binding energy of electrons, E_b, we can introduce the *Photochemical Model*, in which the fluence threshold is determine by:

$$F_{thr}^{Ch} = \frac{h\nu n_{at}}{\alpha} \tag{1.2}$$

where $h\nu$ represents the photon energy, and α is the material absorption coefficient.
However, the thermal and photochemical models can be considered a limit case of the *Physical Model*; in which the thermal and non–thermal mechanism are both contribute to the whole process [12].

Laser Ablation *vs* Pulse Duration

When a *ns*-class laser interact with a medium can produce different effect than a fs-class laser. In literature there are several experiments comparing laser ablation of solid target by nanosecond and femtosecond laser [13, 14].
Due to very short pulse for *fs*–laser respect the *ns* ones, the ablation process can be considered a directly transition from solid to plasma. In this way the thermal conduction process can be neglected, due to fast plasma expansion. Instead, when a long pulse interact with a solid target, like in case of *ns*–laser, there is enough time for thermal wave to propagate into the target melting and vaporizing it [15, 16].
In Figure 1.2 two craters are shown produced by a *fs*–laser (short or ultra–short pulses) and *ns*–laser (long pulses). It is clear to observe that in the case of short pulses (Figure 1.2a) there are not signs of heating in the ablated crater; on the contrary, Figure 1.2b shows how a *ns*–laser produces thermal effects that lead to the local melting of the material and consequent re-solidification.

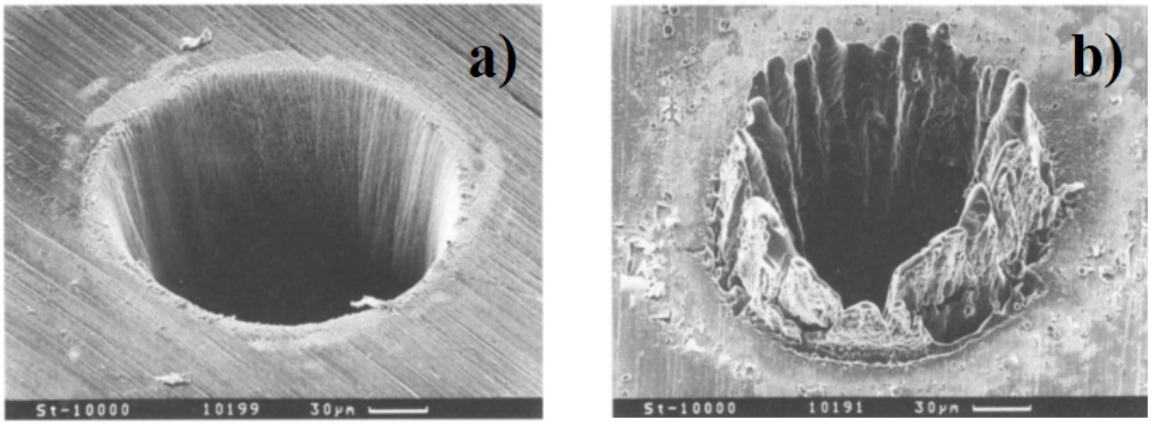

Figure 1.2: *SEM photograph of the Crater depth in 100 µm of thick steel foil produced by: fs–class laser with 200 fs pulse duration, 120 µJ energy and 780 nm wavelength (a), and ns–class laser with 3.3 ns pulse duration, 1 mJ energy and 780 nm wavelength (b) (image reprinted from ref [15]).*

1.1.2 Matter Ionization

An high intensity electromagnetic wave that impacts by material, can ionize it through different phenomena. Thus, it is important, first of all, to transcribe the well-known correlation between intensity and electric field of the wave [17]:

$$I\left[\frac{W}{cm^2}\right] = \frac{\epsilon_0 c \xi^2}{2} \cong 1.32 \times 10^{-3} \left(\xi\left[\frac{V}{cm}\right]\right)^2 \tag{1.3}$$

where I is the light intensity in W/cm^2, ϵ_0 is the vacuum permittivity, c is the speed of light and ξ is the electric field magnitude in V/cm. Therefore, if we take into account an hydrogen atom, and as distance between electron and proton the Bohr radius, the atomic binding field of electron is of the order of 5×10^9 V/cm. From Equation 1.3 the intensity that guarantee ionization for all target is of the order of $\sim 10^{16}$ W/cm^2, even if in reality it can occur also below this intensity value by multiphoton effects.

Multiphoton Ionization

The well–know Photoelectric Effect claims that if a photon, of a certain energy, interacts with an electron bound to an atom, can give all its energy, disappearing from the dynamics of interaction; the electron having acquired equal or greater energy to the bonding ones can then be emitted from the belonging atom. This is a single-photon linear process. However, ionization of an atom is possible if the electron absorbs a single high–frequency photon or several lower frequency photons (*MultiPhoton Ionization*, MPI).

The probability of absorbing n photons depends strongly on the intensity of the laser itself (photon density), I_L; through a perturbation development it has been found that:

$$\Gamma_n = \sigma_n I_L^n \tag{1.4}$$

where σ_n is the ionization processes cross section. The first experimental results occurred with the use of laser intensity grater than $10^{10}\ Wcm^{-2}$, highlighting the MPI [18,19].

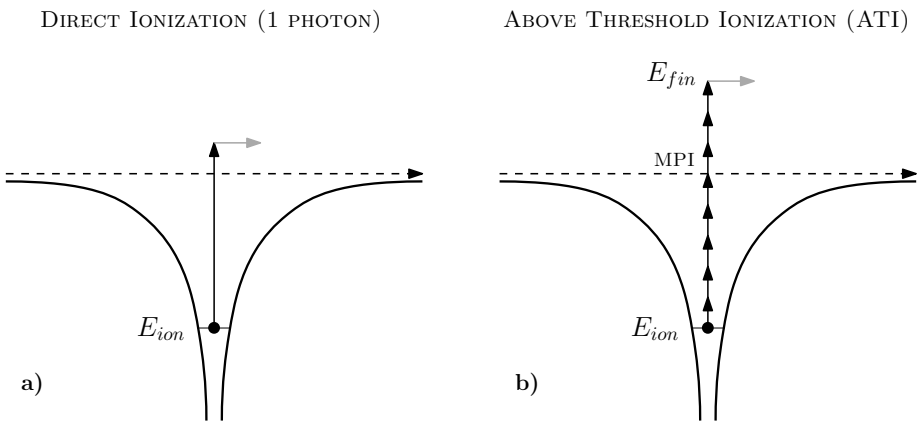

Figure 1.3: *Schematic picture of: a) photoelectric effect where an electron with binding energy E_{ion} absorb one photon with energy $\hbar\omega$ and is subsequently released from the atom; b) ATI where an electron with binding energy E_{ion} absorb more photons with energy $\hbar\omega < E_{ion}$ and is subsequently released from the atom with a certain kinetic energy E_{fin}.*

An extension of MPI is the *Above Threshold Ionization* (ATI), shown in Figure 1.3, in which an electron can absorb more photons than strictly necessary to free it from the atom. The final kinetic energy, E_{fin}, of the electron is given by:

$$E_{fin} = (n + n_{ATI})\hbar\omega - E_{ion} \tag{1.5}$$

where n is the number of photon necessary to MPI processes, n_{ATI} is the is the number of excess photons absorbed, $\hbar\omega$ is the photon energy and E_{ion} is the electron binding energy.

Tunneling Ionization

Strong electromagnetic field that interact with matter can ionize it by others phenomena. An important assumption of MPI is that atomic binding remains constant during the interaction. We can consider this true if the intensity laser remains below of the value of $\sim 10^{16}\ Wcm^{-2}$, at which point the external field becomes enough strong to distorts the Coulomb field felt by binding electron.

This problem can be approached by a classical treatment in which di Coulomb binding potential is perturbed by an homogeneous and stationary external field:

$$U(x) = -\frac{Ze^2}{x} - e\xi x \tag{1.6}$$

where Z is the atomic number and e is the elementary charge. So, Equation 1.6 says that the coulomb barrier can become finite, and for quantum mechanics, an electron can escape by tunneling with a finite probability given by Keldysh's formula [20].

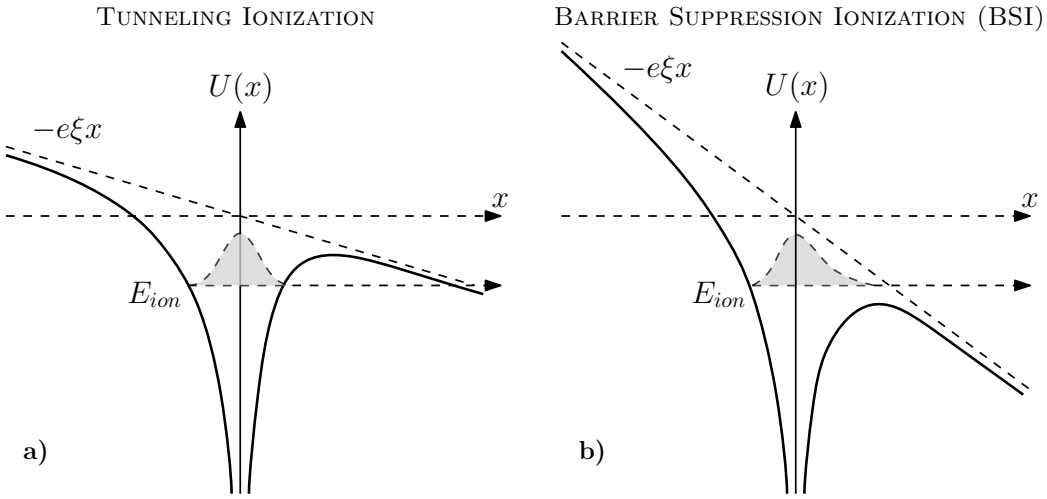

Figure 1.4: *Schematic picture of tunneling ionization (a), and Barrier Suppression Ionization (b), by strong electric field.*

In Figure 1.4a is shown a schematic picture of how the Coulomb binding potential can become finite. If the barrier falls below E_{ion}, the electron will escape spontaneously; this phenomena is called *Barrier Suppression Ionization* (BSI), shown in Figure 1.4b. However, short laser pulse duration is a prerequisite for observing tunneling or BS ionization [21, 22].

MPI and Tunneling ionization Competition

Keldish and Perelomov more than 40 years ago, introduced a parameter γ, for discriminate multiphoton ionization from tunneling ones regimes [20, 23].

$$\gamma = \omega_L \sqrt{\frac{2E_{ion}}{I}} \backsimeq \sqrt{\frac{E_{ion}}{\Phi_{pond}}} \tag{1.7}$$

where ω_L is the angular laser frequency and Φ_{pond} is the ponderomotive potential, which is indicative of the electron energy acquired by oscillation in the laser field; see section 1.1.3.

$$\Phi_{pond} = \frac{e^2 \xi_L^2}{4 m_e \omega_L^2} \tag{1.8}$$

where ξ_L is the electric field magnitude of the incident beam and m_e is the electron mass. Thus, from Equation 1.7 we can distinguish two regimes; when the beam intensity is low (less than $\sim 10^{16}\ Wcm^{-2}$) gamma factor is greater than 1, and the MPI is the predominate mechanism to ionization ($\gamma > 1$); when the intensity is very high (greater than $\sim 10^{16}\ Wcm^{-2}$), gamma factor is smaller than 1, so tunneling and BSI are channels followed for ionization ($\gamma < 1$). When $\gamma \approx 1$ both of two ionization types are present.

1.1.3 The Ponderomotive Force

After matter ionization a plasma is been create. The external wave that propagating can interact with free electrons, pushing the last ones away from where the field is most intense through the *Ponderomotive force*. This is a non-linear effect, and play a role very important specially in ultra-short laser pulse.
A simple relation can be derived from the perturbative and non-relativistic study of a charge particle in a monochromatic electromagnetic wave field. For simplicity, the writer suppose that the wave (with frequency ω and wave vector $\mathbf{k}$) propagates along the *z–axis*, as shown in Figure 1.5; so the equation of the particle motion (with $q = ze$ charge, and m mass) can be decomposed into an equation along the *x–axis*, where it is the electric field to cause the

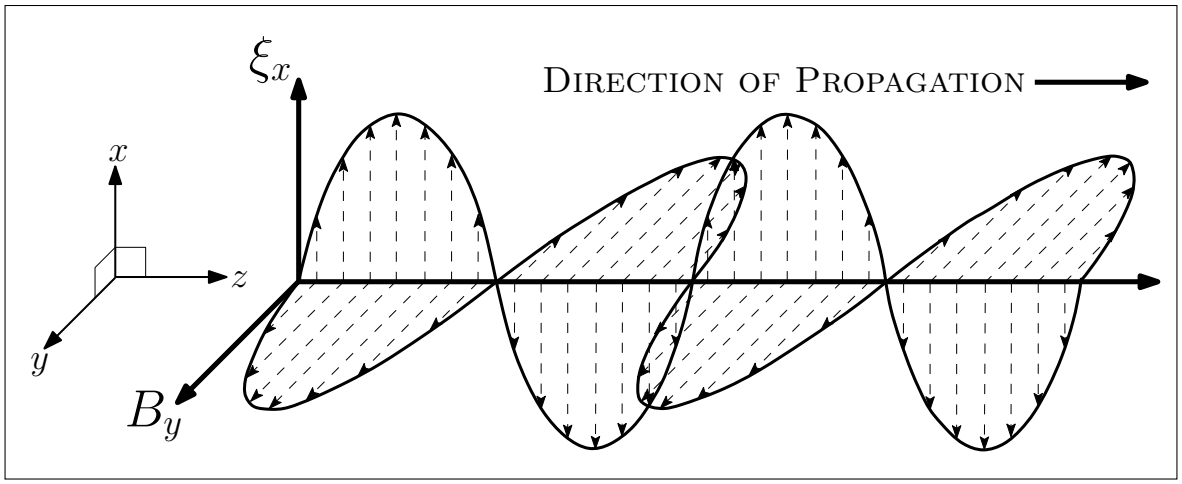

Figure 1.5: *Schematic picture of electromagnetic wave propagation along z – axis.*

variation in the charged particle motion; and in one along *z–axis* due to the magnetic field (directed along *y–axis*).

$$\frac{\partial \mathbf{v}_x}{\partial t} = \frac{q}{m}\boldsymbol{\xi}(\mathbf{x},t) \tag{1.9}$$

$$\frac{\partial \mathbf{v}_z}{\partial t} = \mathbf{v}_y \frac{q}{m}\boldsymbol{B}(\mathbf{y},t) \tag{1.10}$$

where $\mathbf{v}_x$ and $\mathbf{v}_z$ are the electron velocity along the *x–axis* and *z–axis* respectively, $\boldsymbol{\xi}(\mathbf{x},t)$ and $\boldsymbol{B}(\mathbf{y},t)$ are the electric and magnetic field of the wave. A Taylor expansion of the electric field is given by:

$$\boldsymbol{\xi}(\mathbf{x},t) \simeq \boldsymbol{\xi}_0(\mathbf{x})\cos\phi + \mathbf{x}\frac{\partial \boldsymbol{\xi}_0(\mathbf{x})}{\partial \mathbf{x}}\cos\phi + \ldots \tag{1.11}$$

where $\boldsymbol{\xi}_0$ is the wave maximum amplitude and $\phi = \mathbf{k}\cdot\mathbf{z} - \omega t$ is the wave phase. If we substitute the Equation 1.11 into Equation 1.9, and integrating it, at the lowest order we can obtain the velocity and position of the particle studied. However, the velocity oscillation, known as "**quiver velocity**", of the particle definite by:

$$\mathbf{v}_{osc} = \frac{q\boldsymbol{\xi}_0}{m\omega} \tag{1.12}$$

Thus, at first order we have simple electron oscillation around equilibrium position. When we take into account the second order of the Taylor expansion for the field in Equation 1.9, through simple mathematical substitutions, and taking the cycle-average yields the ponderomotive force is given by [2]:

$$\mathbf{F}_p \equiv -\frac{q^2}{4m\omega^2}\frac{\partial \boldsymbol{\xi}_0^2}{\partial \mathbf{x}} \tag{1.13}$$

in more compact form, the Equation 1.13 can be rewrite as:

$$\mathbf{F}_p(\mathbf{x}) = -\boldsymbol{\nabla}\Phi_{pond}(\mathbf{x}) = -\frac{q^2}{4m\omega^2}\boldsymbol{\nabla}\left|\boldsymbol{\xi}_0(\mathbf{x})\right|^2 \tag{1.14}$$

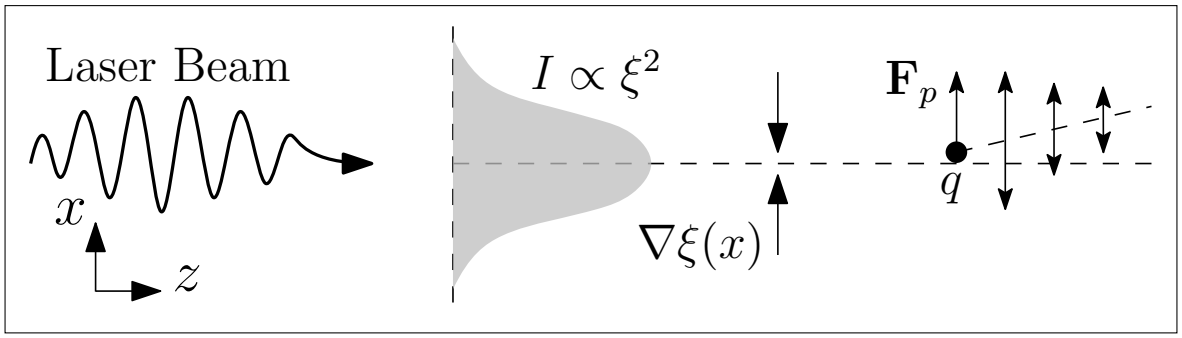

Figure 1.6: *Pondermotive force acting on a charged particle (with mass "m" and charge "q"). Image inspired from ref [2].*

From the Equation 1.14 we see immediately from where the Equation 1.8 for the ponderomotive potential is derived. However, some important implications derive from the Equation 1.14.
First of all, the ponderomotive force pushes the charged particles into the region where the field is lower regardless of their charge, as schematically outlined in Figure 1.6. In fact, the proportionality to q^2 means that the force has the same direction for both, positive and negative charged particles. Moreover it is inversely proportional to the mass of the particle on which it acts. The writer wants to remark that this derivation formula is good in the non-relativistic case; for relativistic case see Paragraph 1.1.4. Thus the force acting on a electron will be about 3 orders of magnitude higher than it acting on a proton. Some experimental results confirm the electron acceleration due to ponderomotive force [24, 25].

1.1.4 Relativistic Regime

An high intensity laser beam that interact with plasma, can accelerate electrons by the field itself, while ions can be considered at rest, due to their large charge to mass ratio with respect to the first. Electrons accelerated, acquire a kinetic energy greater than their mass at rest, and they could transit in highly *relativistic regime*.
It is usually, in high intensity field, to introduce the *dimensionless normalized vector*, that is correlate to electric field of the laser beam by the following:

$$a_0 = \frac{e\xi_L}{m_e c\omega_L} \tag{1.15}$$

where c is the light velocity. Comparing Equation 1.12 with the last one, give:

$$a_0 = \frac{v_{osc}^{(e)}}{c}$$

where $v_{osc}^{(e)}$ is the electron quiver velocity in the external field. So, the a_0 parameter provides a quantity that is indicative for the incidence of relativistic effect in the electrons dynamics. It is clear that if the electron velocity is close to that of light, a relativist treatment for Equation 1.15 is required. If we recall the Equation 1.3, and remembering that angular frequency is correlate to laser wavelength (λ) from the expression $\omega_L = 2\pi c/\lambda$, the Equation 1.15 can be rewrite as follows:

$$(2\pi)^2 \frac{\epsilon_0 m_e^2 c^5}{2e^2} a_0^2 = I\lambda^2 \quad \Longrightarrow \quad I\lambda_\mu^2 \approx 1.37 \cdot 10^{18} a_0^2 \quad \left[\frac{W \cdot \mu m^2}{cm^2}\right] \tag{1.16}$$

where λ_μ indicate the wavelength express in μm. This relation means that laser beam linearly polarized that have an intensity greater than $\sim 10^{18}$ W/cm^2 will accelerate electrons in the relativistic regime [26,27]. From the last equation we note that the quiver velocity of electron scale as $I\lambda_\mu^2$.

Ponderomotive Force in Relativistic Regime

To obtain a relativistic formula for the Equation 1.14 it is necessary to consider a fluid cold plasma model. The motion of particles in presence of an electromagnetic field is given by Lorentz equation:

$$\frac{d\mathbf{p}}{dt} = q\left(\boldsymbol{\xi} + \frac{1}{c}\mathbf{v}\times\mathbf{B}\right) \tag{1.17}$$

where $\mathbf{p}$ is the particle momentum. Rewriting the last one in terms of vector potential $\mathbf{A}$, the equation becomes:

$$\left(\frac{\partial}{\partial t} + \mathbf{v}\cdot\boldsymbol{\nabla}\right)\mathbf{p} = q\left[-\frac{1}{c}\frac{\partial\mathbf{A}}{\partial t} - \boldsymbol{\nabla}\phi + \frac{\mathbf{v}}{c}\times(\boldsymbol{\nabla}\times\mathbf{A})\right] \tag{1.18}$$

where $\mathbf{v}$ is the particle velocity and ϕ is the potential. We can separete the momentum into two component $\mathbf{p} = \mathbf{p}_\perp + \mathbf{p}_\parallel$. If the fluid is at rest initially the transversal component follows the vector potential:

$$\mathbf{p}_\perp = \frac{q\mathbf{A}}{c}$$

as in previous case (non-relativistic ones). Averaging over a laser cycle, we arrive at the following expression for the ponderomotive density force in relativistic regime from the longitudinal momentum component:

$$\mathbf{F}_p = \frac{d\mathbf{p}_\parallel}{dt} = -mc^2\boldsymbol{\nabla}\overline{\gamma} \tag{1.19}$$

where $\gamma = (1 + p_\parallel^2/m^2c^2 + a_0^2/2)^{1/2}$; for a rigorous derivation analysis for pondermotive force in relativistic regime see [28, 29].

Electrons ejection from the Focused beam

In Section 1.1.3 we have already seen that in non-relativistic case the electron is pushed out from the beam focus, at 90° angle deflection with respect laser beam axis. At higher intensities, in the relativistic regime, the electrons are pushed in forward direction with respect to laser beam axis.
The ponderomotive force in relativistic regime act as force that deriving from radiation pressure of a pulse laser. The laser pressure, at high intensity, can be larger than the plasma pressure, even for extremely dense plasmas. The pressure in terms of $I\lambda_\mu^2$ can be write as follows [30]:

$$P_L = 330\frac{I\lambda_\mu^2}{10^{18}} \qquad Mbar \tag{1.20}$$

For example, a laser with $I\lambda_\mu^2 = 3\times10^{18}\ W\cdot\mu m^2/cm^2$ exert a pressure of about 1 $Gbar$. First of all we observe that the final kinetic energy of the electrons is given by:

$$E_e = (\gamma - 1)mc^2 \tag{1.21}$$

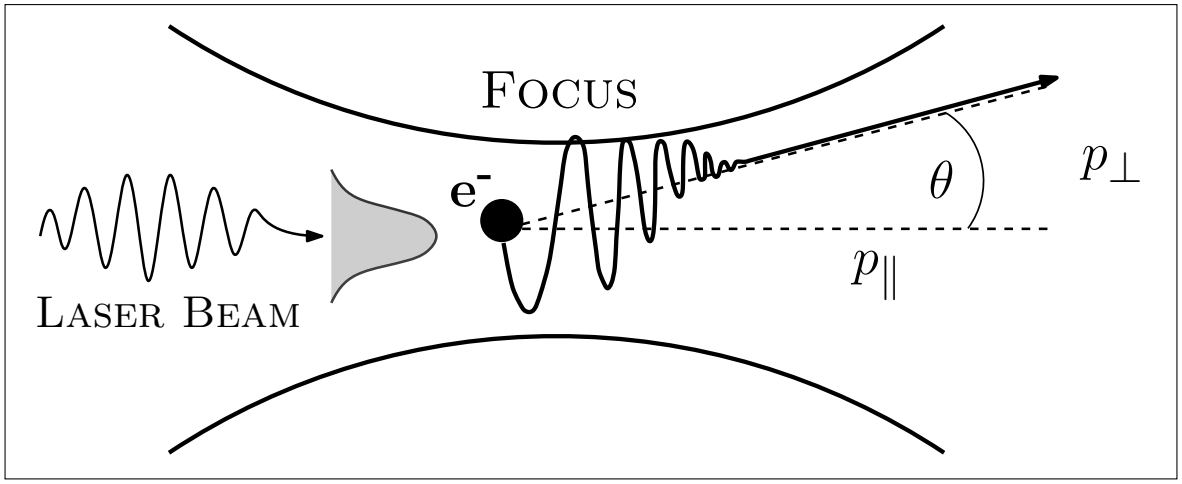

Figure 1.7: *Electron motion in a laser beam focus, in relativistic regime interaction (image inspired from ref [2]).*

We can assume that the energy associated with the electron is given by the potential that they feel during the interaction with the laser light. So in this way, the electrons temperature scales as [31]:

$$T_{hot} \approx \left(\sqrt{1 + \frac{I\lambda_\mu^2}{1.37 \times 10^{18}}} - 1 \right) 511 \; KeV \tag{1.22}$$

For example, a laser with $I\lambda_\mu^2 = 4 \times 10^{18} \; W \cdot \mu m^2/cm^2$ the electrons temperature will be about $\sim 500 \; keV$.
From Equation 1.21, since the parallel momentum is conserved, we must have:

$$p_\parallel = \frac{E_e}{c} = (\gamma - 1)mc \tag{1.23}$$

The relation that correlate parallel momentum with perpendicular ones is the following:

$$p_\parallel = \frac{p_\perp^2}{2mc} \tag{1.24}$$

The Figure 1.7 shown the electron motion in the focus laser beam. Here we can see the parallel and perpendicular component of the electron momentum. From geometrical consideration we can obtain the ejection angle from the focus:

$$\tan\theta = \frac{p_\perp}{p_\parallel} = \sqrt{\frac{2}{\gamma - 1}} \tag{1.25}$$

or

$$\cos\theta = \sqrt{\frac{\gamma-1}{\gamma+1}} \tag{1.26}$$

Thus, when the γ factor is large enough, and the electric field is sufficiently high (of course, from relation of γ that depends on a_0 parameter and Equation 1.15), the electrons are ejected from the focus beam at small angles.
This simple one-to-one relationship between exit angle and energy implies that the laser beam, for ultra-short pulse, acts both as accelerators and spectrometer for free electrons placed near its focus [2, 32].

1.1.5 Plasma Collisions

The simple and the most obviously way to absorb laser energy in plasma, is under collision. At low intensity, below $10^{15}\ Wcm^{-2}$, electrons that interacts with the external electromagnetic field, becomes to oscillating with a velocity $\mathbf{v}_{osc}$ as we previously see. While electron–electron collisions contribute only for distribution function thermalization, and ion–ion collisions take place in long times due to their larger masses, the interaction electron–ions becomes important for evaluating the absorbed energy. This process is know as *Inverse Bremsstrahlung* [33–35].
To include the collisions effect, we have to consider an appropriate term in Lorentz equation (1.17), proportional to the particle velocity; so the Lorentz equation becomes:

$$m_e\frac{\partial \mathbf{v}_{osc}}{\partial t} = -e\left(\boldsymbol{\xi} + \frac{1}{c}\mathbf{v}_{osc}\times\mathbf{B}\right) - m_e\nu_{ei}\mathbf{v}_{osc} \tag{1.27}$$

where ν_{ei} is the electron–ion collision frequency, calculated by classical scattering theory, and given by [36]:

$$\nu_{ei} = \frac{\sqrt{32\pi}}{3}\frac{n_e z e^4}{m_e^2 v_{th}^3}\ln\Lambda \simeq 2.91\times10^{-6} Z n_e (T_e[eV])^{-3/2}\ln\Lambda \tag{1.28}$$

where n_e is the electron density in cm^{-3}, z is the number of free electrons, T_e is the temperature in eV and v_{th} is the thermal velocity of electron in plasma given by

$$v_{th} = \omega_{pe}\lambda_D \tag{1.29}$$

Here, ω_{pe} represents the electron frequency in plasma and is given by:

$$\omega_{pe} = \sqrt{\frac{n_e e^2}{\epsilon_0 m_e}} \tag{1.30}$$

while, λ_D is the Debye length, and it is the spatial distance within the mobile electric charges that shield the electric field inside the plasma; its expression is the following:

$$\lambda_D = \sqrt{\frac{\epsilon_0 k_B T}{n_e e^2}} \tag{1.31}$$

where k_B is the Boltzmann constant. Returning to the Equation 1.27, $\ln \Lambda$ represents the Coulomb logarithm, that take into account the classical electron-ion scattering cross section. It has the following form:

$$\ln \Lambda = \ln\left(\frac{b_{max}}{b_{min}}\right) = \ln\left(\lambda_D \frac{k_B T_e}{z e^2}\right) \tag{1.32}$$

where b is the impact parameter in classical treatment [37]. Equation 1.28 shows that the importance of collisions decrease as temperature increasing.

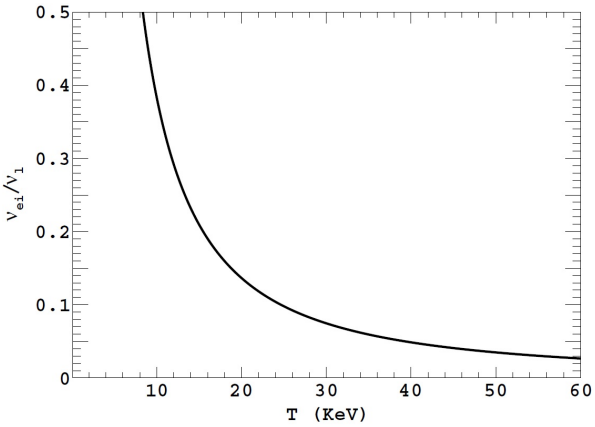

Figure 1.8: *Normalized electron–ion collision frequency with respect laser frequency versus electron temperature. The curve has been obtained from a solid density of* 6×10^{23} cm^{-3}, $z = 1$ *and laser wavelength of 800 nm.*

However, the Equation 1.28 was estimate in Figure 1.8, where the normalized electron–ion collisions frequency in laser frequency units is reported as function of electron temperature for a solid density plasma. The collisional frequency decreases below 5% of the laser frequency at $T_e = 30$ keV (for a Ti:Sapphire laser with a wavelength of 800 nm), which is reach very fast in ultra–short pulse interactions.
When a short laser pulse interact with a solid target, the collisional absorption is neglected before the laser peak reaches the plasma. In this regime the electron quiver velocity v_{osc}, becomes comparable with the thermal ones.

For intensities above 10^{15} W/cm^2 or so, the plasma temperature rises sufficiently fast, and the electron–ion collision became ineffective. In this way the temperature scale as:

$$T_e \propto I_a^{4/9} t^{2/9} \tag{1.33}$$

where I_a is the absorbed intensity and t is the time coordinate. So, for an absorbed intensity of 10^{15} W/cm^2 after just 10 fs the electron temperature can reach the value of 400 eV [2, 39]. For this reason, in ultra–intense laser regime, we can consider a model without collision; in this way the laser absorption and heating electrons must to be mainly attributable at collisionless phenomena [38].

1.2 Wave–Plasma Interaction

The propagation of laser pulse in a plasma is governed by the Maxwell equations in matter [40]. It is useful to introduce now the polarization vector of the plasma, $\mathbf{P}(\boldsymbol{\xi}, t)$, that represents the dipole moment for unit volume when an electric field interact with the material of interesting. This polarization vector, can be expanded in series, if we assume that electrons responds instantaneously to external field [41]:

$$\mathbf{P}(t) = \epsilon_0 \sum_{n=1}^{\infty} \chi_{ij}^{(n)}(\boldsymbol{\xi}, t)\boldsymbol{\xi}(t) = \epsilon_0 \left(\chi_{ij}^{(1)} + \chi_{ij}^{(2)}(\boldsymbol{\xi}, t)\chi_{ij}^{(3)}(\boldsymbol{\xi}, t) + \dots \right) \boldsymbol{\xi}(t) \tag{1.34}$$

where χ is the susceptibility. At the first order approximation $\chi_{ij}^{(1)}$ the proportionality is constant, and it depends only on the microscopic structure, in this case the plasma. Higher orders take into account non-linear effects.
The first order of susceptibility corresponds to a linear response of plasma, and this means that we consider a cold, fluid and homogeneous plasma. In this way susceptibility do not depends on the external field, and the Equation 1.34 becomes:

$$\mathbf{P}(t) = \epsilon_0 \chi^{(1)} \boldsymbol{\xi}(t) \tag{1.35}$$

Let's take into account the second time derivatives of the Equation 1.35 for a purely transversal plasma response. We have to denote that the polarization vector derivate with respect to time represents the bound current, that can be express in terms of quiver electron velocity. By comparing these two simple observations, we obtain the expression for susceptibility at first order:

$$\chi^{(1)} = -\frac{e^2 n_e}{\epsilon_0 m_e \omega^2} = -\frac{\omega_{pe}^2}{\omega^2} \tag{1.36}$$

where the electron frequency in plasma is given by $\omega_{pe} = e^2 n_e / \epsilon_0 m_e$. However the refractive index η, is related at susceptibility by the expression:

$$\eta = \sqrt{1 + \chi^{(1)}} = \left(1 - \frac{\omega_{pe}^2}{\omega^2} \right)^{1/2} = \frac{c}{v} \tag{1.37}$$

From Equation 1.37 it is possible to obtaining the *dispersion relation* that contains the solution for the plasma wave and for the transversal electromagnetic modes that propagates through the plasma [42]:

$$\omega^2 = \omega_{pe}^2 + c^2 k^2 \tag{1.38}$$

Dispersion relation show in Equation 1.38, means that the plasma frequency ω_{pe} sets a lower value for an electromagnetic wave frequency that across the plasma. Of course, a laser pulse

with frequency ω can propagate into a plasma until the density reaches a critical value:

$$n_{cr} = \frac{\epsilon_0 m_e \omega^2}{e^2} = \frac{1.1 \times 10^{21}}{\lambda_\mu^2} [cm^{-3}] \tag{1.39}$$

Therefore, for example if we use a Ti:Sapphire laser with foundamental wavelength of 0.8 μm, the critical density is $\sim 1.7 \times 10^{21}\ cm^{-3}$. Thus, the laser–plasma interactions take place in an *under–dense plasma* $n_e < n_{cr}$ or in the region called *near–critical* $n_e \approx n_{cr}$. While if the electron density have value above the critical ones, this region in called *over–dense plasma* $n_e > n_{cr}$ [43–45].
Since a relativistic treatment is required, the Equation 1.39 must be multiply for relativistic factor γ, which is define:

$$\gamma = \sqrt{1 + p^2 + a^2} \tag{1.40}$$

where $p = |\mathbf{p}|/m_e c^2$ is the normalized magnitude of the electron momentum, and $a = e|\mathbf{A}|/m_e c^2$ is the adimensional amplitude of the electro-magnetic vector potential. The critical density in relativistic case becomes:

$$n_{cr} = \gamma \frac{\epsilon_0 m_e \omega^2}{e^2} = \gamma \frac{1.1 \times 10^{21}}{\lambda_\mu^2} [cm^{-3}] \tag{1.41}$$

The Equation 1.41 shown that if the relativistic factor is greater than one $\gamma > 1$, the laser pulse can propagate in the region which is classically defined as over–critical density; this phenomena is called *relativistic induced transparency* [46, 47].

1.2.1 Laser Propagation in Underdense Plasmas

When a laser pulse propagates through an underdense plasma, it excites an oscillating plasma wave at frequency ω_p. The frequency of plasma oscillation is about the electrons oscillatory frequency due to their high charge to mass with respect to the ions, so $\omega_p \cong \omega_{pe}$.
To find the maximum electric field that can propagate into a plasma, *Akhiezer and Polovin* provided their solutions for cold plasma oscillations [48]. First of all, we have to take into account that the fluid velocity cannot exceed the phase velocity. If it happens, some of the electron charge sheets may cross each other, and the wave lost its coherence (*wavebreaking*). The maximum electric field is given by [49]:

$$\xi_{max} = \frac{m_e \omega_{pe} v_p}{e} \tag{1.42}$$

where v_p is the phase velocity. This is called cold wavebreaking limit.
If we consider a warm plasma the scenario is different, due to thermal effects that act to reduce the maximum attainable wave amplitude. The reasons are that the plasma pressure

resists the tendency for the density to explode, and thermal electrons moving in the direction of the wave may be trapped at a lower wave amplitude, then cold electrons would be. The equation for maximum electric field is the following [50]:

$$\xi_{max} = \frac{m_e \omega_{pe} v_p}{e} \left(1 - \frac{\mu_{th}}{e} - \frac{8\mu_{th}^{1/4}}{3} + 2\mu_{th}^{1/2} \right)^{1/2} \tag{1.43}$$

where $\mu_{th} = 3k_B T_e / m_e v_p^2$. In a cold plasma limit ($\mu_{th} = 0$), Equation 1.43 reduces to the maximum amplitude introduced earlier (Equation 1.42). This is obtained in non-relativistic regime. For the relativistic ones see ref [51].

Instabilities

Laser plasma instabilities refers to a laser wave coupling with other wave type in the plasma interaction, such us ion acoustic wave, electrons plasma wave, and how the electromagnetic wave can influences itself the propagation by decay. The instabilities in plasma is mainly due by density fluctuations into itself, caused by ponderomotive force of laser intensity fluctuations.
A laser pulse that propagate into a plasma can interact by electron plasma wave; so the condition for decay wave vector, $\mathbf{k}_d$, is:

$$\mathbf{k}_d = \mathbf{k}_l - \mathbf{k}_p \tag{1.44}$$

where $\mathbf{k}_l$ and $\mathbf{k}_p$ are the wave vector for laser pulse and electron plasma ones respectively. The beating from the incoming and scattered waves causes fluctuation in electric density. If this phenomena is consistently, it can indices an ion density oscillation that constitute an acoustic wave. A fluctuation in the ions density induces fluctuations in electron density in turns, and thus the instability grows further.
The interaction type between laser pulse and plasma wave determine the resulting instability. For example the interaction between the laser pulse and an ion acoustic wave is called *Stimulated Brilluin Scattering* (SBS), or an interaction laser–electron plasma wave is called *Stimulated Raman Scattering* (SRS). Interactions between electron–electron plasma wave is called *Two Plasmon Decay*, and so on [36, 52–54].

Relativistic Self-Focusing

When a relativistically intense laser beam propagating in underdense plasmas a phenomena called *Relativistic Self-Focusing* can occurs. Relativistic self-focusing is due mainly from the mass increase of relativistic electron close to laser axis and from their ejection to focused beam, through ponderomotive force, as we just seen. In terms of refractive index, this phenomena occurs when this has a maximum on the focal axis, or when $\partial\eta/\partial r < 0$, where r

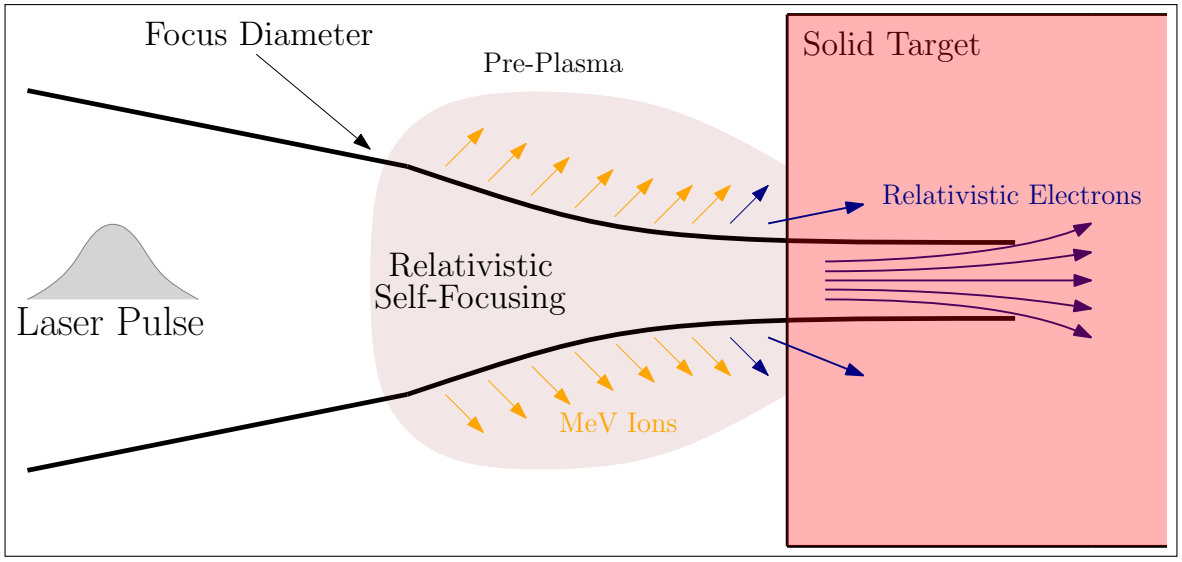

Figure 1.9: *Schematic illustration of relativistic self-focussing phenomena in a pre-plasma with density less than critical density.*

represents the radial distance from focal axis. Assuming an uniform plasma density, if the quasi–static approximation can be applied, the refractive index for long pulse becomes [2]:

$$\eta = 1 - \frac{1}{2}\frac{\omega_{pe}^2}{\omega^2}\left(1 - \frac{a_0^2}{2}\right) \tag{1.45}$$

Since the laser beam amplitude falls off transversely, $\partial a_0/\partial r < 0$, so the refractive index will be, $\partial\eta/\partial r < 0$. The negative transverse gradient of the refractive index can lead to optical guiding. On the other hand, *Sprangle et al.* demonstrate that pulses shorter than a plasma wavelength cannot be relativistically guided [55]. Figure 1.9 show an illustration of the relativistic self-focusing phenomena in underdense plasma.
Thus, we can to define a critical value for the power of laser, that indicate the threshold to undergoes relativistic self-focusing. For a laser beam the propagate in underdense plasmas with plasma frequency ω_{pe} smaller than the laser frequency ω, the power critical value is given by [56, 57]:

$$P_{cr} \backsimeq 17\frac{\omega}{\omega_{pe}} = 17\frac{n_{cr}}{n_e} \quad [GW] \tag{1.46}$$

For example, the critical power for $n_e = 0.1 n_{cr}$, is about $P_{cr} \backsimeq 170\ GW$; which can be largely exceeded by modern terawatt and petawatt lasers [58, 59]. This is also been experimentally demonstrated, where for $P < P_{cr}$ ionization induced defocusing, while for $P > P_{cr}$ relativistic self-focusing occurs [60, 61].

1.2.2 Laser–solid interaction: Overdense Plasmas

The interaction between laser pulse and overdense plasmas depends sensitively on the laser parameters, such us intensity, wavelength, pulse duration, temporal profile and so on. The laser beam induce in front of target processes like melting, surface evaporation and ionization, thus a plasma is crate with a density many times the critical ones. As we previously described, in this regime, plasma becomes opaque for incident laser beam with frequency ω, as you can see from Equation 1.39. The electron density created in this region is given by:

$$n_e = \frac{N_A \rho}{A} Z \tag{1.47}$$

where N_A is the Avogadro number, ρ is the solid density, A is the atomic number and Z is the effective ion charge. So for example, if we take into account an Aluminium target, which have $\rho = 2.7\ g/cm^3$, $A = 27\ amu$ and effective charge equal to 9, the density electron is about $n_e \sim 5.4 \times 10^{23}\ cm^{-3}$. In a previously example we have seen that the critical density for a Ti:Sapphire laser was about $n_{cr} \sim 1.7 \times 10^{21}\ cm^{-3}$, so more less than electron density in aluminium of two hundreds times.
When a long pulse interact by a solid target an underdense plasma region is create in front of it. But for short pulse duration there is not enough time for a substantial region of coronal plasma to form in front of solid target.
Of course, in short pulse duration, if the *contrast* of the laser system is not sufficiently high, the formation of pre–plasma profile is observed. In this way, thanks to this steep density gradient, the laser pulse interact directly with the solid–density plasma which is just created; thus, the absorption of main pulse laser energy becomes possible at or below the critical density [62, 63].

Charge distributions in overdense plasmas

The determination of the charge state distribution in a laser–induced plasma is not a topic of easy task. For high density and optically thick plasma, absorption and emission processes are balanced; in these conditions plasma is in Local Thermal Equilibrium (LTE), and the ionization degree, Z^*, can be determined by Saha-Boltzmann equation [64]:

$$\frac{1 - Z^*}{Z^{*2}} = 4.14 \times 10^{-16} n_0 T^{-3/2} \exp\left[\frac{E_{ion}}{k_B T}\right] \tag{1.48}$$

where n_0 is the total density in plasma. Ionization degree is defined as the ion density with respect the total density in LTE plasmas $Z^* = n_i / n_0$.
While Saha–Boltzmann equation offers a good starting point, when a short laser pulse interacts with solid targets can produce optically thin plasmas; this means that the radiation from the recombining ions can escape completely from the plasma, and so the LTE condition not is satisfied. In this situation it requires the solution of time–dependent atomic rate equations in order to determine the charge distribution [65].

Skin Effect

When we can consider the approximation of cold plasma, i.e. when electron motion could be neglected, the relation between current in plasma, $\mathbf{J}$ and the electric field $\boldsymbol{\xi}$, is given by Ohm law:

$$\mathbf{J} = \widehat{\sigma}\boldsymbol{\xi} \tag{1.49}$$

where $\widehat{\sigma}$ is the conductivity tensor, that for an isotropic medium is a scalar, σ. In general case the conductivity is a complex quantity accounting for electron inertia. For real σ the amplitude of electric field decreases exponentially from the surface:

$$\xi = \xi_0 e^{-x/\delta} \cos(x/\delta - \omega t) \tag{1.50}$$

where δ is the skin depth, given by:

$$\delta^{-1} = \mathbb{R}e\left[\frac{4\pi i\omega\sigma}{c^2}\right]^{1/2} \tag{1.51}$$

If the collision frequency, ν, is independent of electron energy, the conductivity will be [66]:

$$\sigma = \frac{n_e e^2}{m_e(\nu + i\omega)} \tag{1.52}$$

We can substitute Equation 1.52 in Equation 1.51, obtaining the classical skin depth [67]:

$$\delta = \frac{\delta_0}{\cos(\psi/2)} \tag{1.53}$$

where

$$\delta_0 = \frac{c}{\omega_{pe}}\left(1 + \frac{\nu^2}{\omega^2}\right)^{1/4} \qquad \psi = \tan^{-1}\left(\frac{\nu}{\omega}\right)$$

At low frequency, $\omega \ll \nu$, the skin depth is $\delta = (c/\omega_{pe})\sqrt{2\nu/\omega}$ and the energy dissipation is due to collisions. This is called *normal skin effect*. At high frequency, $\omega_{pe} \gg \omega \gg \nu$, so the skin depth is $\delta = c/\omega_{pe}$; in this condition the wave is reflected from the plasma without energy dissipation. This phenomena is called *anomalous skin effect*, and it is a collisionless effect [39, 68].

Resonance absorption

When a high field incident obliquely on a metallic solid or a sharply bounded overdense plasma, a large absorption rate can be accounted for electrons that are pulled into the vacuum and sent back into the plasma. This phenomena is effective when the overdense plasma density is well over the critical density and when a strong density gradient or discontinuity is present. In this way, the presence of an underdense plasma in not necessary [27].

When the incident electromagnetic wave is close enough to the critical density layer (n_{cr}), the laser's electric field can excite local plasma oscillations at the same frequency ($\omega_{pe} = \omega_L$). The energy is transferred resonantly in a collisionless process, and this phenomenon is called *resonance absorption*, which is the major absorption process.

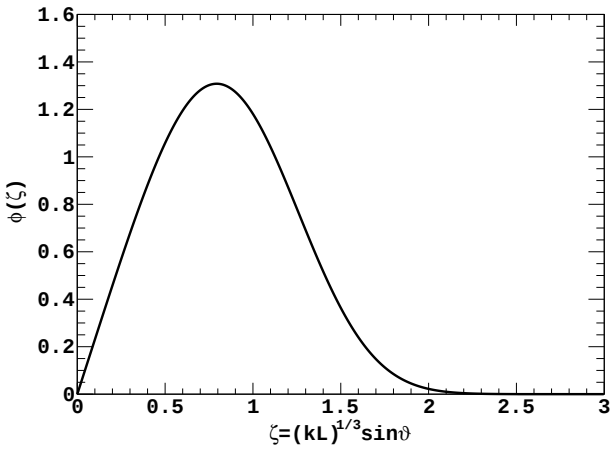

Figure 1.10: *Angular absorption behaviour predict by Denisov [69].*

For long density scale lengths $kL \gg 1$, where $k = 2\pi/\lambda$ and $L = |\nabla n_e(x)/n_e|$, the absorption fraction of the incident wave depends on the parameter:

$$\zeta = (kL)^{1/3} \sin\vartheta \tag{1.54}$$

where ϑ is the usual angle of incidence. In this limit, the angular absorption $\phi(\zeta)$ behaviour is given by [69]:

$$\phi(\zeta) \backsimeq 2.3\zeta \exp\left(-\frac{2\zeta^3}{3}\right) \tag{1.55}$$

The Equation 1.55 is called Denisov Function, and its behaviour is shown in Figure 1.10. Finally, the fractional absorption is given by:

$$\alpha_{ra} = \frac{1}{2}\phi^2(\zeta) \tag{1.56}$$

The behaviour is more or less independent of the damping mechanism provided the pump amplitude is small [2].

Brunel Mechanism

In a step profile, the longitudinal oscillation of the electrons go across a step density gradient, with an amplitude $x_{pe} \backsimeq e\xi_L/m_e\omega^2 = v_{osc}/\omega$. The resonance breaks down if this amplitude exceed the density scale length L, i.e. if $v_{osc} > L$ [2].
Thus in Brunel Mechanism collisionless precess is characterized by a step like plasma profile and a strong longitudinal field. In this way, the electrical field of the laser beam, can drag electrons from plasma surface directly into vacuum. Laser field, then reverse its direction, and same electrons will be turned around and accelerated back into plasma.
Brunel [27] proposed a model based on the capacitor approximation, (see Figure 1.11) in which the magnetic field of the wave is ignored (i.e. the $\mathbf{v} \times \mathbf{B}$ is neglected), ed assume that the external electric field ξ_L has some component ξ_d normal to the target surface, which pulls

electrons back and forth across their equilibrium position position. If laser beam incide with an angle ϑ, the driving electric field is given by:

$$\xi_d = 2\xi_L \sin\vartheta \tag{1.57}$$

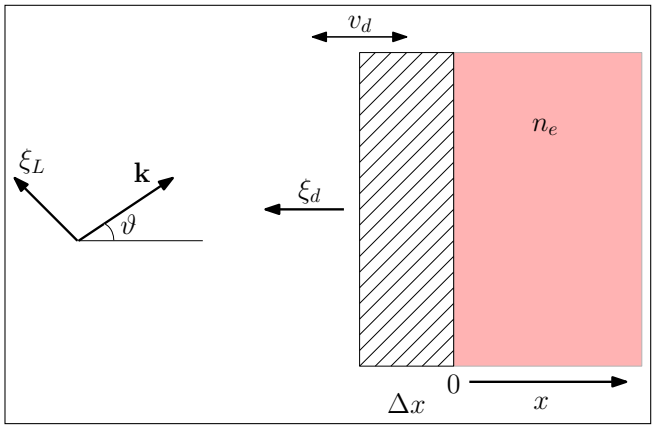

Figure 1.11: *Schematic capacitor model in the Brunel Mechanism.*

Deriving field pulls a sheet of electron out to Δx distance from its initial position. The surface number density of this sheet is $\Sigma = n_e \Delta x$, so the electric field created between $x = -\Delta x$ and $x = 0$ is $\Delta E = 4\pi e\Sigma$. Thus, solving for Σ we have:

$$\Sigma = \frac{2\xi_L \sin\vartheta}{4\pi e} \tag{1.58}$$

Electron charge sheet have acquired a velocity $v_d \backsimeq 2v_{osc}\sin\vartheta$, while return to original position.

Assuming these electrons are lost to solid, the average energy density absorbed for laser cycle is:

$$P_{abs} \backsimeq \frac{1}{16\pi^2}\frac{e}{m_e\omega}\xi_d^3 \tag{1.59}$$

Comparing the average energy absorbed (Equation 1.59), with the incoming laser power, we obtain the fractional absorption rate:

$$\eta_{abs} = \frac{P_{abs}}{P_L} = \frac{4}{\pi}a_0\frac{\sin^3\vartheta}{\cos\vartheta} \tag{1.60}$$

where $a_0 = v_{osc}/c$, is the dimensionless laser amplitude. Some corrections must be made to the Equation 1.60, because it does not take into account the effect of the reduced field amplitude due to absorption, and the returning velocity of electron that could be relativistic. However, from the Brunel model is possible to estimate the electron temperature, in terms of kinetic energy, from the following equation:

$$T_e^{(B)} = 2m_e v_{osc}^2 \sin^2\vartheta \cong 3.7\times10^{16}\left(I\lambda^2\left[\frac{W\ \mu m^2}{cm^2}\right]\right)\quad [keV] \tag{1.61}$$

The capacitor model is not self–consistent, since a zero field in the target region would require a surface charge density which is artificial. If the laser impinges normally on the plasma surface (or if no longitudinal component of electric field is available), Brunel mechanism is not activated [70,71].

Relativistic J × B heating

In intense laser–matter interaction the non-linear effect which result from the coupling of the electron current that oscillating along the electric field, **J**, with the magnetic field of the incident wave **B**, namely "**J** × **B**" acquire a lot of importance [72].
For relativistic irradiances, **J** × **B** heating, deriving from the oscillating component of the ponderomotive force, is effective. In particular, it is assumed that the temperature of hot electrons resulting from this absorption mechanism is of the order of the ponderomotive potential. For a linear polarized wave, $\xi = \xi_0(x)\hat{y}\sin\omega t$, that travel along *z–axis* the longitudinal force (**J** × **B**), is the following:

$$F_x = -\frac{m_e}{4}\frac{\partial v_{osc}^2(x)}{\partial x}(1-\cos 2\omega t) \tag{1.62}$$

The first term is the usual ponderomotive force, which in this context tends to push electron density profile inwards. The second term is a high frequency oscillating component which leads to heating. This **J** × **B** term, which works for any polarization apart from circular ones, is most efficient for normal incidence and becomes significant at relativistic velocity.
Physically, it is very similar to Brunel Mechanism, in that electrons are directly accelerated by a laser field incident on a step–line density profile. The main difference between this phenomena and the Brunel ones is that the driving term is **J** × **B** component of the Lorentz Force, which oscillate at twice of the laser frequency [2,73].

1.3 Ion Acceleration in Plasma

Until now, we have excluded the ions from our treatment, considering them fixed in the reticular positions. After laser–matter interaction, however, electrons are rapidly pushed out of the target and the electric field generated from charge separation, that can reach the value of some *TV/m*, is responsible of the ion acceleration. Ions can be accelerate at high energy, in *multi–MeV* range [74–76]. On the other hand, the quiver motion in laser field is negligible for ions, with respect electrons:

$$\frac{v_i}{c} = \frac{ze\xi}{m_i\omega c} = \frac{zm_e}{m_i}a_0 \tag{1.63}$$

where a_0 is the dimensionless laser amplitude, m_i and v_i are the ion mass and velocity respectively. Thus to accelerate ions to relativistic velocity, directly via laser field ($v_i \sim c$), from Equation 1.63 and due to bigger mass of proton with respect electron, we expect $a_0 \sim 1800$. From Equation 1.16, we should have $I\lambda^2 \sim 4.4\times10^{24}\ Wcm^{-2}\mu m^2$ or greater than this, far from value currently available. However in a plasma, electrons mediate between laser field and ion acceleration through electric field by charge separation.

Coulomb Explosion

During the ablation process, electron emission by target cause an accumulation of uncompensated positive charge that feel a strong electric field due to their proximity. When the electric field is strong enough to overcome the bond among the ions, the ions will be ejected out of the target. This phenomena is called *Coulomb Explosion* [77–79].
The estimation of the threshold electric field with respect to Coulomb Explosion can be made by assuming that the electrostatic energy density per individual atom exceeds a threshold value related to the required sublimation energy per atom. Thus, it is possible to estimate this threshold value of the electric field as follows:

$$\xi_{th} = \sqrt{\frac{2\Lambda_{sub}^{(at)} n_0}{\epsilon_r \epsilon_0}} \tag{1.64}$$

where $\Lambda_{sub}^{(at)}$ is the sublimation energy per atom, n_0 is the lattice atomic density and ϵ_r is the relative electric permittivity. For example, for gold target, the threshold electric field is about $\sim 2.8 \times 10^{10}$ V/m. Equation 1.64 is valid in the approximation of cold lattice, roughly during short pulse exposure. For longer pulse we have to take into account the heated lattice atoms, that due to higher vibrational energy can escape from the surface. Thus, the thermal reduction of the threshold field can be expressed as:

$$\xi_{th} = \sqrt{\frac{2(\Lambda_{sub}^{(at)} - 3k_B T_l) n_0}{\epsilon_r \epsilon_0}} \tag{1.65}$$

where T_l is refereed to the lattice temperature in the region of laser pulse interaction [80].

1.3.1 BPA Acceleration Regime

The *Backward Plasma Acceleration* (BPA) is an acceleration regime that refers to plasma that expand in the laser beam opposite direction (as you can see from Figure 1.12). Although, also by short pulse there is an acceleration in backward direction (with lower intensity compared to forwards ones, by thin target interaction), here we analyse only the long pulse interaction by thick target.
We have just mentioned that ion acceleration is due to electrostatic Debye sheath caused by the charge separation. In this way, the mean ions energy will therefore be directly correlate to the potential generate by hot electrons, whose kinetic energy is of course proportional to T_e. Thus, we expect:

$$E_{ion} \propto k_B T_e \tag{1.66}$$

This scaling law has been confirmed in a great number of experiments [81]. The symbol of proportionality indicates that a term concerning the ion charge state, z, has been omitted.

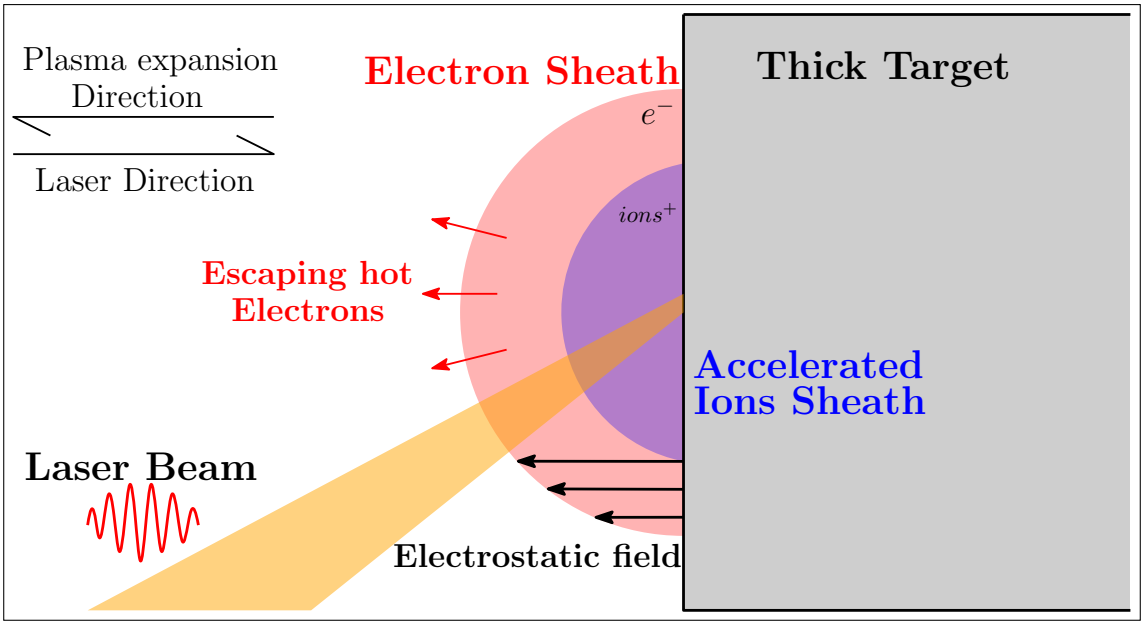

Figure 1.12: *Schematic Backward Plasma Acceleration by laser pulse.*

For non-relativistic ions, we can evaluate energy also by classical expression:

$$E_{ion} \sim \frac{1}{2} m_i v_i^2 \sim z k_B T_e \tag{1.67}$$

This is a simple but useful approach. Notice that even for highly relativistic electrons temperatures the ions velocity remain largely non-relativistic. For example, if we consider an electron temperature of 10 *MeV*, from Equation 1.67 we obtain a proton velocity of $v_H \sim 0.15c$.

Ion velocity Distribution

When the plasma density is low, we have already see, that the particles collision can be neglect. Particles velocity are affected by a Boltzmann distribution like the following:

$$f(v) = 4\pi n \left(\frac{m}{2\pi k_B T} \right)^{3/2} v^2 \exp\left[-\frac{m v^2}{2 k_B T} \right] \tag{1.68}$$

where n, m and v are the density, mass and velocity of the ion species take into account, respectively [82]. If the plasma density is high, collisions occurs, and Boltzmann distribution evolves from Equation 1.68 to which is called *full–range Maxwellian*:

$$f(v) = 4\pi n \left(\frac{m}{2\pi k_B T} \right)^{3/2} v^2 \exp\left[-\frac{m}{2 k_B T} (v - u_k)^2 \right] \tag{1.69}$$

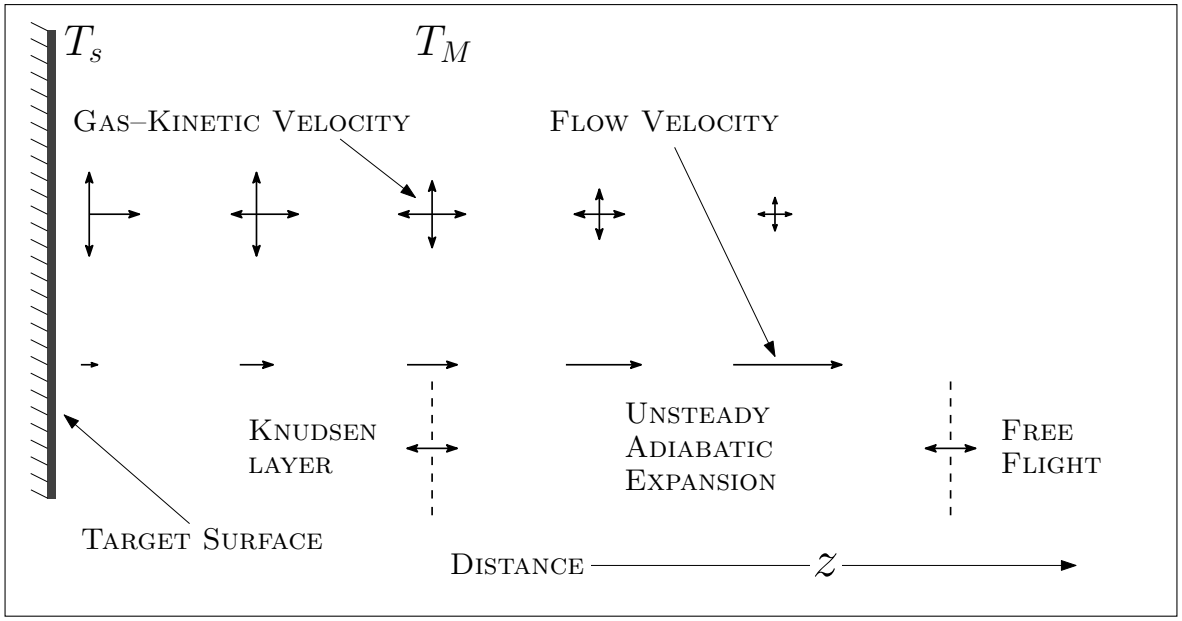

Figure 1.13: *Scheme describing the expansion of a ionized gas in vacuum.*

where u_k is the center of mass velocity. Here the index k indicates the *Knudsen Layer*, i.e. the region within a few mean free paths where collision processes occurs. Beyond the Knudsen–layer boundary the system is better described by the formalism for adiabatic expansion (Unsteady adiabatic expansion) [83, 84]. After this region the particles transit in the free flight region, as shown in Figure 1.13.
Adiabatic expansion velocity can be written as followings:

$$u_k = \sqrt{\frac{\gamma k_B T}{m}} \tag{1.70}$$

where γ is the adiabatic expansion coefficient. However, the effects of acceleration due to the electrostatic potential, caused by charge particles separation, have not been take into account up to now.
Trying to interpret the in of the various charging states on the distribution of energy, *Torrisi et al.* [85] hypothesized the existence of another velocity component, beyond thermal and adiabatic, which is the coulomb velocity, as shown in Figure 1.14. This is due to the electric field that occurs in the plasma due to the separation between the opposite charges. In fact considering the different mobility of ions and electrons and their consequential separation, there is the generation of an electric field, and therefore of a force that will tend to accelerate charge ions ze. The distribution function that take into account the electrostatic acceleration

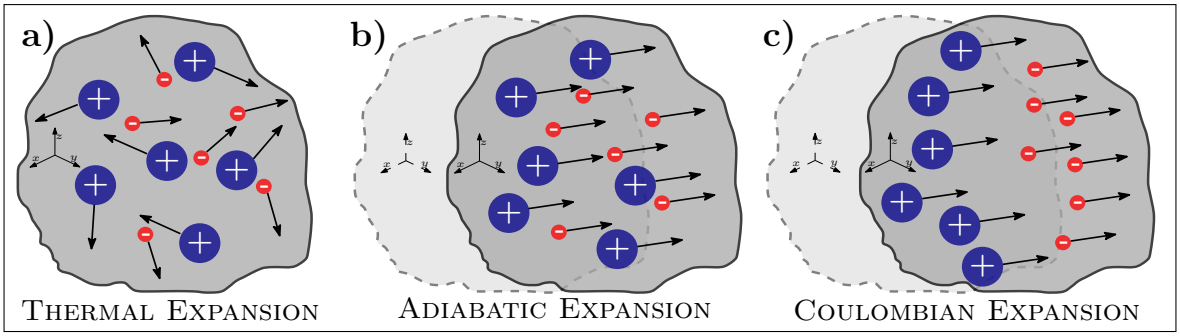

Figure 1.14: *Representation of the thermal expansion (a), adiabatic expansion (b) and Coulombian expansion (c), of particles emitted by laser–generated plasmas in vacuum.*

field, is called **Coulomb–Boltzmann Shifted**:

$$f(v) = A\left(\frac{m}{2\pi k_B T}\right)^{3/2} v^3 \exp\left[-\frac{m}{2k_B T}(v - u_k - u_c)^2\right] \tag{1.71}$$

where A is a normalization parameter and u_c is the velocity due to electrostatic field:

$$u_c = \sqrt{\frac{2ze\xi\lambda_D}{m}} = \sqrt{\frac{2zeV}{m}} \tag{1.72}$$

where the plasma potential $V = \xi\lambda_D$, is the electrostatic potential due to electrostatic field ξ established between charged particles at distant of λ_D. The validity of the Equation 1.69 and Equation 1.71 has been demonstrated in many experiments [86–89].

1.3.2 TNSA Acceleration Regime

Target Normal Sheath Acceleration (TNSA) refers to an acceleration scheme where the laser beam is focused on a thin target (with range thickness from sub–micrometer to a few micron) and the most energetic ions and electrons are emitted in forward direction [90].
In this regime, we assume the interaction of an intense laser pulse ($> 10^{16}$ W/cm^2) with a solid thin foil target, that generate hot electrons with energy correlate to laser intensity. An interesting aspect is relate to the interaction of the main pulse with preplasma, which is generate by prepulse as we will see. However, the hot cloud electrons penetrate into foils, and escapes behind the target, in forward direction. Those electrons are then electrostatically confined to the target and circulate back and forth through the target, laterally expanding and forming a charge–separation field on both sides over a Debye length. The electrostatic field in forward direction reach the value of several TV/m, and ions located on this target's face are accelerated by longitudinal field. As the ions start from a cold solid surface just driven by quasi–static electric fields, the resulting beam quality is extremely high, as we shall see [91]. This process just described is shown in Figure 1.15.

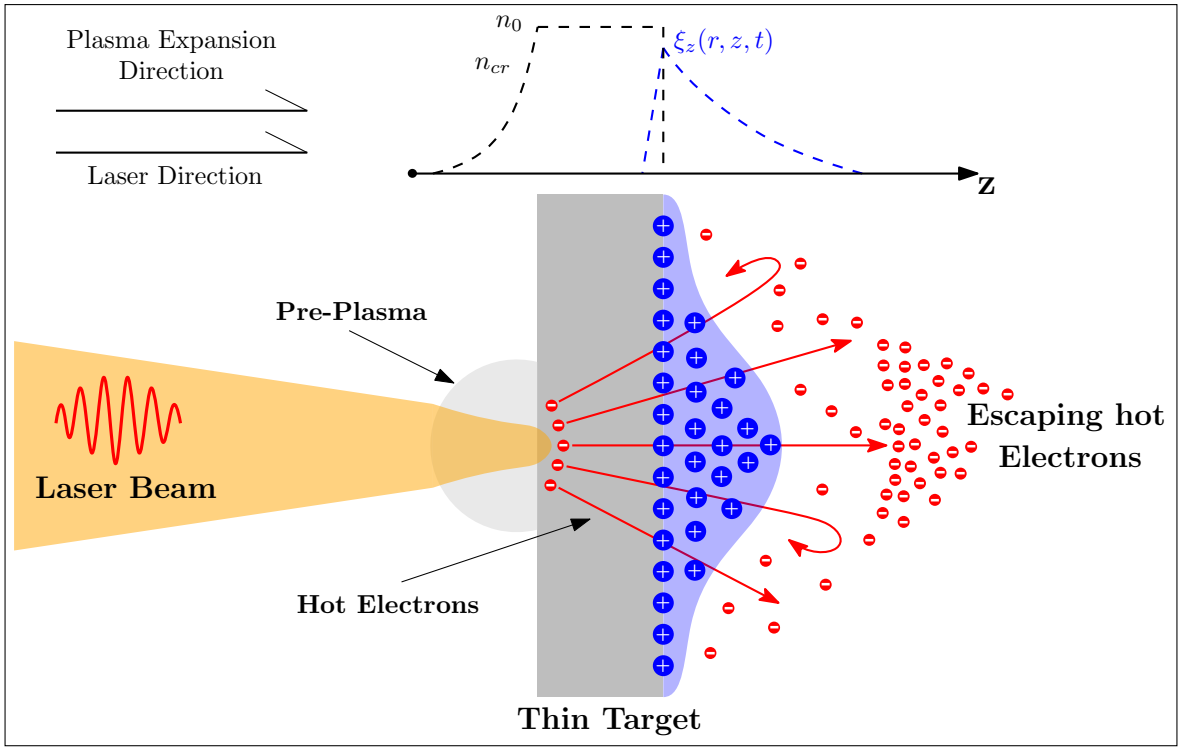

Figure 1.15: *Schematic Target Normal Sheath Acceleration by short laser pulse.*

Structure of a short laser pulse

Typical TNSA experiment is made by a Chirped Pulsed Amplification (CPA) [92] laser system, that deliver an energy ranging from hundreds of *mJ* to *kJ* order, transported by a single pulse of *fs* or *ps* length, thus reaching a peak power ranging from hundreds of TeraWatt up to PetaWatt. Titanium–Sapphire laser (Ti:Sapphire, Ti:Al_2O_3) are today the most common laser for its capacity to reach high intensity and ultra–short pulses (30–300 *fs*) with high repetition rate.
However, high intensity laser are always preceded by the so–called prepulse, a radiation due to Amplified Spontaneous Emission (ASE) [93]. Figure 1.16 shown a typical temporal structure of a Ti:Sapphire laser. The ASE has a typical contrast of $\sim 10^6$–10^{10} (ratio between main pulse and prepulse intensity), and a duration of few *ns*. There is also a few to several tens of *ps* pedestal with a typical contrast of $\sim 10^3$–10^5; this pedestal is due by misalignment and imperfection in the compressor gratings or by some other high–order dispersion source. The prepulse, sometimes can destroys the target; we consider a "normal" contrast that preceding light does not destroy completely several μm target, but it is only useful for create a preplasma in front of target before the main pulse hits the latter.

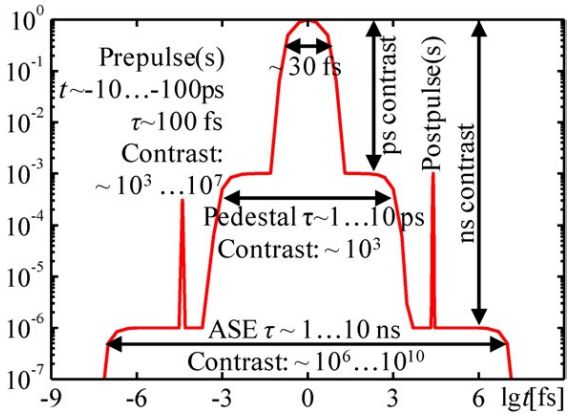

Figure 1.16: *Temporal structure of a Ti:Sapphire laser, with several kind of preceding pulse, namely prepulses (Image reprinted from ref [94]).*

For efficient acceleration by TNSA mechanism, a sharp plasma boundary is required, otherwise the accelerating sheath field is reduced from $\propto 1/\lambda_D$ to $\propto 1/l_p$ (see Equation 1.75), where the Debye length is replaced by the plasma scale length l_p, with $l_p > \lambda_D$. The interaction of main pulse with preplasma can be seen as laser–underdense plasma interaction (see section 1.2.1). On the other hand, the target rear side have to remain unperturbed before the arrival of hot electron accelerated by main pulse. Of course, the required contrast is higher for thinner targets, which provide condition for higher ion energy. It is possible estimate the necessary ASE for a given target thickness as shown in ref [94].

The front of target, so, start to deteriorate when the prepulse fluence approaches the laser–induced damage threshold, as we see in section 1.1.1. Thus an estimation for required contrast for the prepulse with duration τ_{pre}, is given by:

$$C = \frac{I_L \tau_{pre}}{F_{thr}} \tag{1.73}$$

where I_L is the main pulse intensity, and F_{thr} is the fluence threshold damage in target [94]. So for example, if we have an ablation fluence threshold of 2 J/cm^2, a main pulse intensity of $\sim 10^{18}$ W/cm^2 and a prepulse duration of $\tau_{pre} = 10$ ps, from Equation 1.73 we obtain a required contrast of 5×10^8. The importance of preplasma formation is due to the introduction of phenomena, such as Relativistic Sefl Focusing and others, which allow to obtain more efficient ion acceleration.

Acceleration Mechanism

When an high–intensity laser interacts with a thin foil target a large number of electrons will be accelerate in forward direction into the target through a number of mechanisms depending on the interaction and target conditions [95]. We can identify the existence of two electrons populations; the first is made by hot electrons, directly created by laser pulse, and the second are the conductions electrons which are put in motion by the first ones.
Hot electrons propagate normal to target surface, and it is considered the fast component of the electrons population. The density of these is of the order of critical density, that depends on the laser pulse parameter, and its temperature is of the order of ponderometive

potential. The free motion of this hot electron beam through the target requires the presence of a return current that locally compensates the flow of the hot electron component. In case of insulator target, this free electrons components is given by laser–ionization matter and thermal ionization. However, the density of conductions electrons are comparable with bulk density, which is match bugger then the hot electrons density. Since expression of current density, at total flow neutralization we have:

$$n_e^h v_e^h = n_e^c v_e^c \tag{1.74}$$

where n_e^h and n_e^c are the electrons density for hot and conduction species respectively, and $v_e^{h,c}$ the respective velocity component. Thus, due to high density value for conduction electrons, the required velocity for current neutralization is small and their temperature is much lower than that of the hot electrons [96].
While a limited number of energetic electrons will effectively leave the target, most electrons will be backed within the thin foil volume and they will form a sheath extended approximate a Debye length from the initially unperturbed rear surface, which drive the ion acceleration scheme. This interaction is shown in Figure 1.15, and the initial acceleration field is:

$$\xi_0(z) = \frac{k_B T_e^h}{e\lambda_D} = \sqrt{\frac{n_e^h k_B T_e^h}{\epsilon_0}} \tag{1.75}$$

where T_e^h is the hot electrons temperature. The electric field generated in this regime have intensity of about TV/m. During the interaction laser–matter hot electrons recirculate through the target, in this way they can lead an enhancement of ion acceleration.
TNSA mechanism can in principles accelerate any ion species present in surface layer, but in most experiments there is a preferential acceleration for light ions in contaminant layer, than ions bulk. Protons, which have the highest charge–to–mass ratio, are of course the dominant component of the ion beam [97, 98]

1.3.3 RPA Acceleration Regime

At very high intensity laser ($> 10^{17}\ Wcm^{-2}$), the light does not only heat the electrons in the target, but the pondermotive force also induced a secular motion on the particles due to first term of Equation 1.62. This force is related to *radiation pressure*. If the laser pulses is modelled as a plane wave and interact by a semi–infinite target, with reflectivity R, the radiation pressure P_{rad}, defined as the momentum transferred by electromagnetic wave to target per unit time and surface, is given by Maxwell expression:

$$P_{rad} = (1 + R)\frac{I_L}{c} \tag{1.76}$$

The radiation pressure P_{rad} is given by integral over the target volume of the temporal average of the $\mathbf{J} \times \mathbf{B}$ force over a period of electromagnetic field, i.e. of the ponderomotive force per unit of volume $\mathbf{F}_p$.

As we already seen at the beginning of this section, since ions inertia is much higher then that of the electrons, the ponderomotive force is negligible for ions but pushes electrons. If electrostatic force balances the ponderomotive ones for electron, we will have:

$$\mathbf{F}_p = en_e\boldsymbol{\xi}_{es} \tag{1.77}$$

In this way, the total electrostatic pressure on ions P_{es}, is given by integral of $zen_i\boldsymbol{\xi}_{es}$. In condition of quasi–neutrality we have that $zen_i = en_e$, so:

$$zen_i\boldsymbol{\xi}_{es} = en_e\boldsymbol{\xi}_{es} = \mathbf{F}_p \qquad \Longrightarrow \qquad P_{es} = P_{rad} \tag{1.78}$$

In these condition we can assume that the ions target are effectively pushed by radiation pressure P_{rad} [99].
However, for laser pulse linearly polarized Radiation Pressure Acceleration (RPA) is in competition with TNSA mechanism until $\sim 10^{21}\ Wcm^{-2}$; at above intensity values RPA is the predominant mechanism of acceleration. Taking into account circularly polarized pulses and normal incidence on target, the generation of energetic electrons is strongly suppressed ruling TNSA out, so that RPA dominates at any intensity [100–102].
In RPA mechanism we can distinguishes between two regime of acceleration due to target thickness: if the target is thick the regime is called *Hole Boring* (HB); otherwise for thin target the RPA regime acceleration is called *Light Sail* (LS).

Hole Boring

In this model, we can consider a semi–infinite target with homogeneity density profile [45]. In Figure 1.17 HB mechanism is well described in one dimension. Here, the first step corresponds to initial stage in which the electrons have piled up by radiation pressure.

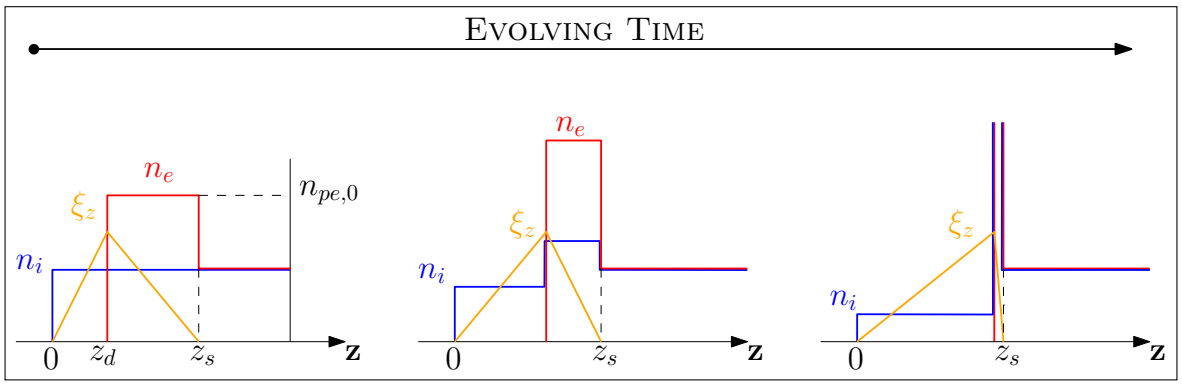

Figure 1.17: *Evolving time for profile model in 1D of ion density n_i (blue line), electron density n_e (red line) and longitudinal electric field ξ_z (orange line).*

An electric field ξ_z appears due to space–charge separation, which balances the ponderomotive force. Assuming that the electrons are in equilibrium and ions have not moved significantly yet at this stage, as we just explained, we will have:

$$P_{es} = \int e n_e \xi_z dz = 2\frac{I}{c} \tag{1.79}$$

assuming total reflection ($R = 1$). The distance $\ell_s = z_s - z_d$ is the penetration of ponderomotive force into target, and is thus of the order of the collisionless skin depth $d_p = c/\omega_{pe}$. The simplified profiles allow the ion equation of motion to be solved analytically, if all ions are initially in the $z_d < z < z_s$ region, get to the $z = z_s$ point at the same time, so that a singularity appears in the ion density. The corresponding energy spectrum is a flat–top distribution extending from zero to the cut–off value [99]:

$$E_{max} = \frac{1}{2} m_i v_{max,i}^2 = 2 m_i c^2 \Pi \tag{1.80}$$

Here $v_{max,i}$ is the maximum ions velocity, and Π is given by the following equation:

$$\Pi = \frac{I_L}{m_i n_i c^3} = \frac{Z}{A}\frac{n_{cr}}{n_e}\frac{m_e}{m_p} a_0^2 \tag{1.81}$$

where m_p is the nucleon mass (proton) and A is the mass number. In case of ions relativistic velocity the Equation 1.80 becomes [103]:

$$E_{max} = 2 m_i c^2 \frac{\Pi}{1 + 2\sqrt{\Pi}} \tag{1.82}$$

However, the highest intensity laser available today ($\sim 10^{20}\ W/cm^{-2}$) shown proton energy cut–off near 100 MeV [104].

Light Sail

When a laser intensity is extremely high, and the target is thin enough, the radiation pressure can cause another very efficient acceleration mechanism, the so-called Light Sail–RPA (LS) or Laser Piston regime, as you can see in Figure 1.18 [105].
In LS regime the target is accelerated as a whole, unlike HB regime where e only ions in a surface layer of the target are accelerated by RPA. For a very thin target having $\ell \lesssim \ell_s$ (look Figure 1.17), where ℓ is the target thickness and $\ell_s = z_s - z_d$, all ions of foil are accelerated in a single bunch. However, for such thin targets the transmission of the laser pulse through the target must be taken into account. The radiation pressure on a thin target in its rest frame, at normal incidence and neglecting absorption, is given by:

$$P_{rad}^{(LS)} = 2R\frac{I_L}{c} \tag{1.83}$$

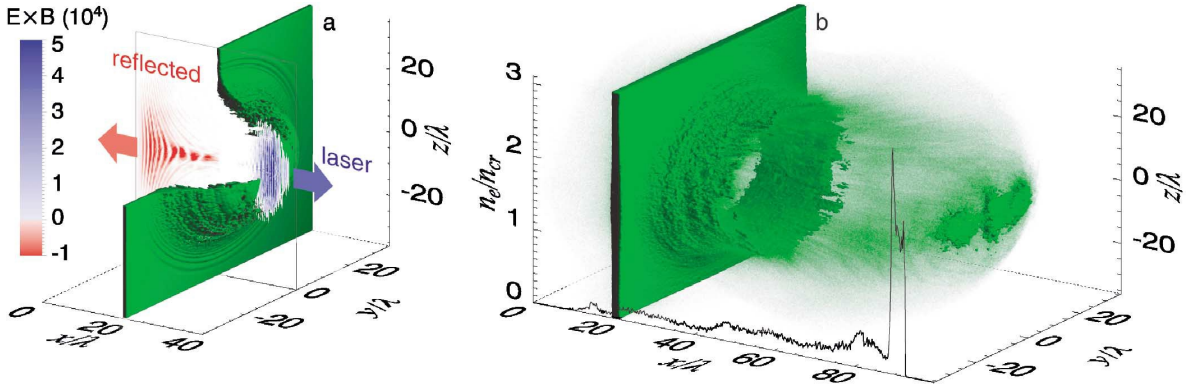

Figure 1.18: *Ion acceleration in the radiation pressure dominant (laser piston) regime, 3D PIC simulations. The laser pulse is linearly polarized with intensity of* $1.37 \times 10^{23}\ W cm^{-2}$*, the incidence is normal, and the target is made of protons. The target thickness is* $l = \lambda$ *and have a density of* $49 n_{cr}$*. (a) The ion density isosurface for* $n_i = 8 n_{cr}$ *and the x component of the normalized Poynting vector* $(e/m_e \omega c)^2 \boldsymbol{\xi} \times \mathbf{B}$ *in the* $(x;y=0;z)$ *plane at* $t = 40 \times 2\pi/\omega$*. (b) Isosurface for* $n_i = 2 n_{cr}$*, and green gas for lower ion density at a later time of* $t = 100 \times 2\pi/\omega$*; the black curve shows the ion density along the laser pulse axis (image reprinted from ref [105]).*

For relativistic laser intensity, the reflectivity depends non-linearly on the laser intensity because of self–induced transparency effects. The scaling law for ions energy is [99]:

$$E_{max}^{(LS)} = m_i c^2 (\gamma_f - 1) \tag{1.84}$$

where γ_f have the following expression:

$$\gamma_f = (1 - \beta_f^2)^{-1/2} \qquad \beta_f = \frac{(1+\varepsilon)^2 - 1}{(1+\varepsilon)^2 + 1} \qquad \varepsilon \backsimeq 2\pi \frac{Z}{A} \frac{m_e}{m_p} \frac{a_0^2 \tau_L}{\zeta}$$

where τ_L is the pulse duration and the relevant parameter ζ is defined as follows:

$$\zeta = \pi \frac{n_e}{n_{cr}} \frac{\ell}{\lambda} \tag{1.85}$$

For $a_0 > \zeta$ the reflectivity is about 1, for $a_0 < \zeta$ the reflectivity drops abruptly as a_0^{-2}. Thus, the condition $a_0 = \zeta$ is the best compromise between increasing the boost on the foil and decreasing its mass. The appealing features of LS are the monoenergetic ion spectrum expected for a sudden displacement of the whole foil target and the possibility to achieve high energies due to repeated acceleration and the low surface mass [99, 106]. In LS regime, by high intensity laser ($\sim 10^{22}\ W/cm^2$) and very thin foil (hundreds of nanometre) the GeV[1] barrier of ion energy could be approached as confirmed by Particle–in–Cell simulations [107–109].

[1] Pay attention, not experimentally confirmed or disregarded yet.

Chapter 2

Charged Particles Beams: Transport and Focusing

This chapter is dedicated to the transport and focusing, or of course defocusing, of ion beams. At the beginning some basic notions about particle beams features will be discussed, such as the introduction of phase space, transverse emittance, brightness and more. For ion beams, as in the interest case, the charge space separation, due to the coulombian interaction, will also be examined. Secondly, some transport and focusing devices will be presented, such as quadrupoles, sextupoles, and electric or magnetic lenses. An analogy with the optical ones is given in the text. Finally, some experimental measurements are presented and discussed, which they carried out about ions and electron beams emitted by laser–generated plasma of 10^{10} Wcm^{-2} intensity order, that pass through magnetic fields with cylindrical symmetry, which act as magnetic lenses. The use of magnetic fields allows to increase the ion current that reaches the detector, thanks to an effect of focusing by field on charged particles. The electrons, on the other hand, because of their smaller mass, form a trap in front of the magnet (located close to the target), which as result causes an increase in the longitudinal electric field accountable for the ion acceleration. Therefore, as we will see, an increase in the current yield of the detected ions and their energy is possible with devices of this kind. The experimental results will be compared and confirmed with the simulations carried out using the COMSOL Multiphysics software.

2.1 Ion Beam Features

It is now useful to introduce the basic principles of the charged ion beams. The motion of particles is governed by Lorentz Force, that we already see at Equation 1.17. Let us consider charged beam as a flux of ions, where each particle can be described by three spatial coordinate (x, y, z), denoted by $\mathbf{q}$, and also three momentum coordinate (p_x, p_y, p_z). Thus, the particles distribution function is dependent from these six coordinates, and also from time:

$$f(x, y, z, p_x, p_y, p_z, t)$$

The last equation defines the particles beam in the six–dimension *phase space*. By integrating the distribution function over a phase space region, we can obtain the number of particles found in that region of phase space [110]:

$$dN = f(\mathbf{q}, \mathbf{p}, t) d^3q d^3p \tag{2.1}$$

The phase space gives a concise knowledge of the particle state, or more generally, of a particles ensemble, depending on time. Let us suppose that ion beams propagate along *z–direction*, we can introduce the *paraxial approximation*, which consists to consider $p_z \gg p_x, p_y$, and p_z the same for all particles. In this way, we can rewrite the coordinate as follows:

$$x' = \frac{dx}{dz} = \frac{p_x}{p_z} \tag{2.2a}$$

$$y' = \frac{dy}{dz} = \frac{p_y}{p_z} \tag{2.2b}$$

Thus, we can introduce the *trace space*, which is the coordinates space (x, y, x', y') to describe the transverse motion instead of (x, y, p_x, p_y).

2.1.1 Transverse Emittance

For calculation and modelling purposes, a simple shape is needed to model the ion beam envelope in (x, x') trace space, or in the same way in (y, y'); for convenience, the calculation will be developed only in the plane (x, x').

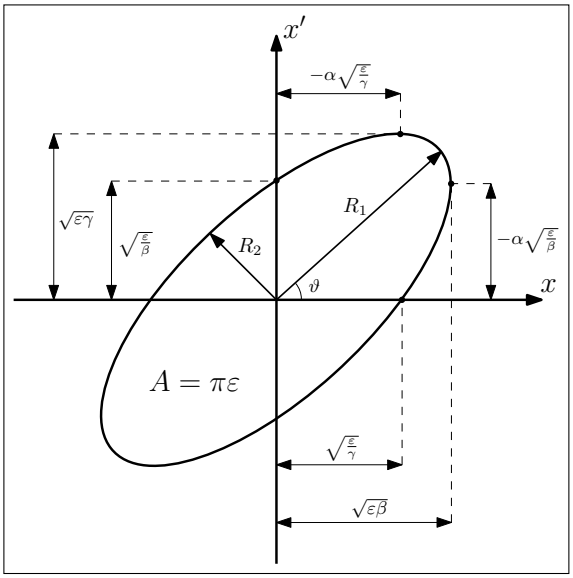

Figure 2.1: *Emittance ellipse geometry in (x, x') plane, with fundamental dimensions.*

Usually, ion beam have a Gaussian spatial profile in both directions x and x'. From this observation, it is natural to use an ellipse as a model in the trace space, since the 2D contours of the Gaussian distributions are ellipses. The equation of an ellipse centred in the origin system is:

$$\gamma x^2 + 2\alpha x x' + \beta x'^2 = \varepsilon \tag{2.3}$$

where we have chosen the scaling:

$$\gamma\beta - \alpha^2 = 1 \tag{2.4}$$

In Equation 2.3, ε is the *transverse emittance*, and α, β and γ are namely *Twiss parameters*, defining the ellipse orientation and aspect ratio, as you can see in Figure 2.1.

The ellipse area can be write as follows:

$$A = \pi\varepsilon = \pi R_1 R_2 \tag{2.5}$$

where R_1 and R_2 are the major and minor radii respectively, as shown in Figure 2.1 [111]. In other words, the *beam emittance* is a parameter equal or related to the area (or volume) occupied by a particle beam when they are represented in a phase space consisting of position and momentum. The unit of emittance is often given in π–*mm*–*mrad*. The same consideration can be do for (y, y') plane. Using Liouville's theorem [112], we immediately see that if only conservative forces are present the emittances ε_x and ε_y are conserved.
Since it is difficult to measure the full width of the beam we can look for a minimum–area ellipse containing some fraction of the wanted beam (e.g. $\varepsilon = 95\%$). The emittance from these width measurements is then referred to as the *rms–emittance* (Root Mean Square Emittance) is a purely statistical value, defined as follows:

$$\varepsilon_{rms} = \sqrt{\langle x'^2\rangle\langle x^2\rangle - \langle xx'\rangle^2} \tag{2.6}$$

where if $f(x, x', y, y')$ is the distribution function of the ion beam, $\langle x^2\rangle$ is defined as follows:

$$\langle x^2\rangle = \frac{\int\int\int\int x^2 f(x, x', y, y')dxdx'dydy'}{\int\int\int\int f(x, x', y, y')dxdx'dydy'} \tag{2.7}$$

in analogous way are defined $\langle x'^2\rangle$ and $\langle xx'\rangle$. For the statistic nature of the rms–emittance, it is used unit of *mm*–*mrad* without π. For these formulas, it is assumed that the emittance distribution is centred at the origin, so that $\langle x\rangle = 0$ and $\langle x'\rangle = 0$ [113].

2.1.2 Brightness

Emittance and Brightness are two parameters used for ion beam quality characterization. However, in most experiments which use ion stream, an important quantity is the intensity, namely the number of particle emitted within a particular energy range per second. The flux of particle at this energy, Φ, that cross the surface A, is given by:

$$\Phi = \frac{i}{A} \tag{2.8}$$

where i is the ion beam current intensity of a given particle energy. The *Brightness* is commonly defined as follows:

$$B = \frac{\Phi}{d\Omega} = \frac{di}{dAd\Omega} \tag{2.9}$$

as current density per unit solid angle. The unit of measure of brightness is $Am^{-2}Sr^{-1}$, or its multiples and submultiples. Equation 2.9 can be rewrite in terms of emittance, in the (x, x')

trace space, denoted by ϵ_x, and in (y, y') trace space, denoted by ϵ_y, as follows [111]:

$$B = \frac{2i}{\pi^2 \varepsilon_x \varepsilon_y} \tag{2.10}$$

Notice that sometimes the factor $2/\pi^2$ is left out or the RMS–emittance is used.

2.1.3 Space Charge

Inside an ion beam, the particles are close to each other, and they feel the effects of a repulsive coulombian force, because of their same polarity. The effect of this repulsive coulombian force is a defocusing in both transverse planes. The force strength depends on the beam parameters (intensity, particle type energy and beam size), the field generated by the beam itself can be derivate from these parameters as follows in the coming paragraphs.

Self Field

The ion beam charge density, ρ, plays a major role in beam extraction systems, where current densities are high and velocities are low compared to other parts. It is defined as follows:

$$\rho = \frac{\Phi}{v} = \frac{i}{Av} \tag{2.11}$$

where v is the ions velocity. Its unit of measurement is C/m^3. The space charge induces forces, which increase the divergence and emittance, *blowing up* the beam.
Let us assume a cylindrical constant current–density beam with radius r, that propagates by constant velocity v_z along z–*axis*, as reported in Figure 2.2a, the electric field generated by beam itself is given by [114]:

$$\xi_{beam} = \begin{cases} \frac{i}{2\pi\epsilon_0 v_z} \frac{r}{r_{beam}^2} & \text{if } r \leq r_{beam} \\ \frac{i}{2\pi\epsilon_0 v_z} \frac{1}{r} & \text{otherwise} \end{cases} \tag{2.12}$$

The potential inside a beam tube with radius r_{tube} is therefore [114]:

$$\phi_{beam} = \begin{cases} \frac{i}{2\pi\epsilon_0 v_z} \left[\frac{r^2}{2r_{beam}^2} + \log\left(\frac{r_{beam}}{r_{tube}}\right) - \frac{1}{2} \right] & \text{if } r \leq r_{beam} \\ \frac{i}{2\pi\epsilon_0 v_z} \log\left(\frac{r}{r_{tube}}\right) & \text{otherwise} \end{cases} \tag{2.13}$$

In Figure 2.2b is shown the plot of electric field and potential (Equations 2.12–2.13) for a proton beam at 5 keV energy and 10 mA of current intensity, with a radius of 20 mm and a radius tube of 100 mm. The electric field in the constant-current-density case, given by Equation 2.12, is linear with radius and therefore does not cause emittance growth, but it does cause increasing divergence of the beam [114].

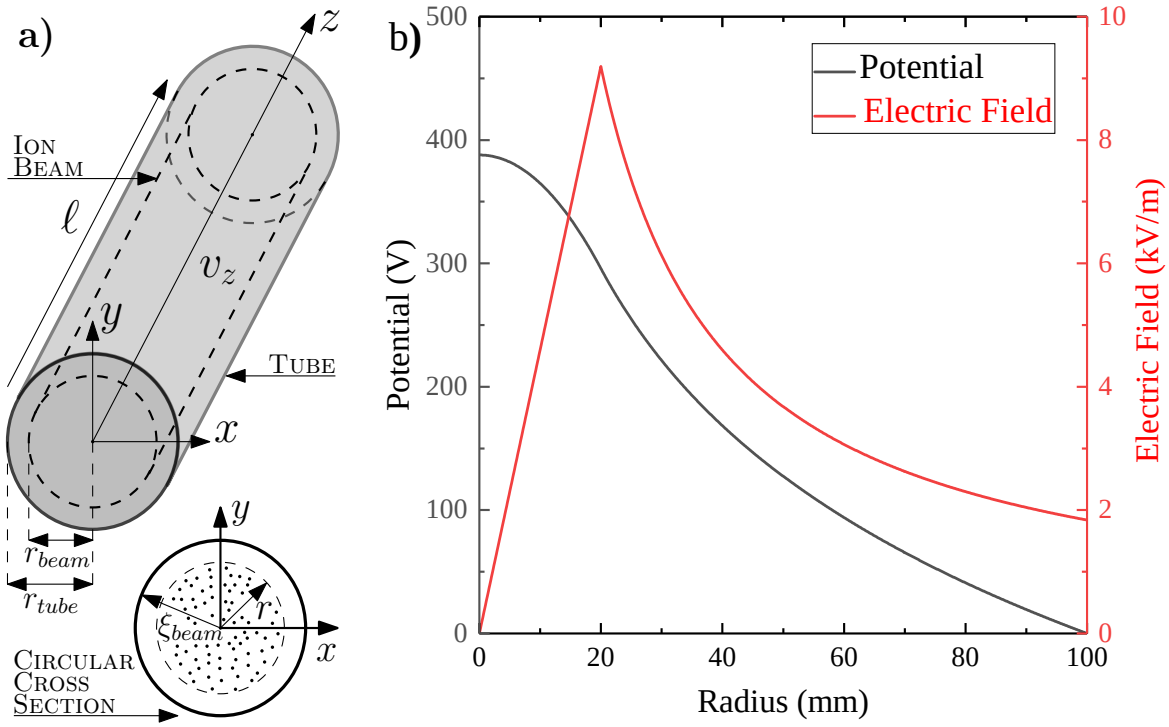

Figure 2.2: *Uniform charged cylinder of length ℓ and its circular cross section (a). Plot of potential and electric field inside the cylindrical tube of 100 mm radius, generated by proton beam at 5 keV energy, 10 mA current intensity and 20 mm radius (b).*

Space Charge Compensation

The potential of accelerated ions acts as a trap for oppositely charge particles in the areas where there aren't external electric fields to drain created charges. The most important process for production of this charge particles is the ionization of the background gas within the beam. So, this trapped particles, reduce the charge density of the beam and decrease the depth of the potential, thus decreasing the magnitude of the beam space–charge effects described in the last paragraph. This process in known as *space–charge compensation*. For an exhaustive treatment see ref. [115–117].

If we take into account a laser–generated plasma dynamics, without any space–charge compensation the ions would be pushed outside form targets by 4π of solid angle, due to coulomb explosion previously described. However, the accelerated ions can attract electrons from the electron sheath and accelerate them because of their positive potential. The electrons, that have a greater charge–to–mass ratio with respect ions, exhibits the same velocity distribution as ions and guarantee a space–charge compensated beam.

2.2 Ion Beam Transport and Focusing

Laser–driven ion acceleration produces positive charges that have a Boltzmann–like distribution in energy and obviously in velocity, and a certain position in a fixed time. Thus, each of these ions can be represented in phase space, as described in the previous paragraph.
Ions generated by laser pulses, are not simple to transport due to their wide range of energy and angular distribution emission. Transporting ions is equal to manipulate their transversal phase–space, by preserving the emittance. Ion lens possesses an intrinsic chromaticity, similar to optical ones, which takes care of the energy selection by itself; in this way, not is possible to transport all ions emitted from target due to their broad energy spectrum.
This section represents an overview of ion's transport and focusing by electric and magnetic devices. Before considering different aspect of ion beam phase–space manipulation, we will briefly examine the basic concept involved in image formation by light optic.

2.2.1 Analogies with Light Optics

Due to ion beam optics involves many concepts as light optics, we will first review some basic optical principles. Glass lenses are the heart of many optical devices, bases on the *Snell law* of refraction, i.e. the deviation in the direction of light ray when they cross a surface with different refractive index. The refractive index, is a dimensionless number, that describes how fast the light propagates into a medium; it is defined as $n = c/v$, where v il the light velocity in the medium. In the air the refractive index is close to 1, $n = 1.000293$.
Magnetic or electrical focusing/defocusing devices for an ion beam act as optical lenses do in the case of geometric optics. The word "lens", derived from the light optics, and it is therefore primarily associated with the axial–symmetry cases. Devices where the field is two dimensional and symmetric about a plane, are called cylinder lenses, in analogy to the corresponding components in light optics. A simple geometry of this, is a system of cylindrical electrodes, like in the case of Einzel lens, which will be discussed shortly, but this should not be confused with cylindrical lenses [118].
As it is well known, for a lens, the point where the optical rays that coming from an object converge is called the *focal point*. Obviously, the distance in air from the lens principal plane to the focal point is called the *focal length*. For thin lens approximation with refractive index n, in air, the focal point is given by lensmaker's equation, see [119]. The common thin lenses can be distinguished in "converging" or positive because parallel rays which pass through these lenses, are bending towards each other; and "diverging" or negative lenses because parallel rays of light passing through these devices tend to move away from each other [120].
Of course, the quantities that have been introduced up to now are also applicable in the treatment of ion optics. Nevertheless, we must also take into account that there are some fundamental limitations, some of which are for example the fact that ions have a charge while photons do not, which can lead a mutual repulsion of the individual particles resulting in a tendency of the ion beam to spread; the mass carried by the particles unlike photons

that do not have it; in light optics the refractive index changes abruptly between two different medium, instead in ion optics the changes of it are continuous; and so on. For a more exhaustive treatment of the problem see [121].
To conclude, an effect of great importance that occurs with both optical and electromagnetic devices, is that of *chromatic aberrations*, due to light rays could have different wavelengths or particle beams with different energies. Because to the dependence of the refractive index on the wavelength, $n(\lambda)$ (phenomenon called *dispersion*), the focal length of the lens will be different for each wavelength present in the beam. As final effect, for wavelengths with broader uncertainty the image sharpness will be more distorted [122].

2.2.2 Magnetic or Electric guide for ion beams

In the following section we will take into account magnetic or electric devices employed in ions bunch transport. We will see the operating principles of magnetic quadrupole, magnetic sextupole and electric quadrupole.

Magnetic Quadrupole

The starting point of this treatment is the Lorentz Force, introduced in Equation 1.17, that acts on the charge particles motion. A magnet quadrupole is a device made by four poles in a regular configuration, i.e. every $\pi/2$ angle, as you can see in Figure 2.3.

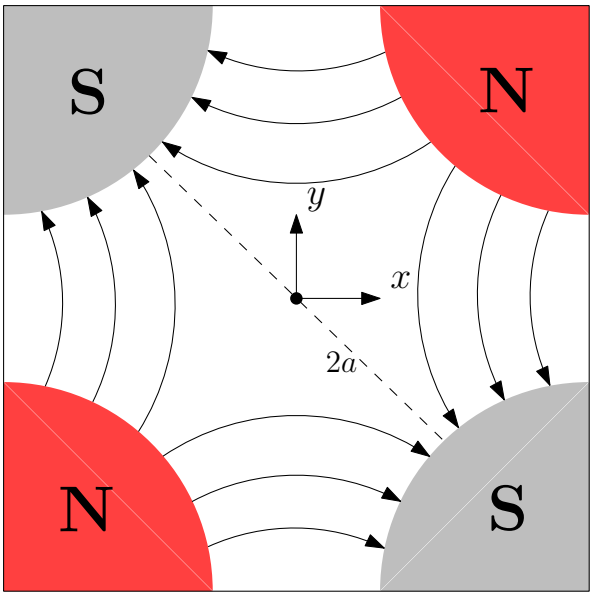

Figure 2.3: *Simple magnet quadrupole employed to ion beam focus in x–z plane.*

The next treatment refers to Figure 2.3, where the particle motion is along *z–direction*, i.e. direct in opposite way to normal of this paper. In this way, an ion beam that cross a magnetic quadrupole feels a force proportional to ion distance from the centre of the quadrupole. However a single magnetic quadrupole, as described in Figure 2.3 is enough only to focus ion in one plane, *x–z* for example, and defocusing particles in the other plane, *y–z* for example. Of course, it is simple to see that magnetic field magnitude not is the same in each region of the space. So, we can introduce the gradient of magnetic field as follows [123]:

$$g = \frac{\partial B_y}{\partial x} = \frac{\partial B_x}{\partial y} = \frac{B_0}{a} \tag{2.14}$$

Equation 2.14 says that the gradient of magnetic field, represents by g, is equal to the ratio between the magnitude of magnetic field in a pole B_0, by the half distance between to opposite pole a, as you can see in Figure 2.3. Thus, a focal distance for an ion beam in this device can be write:

$$f = \frac{p}{gqL} \tag{2.15}$$

where p is the particle momenta, q is its charge and L is the length of the magnet quadrupole. It is clear from Equation 2.15 that a particle will have a greater energy, and therefore a greater moment, will have a longer focal length. The focal length, on the other hand, decreases as the electric charge or the external magnetic field increases. In addition, the latter is also directly proportional to the distance of the ion from the centre of the quadrupole.
However, to guide an ion beam is mandatory have at least two magnetic quadrupole rotated by $\pi/2$ angle with respect the beam propagation direction. Thus, at fist step the ion beam is focused on *x–z plane* and defocused on *y–z plane*, and in the next step it is defocused on *x–z plane* and focused on *y–z plane* for example, as shown in Figure 2.4. In this way, an ion beam can be guided through a magnetic quadrupole with minimal ion loss. In case of two magnet quadrupoles rotated by $\pi/2$ the focal distance can be write as follows:

$$\frac{1}{f} = \left(\frac{qB_0}{ap}\right)^2 L^2 z \tag{2.16}$$

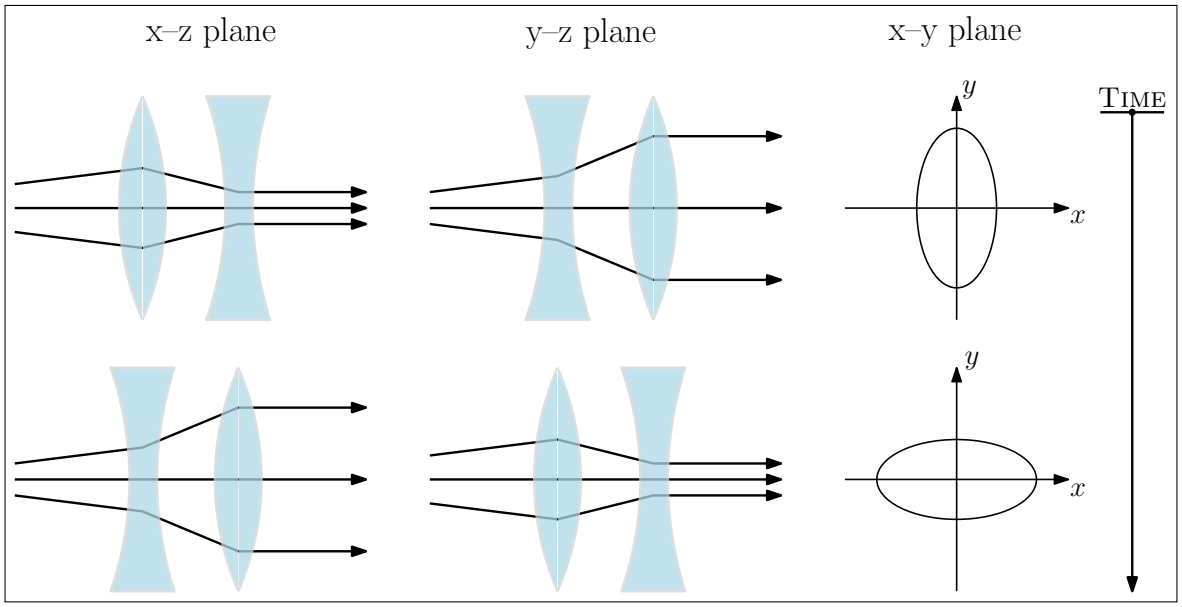

Figure 2.4: *Evolving time of focusing and defocusing in different plane by combination of two magnetic quadrupole rotated again each other by π/2 angle with respect z–axis.*

Magnetic Sextupole

In the previous paragraph we seen that the focal length of a magnet quadrupole is function of particle momenta. In others words, by an analogy with the similar effect of light optics, where the focal length of a given optical lens varies by wavelength of incidence light, the focal distance of the magnet quadrupole is longer for higher particles energy, and shorter for lowest energy of the ions. A more sophisticated magnetic devices, to control ion beam with different chromatic aberration due to dipole or quadrupole, are sextupole, octupole or generally multipoles [124, 125].
Let us take into account magnet sextupole; this device is used for correct the resulting chromatic errors. If the ion beam propagates along *z–axis*, the magnet sextupole generate a non-linear field given by:

$$\begin{aligned} B_x &= g'xy \\ B_y &= \tfrac{1}{2}g'(x^2 - y^2) \end{aligned} \tag{2.17}$$

where g' is the magnetic field gradient. The momentum–independent sextupole strength is defined as follows [123]:

$$m = \frac{qg'}{p} \tag{2.18}$$

However, as we anticipate at the beginning of this section, magnet sextupole are often use to obtain an additional focusing (or instead, defocusing) immediately after a magnet quadrupole. Figure 2.5 shown the difference between the focal length, when only a magnet quadrupole is used, and when a sextupole is added to the last one, for an ion beam that have an energy can be various of $\pm\delta E$. If the strength of the magnet sextupole is set appropriately, thus the combination system have the same focal length for particles with positive, negative or zero energy deviation.

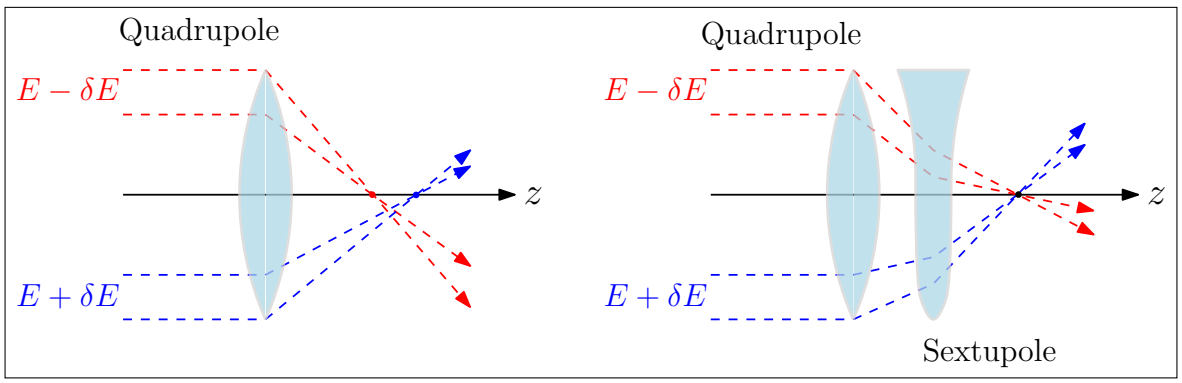

Figure 2.5: *Magnet quadrupole focal length for different particle energy (left), and chromatic aberration correction due to introduction of sextupole (right).*

However, it must be taken into account that the δE in the case of accelerators is very small, in the order of 0.1%; while when dealing with plasmas generated by lasers δE assumes extremely high values, due to the continuous energy distribution. There are currently devices that allow to select an energy range, limiting the δE and obtaining good transport efficiencies. However, transporting all the ions emitted by the plasma is now extremely complicated.

Electric Quadrupole

Now we will introduce electric device employed in ion beam transport, namely Electric Quadrupole, which is a device made by four electrodes in regular configuration, as in magnetic quadrupole, i.e. every $\pi/2$ angle. These electrodes are called *rods*, Figure 2.6.
Let us take into account two opposite rods, at a certain time t, that have applied a potential of $[U + V\cos(\omega t)]$; the opposite rods will have the same potential but in opposite sign $-[U + V\cos(\omega t)]$. In these two expression U is the potential part time–independent (dc), up to kV, while V is the part of potential that change with respect time (ac), up to 5–6 kV, through angular radio–frequency ω, in *MHz* range. The potential distribution, Φ_0, at the time t, is shown in Figure 2.6, and it can be described by the following expression [126, 127]:

$$\Phi_0 = [U + V\cos(\omega t)]\frac{x^2 + y^2}{2r_0^2} \tag{2.19}$$

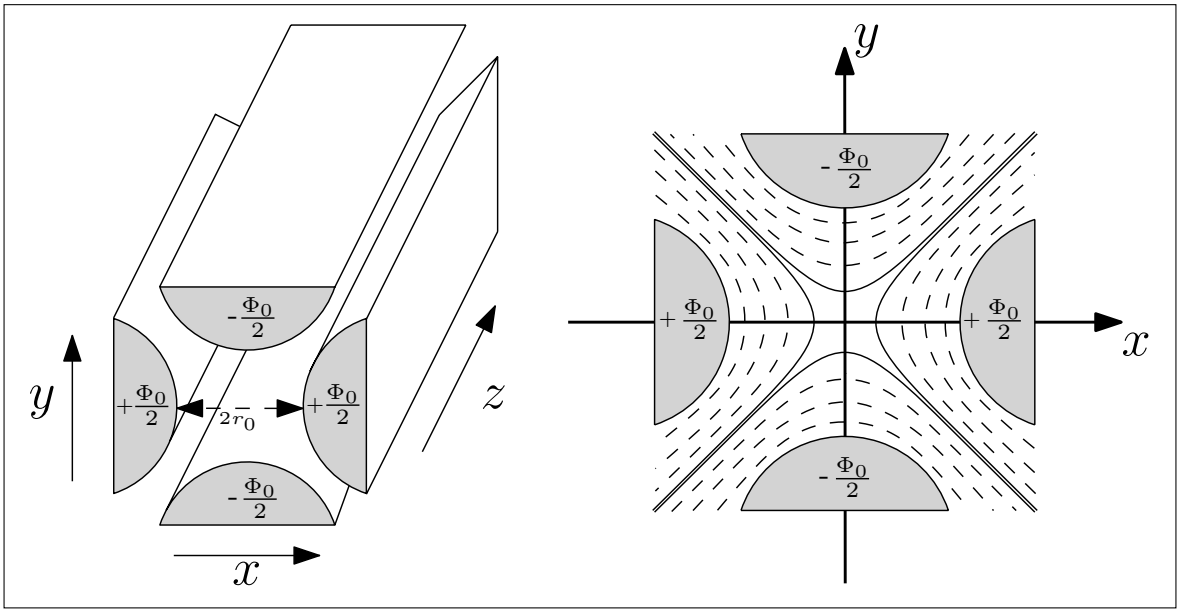

Figure 2.6: *Schematic electric quadrupole structure (on the left), equipotential lines in x–y plane (on the right).*

where x and y are the coordinates shown in Figure 2.6, and r_0 is the distance between the central axis (z–*axis*, chosen at the center of the electrodes) and the surface of the rods. The electric field can be defined by the voltage applied to the rods, from Equation 2.19:

$$\xi_x = -\frac{\partial \Phi_0}{\partial x} = -[U + V\cos(\omega t)]\frac{x}{r_0^2} \tag{2.20a}$$

$$\xi_y = -\frac{\partial \Phi_0}{\partial y} = [U + V\cos(\omega t)]\frac{y}{r_0^2} \tag{2.20b}$$

$$\xi_z = -\frac{\partial \Phi_0}{\partial z} = 0 \tag{2.20c}$$

The strength, **F**, exerted on a charged particle, is given by the electric field, shown in Equation 2.20, multiplied by the charge of the particle. Thus, by Newton law we will have:

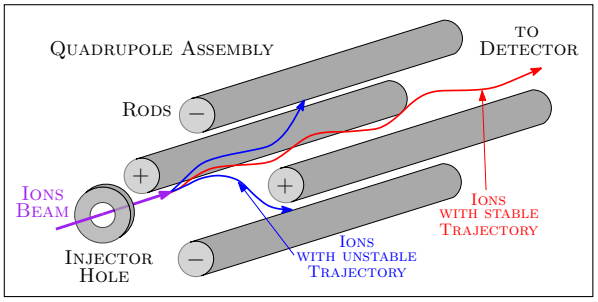

Figure 2.7: *Example of trajectories of an ion beam within an electric quadrupole.*

$$\frac{d^2x}{dt^2} + \frac{qx}{mr_0^2}[U + V\cos(\omega t)] = 0 \tag{2.21a}$$

$$\frac{d^2y}{dt^2} - \frac{qy}{mr_0^2}[U + V\cos(\omega t)] = 0 \tag{2.21b}$$

$$\frac{d^2z}{dt^2} = 0 \tag{2.21c}$$

The solution of differential equations 2.21 gives a complete description of the trajectory of each ion, in terms of the initial conditions of the ion.

The solution of the last differential equation along z–*axis* indicates that the ion beam velocity remains unchanged. On the other hand, the first two equations are examples of the Mathieu equation, which can be solved numerically. The voltages applied to the rods affects the trajectory of the ions that cross it; for a given voltage, continuous and alternating, only ions with a certain mass–to–charge ratio can pass through the electric quadrupole, while the others are diverted out of the original path and removed from the beam, as reported in Figure 2.7. Quadrupole lenses are typically used as doublets or triplets for solutions that are focusing in both transverse directions.

2.2.3 Ion beam focusing systems

In the following section two focusing devices are introduced: the first operate by electrical deflection (Einzel lens), and the second by magnetic deflection (Magnetic lens). Particular care has been taken in the last one, to which some experimental results will be presented.

Einzel lens

The *Einzel Lens* is a device used for focus or transport ion beam. It is made by three cylindrical electrodes, where the first and third are put on the same potential V_0, and the central electrode is put at different potential V_E.
The Einzel focus power is dependent from the potential applied at three electrodes and also from the geometry. We can define a potential ratio, R, as follows:

$$R = \frac{V_E - V_0}{V_0} \tag{2.22}$$

From behaviour of R it is possible to distinguishes two regimes: *Deceleration–Acceleration mode* (for $R < 0$) and *Acceleration–Deceleration mode* (for $R > 0$), as you can see from Figure 2.8. Both of these two modes are focusing, but in decel–accel mode the refractive power of the lens is much higher then in the accel–decel mode, at the same lens voltage. Moreover the focal length is smaller in decel–accel mode. On the other hand, accel–decel mode could be preferred if higher voltage can be handled, because it has lower spherical aberrations than decel–accel Einzel lenses, especially when the refractive power is high.
Figure 2.8 shown the behaviour of the refractive power on the applied potential to the three cylindrical electrodes; this is obtained only numerically [114, 128].

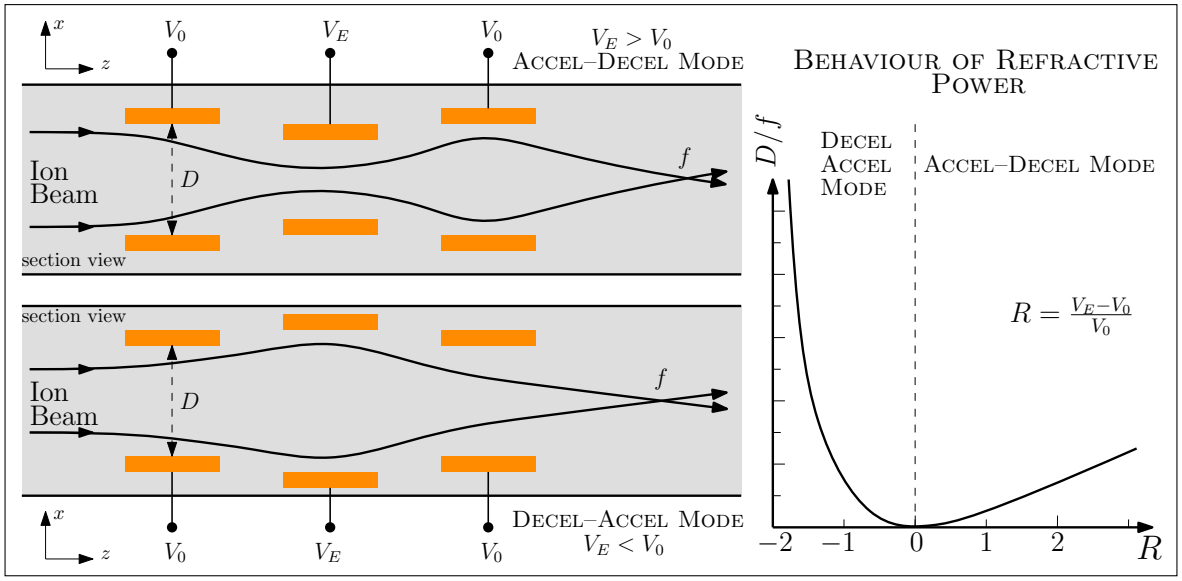

Figure 2.8: *Section view of Einzel lens geometry for acceleration–deceleration mode and deceleration–acceleration mode (on left); behaviour of refractive power on applied potential in the two modes (on right).*

Magnetic lens

A magnetic lens is employed to focus an ion beam due to its magnetic field with rotational symmetry. An uniform magnetic field applied to ion bunch produces a deflection of the particles, but no focus effect. It is required a field with axial symmetry to have focus effect. The starting point of this treatment is once again the Lorentz equation, introduce in Equation 1.17. Since the latter, a magnetic field can produces an ion deflection only when the particle velocity is not parallel to field. Thus, an ion that travel on the central axis, in a field with cylindrical symmetry is not affect by any force. This axis, so represent the *optical axis*.

In Figure 2.9 there is a representation of a cylindrical magnet view in section, the beam propagates in *z–direction*. It is more advantageous to use cylindrical coordinate, due to magnetic field possesses axial symmetry. So we introduce z, that indicate symmetry axis, r, is the radial distance from *z–axis*, and Φ that is the azimuthal angle, and represents the direction of the radial vector relative to plane of initial trajectory of the particle.

Let's study the motion of a positively charged particle approaching the magnetic field, assuming that it starts from an axial point O and enters the field with an angle formed by its

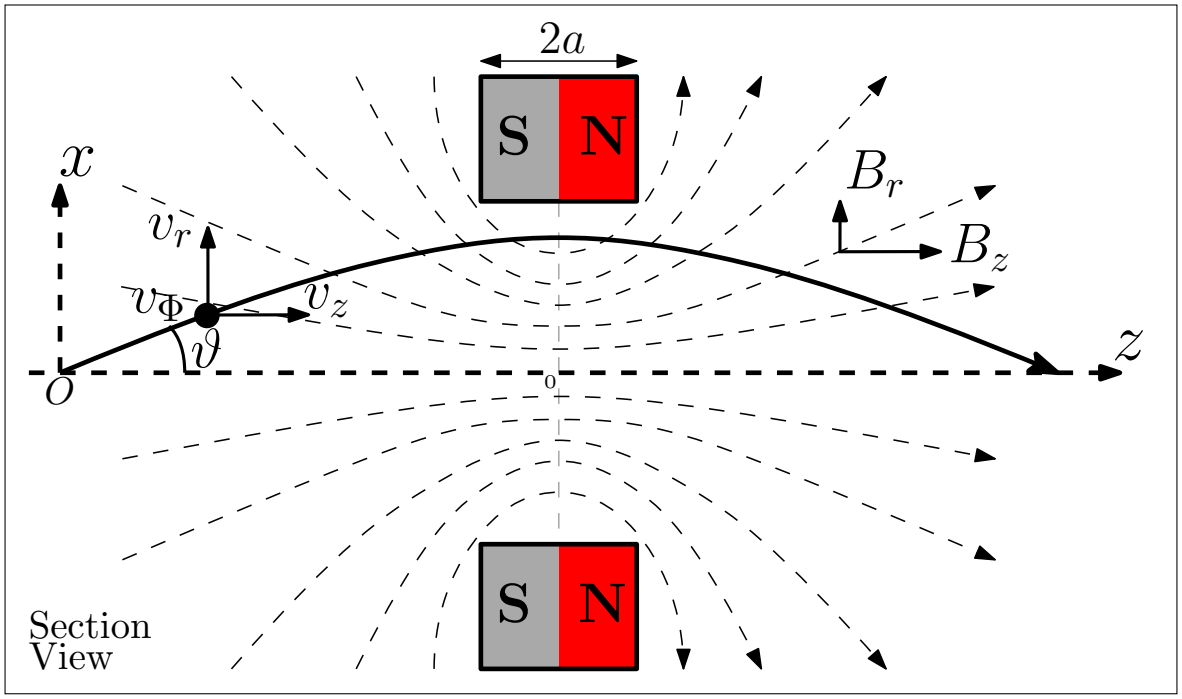

Figure 2.9: *Section view of magnetic flux line due to a thin electromagnet or a permanent magnetic ring. In this picture is represented the trajectory of an ion with mass m and charge +q in the non–uniform magnetic field.*

direction of propagation and the central axis of the field itself, as shown in Figure 2.9. By decomposing the velocity vector of a single ion and the magnetic field, into the corresponding cylindrical components just introduced, the Lorentz force can be rewritten as follows:

$$F_\Phi = q(v_z B_r) - q(B_z v_r) \tag{2.23a}$$
$$F_r = q(v_\Phi B_z) \tag{2.23b}$$
$$F_z = -q(v_\Phi B_r) \tag{2.23c}$$

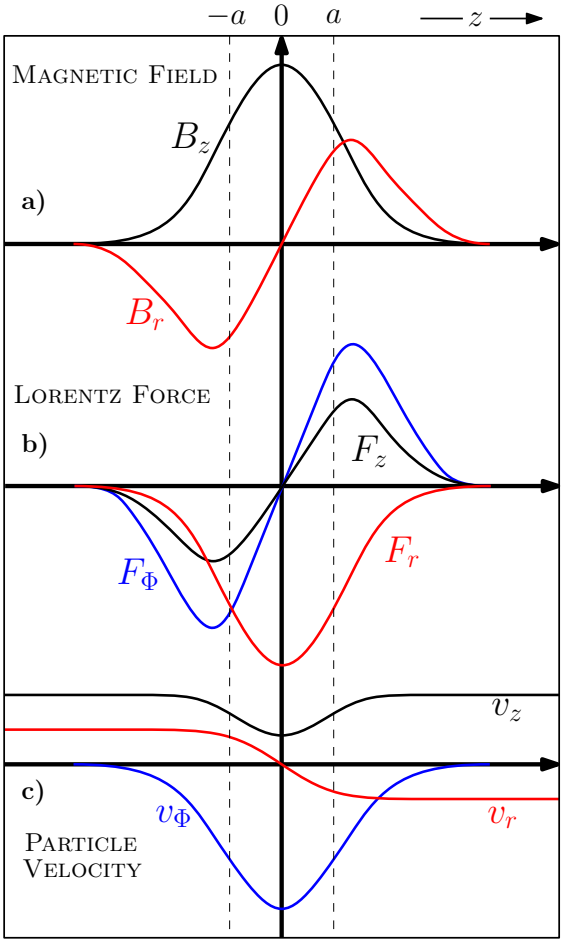

Figure 2.10: *Behaviour of axial z, radial r and azimuthal Φ component for: a) Magnetic Field, b) Lorentz Force and c) ion velocity in the system of interest.*

When the ion approaches the magnetic field, it has only an axial velocity, described by v_z and a radial velocity v_r. At the beginning, the main component of the magnetic field is the radial ones B_r, and so in Equation 2.23a the predominant part is qv_zB_r. This contribute has negative magnitude, since B_r is negative, because the line field go away from the magnet. When ion approaches the central of magnetic field, the component B_r decrease in absolute value, and B_z increase, but from Equation 2.23a, F_Φ remain negative due to sign in the second part of this expression $(-qB_zv_r)$. In this way, due to azimuthal force F_Φ, the particle begin to perform a spiral counterclockwise motion around the magnetic field, acquiring an increasing tangential speed v_Φ directed out of the plane of Figure 2.9.
This increase in the tangential component of the speed, v_Φ, means that a new radial force, F_r, begins to act on the particles, as you can see from Equation 2.23b. The radial force is always negative, because the azimuthal velocity is negative also (counterclockwise rotation). This implies, the F_r is direct towards *z–axis*, and so produce a focusing effect; in this way a non-uniform magnetic field with cylindrical symmetry acts as a convex lens.

In Figure 2.10 is shown the qualitative behaviour of the magnitude for magnetic fields,

Lorentz force and ion velocity components in function of the *z–distance*. Here, $\pm a$ represents the semi–length of the magnetic lens, and 0 is the central point on *z-axis*, as shown in Figure 2.9. So, if the radial force F_r will be enough, the radial motion will be invert, and the particle will approach the *z–axis*.

When the particle cross the zero position (central of the magnet), the radial velocity will invert its direction, and becomes negative. Thus, from Equation 2.23a, the second term becomes positive. On the other hands, after zero position, the field line will diverge, and B_r assumes positive value; so also the first term in Equation 2.23a becomes positive. Therefore, azimuthal component of force will be positive and acts to reduce the azimuthal velocity until zero: the spiral movement of the ion is stopped. However, it is necessary to take into account that the particle is located in another plane now with respect the beginning one [122].

Another important aspect il relate to ion velocity, that must be remain constant in a magnetic field. The change of radial and azimuthal velocity magnitude imply that the axial component v_z have to decrease in accordance with Equation 2.23c, that is negative for z value less than zero ($v_\Phi < 0$ and $B_r < 0$). Since $z > 0$, F_z is positive ($v_\Phi < 0$ and $B_r > 0$) and it acts in the same direction as the motion of the particle until it restores the starting value of the axial velocity v_z, as shown in Figure 2.10.

Ultimately, the passage of the positively charged particle through a magnetic lens, with cylindrical symmetry, produces a focusing effect due to the radial force that is always directed towards the center of the lens. The origin of this force is due to the spiral motion that the particle makes within the magnetic field. The azimuthal velocity component, responsible for the spiral motion of the ion, increases to the center of the lens, and then decreases again immediately afterwards, until it is reduced to zero when the whole field is crossed. As a final effect, the radial component of the particle velocity is reversed in direction, obtaining a focusing effect.

We have just seen that the radial component of the magnetic field B_r plays an import role in the focusing of an ion beam. If a solenoid was employed, instead a thin magnetic lens, B_r will be present only in the fringing field at either end. In this way, a solenoid is useful only to focus at the two extremity of it, but in the center, where the field is uniform, not produce any focus effect for a broad stream that travel parallel to *z–axis*. This is why solenoids are often used for the transport of ion beams, while thin magnetic lenses are used to focus them.

Focal Length of an Axial Magnetic Field

Magnetic lens, or system of magnetic lenses, are employed to focus ion beam, as in the optical lens occurs. For magnetic lens, the relation between focal length and applied magnetic field is the following [122]:

$$\frac{1}{f} = \frac{q^2}{8mE_0} \int \mathbf{B}^2 d\mathbf{z} \tag{2.24}$$

where q and m are the charge and mass of the ions respectively, E_0 is its energy, and $\mathbf{B}$ is the magnetic field generated by the lens. We can now distinguishes from two cases: the first one is that of long field, generated by solenoid for example, and the second is that of short magnetic field, generated by thin lens.
Let us consider a solenoid with length $\ell = 2a$. If this is long enough we can consider the field magnitude as a rectangular shape: $B_z = B_0$ in a region from $-a < z < a$, and it is zero outside of this region. The total area of this rectangle is $2aB_0^2$, and we can substitute in Equation 2.24:

$$\frac{1}{f} = \frac{q^2}{8mE_0} 2aB_0^2 = \frac{q^2}{8mE_0} \ell B_0^2 \tag{2.25}$$

Note that a solenoid is more useful to guide an ion beam, because to its length, differently from thin magnetic lens.
Otherwise, if we take into account a thin magnetic lens, we have to consider the assumption that $\mathbf{B}$ increase smoothly towards its maximum value B_0 (in the center of lens). A function that can be described this shape is the Lorentzian one:

$$B_z = \frac{B_0}{1 + z^2/a^2} \tag{2.26}$$

The last equation represents the plot of B_z in function of z, already seen in Figure 2.10(a). In this a is the Half Width at Half Maximum (HWHM), while $2a$ represent the Full Width at Half Maximum (FWHM). If we use this shape for magnetic field, the integral in Equation 2.24 becomes $(\pi/2)aB_0^2$. By substituting in Equation 2.24 we obtain:

$$\frac{1}{f} = \frac{\pi}{16} \frac{q^2}{mE_0} aB_0^2 \tag{2.27}$$

For example, if we consider a proton beam with $q = 1.602 \times 10^{-19}\ C$, $m = 1.672 \times 10^{-27}\ kg$, and energy of $150\ eV = 2.4 \times 10^{-17}\ J$ that cross a magnetic field with magnitude $0.3\ T$ and length $a = 5\ mm$, by Equation 2.27 we will obtain a focusing power $1/f = 66.5\ m^{-1}$, and a focal length of $f = 15\ mm$. If the focal length is less then twice of the FWHM of the lens $(2a)$, we could question the approximation of a thin lens. For more exact theory see ref [129].
Finally, the Equation 2.24 refers to non-relativistic case, in which the mass of charged particles is equal to its mass at rest. The relativistic increase in mass, can be incorporated in Equation 2.24, including relativistic Lorentz factor γ as follows [130]:

$$\frac{1}{f} = \frac{q^2}{8\gamma^2 mE_0} \int \mathbf{B}^2 d\mathbf{z} \tag{2.28}$$

This increment of mass due to relativistic effect, produce an increase in the focal length; so an ion that move at relativistic velocity will be focus at greater distance.

2.3 Focusing of Ion emitted by Laser–generated Plasma

Published Paper [2017]

Magnetic focusing of emitted ions from laser-generated plasma: enhancement of yield and energy

L. Torrisi and G. Costa
Dipartimento di Scienze Fisiche, MIFT, Università di Messina, V.le F.S. D'Alcontres 31, 98166 S. Agata, Messina, Italy

Published as: L. Torrisi and G. Costa: "Magnetic focusing of emitted ions from laser-generated plasma: enhancement of yield and energy", *Laser and Particle Beam*, Volume: **35**(2), Pages: 202–209 (2017)
Available from: 10.1017/S0263034617000015
Publication Date: Received 28 December 2016; Accepted 8 January 2017; Published 20 February 2017

In this section we will discuss a work concerning the focusing of ions emitted by plasmas, which as we will see, will have as final effect the increase in the number of detected particles, and an increase in energy due to an increment of the electrostatic field of acceleration [**131**]. In this study, low intensity laser, with nanosecond pulse duration, and $10^{10}\ W cm^{-2}$ intensity, is employed to generate carbon and aluminium non–equilibrium plasmas at a temperature of about 33 eV accelerating ions at energies of the order of 130 eV per charge state. The ion emission occurs manly along to the normal target surface and can be detected using ion collectors employed in time-of-flight (TOF) configuration. TOF is a time measurement of a particle (in this case), which travel a known distance through a medium (or in vacuum). The energy of particles detected can be evaluated using the signal obtain through a fast oscilloscope, by the following equation:

$$E = \frac{1}{2} m \left(\frac{L}{\mathrm{TOF}} \right)^2 \tag{2.29}$$

where m is the ion mass and L is the known flight distance. Equation 2.29 is valid in non–relativistic case, that for these laser intensities the velocities of the ions emitted by the target are widely in non-relativistic regime.
The introduction of a cylindrical symmetric magnetic field, with the optical axis parallel to the propagation direction of the particles emitted from the target, allows to focus the emission of ions by increasing the detected ion current, as was observed in section 2.2.3. In the following text, an approach of this is presented based on an ion optical system consisting of rings permanent magnets of 0.035 T each in their center, in which the laser–irradiated target is immersed. Simulations programs, based on the COMSOL software [132–134], and experimental data demonstrated that the light ion focalization, for protons, carbon, and aluminium ions occur in a very reproducible and predictable manner. This approach uses permanent magnets that do not need to be replaced, hence allowing the application in upcoming high-energy, high–repetition rate lasers.

2.3.1 Experimental Apparatus Description

A Nd:Yag laser operating at 1064 *nm* wavelength, 3 *ns* pulse duration and energy from 1 to 300 *mJ*, with a spot of 0.5 mm^2 surface and intensity of 10^{10} W/cm^2, operating in single pulse or in repetition rate up to 10 *Hz*, was used for our experiment.

The optical focusing lens is placed externally to the vacuum chamber (10^{-6} *mbar* pressure) and the laser goes inside though a quartz window. The incidence angle is 45° and the investigated ion emission occurs along the normal to the target surface (in BPA regime) as reported in the scheme of Figure 2.11. The targets were sheets of glassy carbon ($-CH_2-$) and pure aluminium (Al), with 2 cm^2 of surface and 1 *mm* of thickness. The plasma diagnostics was performed by an Ion Collector (IC) with secondary electron suppression grid, which acts such as a Faraday cup, and placed at a target distance of 142.5 *cm*.

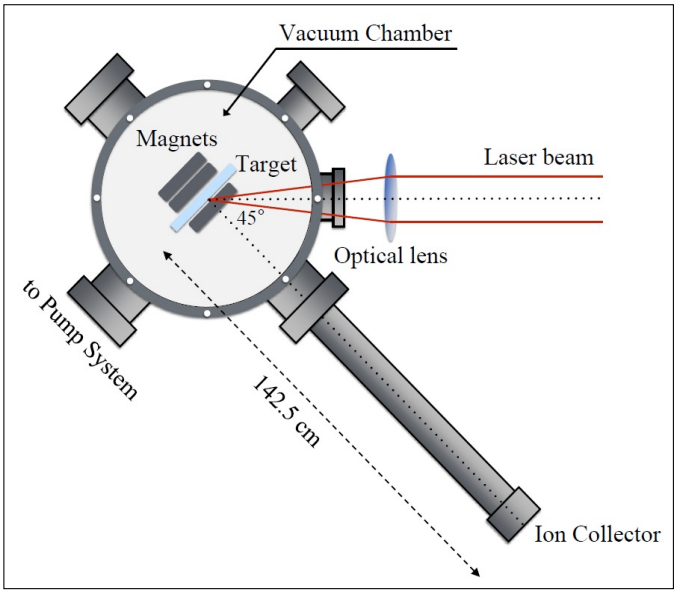

Figure 2.11: *Experimental setup illustration.*

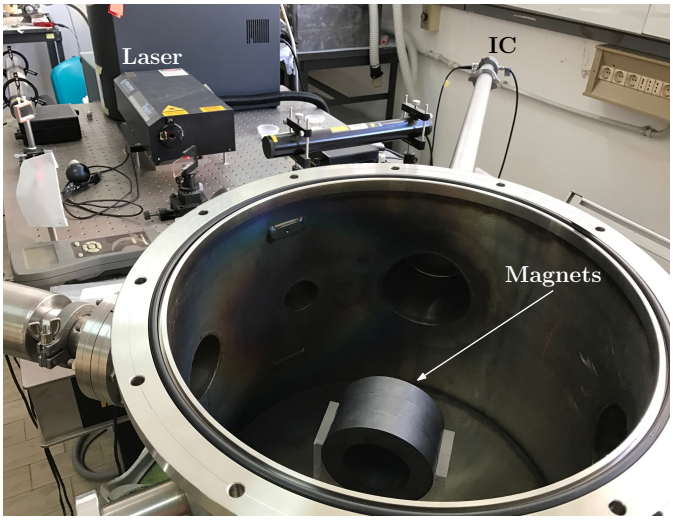

Figure 2.12: *Picture of scattering vacuum chamber.*

IC is connected in TOF approach to a fast storage oscilloscope (Tektronix TDS5104B, 1 *GHz*, 5 *GS/s*). The oscilloscope acquires using as trigger the laser pulse on a time scale of the order of 4 *μs*/division and a signal yield of the order of 10 *mV*/division. A picture of the experimental setup is shown in Figure 2.12.

In order to focus the ion beam generated by laser–plasma, permanent magnetic rings made of ferrite were inserted into the experimental apparatus, as shown in Figure 2.11 or in Figure 2.12.

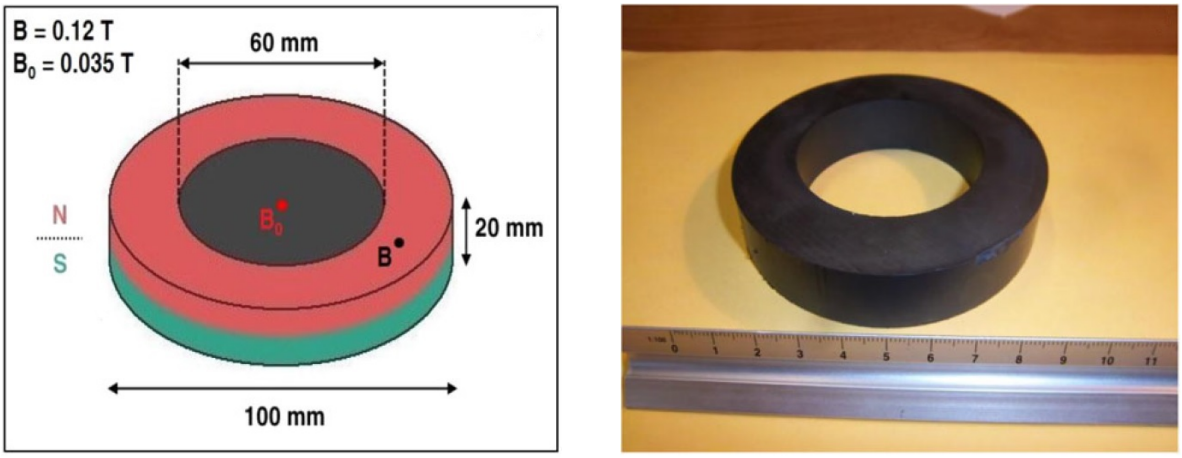

Figure 2.13: *Design of a magnetic ring (on the left) and its picture (on the right).*

A magnet has an outer diameter of 100 *mm* and an internal one of 60 *mm*, with a thickness of 20 *mm*, a scheme, and a photo of one magnet is reported in Figure 2.13, respectively.
The magnetic field products by permanent magnet, was experimentally measured by a Gauss-meter (Hirst GM08), finding the value of 0.12 T on the surface of it and 0.035 T at its center. The field has a cylindrical symmetry, and its optical axis is positioned along the normal to the target surface, in correspondence of the laser spot position. We used four experimental configurations of magnets to conduct measurements, which are:

1. Target without Magnet ($B = 0\ T$).
2. Configuration FB–1: one magnet in front of target and one back of it. The target is positioned in the rear of the first magnet and followed by other magnet. The measured magnetic field is 0.071 T.
3. Configuration FB–2: one magnet in front of target and two back of it. The target is positioned in the rear of the first magnet and followed by other magnets. The measured magnetic field is 0.097 T.
4. Configuration FB–4: one magnet in front of target and four back of it. The target is positioned in the rear of the first magnet and followed by other magnets. The measured magnetic field is 0.12 T.

Thus, the maximum number of applied magnets was five, where one is located in front of the target and from one up to four placed in the rear side of it. Results comparison, obtained with or without magnetic field, was performed in the same experimental conditions.

2.3.2 Results

In this next section we will show the results obtained by irradiating a glassy carbon or aluminium target under the conditions just described.

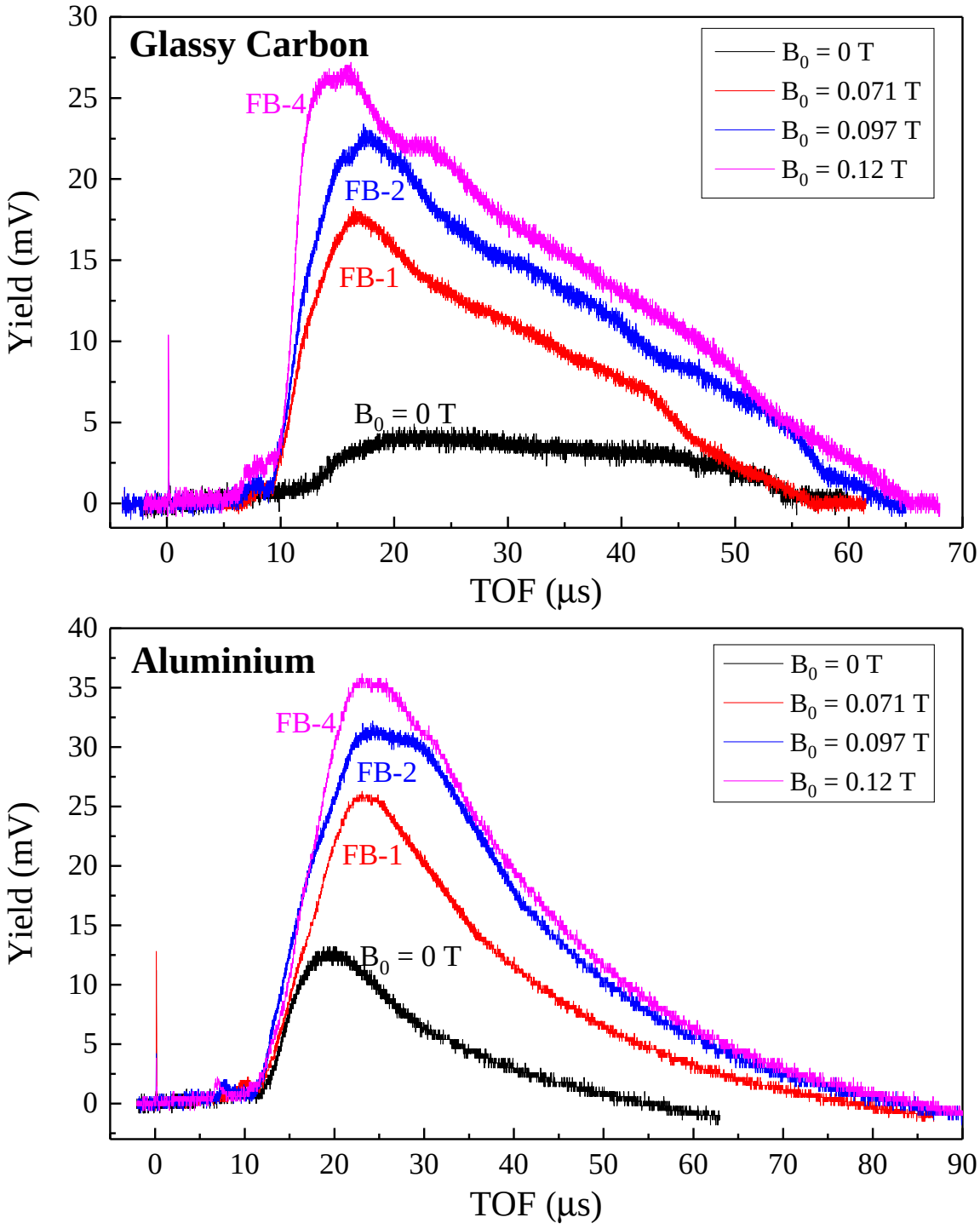

Figure 2.14: *IC–TOF spectra comparison for Glassy Carbon and Aluminium plasma emission using different axial magnetic fields.*

The first result presented is Glassy Carbon target Spectra, acquired in single pulse without magnet or with a magnetic rings placed in front of target and by changing their number in back of the target from one up to four. TOF measurements are reported in Figure 2.14. Glassy Carbon Spectra indicate that the maximum yield of carbon ions increases with the applied magnetic field growing from about 4 mV at $B = 0\ T$ up to about 27 mV using the configuration FB–4 (1 magnet front–target–4 magnets back). This means that the magnets rings enhance the axial ion emission toward the IC detector producing a sort of axial ion focusing. The peak shape indicates that all the emitted carbon ion species are enhanced due to focusing magnetic field.
The second spectra shown in Figure 2.14 is acquired irradiating aluminium target in single pulse and detecting the emitted ions in TOF approach, by changing the number of applied magnetics rings as in th previous case. This spectra indicate that the maximum yield of aluminium ions increases with the applied magnetic field growing from about 13 mV, using the configuration $B = 0\ T$, up to about 36 mV for the FB–4 configuration.

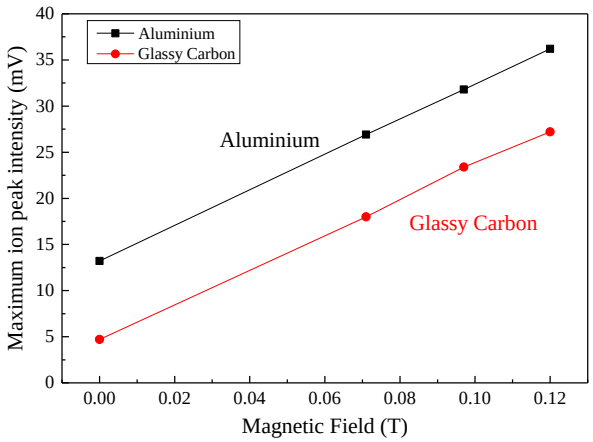

Figure 2.15: *Maximum ion peak intensity versus applied magnetic field for Glassy Carbon and Aluminium.*

This means that focusing magnets, enhancing the axial ion emission directed toward the IC detector. The peak shape indicates that all the emitted aluminium ion species are enhanced and a little amount of hydrogen, less than for glassy carbon, present as contaminant, is also increased.
This increase, both in terms of maximum yield intensity (mV) than in terms of total yield (area subtended by the ion peak), is a linear function of the applied magnetic field, as reported in the plot of Figure 2.15 for Carbon and Aluminium maximum ion yields.

Both for glassy carbon and aluminium targets, the ion yield increases in maximum intensity (mV) and also in total number of particles detected (area subtended by the ion peak). The increment is a linear function of the applied magnetic field, as reported in the graph show in Figure 2.15 for the maximum intensities detected. Note that ions yield for aluminium is always higher with respect to carbon, both without or with magnetic rings. One cause of this result is due to the different evaporation temperature, very high for carbon (4830 $°C$) with respect to aluminium one (2450 $°C$). The lower evaporation temperature for Aluminium reduces its ablation threshold and permits to obtain a large number of Aluminium ions and vapor pressure than for Carbon.

Returning to Figure 2.14, for Glassy Carbon target, the proton peak starts at about 9 μs in absence of magnetics rings and at about 6.5 μs in presence of them (FB–4), corresponding to a kinetic energy of about 130 and 250 eV, respectively. This indicates that magnetic rings cause also an energy enhancement, and not a yield increment only; this energy increase in the case of protons is about 92%. The carbon ion peak starts at about 15 μs in absence of magnetics rings and at about 11 μs in presence of them, which corresponding to a kinetic energy of about 563 and 1047 eV, respectively. The increment of energy for carbon ions is about 86%. The energy released by the plasma to the protons, due mainly to Coulomb interactions in the charge separation zone, represents the conferred energy per charge state of the plasma acceleration. Thus, from the maximum carbon energy to maximum protons ones ratio we obtain a value of 4, indicating that the faster carbon ions are the C^{4+}. For lower charge states of carbon ions, energy decreases to about 140 eV for C^{1+}. The ion energy distribution produces a long tail of the carbon ion peak, shown in TOF spectrum, which is elongated due to C_xH_y groups produced in the hot plasma, according to literature [135].

According to the Lotz theory of the ionization cross section [136–138], the number of ions, which have a certain charge state, decreases as the charge state increases, so the fast C^{4+} ions present in the plasma will be lower with respect to that of the slower C^{1+}. Since NIST ionization potential database [139], the carbon fourth and fifth charge state have 64.5 eV and 392 eV ionization potential respectively, which means that plasma should contain electrons with a maximum energy between 64.5 and 392 eV. Assuming the maximum electron energy to be of about 150 eV with Boltzmann distribution, the mean energy of the plasma should be about 1/3 of this maximum value, i.e. 50 eV, that corresponding to a plasma temperature of about $k_BT = 2E/3 = 33\ eV$.

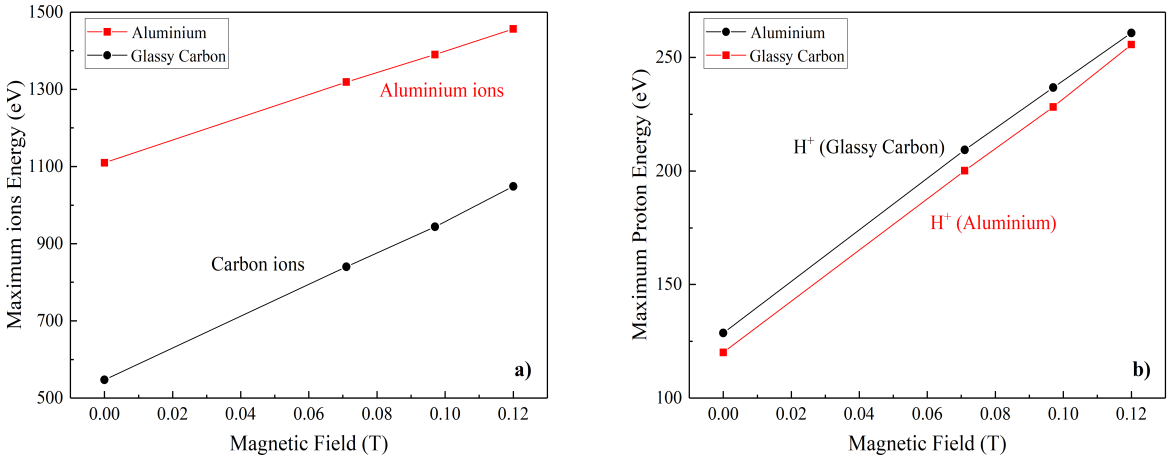

Figure 2.16: *Maximum ion energy (a) and maximum proton energy (b) for carbon and aluminium plasmas on applied cylindrical magnetic field.*

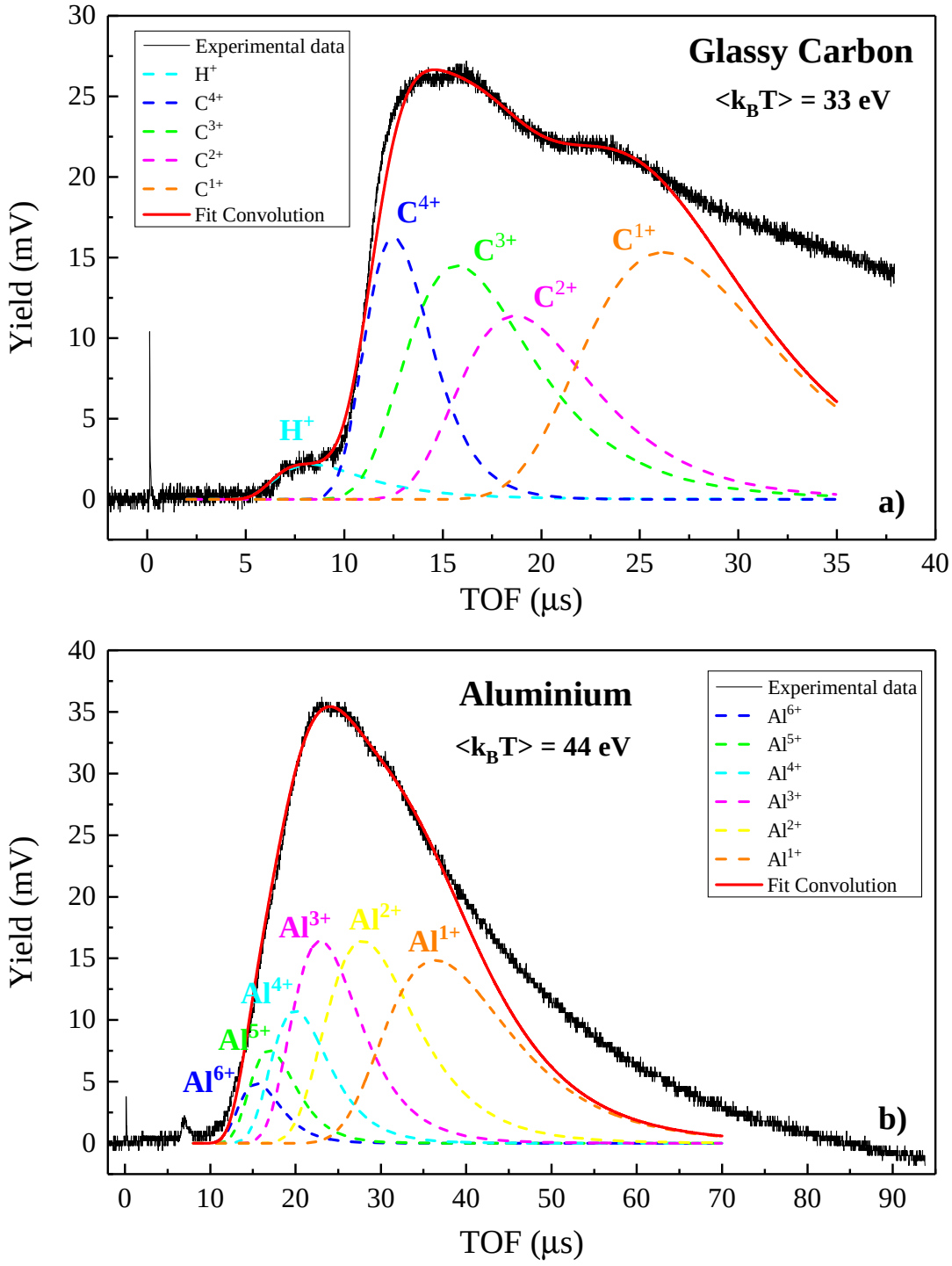

Figure 2.17: *IC–TOF spectra deconvolution by CBS distribution for ion emission from glassy carbon (a) and aluminium (b) plasmas.*

On the other hand, for aluminium target, shown in Figure 2.14, the main peak starts at about 16 μs in without any magnetics rings and at about 14 μs in presence of the maximum magnetic field, corresponding to a kinetic energy of about 1113 and 1455 eV, respectively. Also in this case we have obeserved an ion energy enhancement, that for aluminium ions is about 30%, thus resulting more contained with respect to the glassy carbon case. Although for aluminium target the proton emission is less evident with respect to carbon one; a little proton signal is visible in the spectra occurring at about 9.5 and 6.5 μs without and with external magnetic field, which correspond to the energy of 120 and 250 eV, respectively, indicating proton acceleration similar to the case of the glassy carbon target. By dividing the maximum aluminium energy to proton one, it is deduced a maximum aluminium charge state of about 6+. This means that the maximum electron energy should be within the ionization potential of Al–VI and Al–VII, which is 190 and 241 eV, respectively [139]. Thus in this case, it is possible to assume that the maximum electron energy is little higher than for carbon plasma, it is of about 200 eV, that corresponding to a mean Boltzmann energy of about 66.7 eV and plasma temperature is of the order of $k_B T = 2E/3 = 44\ eV$.
The kinetic energy enhancement for aluminium and carbon ions is reported in Figure 2.16(a), while for protons is shown in Figure 2.16(b). The enhancement is linear with the applied value of the axial magnetic field.
The confirm of the evaluated temperatures and of the supposed number of charge states in Carbon and Aluminium laser-generated plasma comes from the deconvolution of the IC spectra using the CBS function time–dependent, as that see in Equation 1.71 [140]:

$$f(t) = A\left(\frac{m}{2\pi k_B T}\right)^{3/2} \frac{L^4}{t^5} \exp\left[-\frac{m}{2k_B T}\left(\frac{L}{t} - \sqrt{\frac{\gamma k_B T}{m}} - \sqrt{\frac{2zeV}{m}}\right)^2\right] \tag{2.30}$$

where A is a normalization constant, m and ze are the mass and charge of the ion, L and the distance between target to detector, γ represents the expansion adiabatic (which is 1.67 for monatomic species), and finally V and $k_B T$ are the plasma potential and temperature.
Figure 2.17 shows two typical examples of IC spectra deconvolution relative to the carbon plasma (a) and to the aluminium plasma (b) obtained with the FB–4 magnetic configuration, which have a field magnitude of 0.12 T. The spectrum relative to carbon plasma shows the deconvolution of hydrogen and of four charge states of carbon ions with a Boltzmann distributions width ocorresponding to a mean temperature of 33 eV. The spectrum relative to aluminium plasma shown six charge states of aluminium ions with a Boltzmann distributions width corresponding to a mean temperature of 44 eV.

Simulations by COMSOL Multiphysics

COMSOL Multiphysics simulation software allows to simulate the ion focusing due to presence of the magnets rings, as reported Figure 2.18.

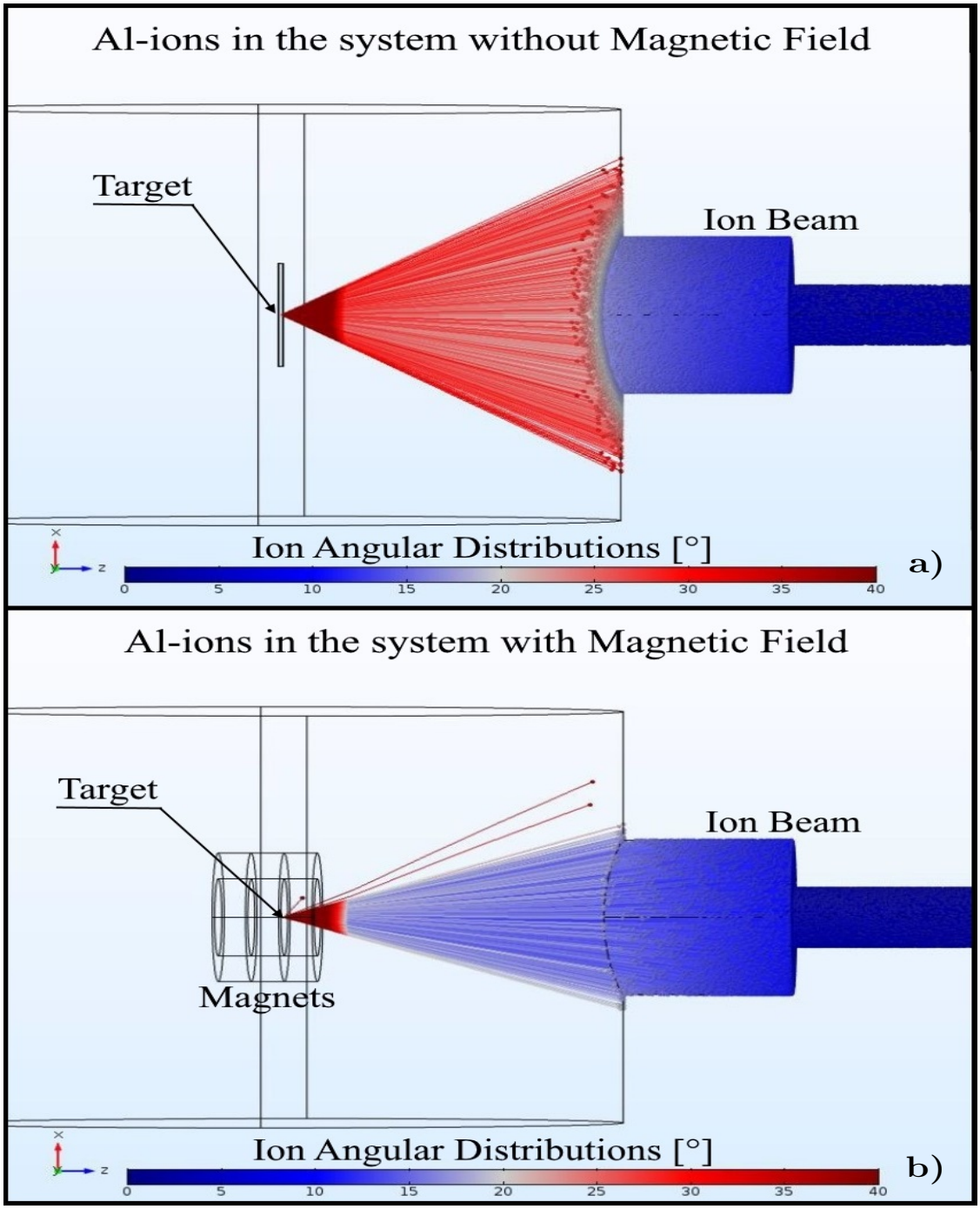

Figure 2.18: *COMSOL simulation of the Aluminium ion emission from the laser-irradiated target without (a) and with FB–2 (0.097 T) configuration of magnetic field (b).*

The simulation was perform for aluminium ions emitted with the angular distribution given by literature [141], without magnetic field application Figure 2.18(a) and with the FB–2 magnetic configuration (0.097 T) Figure 2.18(b).

Simulations are agreed with the experimental ions yield enhancement for aluminium and carbon plasmas, due to a magnetic focusing toward the IC detector. Such focusing effect enhances the ion current of about a factor 6.6 for the Carbon ions and of about 2.8 for Aluminium ions for FB–4 magnetic configuration. This result is obtained both experimentally and by simulation, which indicates that the magnetic focusing decreases with the atomic mass of ions. To focus heavy ions toward the IC placed axially at 1.425 m from the target, higher magnetic field should be applied to ion beams, as confirmed by simulation.

The ions energy increases, when magnetic rings are place in the system, can be explained through the formation of an electron trap in front of target, due to apply magnetic field, that drives ions plasma acceleration, as presented in previous work [142]. The magnets, in fact, modify the electrons trajectories emitted from the plasma. As final result they produce some zones where the electrons accumulation density is high, close to the target surface, that increase the spatial Coulomb forces acting on ions emitted from laser–generated plasma. The accumulation density is a dependent on the time and on the space. However the maximum value that it could reach, depends mainly on the electron yield emission, their energy distribution and applied axial magnetic field. The COMSOL simulation software permits to compute the trajectories of the electrons emitted from the plasma without and with the magnetic field application. Figure 2.19 shows an example of electron trajectories simulation emitted from the aluminium plasma in FB–2 magnetic configuration.

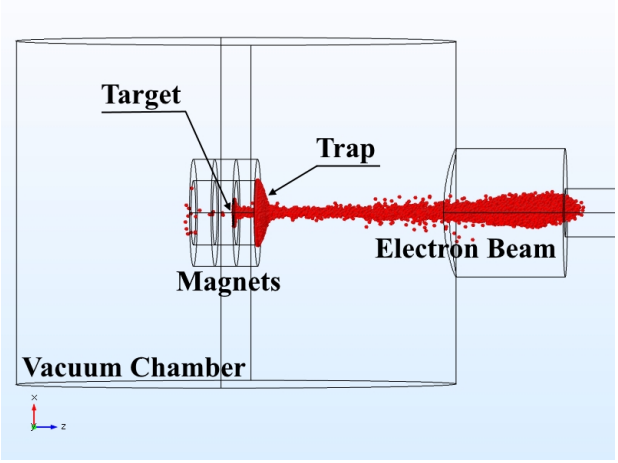

Figure 2.19: *COMSOL simulation of electrons emission from aluminium target in FB–2 magnetic configuration setup. The picture shows a formation of an electron trap, due to apply magnetic field.*

The simulation is performed by 30.000 electrons (N_e) with an average energy (E_e) of 50 eV and a magnetic field of 0.097 T. The maximum density occurs at about 25 ns from the laser pulse hits the target and the trap is localized at about 2.5 cm distance from its surface, as shown in Figure 2.20, where is reported the accumulation density as a function of time, from the laser shot, (a) and of distance, from the target surface, (b). The distance of 2.5 cm correspond to about the end of the magnetic ring placed in front of the target. The electron accumulation density stay at high values for times of about 100 ns from the laser shot; which permits to accelerate slow ions emitted from the plasma.

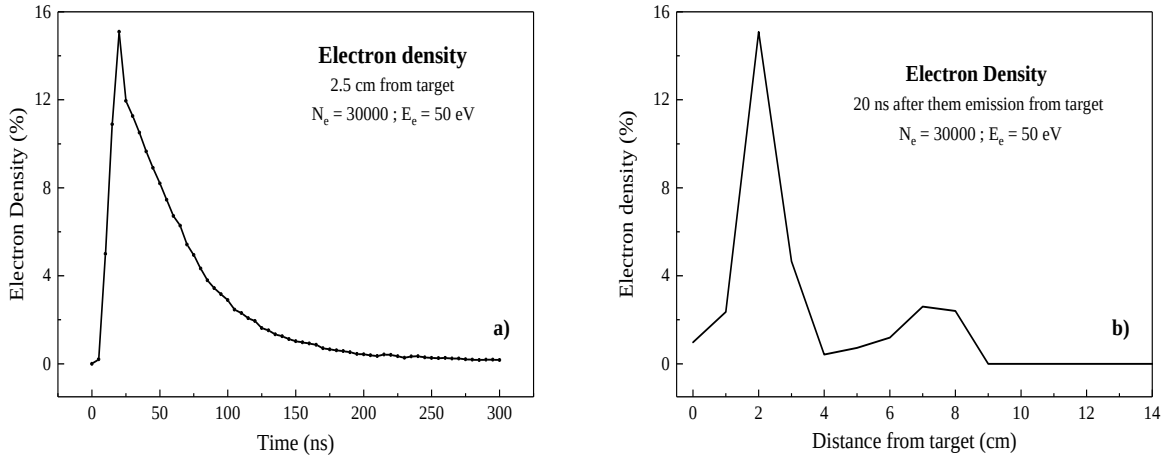

Figure 2.20: *Electron density located at* 2.5 *cm from the target surface as a function of time (a). Electron density after 20 ns from the laser shot as a function of the target surface distance (b).*

After 20 *ns* from the laser shot, the density profile is maintained high to about 4 *cm* from the target, then it decreases strongly at larger distances.
Of course by changing the electrons energy, the density profile will change in intensity, position and occurring time; for example, decreasing the mean electron energy to 10 eV the simulations shows that the trap will increase in intensity, and will be localized at about 2.5 *cm* from the target surface after a time of 50 *ns* from the laser shot.

2.3.3 Section Conclusions

The study presented in this work is of great interest, not only for basic physics, but also for several applications concerning the laser–matter interaction and plasma production, where a magnetic field with cylindrical symmetry can be improved to increase the flow and the energy of the ions emitted by targets due to laser interaction.
The work performed should not be considered as conclusive, but on the contrary should be intended as preliminary and adaptive to stimulate further studies to optimize the applied magnetic field, in order to increase the ion beams emittance, to change the ion and electron angular spreads, and to modify the particle energy, due to electron traps, as we seen. Our experiment was demonstrative, because only two kind of light ions, carbon and aluminium, were used. It should be extended to heavy ions and to higher laser intensities [**143**]. Moreover, the magnetic field must be optimized to be adapted to higher value of laser intensities and ions masses. Similar results can be obtained by laser intensities above 10^{14} W/cm^2.
To summarize, ions current was enhance up to 6.6 times, but, it is possible to optimize the magnetic lens focus in order to reach higher values. Analogously, the electron traps could be create closely to the target, to increase the plasma electric field driving ion acceleration.

Chapter 3

Ion Diagnostics in BPA Regime using Magnetic or Electric Fields

The pulsed laser–generated plasma in vacuum, at low intensities, below than $10^{16}\ Wcm^{-2}$, can be characterized using different physical diagnostics. The charge particles emission in backward direction, can be characterized using magnetic or electric spectrometers. Thus, a magnetic field applied transversally to the ion beams emitted by plasma, produces a deflection on the plane orthogonal to the field's strength lines, according to the Lorentz force, which separates ions based on their momentum–to–charge ratio. This system, in the work that will be discussed, is called Magnetic Spectrometer Chamber (MSC). Similarly, an electrostatic field can be employed to deflect ions, at a 90° angle, by separating them according to their energy–to–charge ratio, as in the case of the Ion Energy Analyzer (IEA). Such techniques are often based on time-of-flight (TOF) measurements. The detectors used for ion gathering can be of various kinds; if the ion current is high enough (> 10 μA) ion collectors (IC) can be used. When the currents are low, devices able to amplify the input signal, such as Secondary Electron Multipliers (SEM), are preferred. COMSOL simulation software is used for the realization of a suitable electromagnet, and for the analysis of ion trajectories in magnetic or electrical deflection systems. Of course, the values obtained from computational calculation are compared with the experimental ones for the evaluation of the relevant physical properties of the laser–generated non–equilibrium plasmas. The experimental results obtained are presented and discussed in the following chapter.

3.1 Plasma Diagnostic in BPA Regime

It is clear that the acceleration of ions in the opposite direction with respect to the propagation of the laser beam (backward) is less efficient than that in the same direction (forward). Many experiments, performed with several laser intensities, show significant decreases in the energies of ions emitted by plasmas in the backward direction rather than coming from the target's rear surface [144–146]. The difference in the acceleration pattern depends, as already seen in the section 1.3, on the electronic cloud that forms in front of the surface of

the target, in both directions, and consequently on the value of the longitudinal electric field that determines the ion acceleration.
In the following discussion, some experimental results obtained through laser–induces plasmas in BPA regimes, at intensity that not exceeding $10^{12}\ Wcm^{-2}$ will be presented. However, these results can be extended up to $10^{16}\ Wcm^{-2}$ laser intensity. In fact, for intensities below $10^{16}\ Wcm^{-2}$, the ions accelerated in BPA regimen have energies not exceeding 500 keV per charge state. In this way it is possible to deflect and analyze them with only magnetic or electric fields. Higher energy values, preclude the use of more intense magnetic or electric fields, not always easily obtainable.

3.1.1 Magnetic Spectrometer Chamber

During the PhD the author of this thesis was involved in the development and optimization of a system for ion analysis and characterization, emitted by laser–generated plasmas in BPA regime, by means of magnetic deflections, called *Magnetic Spectrometer Chamber* (MSC). A photo of the instrument is shown in the Figure 3.1.
The MSC is a semi-moon shaped vacuum chamber connected by a vacuum tube to the primary chamber, where the laser–target interaction takes place. The ion beam is driven in the direction of the MSC (along *z–direction*), and before entering it passes through a system of two pinholes, which ensure a narrow and collimated beam. Once inside the MSC, a magnetic field directed orthogonally to the direction of incidence of the beam, along the *x–axis*, deflects the ions in accordance with the Lorentz force in the *y–z plane*, as shown in the schematization in Figure 3.2. The collimated ion beam is revealed by 32 Faraday Cups, mounted on a mobile sleigh, which are 2.9° from each other.

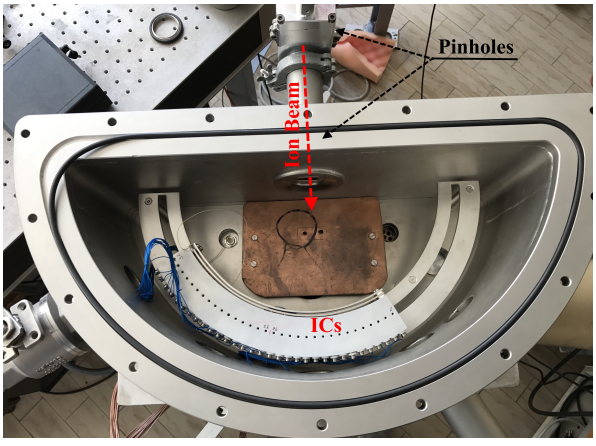

Figure 3.1: *Picture of Magnetic Spectrometer Chamber (MSC).*

The mobile slide covers an angle of 90°, and can be positioned at different points in the chamber to detect ions between 0° and 180°. Further analysis devices can be placed at fixed angles of 0°, ±30°, 45° and 60°, as shown in Figure 3.2. The faraday cup signal is sent to a fast storage oscilloscope; however, since collimators cut down ionic current, it is necessary to work with high input impedances of the megaOhm order. In this way we get a signal amplification, but a slow discharge of the RC circuit. Other devices, capable of amplifying the input ion current can be used as we will see below.

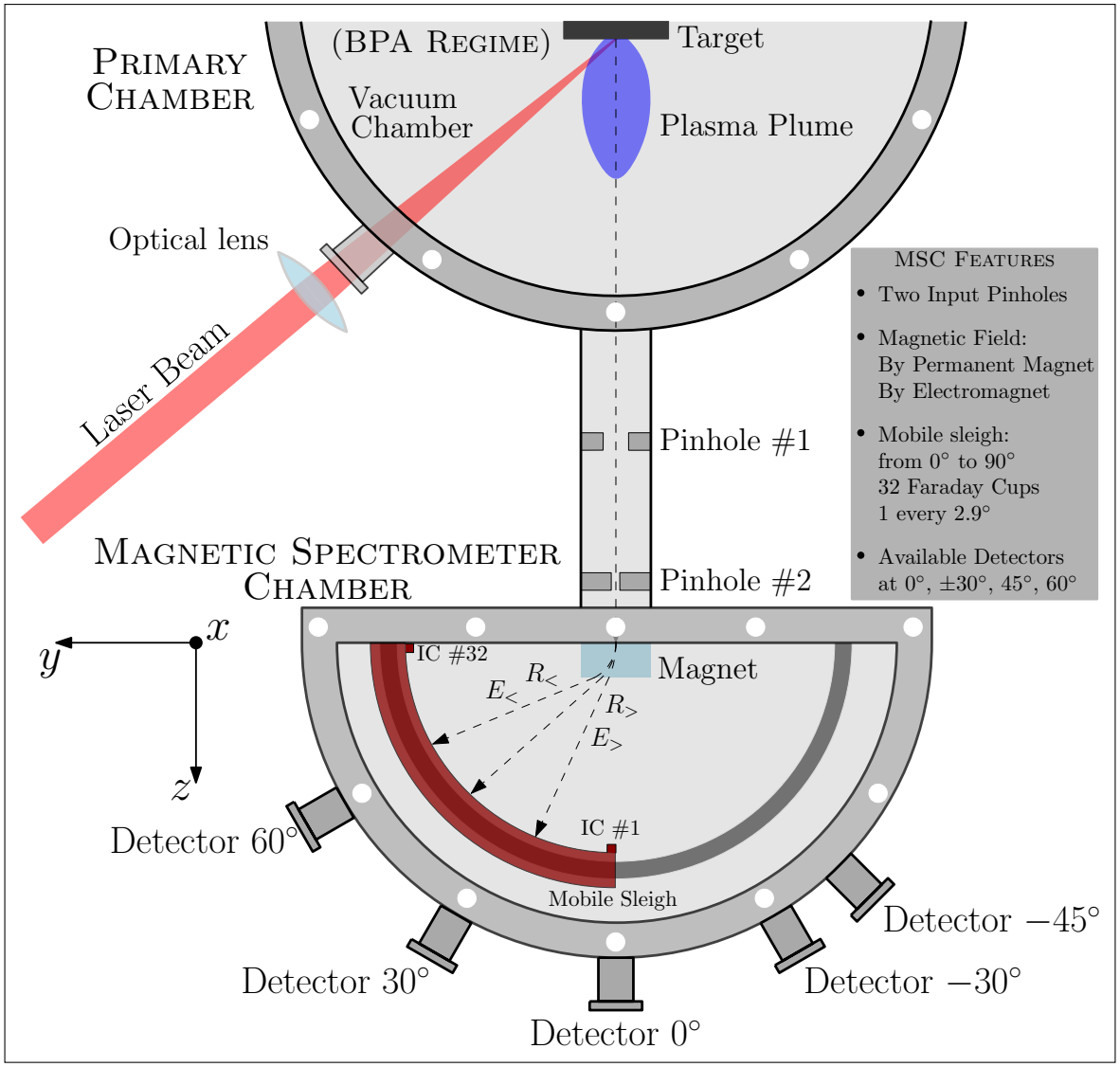

Figure 3.2: *Representation of magnetic Spectrometer Chamber (MSC) at University of Messina.*

This device can be employed also to evaluate the angular distribution of ion beams emitted from the target that cross the collimator system. In fact, if no magnetic field is introduced in the system, and the mobile sleigh containing the 32 faraday cups is placed between 45° and 135°, it is possible to measure the angular distribution of the ion beam that crosses the two input pinholes. An example of what has just been described is shown in the Figure 3.3, obtained for a plasma produced from an aluminium target [147].

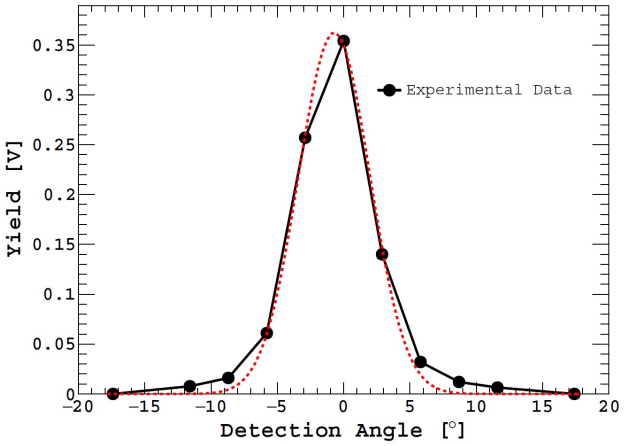

Figure 3.3: *Experimental data (in black) and fit (in red) of the angular distribution for Al-ions, emitted from a target of pure Aluminium.*

The angular distribution reported in Figure 3.3 shown the profile of the ion beam after it passes through the collimation system. The data were obtained by evaluating the maximum yield, proportional to the areas subtended by the TOF spectra, acquired by the faraday cups mounted on the mobile sleigh, versus the angle of detection. The fit, instead, was performed with a normal distribution [148], to evaluate the width of the ion beam:

$$f(x) = \frac{1}{\sqrt{2\pi\sigma^2}} e^{-\frac{(x-\mu)^2}{2\sigma^2}} \tag{3.1}$$

where μ is the mean or expectation of the distribution, and σ is the standard deviation. The correlation between the Full Width at Half Maximum (FWHM), denoted by Γ, and the standard deviation is:

$$\Gamma = 2\sqrt{2\ln 2}\sigma \tag{3.2}$$

thus, we obtain from the fit $\Gamma \approx 6.33°$. This means that the two pinholes generate a Gaussian shaped ion beams, which have very narrow angular aperture, but also with low currents. Since the spectrum shown in Figure 3.3, considering an input oscilloscope impedance of 1 $M\Omega$, we have that the maximum current intensity, obtained at about 0°, from Ohm's law is worth ~ 350 nA. However, for heavier ion beams we expect a narrower angular distribution and a consequent increase in the current intensity detected at the centre of the beam [141]. When a Magnetic Field, orthogonal to particle direction, is applied to collimated ion beam, this is deflected according to Lorentz' force, shown in Equation 1.17, and the ions will be separated based on their mass to charge ratio, making orbits of different radii:

$$R = \frac{mv}{zeB} \tag{3.3}$$

where v is the ion velocity and B is the magnetic field module. Therefore heavier ions, with the same charge state, will be diverted with higher radius, and thus will be less deflected. At the same time, ions with higher charge state, but with the same mass, will be deflected more. It is clear that a device is based on this physical principle will separate the same ions, with the same charge state, according its own velocity. Thus, this device works as a filter for the ratio linear momentum, $\mathbf{p}$, to charge state:

$$\frac{\mathbf{p}}{z} = Re\mathbf{B} \tag{3.4}$$

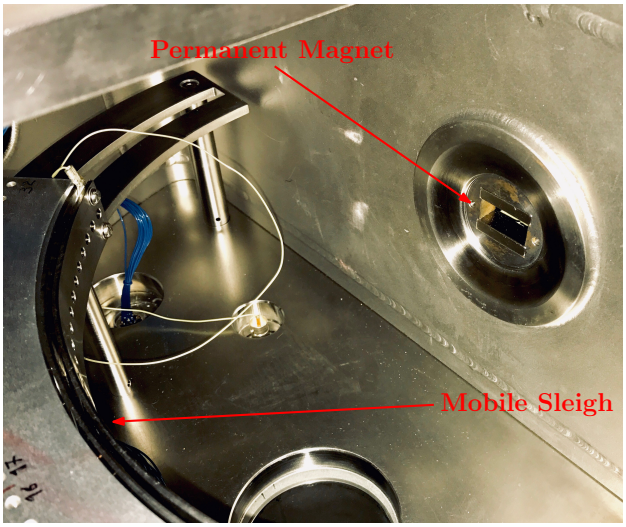

Figure 3.4: *Picture of the inside view of the MSC, where it is possible to see the permanent magnet, and the faraday cups mounted on the mobile sleigh.*

The MSC is a system that can operate in two modes: the first is with a fixed magnetic field (by using a permanent magnet for example); in this way it is possible to study the ions deflections at various angles. In this mode, each trajectory of the ions will correspond to a different value of the radius R, in the Equation 3.4. The second is by fixing an high–resolution detector at a given angle (e.g. at 30° in Figure 3.2), and by varying the the magnetic field module B in the Equation 3.4 (in this case R is fixed for all particles). The Figure 3.4 shows an internal view of the MSC, in which is shown the housing of the permanent magnet, with it inserted, and the mobile sleigh.

By MSC it is possible to o evaluate some of important features about the charged particles that constitute the non-equilibrium plasma, such us velocity, energy, charge state, and more. Figure 3.5 shown the simulation, performed with COMSOL Multiphysics simulation software, for first charge state of Aluminium and Tantalum, in the interest system. The simulations were performed using a Coulomb–Boltzmann distribution for the energy of particles [149], introducing a plasma temperature of 30 eV and a plasma potential of 50 V (with energy ranging from 100 to 700 eV). The magnetic field is fixed with dimensions of $25 \times 25 \times 10$ mm; it has a value of 0.18 T, in the centre of system. This study would be fine if

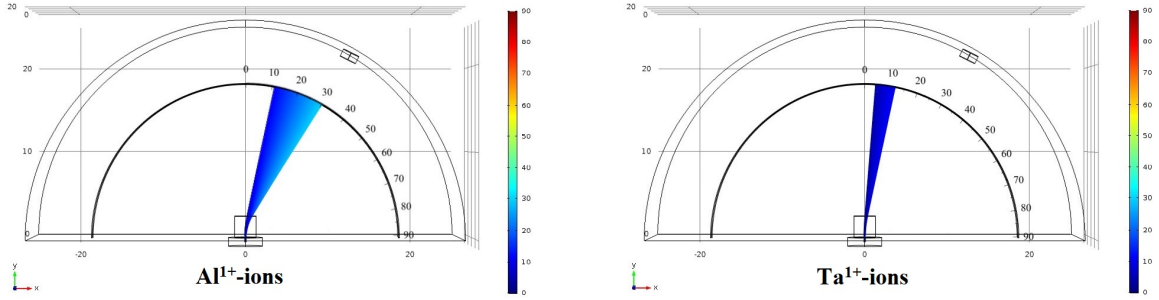

Figure 3.5: *COMSOL Multiphysics simulations about Al^{1+}–ions and Ta^{1+}–ions, in the system of interest, with a transversal magnetic field module of 0.18 Tesla.*

we use the 32 faraday cups of this device. However, due to the low number of ions that out of the two pinholes and their subsequent separation due to magnetic field, the spectrometer resolution is very low.
As mentioned above, a solution to this problem is to use high–resolution detectors, such as an electron multiplier, positioned at a certain angle, which however precludes the use of a variable ion deflection magnetic field. The author also dealt with the design and optimization of an electromagnet for the required aim, of which a brief discussion follows.

MSC Electromagnet Design

Due to the low current intensity of the ions that pass through the two pinholes, it is more useful to use an electron multiplier for the detection of these, which amplifies the signal. One idea is to work with a high–resolution detector at a fixed angle, varying the magnetic field of deflection for the particles. In this way, when **B** varies, different ions momentum–on–charge state values **p**/*z*, are sent to the detector (Equation 3.4).

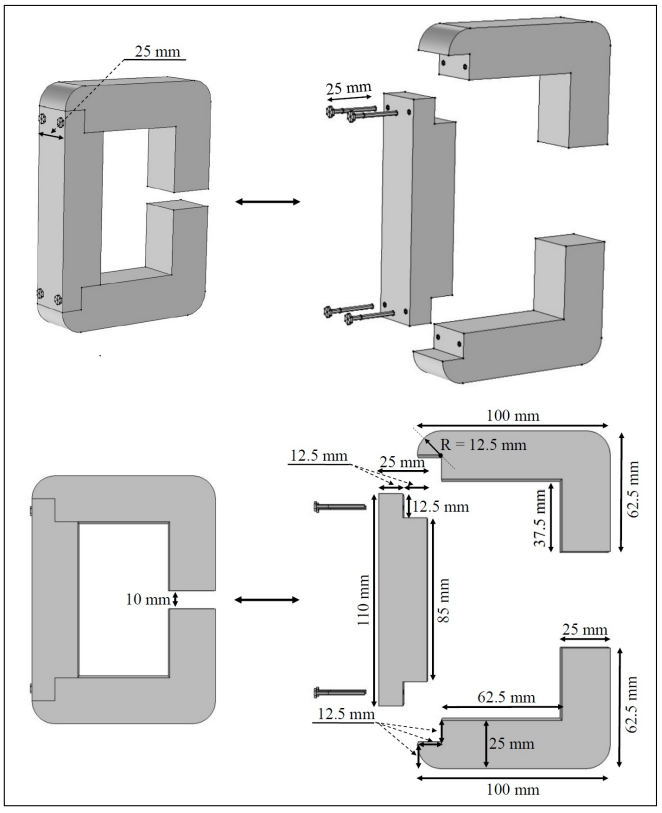

Figure 3.6: *Design of the electromagnet iron core.*

A solution is therefore the inclusion of an electromagnet with appropriate characteristics; for this purpose, the design of the electromagnet was carried out using the COMSOL simulation software. The ion deflection device is composed of an iron core with a "C" shape, as shown in the Figure 3.6. The core can be divided into three parts by removing screws. This allows you to insert different coils according to the fields you want to obtain. The central part has an "I" shape, and is the one on which the copper coil is installed. The cavity, where the particles deflected by the magnetic field will pass through, measures $25 \times 25 \times 10$ *mm*, where the last dimension corresponds to the height of the field.
Various simulations by COMSOL Multiphysics were performed to evaluate the value of the magnetic field in the iron core cavity.

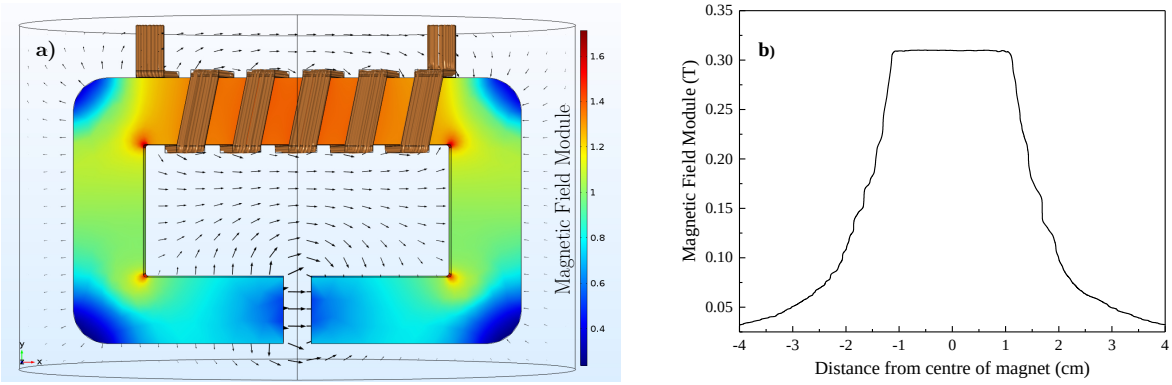

Figure 3.7: *Simulation of electromagnet with 1200 copper windings cross by 3 current's Ampere (a), and magnetic field profile in the core cavity (b).*

A simulation carried out with 1200 copper coils, crossed by 3 A of current intensity, is shown in the Figure 3.7a. The diameter of the copper wire section was 1.25 mm, and The simulation was carried out using the B–H curve for iron, so to obtain non–linear solutions when a current is flowed into the solenoid. The magnetic field obtained in the centre of iron core cavity is shown in Figure 3.7b. It reaches the maximum value of about 0.31 T, which is sufficient to deflect also heavy ions at 30° angle.
In the Figure 3.8 it is possible to observe the electromagnet assembled during the calibration, and its magnetic field calibration curve as a function of the potential applied to the coil wires. Figure 3.8b indicating a maximum field of about 0.35 T obtained applying a power supply of 12 V to the coil resistance of 3.8 Ω.

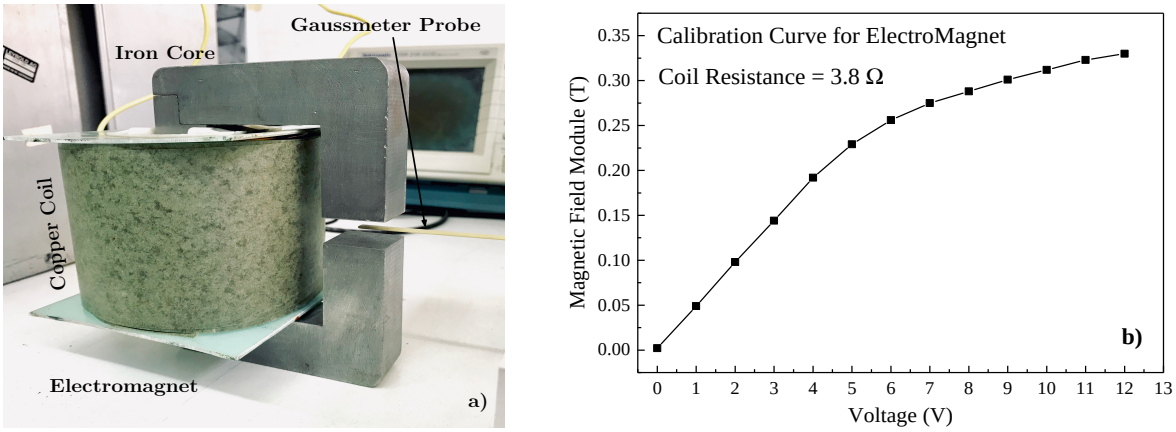

Figure 3.8: *Picture of electromagnet assembly assembled during calibration (a), and magnetic field versus applied voltage measured (b).*

3.1.2 Ion Energy Analyzer

The *Ion Energy Analyzer* (IEA) is another device used for determining the energy spectrum of ions emitted by plasmas in the BPA regime, and for their abundance. This device uses an electric field to filter only ions that possess a certain energy to charge ratio, as we will see.

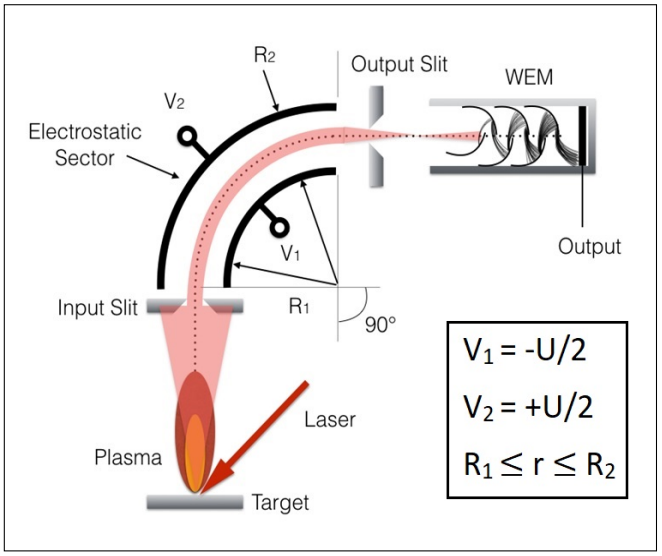

Figure 3.9: *Scheme of Ion Energy Analyzer.*

The main part of the IEA is the deflection system consisting of two cylindrical and coaxial electrodes, placed at the same potential (but in opposite sign), of radius respectively R_1 (inner plate) and R_2 (outer plate), as shown in the Figure 3.9. At the input and output of the electrodes, between 0° and 90°, there is an input and an output slit, respectively, in order to obtain a signal narrow in time. This device combines electrostatic deflection with TOF technique, described earlier. After the output slit, an electron multiplier is usually mounted, so as to amplify the low signal in current intensity.

However, the radial electrical field inside the device is given by the following equation:

$$\xi_r = \frac{V_2 - V_1}{r \ln(R_2/R_1)} \tag{3.5}$$

where r is the radius of equivalent surface $R_1 \leq r \leq R_2$. As reported in Figure 3.9, the potential $V_2 = -V_1 = U/2$. Let us take into account now an ions with mass m and charge ze, which cross the inlet slit with velocity v and have a circular trajectory with $r = R_0$, the force can be write as follows:

$$\frac{mv^2}{R_0} = ze\xi(R_0) \tag{3.6}$$

Equation 3.6 can be rewrite, by using Equation 3.5, in the following form [150]:

$$\frac{E}{z} = \cong keU \tag{3.7}$$

where E is the particle's energy, and k is a geometrical factor given by:

$$k = \frac{R_0}{2(R_2 - R_1)} \tag{3.8}$$

Equation 3.7 suggests that IEA works as an energy–to–charge ratio filter when a potential U is applied on the cylindrical electrodes. Considering ions TOF that reach detector, from cinematic law and Equation 3.7, we can evaluate the arrival time of each particle:

$$t = L\sqrt{\frac{m}{2kzeU}} \tag{3.9}$$

where L is the distance form the ions source to the detector. When U is fixed, every ions with mass m is separated from each other by $(z)^{-1/2}$. Thus, when the ion charge state is greater, the arrival time on the detector is smaller. For example, a Carbon ion ($m = 1.99 \times 10^{-26}\ kg$) with charge state $z = 4$, which travel for a path long 1 m and it is deflected by an IEA with $k = 10$ and $U = 10\ V$, reach the detector in a time of about $\sim 12.5\ \mu s$. The same ion, but with charge $z = 1$, which crosses the system under the same conditions, instead will reach the detector in time of about $\sim 25\ \mu s$.

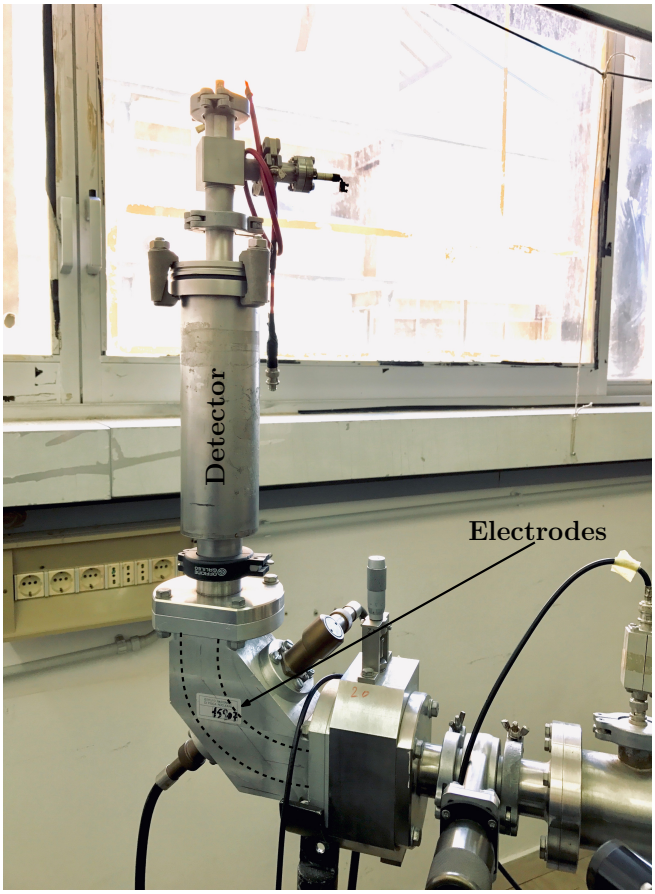

Figure 3.10: *Picture of Ion Energy Analyzer of Messina Laboratory.*

The Figure 3.10 shows the IEA present in the laboratory of plasma physics at the University of Messina. The k–value of this instrument is about ~ 10 and it has the inlet and outlet slits with a radius of 1 mm.
By IEA it is possible to study the energy distribution of the ions that constitute a laser–generated plasma, and also have information about the abundance of these. The way to operate is to change the electrodes' potential, and acquire the spectra obtained by laser–shooting on a non-irradiated target surface. It is clear that measurements and data analysis are often very long, and with some possible inaccuracy due to minor changes in the shape of the laser pulse, environmental parameters, focal point, and more over.
However, the IEA remains a powerful device for diagnosing particles with energy less than hundreds of keV. Higher ions energy require a higher electrostatic deflection field, which could lead to a discharge that would damage the device.

IEA Resolution

When we consider mass spectrometers, such as the IEA, one of the fundamental parameters is the instrument's resolution, i.e. the ability to distinguish between two different measurements. In terms of the energy of the revealed particles, the resolution is given by the following expression:

$$R = \frac{\Delta E}{E} \tag{3.10}$$

where ΔE represents the line width, while E is the measured energy value. The Figure 3.11a reports a typical spectrum detected through the IEA, at University of Messina, in TOF approach, obtained by irradiating a tantalum target with a laser intensity of about 10^{12} W/cm^2. Of course, the ion time of flight in the system is inversely proportional to the particle energy, according to the Equation 2.29. Replacing this in the Equation 3.10, we get that the resolution of the instrument will be given by:

$$R = \left[\frac{t_m(t_f - t_i)}{t_f t_i}\right]^2 \tag{3.11}$$

where t_m is the measured time corresponding to detected peak, t_f and t_i are the extremes of the peak width, as it can be seen in Figure 3.11a. In this example, for Ta^+–ions, the resolution was about 0.18%, instead the corresponding energy was about 660 eV. However, plotting the resolution as a function of ions energy detected, as reported in Figure 3.11b, was estimated an instrument accuracy of about 1.1 eV. Another important feature of a spectrometer is the response linearity as a function of energy; this has been evaluated in Figure 3.11b and shows a good degree of linearity.

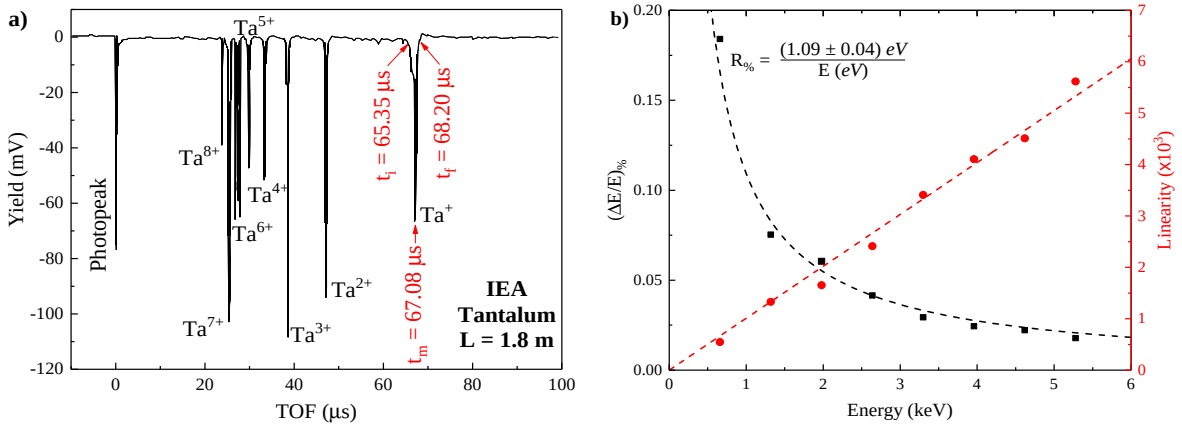

Figure 3.11: *Example of IEA experimental spectrum obtained by irradiating Tantalum target with laser intensity of about ~10^{12} Wcm^{-2} (a), and evaluation from this spectra of experimental detector resolution as a function of ions energy detected (b).*

3.1.3 Ions Detector

A wide range of detection devices can be used to diagnose plasm generated by laser pulses, with the possibility of observing photons, electrons, ions or even neutrons. During the doctorate, the author of this thesis was mainly involved in the diagnosis of ions emitted by plasmas. Due to the fluency of the following discussion, two detectors used for ion diagnostics are now briefly introduced: the Ion Collector and the Secondary Electron Multiplier.

Ion Collector

Ions emitted by laser–generated plasma are usually detected by planar collector, or Faraday Cups, which are namely *Ion Collector* (IC). Electrons and ions are separated by IC due to electric field between a grounded entrance grid and a biased negative collector, as reported in Figure 3.12. The ion current that reach the collector is measured by a fast storage oscilloscope. Some electrons can be emitted from the collector due to the ions' impacts on the this (*emission of secondary electrons*); since the electric field between the collector and entrance grid guides them towards the latter, reducing the error due to this phenomenon.
For a preliminary study, let's consider the scenario in which there is no emission of secondary electrons, the density of ion current can be written:

$$J_i = en_e v = ev \sum_{k=0}^{k_{max}} z_k n_{i,k} \tag{3.12}$$

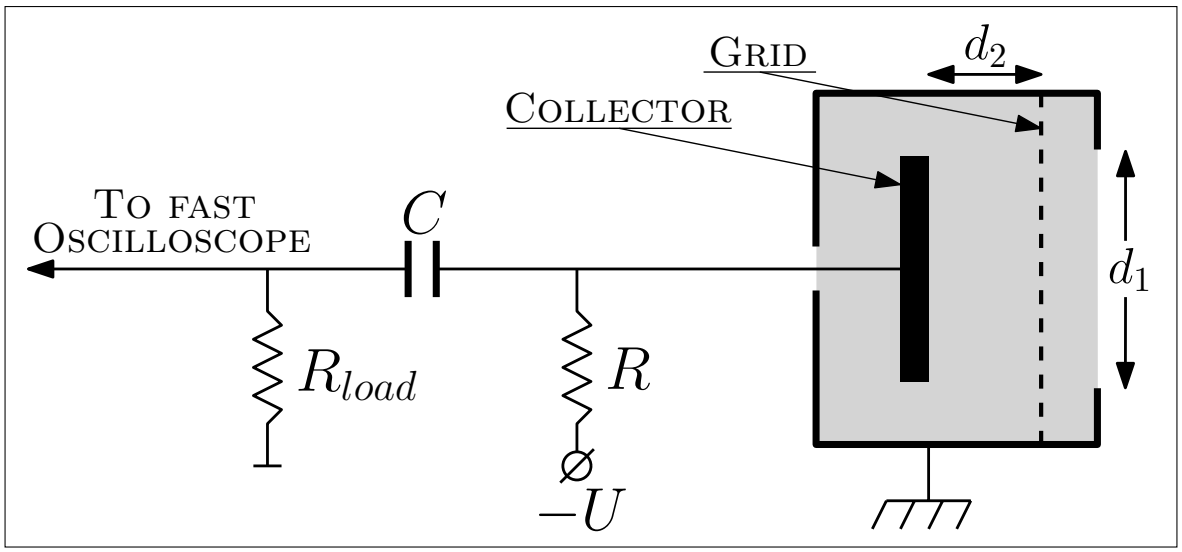

Figure 3.12: *Schematic rappresentation of the IC operating circuit.*

where n_e is the electron density, v is the plasma velocity, k is the number of ion species, $n_{i,k}$ and z_k are the density and charge state of the k^{th} ion specie respectively. Notice that for high density of ions, the collector can be shielded from the plasma by a charge layer due to the applied polarization [150].
Now, if we include in the description also the effects of secondary electron emission, the output current, i_c, in the collector circuit will be given by two contributions:

$$i_c = i_i + i_e = e\epsilon v S \left\{ \sum_{k=0}^{k_{max}} [z_k(t) + \gamma_k(t)]\, n_{i,k}(t) \right\} \tag{3.13}$$

where ϵ is the transparency of the entrance grid (which has a value range between $\sim 70\%$–80%), S is the collector surface, and γ_k is the secondary emission coefficient for the k^{th} ion specie. Since the ion density is $n_i = \sum n_{i,k}$, the latter can be rewrite as follows:

$$i_c(t) = \epsilon e v S \bar{z}(t) n_i(t) \left[1 + \frac{\overline{\gamma}(t)}{\bar{z}(t)} \right] = \epsilon \left[1 + \frac{\overline{\gamma}(t)}{\bar{z}(t)} \right] i_{coll}(t) \tag{3.14}$$

where

$$\overline{\gamma} = \frac{\sum_k \gamma_k n_{i,k}}{\sum_k n_{i,k}} \qquad \& \qquad \bar{z} = \frac{\sum_k z_k n_{i,k}}{\sum_k n_{i,k}}$$

are the average secondary emission coefficient and the average value of the ion charge state respectively; i_{coll} is the ion current in the input grid at a time t. The latter from Equation 3.14 is equivalent to:

$$i_{coll}(t) = \frac{U_c(t)}{\epsilon R_{load} \left[1 + \frac{\overline{\gamma}(t)}{\bar{z}(t)} \right]} \tag{3.15}$$

where U_c is the signal voltage amplitude and R_{load} is the load resistance, (Figure 3.12).

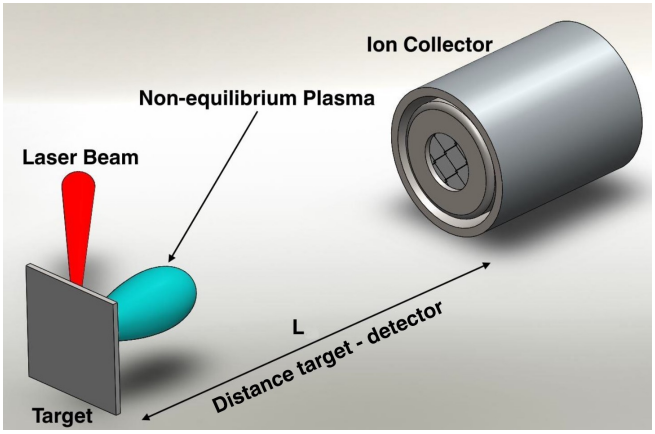

Figure 3.13: *Representation of IC detectors in TOF approach.*

From the relation Equation 3.15 it is possible to obtain the distributions of velocity and energy from simple differential relations. Moreover, thanks to the use of the time–of–flight technique, it is possible to know the speed and energy of the ions with these devices, Equation 2.29, when this is used in TOF approach as illustrated in Figure 3.13.
In the Equation 2.29, for the calculation of the ion energy, the flight time is calculated as follows:

$$\bar{t} = \frac{\int_0^{+\infty} f(t) t \mathrm{dt}}{\int_0^{+\infty} f(t) \mathrm{dt}} \tag{3.16}$$

where $f(t)$ is given by:

$$f(t) = \frac{U_c(t)}{1 + \frac{\overline{\gamma}(t)}{\overline{z}(t)}} \tag{3.17}$$

Devices of this type can detect ions, electrons but also photons. These are used in the evaluation of energy distribution, using the TOF technique, as described. The signal produced within the IC circuit is sent to an oscilloscope and stored for subsequent analysis [150].

Secondary Electron Multiplier

The *Secondary Electron Multiplier* (SEM) is a vacuum–tube structure that multiplies the incident particle. It is based on the emission of secondary electrons due to the collision by a particle on a surface. A SEM accelerates these secondary electrons to an enough energy to produce additional secondary electrons in impact with another surface, in an avalanche multiplication process. This process is achieved by holding the first dynode (electrode), namely also conversion dynode, at high potential between $\pm 1 \div \pm 30\ kV$, with opposite sign to the charge on the detected ions [151].
In Figure 3.14 is shown a schematization of a discrete SEM; this kind of detector are composed in general from 12 to 20 dynodes having good secondary electron emission properties. For the detection of ions, the first dynode is placed at a very high negative potential (in absolute value), and through a voltage drop system the subsequent dynodes are at a lower potential (in absolute value). The final collector for the multiplied electrons detection is at ground potential. By this system, the secondary electrons emitted in the conversion dynode are accelerated towards the second dynode, hitting it and causing the expulsion of other

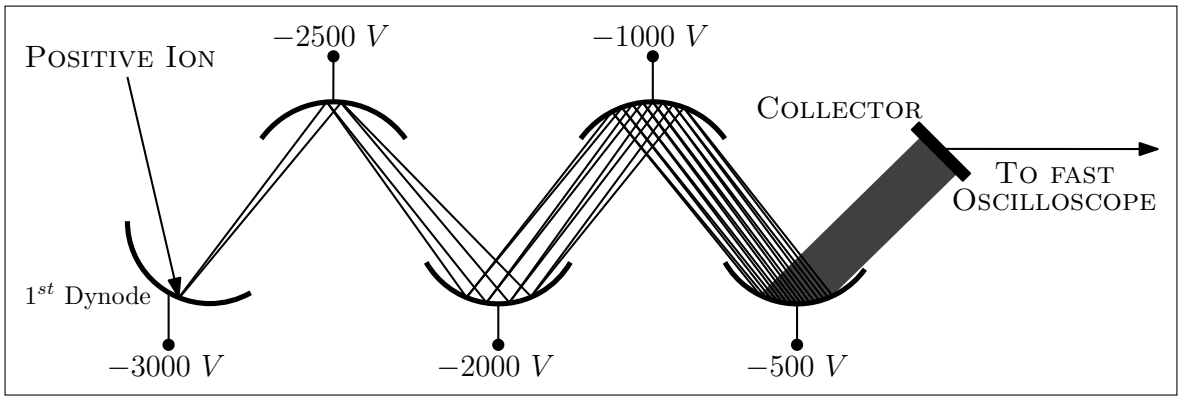

Figure 3.14: *Schematic diagram of a Secondary Electron Multiplier.*

electrons, accelerated towards the third dynode, and so on. Thus a cascade of electrons is generated, and at the end, they are directed towards the collector for the signal reading by a fast storage oscilloscope.
Another design of secondary electron multiplier is that where the discrete dynodes are substituted by a continuous one. A type of continuous–SEM is called channeltron, which is made by a lead–doped glass with a curved shape. As the tube have a uniform electric resistance, a voltage applied at the two extremities produce an continuous accelerating field along its length, for the secondary electrons produced [151].
The response of a SEM in the ion current, i_{SEM}, has been characterized by an amplification factor, namely current gain G_C, given by [152]:

$$G_C = \frac{i_{SEM}}{i_i} \tag{3.18}$$

where i_i is the ions input current. Thus, the analogue particle gain, due to a single ion that interact by the conversion dynode, is defined as follows:

$$G_a = q\frac{i_{SEM}}{i_i} = qG_C \tag{3.19}$$

where q is the charge of the particle. Finally for a real description of the SEM response we have to take into account the detection efficiency of ions, namely by ϵ, to determine the pulse counting gain:

$$G_p = q\frac{i_{SEM}}{i_i\epsilon} = \frac{G_a}{\epsilon} \tag{3.20}$$

which is the number of secondary electrons at the SEM output per single detected ion [153].

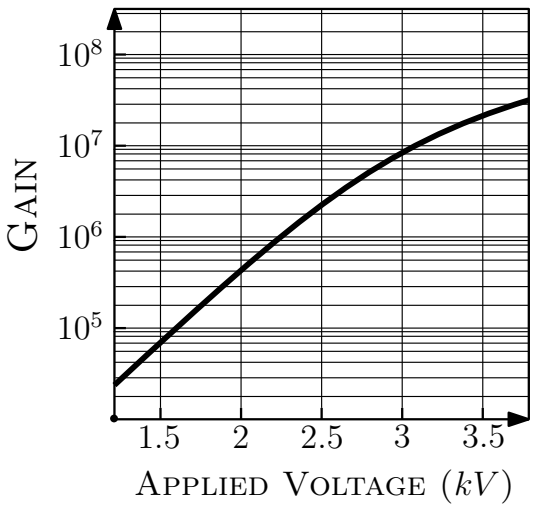

Figure 3.15: *Qualitative behaviour of the SEM' gain vs. the voltage.*

G_p is proportional to secondary emission coefficient, γ, emitted from the first dynode by a single particle and their subsequent multiplication. We denote that the secondary electron emission coefficient depends on incident ion species, its charge state and impact velocity, angle of incident, and from the dynodes surface. Figure 3.15 shows the behaviour of the gain as function of the applied voltage; it can be approach 10^8 with a wide linear dynamic range between $10^4 \div 10^7$.
A continuous dynode not enclosed in vacuum, which respond to the charged particles, X–rays, and ultraviolet radiation is namely *Windowless Electron Multiplier* (WEM). In the measurements that will be presented, a WEM has been used for ion detection.

3.2 Magnetic spectrometer for low energy ions

Published Paper[2018]

Diagnostics of Particles emitted from a Laser generated Plasma: Experimental Data and Simulations

G. Costa and L. Torrisi
Dipartimento di Scienze Fisiche, MIFT, Università di Messina, V.le F.S. D'Alcontres 31, 98166 S. Agata, Messina, Italy

Published as: G. Costa and L. Torrisi: "Diagnostics of Particles emitted from a Laser generated Plasma: Experimental Data and Simulations", *The European Physics Journal: Web of Conferences*, Volume: **167**, Pages: 04005(1–6) (2018)
Available from: 10.1051/epjconf/201816704005
Publication Date: Published 09 January 2018

In this section, a preliminary study concerning the Magnetic Spectrometer Chamber, on which I worked, is presented and discussed [**154**].
A Nd:YAg laser, with fundamental wavelength 1064 *nm*, maximum pulse duration 3 *ns*, and energy variable from 1 up to 300 *mJ*, was employed to irradiate aluminium target, in single shot mode. The laser beam is focused on the target, placed in vacuum chamber at a pressure of about 10^{-6} *mbar*, through an optical lens having a focal length of 50 *cm*. The spot size on the target surface is about 0.5 mm^2. The laser beam incident angle on target surface is 45°.
The particles emitted from the target cross a collimation system consisting of two pinholes with a smaller radius of 1.5 *mm*. The collimated particles beams pass to the centre of a

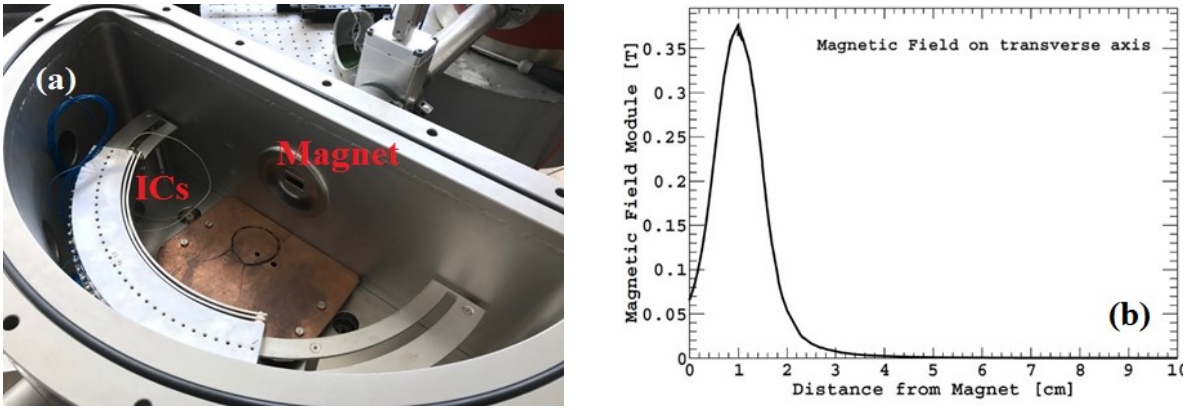

Figure 3.16: *Picture of experimental setup (a), and profile of the magnetic Field Module, at the centre of the system, versus distance along the direction of propagation of the ion beam emitted from laser–generated plasma (b).*

system of two permanent magnets. The magnetic field module is about 0.38 T and it has a length of 10 mm, as shown in the plot of Figure 3.16b. A group of 32 aligned Faraday Cups distributed at 90° angle, and placed on a movable sleigh, as shown in Figure 3.16a, reveal the deflected particles crossing the permanent magnet.
When the ion beam emitted by the plasma passes through the system of two pinholes, a fairly narrow nozzle is obtained which is deflected by the magnetic field present there. The mobile sleigh, containing the 32 ICs, is placed in a position to detect between ±45°. The properties of the magnetic field cause that the ions are deflected from the left side with respect to the observer (attributed to positive value angles). The Figure 3.17 shows the highest yields value revealed; these are calculated from the analysis of the TOF–spectra of the various ICs. These value are proportional to the integral of the subtended areas obtained from each TOF–spectra. The Figure 3.17 shows that the ions deflected at negative angles (right) are few, this is usually the neutral part of the plasma not deflected by the magnetic field.

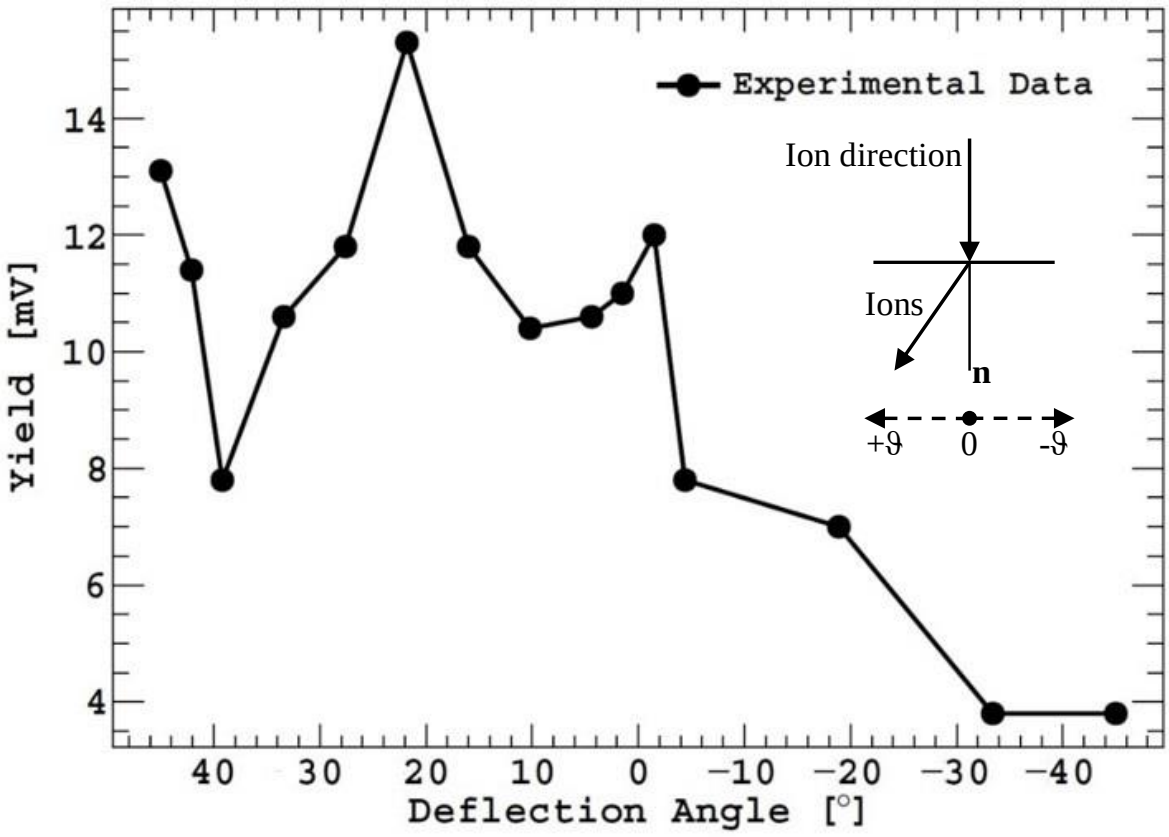

Figure 3.17: *Experimental data of maximum yield distribution at a given deflection angle for pure Aluminum, detected by multi–ion collector system.*

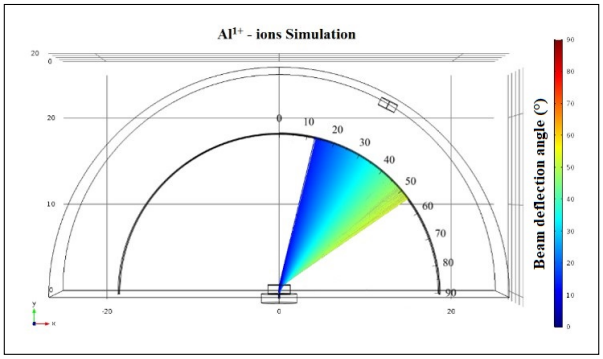

Figure 3.18: *Simulation by COMSOL Multiphysics of the angular deflection, due to magnetic field, of the Al^1+ ions.*

On the left, instead, a structure is visible that can be attributed to the first 4 charge states of aluminium. Charge states higher than 4 could be present, but by means of COMSOL simulation, it is demonstrated that these are deflected at angles higher than 45°, and therefore not revealed in the measure of interest.
The Figure 3.18 shows the simulation of Al^{1+}–ions obtained by implementing the CBS distribution, Equation 1.71, in with COMSOL software. Similar simulations were carried out for the 2+, 3+ and 4+ aluminium charge states.

Figure 3.19 shows the comparison between the experimental data and the convolution of the simulated angular distributions, by changing the temperature and potential of the CBS. The overlap shows an average plasma temperature of 38 eV, and a potential of 57 V. The measurements shown can be made more accurate by using a WEM–detector, as follows.

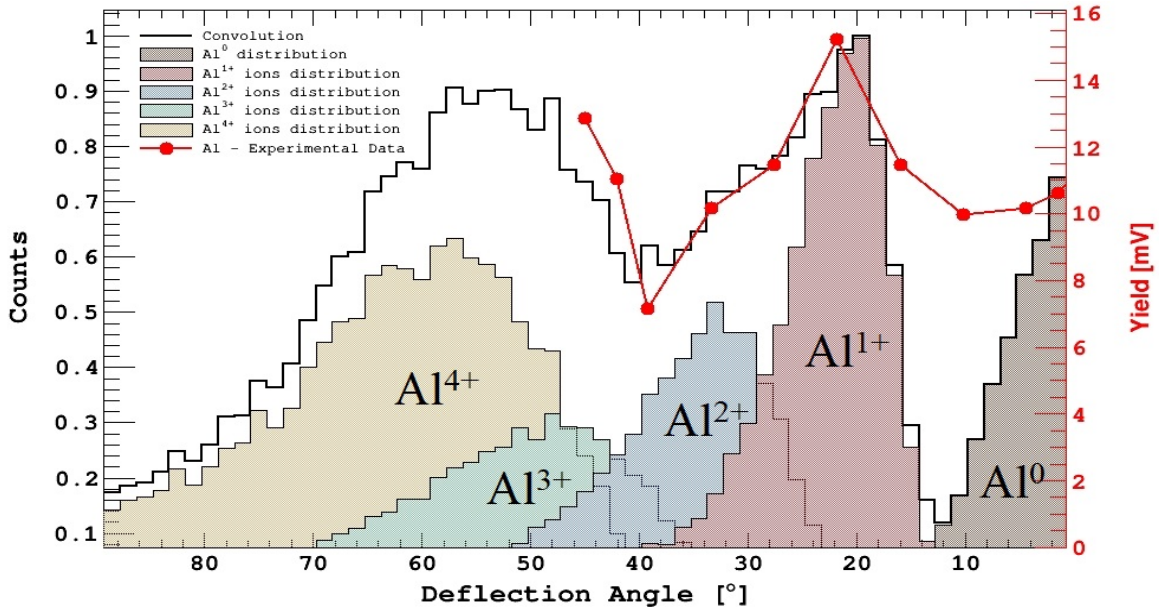

Figure 3.19: *Comparison of experimental spectrum (in red) and convolution of angular distributions of ionic species from 1+ to 4+ of aluminium (black histogram).*

3.2.1 Simple Magnetic Spectrometer for ions diagnostic

Published Paper[2018]

Simple Magnetic Spectrometer for ions emitted from Laser–generated Plasma at 10^{10} W/cm^2 intensity

L. Torrisi and G. Costa
Dipartimento di Scienze Fisiche, MIFT, Università di Messina, V.le F.S. D'Alcontres 31, 98166 S. Agata, Messina, Italy

Published as: L. Torrisi and G. Costa: "Simple Magnetic Spectrometer for ions emitted from Laser–generated Plasma at 10^{10} W/cm^2 intensity", *Laser and Particle Beams*, Volume: **36**(2), Pages: 163–170 (2018)
Available from: 10.1017/S0263034618000095
Publication Date: Received 11 February 2018; Accepted 11 March 2018; Published 22 May 2018

In this section we will study plasmas generated by pulsed laser at intensities of about 10^{10} W/cm^2 irradiating solid targets with a different composition. The ion emission was investigated with TOF measurements, to have information about ion velocity, charge state generation, and ion energy distribution. Measurements are performed by using an electromagnet to generate a magnetic field suitable, in order to deflect ions toward a Faraday cup, at very low current, and/or a Secondary Electron Multiplier, to gain electrical signal [**155**].
A Litron compact high-energy Nd:YAG laser operating at 1064 *nm* wavelength, 3 *ns* pulse duration, 200 *mJ* maximum pulse energy, focused at a spot area of about 0.7 mm^2 was employed in this experiment to generate plasmas in high vacuum (10^{-6} *mbar*). The laser is focused on the target using a lens placed in air, externally to the vacuum chamber, and a glass window of input aperture; it was employed in a single shot. The laser pulse energy is measured using a suitable Joule–meter. A He–Ne laser is employed for all the alignment of the experimental setup. The incident angle of the laser beam on the target is 45°. The ion emission from plasma was measured along the normal to the target surface where its maximum yield is expected.
The target used in this experiment consists of sheets with 0.5 *mm* thickness and 2 *cm* × 2 *cm* surface of polyethylene (PE; –CH_2–), aluminum, and copper. Targets are mechanically moved from outside the chamber by step motors.
The magnetic spectrometer is aligned to the target normal direction along which two pinholes are placed in front of the magnetic field input; the first has 3 *mm* in diameter and the second 1 *mm* in diameter, to collimate the entrance of ions and to define exactly the entrance of ion direction in the field. ICs could be employed to analyze the deflected ions; however, due to the high ion collimation, the current that reach detector is low ($\sim 0.1 \div 10$ *nA*), and for this reason, it is preferable to a use a Windowless Electron Multiplier (WEM) as a detector, to enhance the sensitivity to the detected ions. It was placed at 30° angle with respect to the normal direction, and at 1.27 *m* from the target surface. Its input is vertically collimated at 1

mm aperture to permit a good geometrical position of the deflected and detected ions. WEM uses a power supply of 3 *kV* for the conversion–dynode polarization to produce an electron multiplication with a gain of about 10^5. The WEM detector is employed in TOF approach using a fast storage oscilloscope.

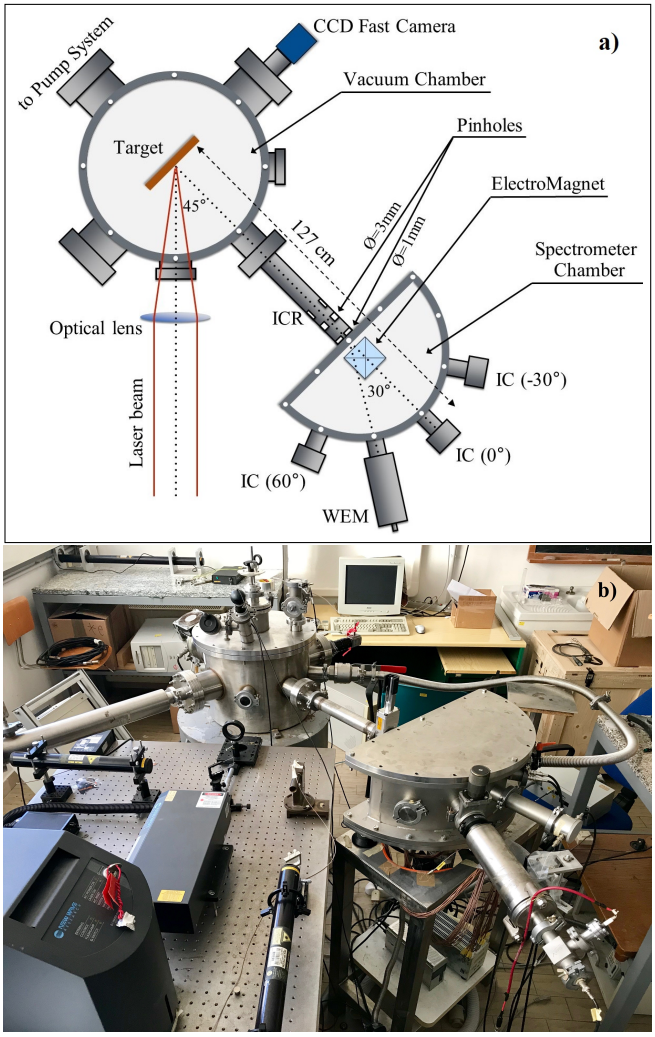

Figure 3.20: *Scheme of the experimental set–up with vacuum chamber for laser–matter interaction and Magnetic Spectrometer Chamber (a) and picture of the apparatus (b).*

Figure 3.20a reports the scheme of the experimental set-up used for this experiment and Figure 3.20b the photo of the apparatus. It is possible to observe the geometry used in its entirety, the WEM position, and the position of other ICs employed to monitor the ions and electrons not arriving on the WEM. A ring–IC (ICR) was employed to control the total flux of the ions emitted from plasma in the direction of the MSC, before the pinholes collimators, at a distance of 90 *cm* from the target.
We introduce in the system an electromagnet that generates a magnetic field depending on the current flowing through its coils. The solenoid produces a magnetic field in an active expansion volume of 2.5 $cm \times 2.5\ cm \times 1\ cm$, as measured by an accurate Gaussmeter (Hirst GM08). Its calibration plot, reporting the magnetic field versus the applied voltage, and it is presented in Figure 3.21c. This graph indicates a maximum field of about 0.35 T obtained applying a power supply of 12 V to a coil resistance of 3.8 Ω. Figure 3.21a reports a picture of the electromagnet entered in the MSC, and used to generate the suitable magnetic field by changing the voltage at its terminals.

Figure 3.21b reports a picture of the electromagnet polar expansion. This photo is taken from the central aperture of the magnetic spectrometer, placed at 0° angle; it is used also

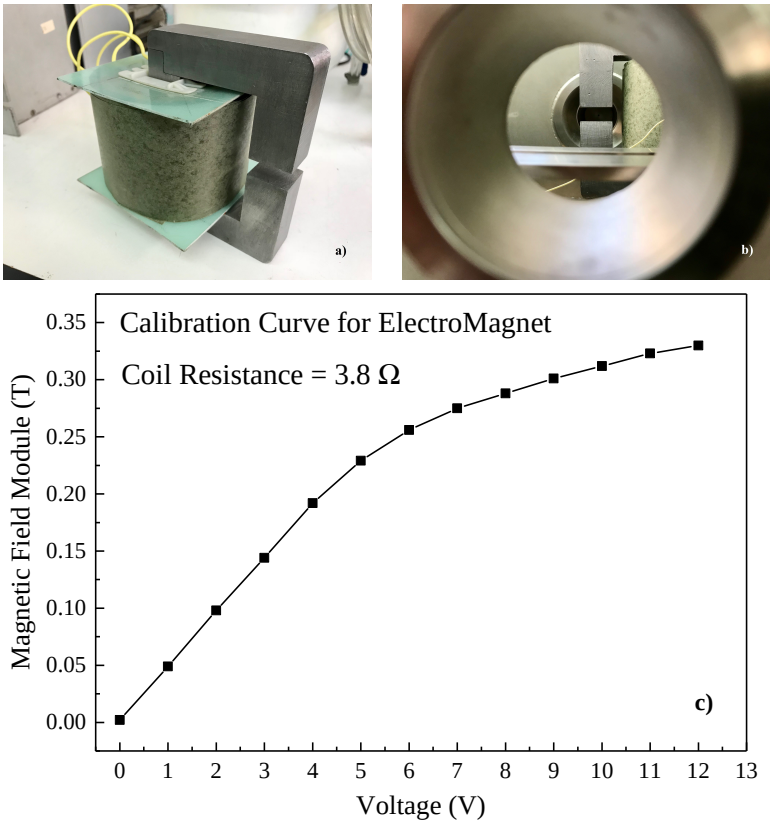

Figure 3.21: *Picture of the electromagnet used for the measurements (a) made of 1200 copper coils wrapped around "C"–shaped soft iron core. Picture of the electromagnet polar expansion, view from the 0° aperture of the magnetic spectrometer, employed to control the system alignment (b). Experimental measurement of the magnetic field, at the center of the cavity of the electromagnet, versus applied voltage, which reaches a maximum value of about 0.35 T, when 12 V of voltage are applied to its electrodes (c).*

to control the system alignment. The magnetic field is applied orthogonally to the direction of the incident ions produced by plasma. Ions cross the magnetic field in the middle of its active volume, on a plane on which the WEM detector is placed.

Finally, a fast CCD camera operating in the visible wavelength region observes the plasma plume luminosity emitted from the target through a glass window at 90° angle with respect to the incident laser direction, as reported in Figure 3.20a. Its exposition time is controllable by the user; its minimum value is 5 μs. CCD camera is triggered by the TTL laser pulse. The wire connectors between laser trigger and CCD camera were reduced to a minimal length in order to reduce the time delay. The images detected by CCD camera are acquired and elaborated through a fast computer.

COMSOL simulation software was employed to perform some simulations of the produced ions from the plasma source, of their deflection applying the magnetic field and of their energy detection. The COMSOL multiphysics simulation software environment facilitates all steps in the modeling process defining the geometry, meshing, specifying the involved physics mechanisms, solving, and then visualizing the results [132–134].

3.2.2 Data Analysis and Results

Irradiating polyethylene, aluminium and copper targets, in the same experimental conditions, we obtained the ICR–spectra reported in Figure 3.22a, 3.22b, 3.22c, respectively.
The PE spectrum shows the faster ions, i.e. protons, are located at about 6.5 μs, which corresponding to a kinetic energy of 100 eV. The minimum carbon TOF ion peak is located at about 10.5 μs, at which energy is 458 eV. Assuming protons energy to represent the energy acquired in the plasma for charge state, the carbon ions are ionized up to 4+. The ICR–signal FWHM is about 10 μs and corresponds to a height of about 3 mV, acquired by an input oscilloscope resistance of 50 Ω and with a mean charge state of 1+ (the charge state 1+ is is the most produced compared to the higher ones, due to ionization potential and ionization cross–section), indicates a number of detected carbon ions of about 3.8×10^9/laser shot.
ICR does not detect all the ions emitted from plasma because its detection solid angle is narrowed and because it is a ring collector that transmits the major ion component along the propagation's direction towards the MSC.
The Al spectrum indicates that the faster protons are located at about 6.5 μs, confirming as in the previous case, the maximum proton kinetic energy of 100 eV. The minimum TOF

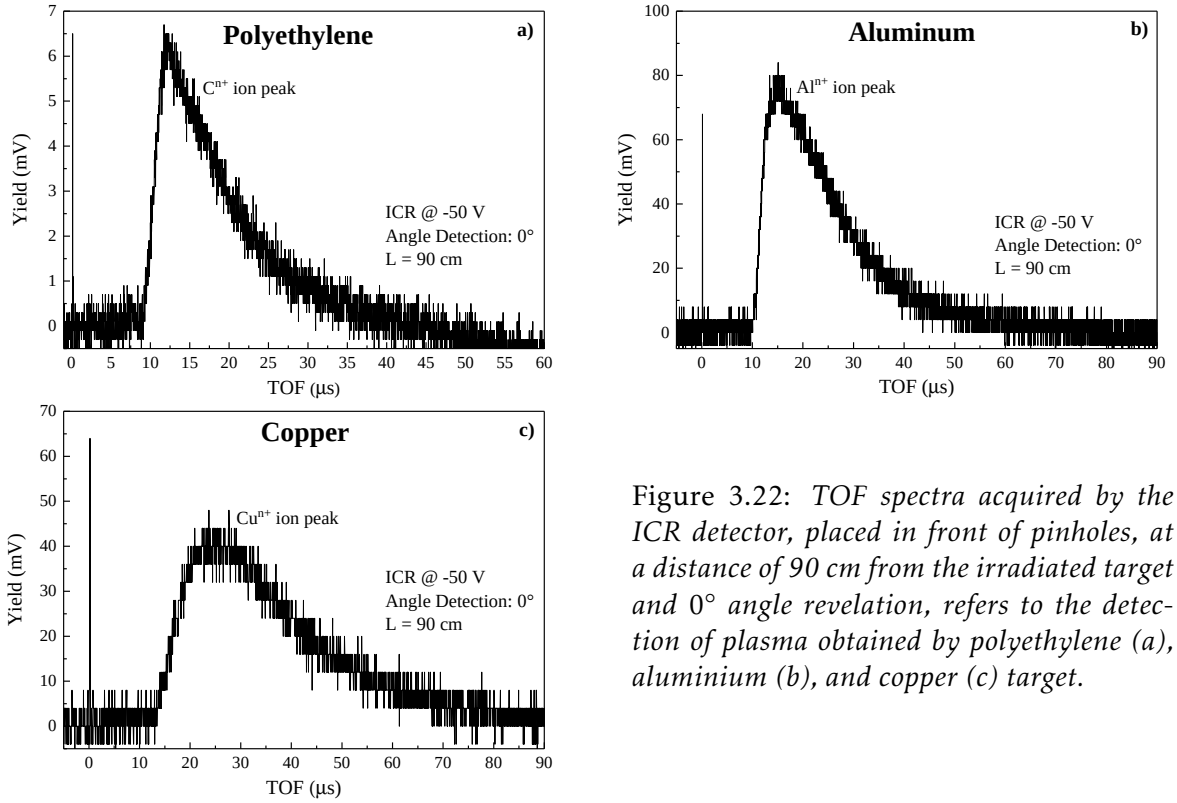

Figure 3.22: *TOF spectra acquired by the ICR detector, placed in front of pinholes, at a distance of 90 cm from the irradiated target and 0° angle revelation, refers to the detection of plasma obtained by polyethylene (a), aluminium (b), and copper (c) target.*

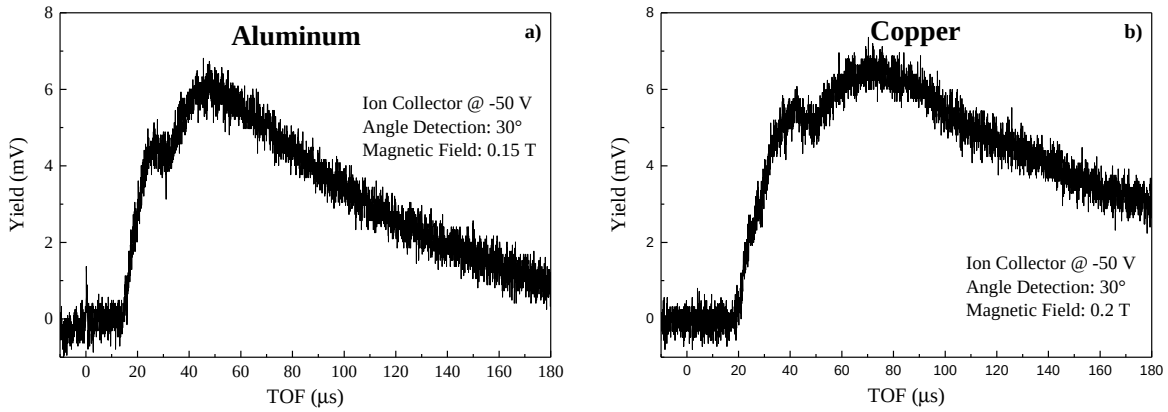

Figure 3.23: *Typical examples of IC–TOF spectra of Aluminium (a) and Copper (b) ions deflect at* 30° *by a magnetic field of 0.15 and 0.2 T, respectively.*

of aluminum ion peak is located at about 12 μs, at which corresponds a kinetic energy of 780 eV. Assuming proton energy to represent the energy acquired in the non–equilibrium plasma for charge state, the Al ions are ionized up to 7+. The ICR–signal FWHM is about 15 μs and corresponds to a height of about 38 mV, acquired by an input oscilloscope resistance of 50 Ω and with a mean charge state of 1+, indicates a number of detected aluminium ions of about 7.1×10^{10}/laser shot.

The Cu spectrum indicates that the faster protons are located at about 6.5 μs, thus the maximum proton kinetic energy was of 100 eV, once again. The minimum TOF of copper ion peak is located at about 16.5 μs, at which corresponds a kinetic energy of 980 eV. Assuming that the proton energy represents the energy acquired in the non–equilibrium plasma for charge state, the Cu ions are ionized up to 9+. The ICR–signal FWHM is about 25 μs and corresponds to a height of about 22 mV, acquired by an input oscilloscope resistance of 50 Ω and with a mean charge state of 1+, indicates a number of detected aluminium ions of about 6.9×10^{10}/laser shot.

By using an IC at 30° angle with respect to the normal to the target surface, the ion signal is low, due to the high pinholes collimation before the magnetic field and to the angular spreading of deflected ions by the magnetic field on the base of their ion energy distribution. Figure 3.23 reports two typical examples of IC–TOF spectra of collimated (1 mm the diameter of the smallest pinhole) aluminium and copper ions defected at 30° by a magnetic field of 0.15 and 0.2 T, respectively. However, IC has an aperture of about 3 cm diameter; thus, it does not permit to distinguish very well between different charge states, detecting charge states 1+ and 2+ together. It is possible to observe that the electrical ion signals decrease to about one order of magnitude with respect to the ICR detector. Thus, if we collimate its aperture to increase the ion energy resolution, the current becomes too low and comparable to the background.

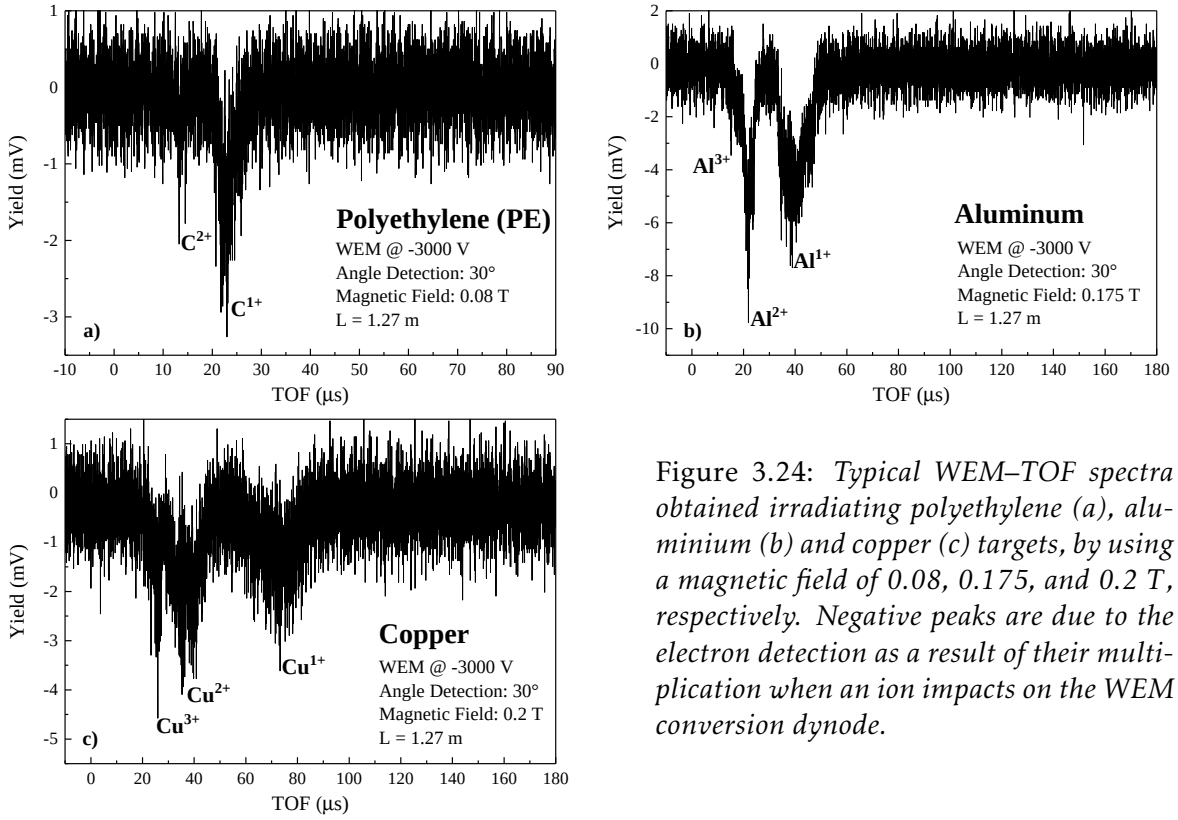

Figure 3.24: *Typical WEM–TOF spectra obtained irradiating polyethylene (a), aluminium (b) and copper (c) targets, by using a magnetic field of 0.08, 0.175, and 0.2 T, respectively. Negative peaks are due to the electron detection as a result of their multiplication when an ion impacts on the WEM conversion dynode.*

After this preliminary analysis of the laser–induced plasma, we irradiated, in the same experimental conditions, the three targets by changing magnetic fields, which act to deflect the ions toward the more sensitive electron multiplier WEM–detector.

Figure 3.24 reports three typical WEM–TOF spectra obtained by irradiating polyethylene, aluminium and copper target, by using a magnetic field of 0.08, 0.175, and 0.2 T, respectively. The spectra initial time is obtained by the photopeak of the ICR detector. Spectra are rich in noise due to the high collimation of the second pinhole. The peaks have negative value due to the detection of the electrons multiplied inside WEM and switched on by the ion impact on the first WEM dynode (ions which are deflected by the applied magnetic field in the horizontal plane). By changing the voltage applied to the coil, i.e. by changing the magnetic field, it was possible to acquire different spectra similar to those reported in Figure 3.24. Each negative peak corresponds to a different charge state for the kind of element investigated (i.e. carbon, aluminium or copper). These peaks are narrow for lighter elements, such as protons, and are and wide for heavier elements, such as copper ions. On the other hand, the peak width is more wide for elements with a lower charge state and narrow for high charge state. These effects are due to the spatial dimension of the beam entering the

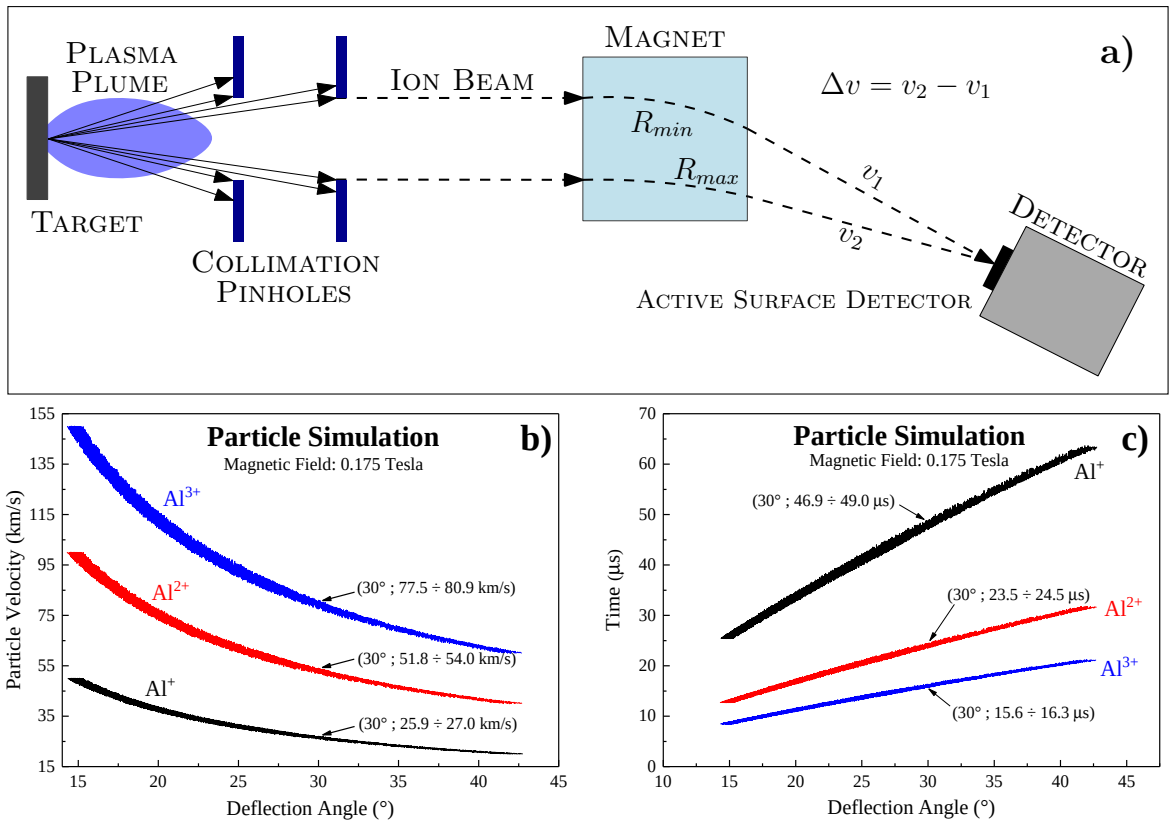

Figure 3.25: *Schematic diagram of the magnetic deflection (a), and ions velocity (b) or arrival time to detector (L = 1.27 m) (c) versus angle deflection by COMSOL Simulation.*

magnetic field, which is responsible of a velocity indetermination, Δv, for the ions that arriving on the active surface of the detector. Thus, same ions, but with different velocities, can be deflected at the same angle, based on their position in the beam, as shown in Figure 3.25a. According to the ion radius in a magnetic field, Equation 3.3, the latter will be proportional to the ratio $(v \pm \Delta v)/q$, which must remain constant for a fixed deflection radius R. It means that for charge state 2+ the Δv indetermination is double with respect to the 1+ charge state. So, from the inverse proportionality between velocity and time, it results that faster ions are more narrow in time. COMSOL simulations, carried out with aluminium ions from 1+ to 3+ and a magnetic field of 0.175 T, confirm this result experimentally observed, as shown in the Figure 3.25b and Figure 3.25c. In fact, at an angle of 30° are deflected aluminium ions 1+ with velocities between 25.9 km/s and 27.0 km/s, thus with a $\Delta v = 1.1$ km/s. For aluminium 2+ instead, at the same angle are deflected the ions that have speeds between 52.8 and 54.0 km/s, with a $\Delta v = 2.2$ km/s, and so on. Figure 3.25c shows that the lower states of charge have a greater uncertainty than the higher ones.

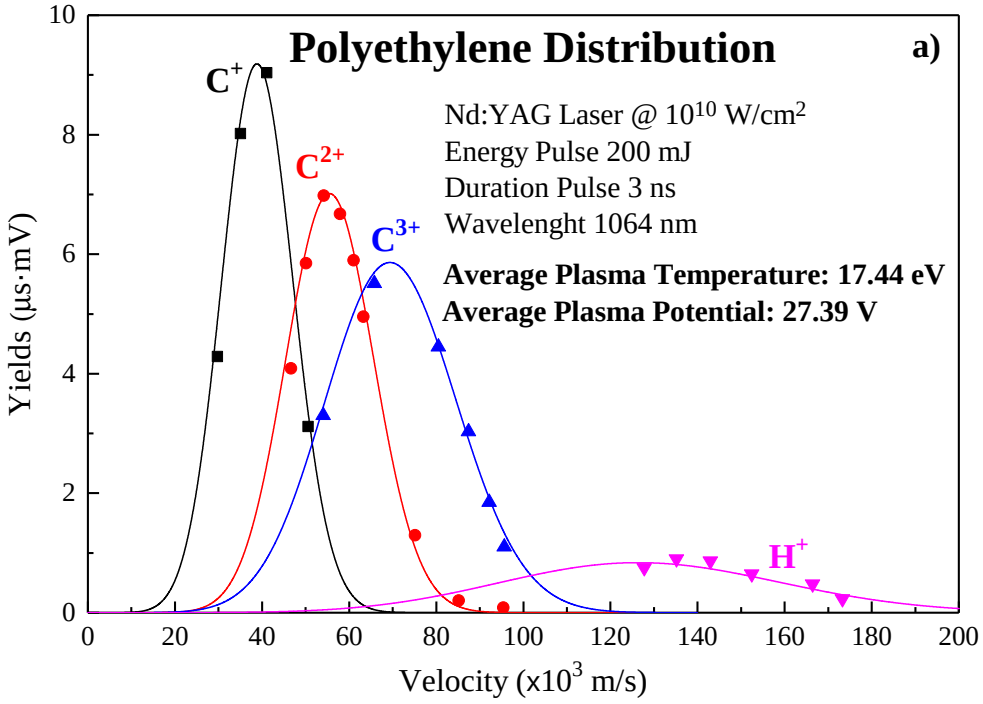

(a) *Polyethylene experimental data fit. The average plasma temperature and potential were estimated to be about* 17.4 *eV and* 27.4 *V.*

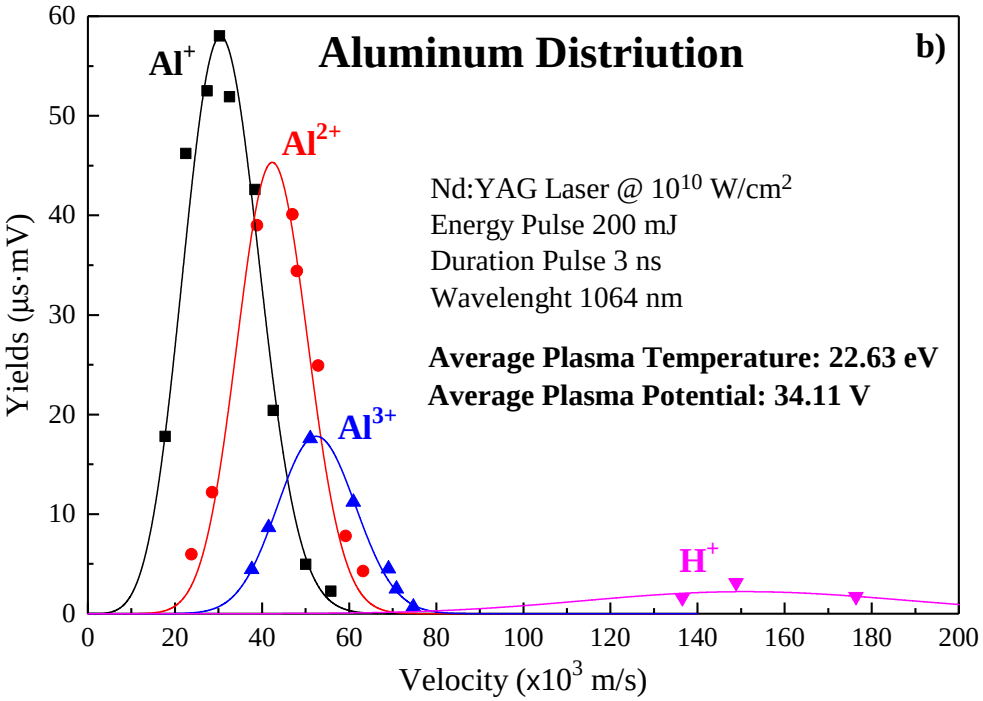

(b) *Aluminium experimental data fit. The average plasma temperature and potential were estimated to be about* 22.6 *eV and* 34.1 *V.*

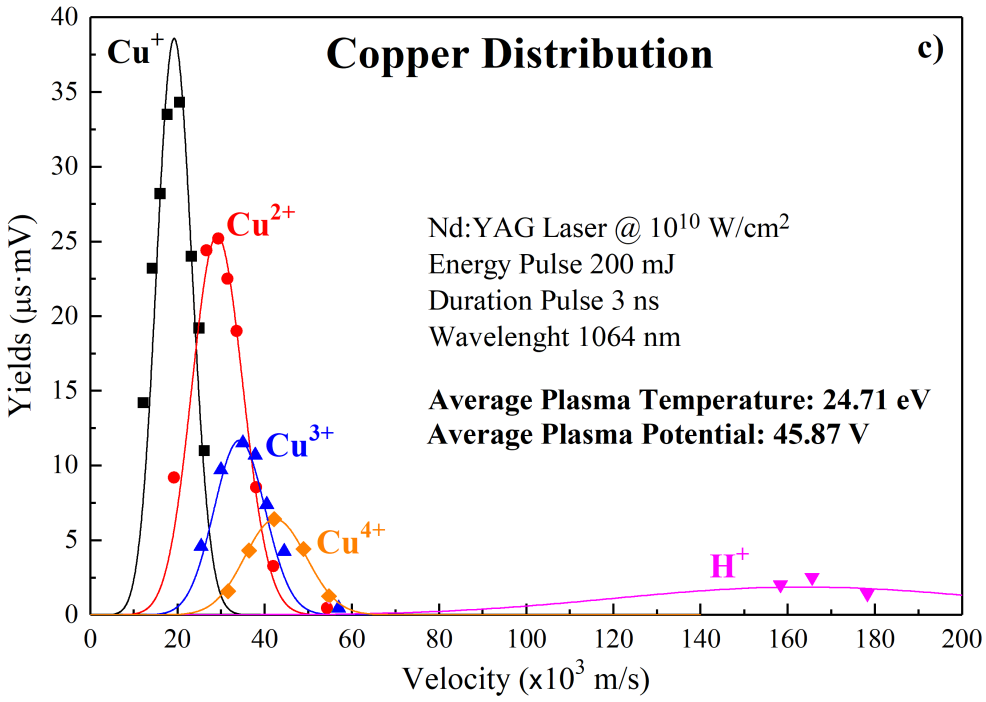

(c) *Copper experimental data fit. The average plasma temperature and potential were estimated to be about 24.7 eV and 45.9 V.*

Figure 3.26: *Ion velocity distributions obtained plotting the WEM ion peak areas as a function of the ion velocity for polyethylene (a), aluminium (b) and copper (c) plasmas. The fits were obtained using the CBS–distribution function.*

By considering the ion yield in terms of the area subtended by each ion peak and by plotting it as a function of the ion velocity, it was possible to plot the ion velocity distributions. These results are reported in the plot of Figure 3.26 for polyethylene (Figure 3.26a), aluminium (Figure 3.26b) and copper (Figure 3.26c) plasmas.
The measurements of ion velocity distributions can be fitted using Maxwell distributions, characterized by a mean velocity value, a maximum yield and a velocity width that is inversely proportional to the plasma temperature. Moreover, it is possible to observe that the distributions of different particles and charge states are different. By increasing the charge state, the distribution shifts toward higher velocity, proportionally to the ion charge state. The regular distribution shift with the charge state is due to the electric field generated in the non–equilibrium plasma and driving the ion acceleration along the normal to the target surface. The experimental data in this regime of laser intensity are in agreement with the theoretical model advanced by *Torrisi* and known as CBS regime, shown in Equation 1.71 [149]. Figure 3.26a shows mainly three carbon ion charge states, C^{+}, C^{2+}, and C^{3+}, with mean kinetic energies of about 95, 192, and 297 *eV*, respectively; other charge states are negligible and comparable with the background. The mean proton energy is about 93 *eV*.

Figure 3.26b shows mainly three aluminum ion charge states, Al^{+}, Al^{2+}, and Al^{3+}, with mean kinetic energies of about 130, 248, and 300 eV, respectively; the other charge states are negligible with respect to these and comparable with the background. In this case, the mean proton energy is about 115 eV.
Figure 3.26c shows mainly four copper ion charge states, Cu^{+}, Cu^{2+}, Cu^{3+}, and Cu^{4+}, with mean kinetic energies of about 125, 288, 403, and 610 eV, respectively; the other charge states are negligible with respect to these and comparable with the background. In this case, the mean proton energy is about 142 eV.
The measured ion energy distributions agree with the Boltzmann fit of the theoretical distribution by CBS approach. From such fits, it is possible to extrapolate an equivalent plasma temperature, $k_B T$, which is of 17.4, 22.6, and 24.7 eV for plasma produced by polyethylene, aluminium and copper targets, respectively. Moreover, the plasma potential, namely V, assumes the value of 27.4, 34.1, and 45.9 V in the three cases, respectively. The temperatures and the potentials increase with the effective atomic number of the plasma atoms, i.e. with the electron density of the produced plasma, in agreement with the literature.
The kinetic energies acquired by the ions are due to the plasma temperature and to the Coulombian effects occurring in the electric fields developed in the non–equilibrium of charge distribution. In particular, the ion velocity along the normal to the target surface has three components: the first due to the thermal interactions, v_T, the second due to the adiabatic gas expansion in vacuum, v_k, and the third due to the Coulombian forces, v_C, depending on the following relations, as shown previously in Equation 1.71, [149]:

$$v_T = \sqrt{\frac{3k_B T}{m}}; \quad v_k = \sqrt{\frac{\gamma k_B T}{m}}; \quad v_C = \sqrt{\frac{2zeV}{m}} \tag{3.21}$$

where $k_B T$ is the plasma temperature, m the ion mass, γ the adiabatic coefficient, e the electron charge, z the charge states number, and V the acceleration potential developed in the non–equilibrium plasma. In order to have an idea of the values assumed by these three different velocity components, Table 3.1 reports the three components of the ion velocity, thermal, adiabatic expansion, and Coulombian, evaluated for the different ions emitted from polyethylene, aluminium and copper plasmas.

Table 3.1: *Thermal, adiabatic expansion and Coulombian component of the ions velocity, evaluated for the different species emitted from polyethylene, aluminium and copper plasmas.*

Ion Velocity	H^{+} (PE)	C^{+}	C^{2+}	C^{3+}	H^{+} (Al)	Al^{+}	Al^{2+}	Al^{3+}	H^{+} (Cu)	Cu^{+}	Cu^{2+}	Cu^{3+}	Cu^{4+}
v_T ($\times 10^4$ m/s)	7.07	2.04	2.04	2.04	8.06	1.55	1.55	1.55	8.42	1.05	1.05	1.05	1.05
v_k ($\times 10^4$ m/s)	5.28	1.52	1.52	1.52	6.01	1.16	1.16	1.16	6.29	0.79	0.79	0.79	0.79
v_C ($\times 10^4$ m/s)	7.24	2.09	2.96	3.62	8.08	1.56	2.20	2.69	9.35	1.17	1.66	2.03	2.34

It is possible to observe that the ion velocity due to thermal interactions and adiabatic expansion is similar, while that due to Coulomb interactions increases with the charge state becoming higher with respect to the thermal ones.
A further investigation of the produced plasma was obtained by the CCD images of the plasma plume for the three targets. These images report the visible emission from plasma during 5 μs exposition time from the laser shot. By fixing the target position and the spatial scale correspondence with the image pixels, it is possible to evaluate the plasma expansion velocity in the vacuum chamber in the three cases, because the exposition time is known and the plasma plume length is measurable. Figure 3.27 reports the CCD images of the plasma plume for polyethylene (top), aluminium (middle) and copper (bottom) targets irradiated in the same experimental conditions.
The evaluation of the visible plume gives a velocity of 6.5×10^3 m/s for polyethylene, 8.7×10^3 m/s for aluminium and 1.1×10^4 m/s for copper targets. These velocities do not correspond exactly to those calculated by using Equation 3.21 and reported in Table 3.1. This is not a perfect correspondence due to some ns delay in the CCD camera acquisition with respect to the laser shot trigger and due to the light sensitivity of the CCD camera, which is limited and does not observe very low levels of visible light. However, the different plume length indicates that it is correlated mainly to the plasma temperature, growing from polyethylene to aluminium and up to copper, more than to the total ion velocity acquired by the different ions inside the plasma.

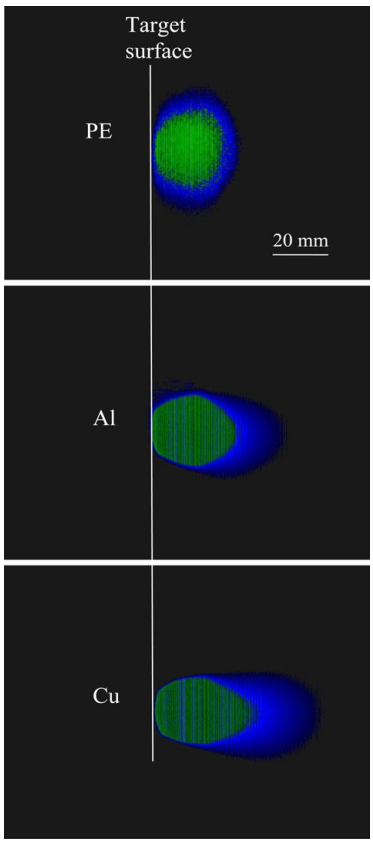

Figure 3.27: *CCD images of plasma plume for PE (top), Al (middle) and Cu (bottom) targets irradiated in the same experimental conditions.*

Results obtained experimentally were confirmed by simulation studies using the COMSOL software in three–dimensional space. Figure 3.28 reports some simulation results concerning the experimental measurements for Al–ions deflected by orthogonally magnetic field, with a Boltzmann velocity distribution, that reach the WEM detector. Figure 3.28a is relative to the detection of Al^{1+} that, moves into a magnetic field of 0.175 T, undergoes a deflection with an average radius of 5.76 cm. Figure 3.28b is relative to the detection of Al^{2+} that, submitted to 0.175 T, undergoes a deflection with an average radius of 4.29 cm. Figure 3.28c is relative to the detection of Al^{3+} that, submitted to 0.175 T, undergoes a deflection with an average radius of 3.49 cm. Due to the overlapping of the three ion energy distributions, the WEM observes the three peaks at different acquisition times, detecting the faster Al^{3+} ions

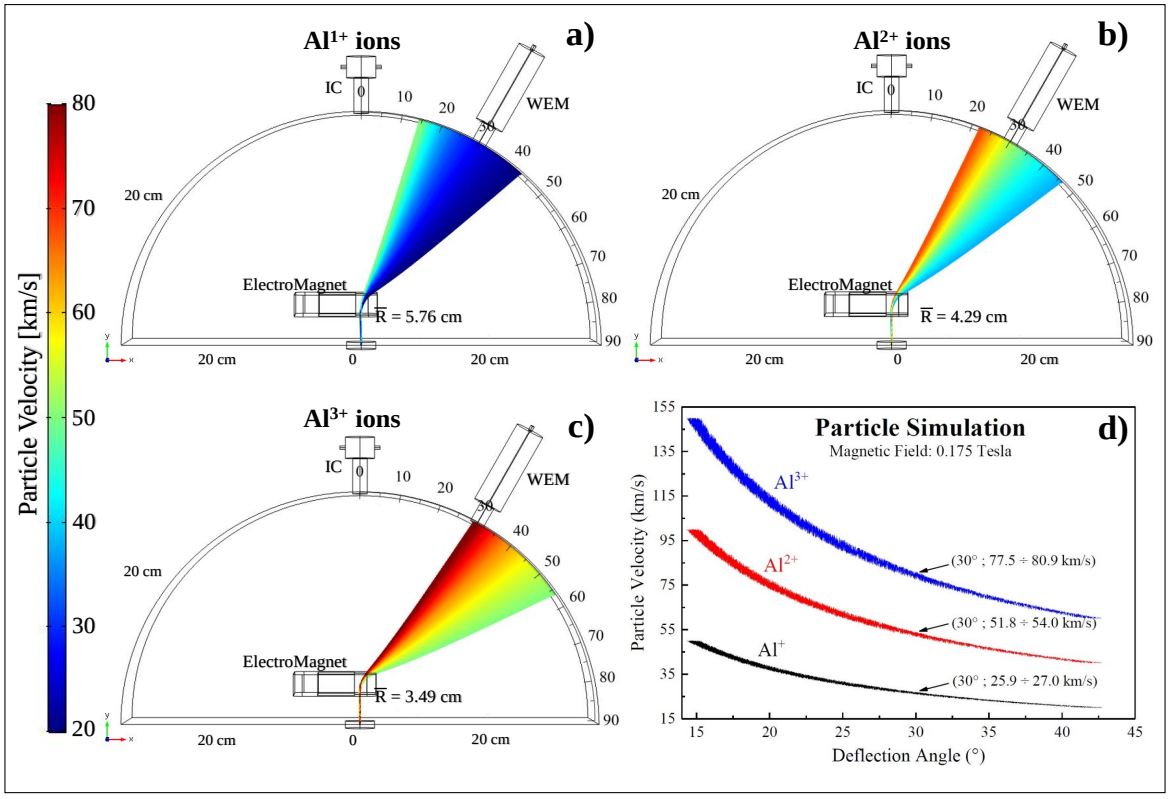

Figure 3.28: *COMSOL Multiphysics simulations concerning Al^{1+} (a), Al^{2+} (b) and Al^{3+} (c) ions deflected by 0.175 T magnetic field, and ions velocity versus the deflection angle (d).*

followed by the slower Al^{2+} and Al^{1+} ones. The false color scale represents the different ion velocity. The plot reported in Figure 3.28d indicates the particle velocity as a function of the deflection angle at 0.175 *T*. The velocity indetermination produces a thickening of the curves relative to the three Al charge states, as we already mentioned.

3.2.3 Section Conclusions

The simple magnetic spectrometer, presented in this section, permits to realize a plasma diagnostics, detecting ions up to about 100 *eV* per charge state of energy and permitting to go back to their energy distributions. The electromagnet employed in our experiments, is simple to build and permits to realize stable and uniform magnetic field up to 0.35 *T* for ions deflection based on Lorentz force. The prototype used in this experiment needs to be improved by reaching higher magnetic field, using a more useful WEM reaching a higher sensitivity in terms of ion current and angular distribution and in terms of its controllable system to deflect ions up to energies of the order of 100 *keV* per charge state.

3.3 Electric spectrometer for low energy ions

Published Paper[2018]

Magnetic and electric deflector spectrometers for ion emission analysis from laser generated plasma

L. Torrisi[1], G. Costa[1], G. Ceccio[1], A. Cannavò[1], N. Restuccia[1] and M. Cutroneo[2]

[1]*Dipartimento di Scienze Fisiche, MIFT, Università di Messina, V.le F.S. D'Alcontres 31, 98166 S. Agata, Messina, Italy*
[2]*Nuclear Physics, Institute, CAS 25086, Řež, Czech Republic*

Published as: L. Torrisi, G. Costa, G. Ceccio, A. Cannavò, N. Restuccia and M. Cutroneo: "Magnetic and electric deflector spectrometers for ion emission analysis from laser generated plasma", *The European Physics Journal: Web of Conferences*, Volume: **167**, Pages: 03011(1–7) (2018)

Available from: 10.1051/epjconf/201816703011

Publication Date: Published 09 January 2018

Ions' diagnostic emitted by laser–generated plasma in BPA regime may be developed by deflection through an orthogonally electrostatic field. A device, previously introduced, ie. the Ion Energy Analyzer (IEA), was used to diagnostic plasma generated by lasers of intensity less than 10^{12} W/cm^2 in the backward direction. Ions emitted by these plasmas generally have energies not exceeding hundreds of keV per charge state. Some experimental measurements performed by electrostatic deflectors, such as the IEA, are presented below [156].

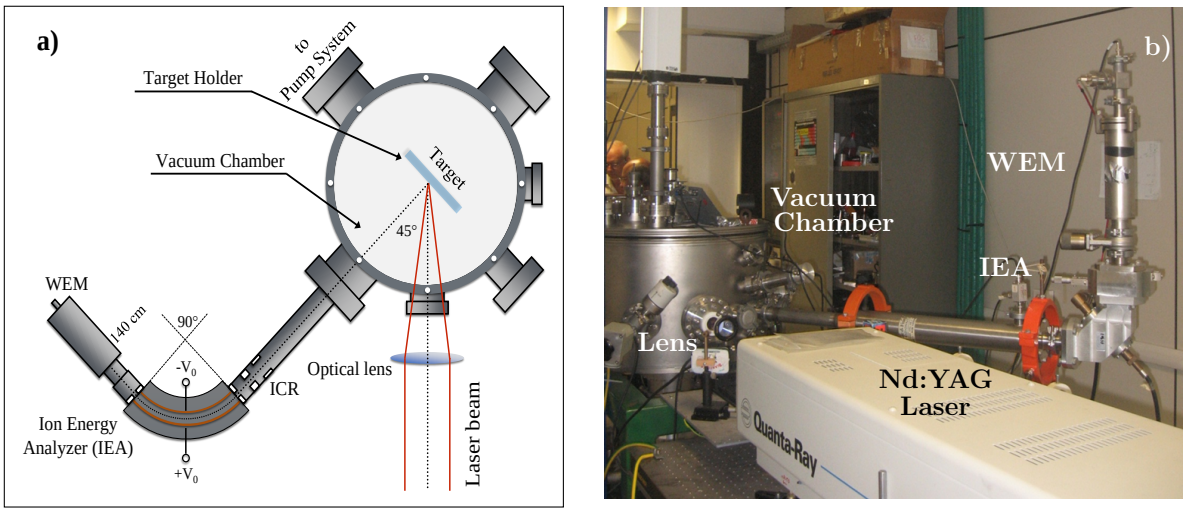

Figure 3.29: *Representation (a) and picture (b) of the experimental setup.*

The experimental setup consists of a Nd:YAG laser, with a fundamental wavelength of 1064 *nm*, pulse duration of 3 *ns* and 500 *mJ* energy, which approaches an intensity of 10^{11} W/cm^2. The laser beam is focused through an optical lens, with a focal length of 50 *cm*, on a tantalum target placed in the center of the vacuum chamber (10^{-6} *mbar*), and hits it with an angle of 45°, as shown in the schematization in Figure 3.29a. Figure 3.29b instead represents a photo of the experimental setup.

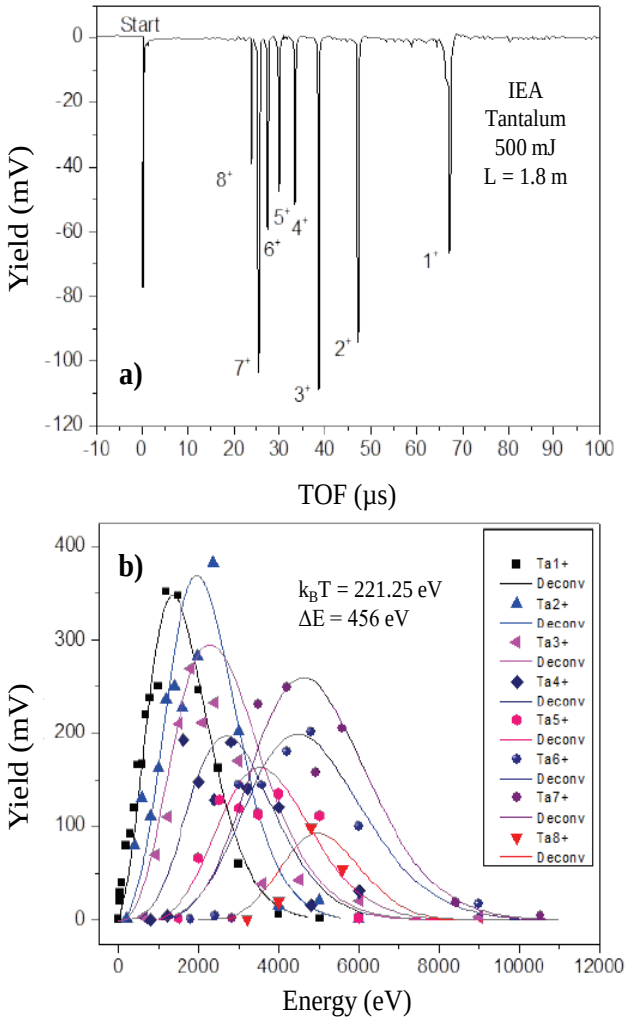

Figure 3.30: *Typical IEA spectrum in TOF approach recording Titanium ions emission by plasma (a) and plot of the ion energy distribution obtained by varying the E/z IEA filter (b).*

The plasma that expands along the normal to the target is monitored through an ICR placed at a distance of 90 *cm*, then it passes through a collimation system, and is later deflected by an electrostatic field between the two electrodes of the IEA. Often the system is realized using an electric field of the order of 1–10 kV/cm, and maintain the k parameter (Equation 3.7) to a value of 10. Thus, for example, if is $E/z = 10$ *keV* it means that the system are using an applied voltage of 1 *kV* and that the electrostatic filter can deflect 10 *keV* ions with a single charged, 20 *keV* with a double charged, 30 *keV* with a triple charged and so on. Limitations are due to the use of the high voltage applied to the electrode in high vacuum. Up to 30 *kV* have been applied without discharge problems.
Finally, the ions deflected by the IEA electrodes arrive on the WEM detector to be detected. The distance between the target and the WEM input window is 1.8 *m*.
Figure 3.30a reports a typical TOF spectrum of Ta–ions detected using the IEA spectrometer. By changing the IEA electrodes potential, similar spectra to this are obtained, where the charge states peaks change in position and yield.

By evaluating the maximum yields of the various WEM-TOF spectra in relation to the energy selected by the Equation 3.7, it is possible to reconstruct the energy distribution of each tantalum charge state that composes the plasma, as shown in Figure 3.30b.
The first charge state of tantalum ions is detected at a TOF of 68 μs, thus has a mean kinetic energy of about 660 keV. Ions are shifted toward higher energy increasing their charge state. From the Boltzmann curve widths and from the regular shift of the distributions with the charge state it is possible to evaluate a plasma temperature of 220 eV and a mean plasma acceleration voltage of 456 V, respectively.

3.3.1 Further data analysis

Further data analysis, in similar experimental conditions, by decreasing laser energy from 500 mJ to 150 mJ, was carried out on a tantalum target [85].
The laser used is a Q–switched Nd:YAG with wavelength 1064 nm, 9 ns of pulse duration and energy set at 150 mJ, operating at an intensity of about $\sim 10^{10}$ W/cm^2. It can work in single–shot or repetition rate at a frequency of 30 Hz. In the present experiment this is set to single–shot. The laser beam is focused on the target, through a optical lens, placed in the air, with a focal length of 50 cm. The target consists of a sheet of pure Tantalum. There are four ICs, placed horizontally at angles of 17°, 30°, 43° and 56° with respect to the direction of the incident laser beam. The IEA is mounted at 43° and its detector is an electron multiplier (WEM), at a distance of 1.5 m [85].

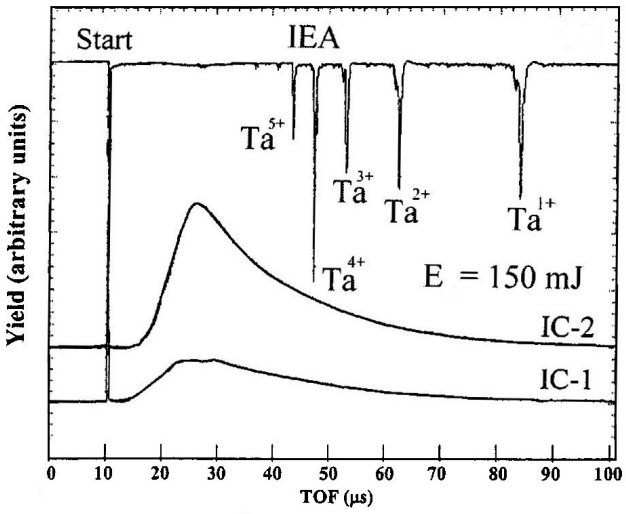

Figure 3.31: *Typical tantalum ion spectra detected by IC and IEA measurements. The spectra are related to Tantalum irradiated by 150 mJ of laser energy (image reprinted from ref [85]).*

The Figure 3.31 shows a typical WEM–TOF spectrum, obtained by irradiating the tantalum target, with an IEA electrode potential of ±50 V. By means of the TOF between the initial photopeak and the negative peaks, knowing the distance between the target and the detector, it is possible to calculate the ions' velocity and the energy through the Equation 2.29. Five tantalum charge states are identified using laser intensities of an order of magnitude lower than in the previous case (where eight charge states were observed). Of course, we also expect lower values for plasma temperature and potential.

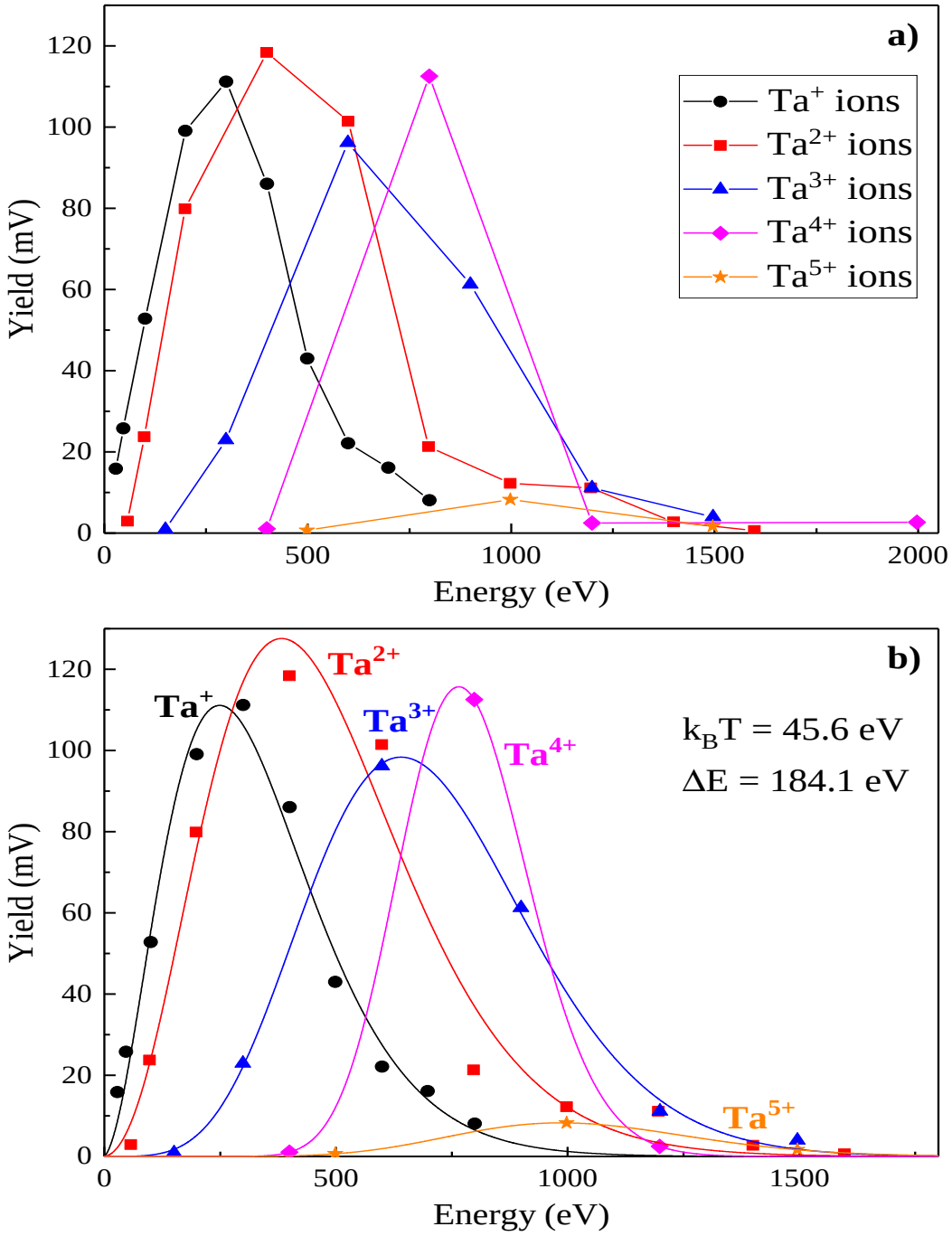

Figure 3.32: *Energy distribution of ions from 1+ to 5+ of tantalum (a), obtained by IEA, and fit of them by CBS distribution function (b).*

By changing the potential at the IEA plates gradually from ±10 V to ±120 V, different values of E/z are selected according to the Equation 3.7; thus a series of spectra similar to the one shown in the Figure 3.31 are obtained. Considering the TOF values and the yields as the voltage changes, it is possible to trace the energy distribution of the ions emitted by the target, as shown in Figure 3.32a. From the literature it can be observed that the points represented by the above mentioned data, are Coulomb–Boltzmann energy distributions; which can be fitted with the following expression [157]:

$$f(E) = \frac{A}{\sqrt{2m}}\left(\frac{1}{\pi k_B T}\right)^{3/2} E \exp\left[-\frac{1}{k_B T}\left(\sqrt{E} - \sqrt{E_k} - \sqrt{E_C}\right)^2\right] \tag{3.22}$$

where A is a normalization coefficient, m is the ions' mass, $k_B T$ is the plasma temperature, E_k and E_C are the adiabatic expansion and the coulombian energy respectively, equal to:

$$E_k = \gamma k_B T/2 \tag{3.23a}$$

$$E_C = zeV \tag{3.23b}$$

with γ the adiabatic coefficient (5/3 = 1.67 for monatomic species), ze and the ions' charge and V the plasma potential in Volts.
Using the CBS energy distribution (Equation 3.22), the five states of charge of the tantalum were fitted, as shown in Figure 3.32b. In this case, the average plasma temperature has been estimated at about 45.6 eV, while the average plasma potential is around 84 V. The energy of the ions emitted by a plasma is the sum of three contributions, the first thermal, the second adiabatic and the third coulombian. From the Equation 3.23 these three contributions are:

$$E_T = \frac{3}{2}k_B T \cong 68.4\ eV; \qquad E_k = \frac{\gamma k_B T}{2} \cong 38.1\ eV; \qquad \frac{E_C}{z} = eV \cong 84\ eV$$

Summing them up will be about $E_{tot}/z = 190.5\ eV$. On the other hand, the average energy difference between the maximum of a distribution and the next, of the Figure 3.32b, is worth about $\Delta E = 184.1\ eV$. This means that experimentally the ions are accelerated to energies of $\sim 184.1\ eV$ per charge state, in excellent agreement with the value found by the fit (E_{tot}/z).
The decrease of about one order of magnitude in the laser intensity, compared to the previous case (Figure 3.30), meant that the plasma temperature dropped by a factor 5, as might have been expected. The energy per charge state acquired by the ions decreased of almost 3 times. The charge states of the emitted ions are also different, with laser intensities of the order of $\sim 10^{10}\ W/cm^2$ 5 charge states are observed while with an intensity of the order of $\sim 10^{11}\ W/cm^2$ 8 charge states have been revealed.
The IEA is therefore a very useful device for studying ions' energy distribution emitted by laser–generated plasmas in BPA regime. One of the defects of this type of device is that it requires a high number of laser shots, which in the long run can damage the target and even compromise the measurements obtained. Moreover, the acquisition time of an energy distribution for each ion species can be considerably long.

3.3.2 Comparison of Magnetic and Electric spectrometer

The MSC and the IEA are two devices that deflect charged particles emitted by a laser–induced plasmas, through a magnetic or electric field, respectively. The functionality of these devices depends strongly on the ions energy to be detected, in fact, high energies, above the hundreds of *keV* per charge state, require very intense fields, not easily reproducible. Here we have compared the two investigation techniques in the study of ions emitted by plasmas in backward direction, with respect to the incidence of the laser beam [158].

A Nd:YAG laser with 1064 *nm* fundamental wavelength, 3 *ns* pulse duration, and pulse energy from 1 to 300 *mJ* was employed to irradiate solid targets in vacuum (at 10^{-6} *mbar*). The targets used consist of thick sheets, of 2×2 *cm* planar dimensions, made of aluminium and copper. They are attached on a target holder that can be rotated 45° counterclockwise, to study the produced plasma by a magnetic deflector (Magnetic Spectrometer Chamber, MSC), or 45° in a clockwise direction, to analyze the produced plasma by an electric deflector (Ion Energy Analyzer, IEA), as well as shown in Figure 3.33.

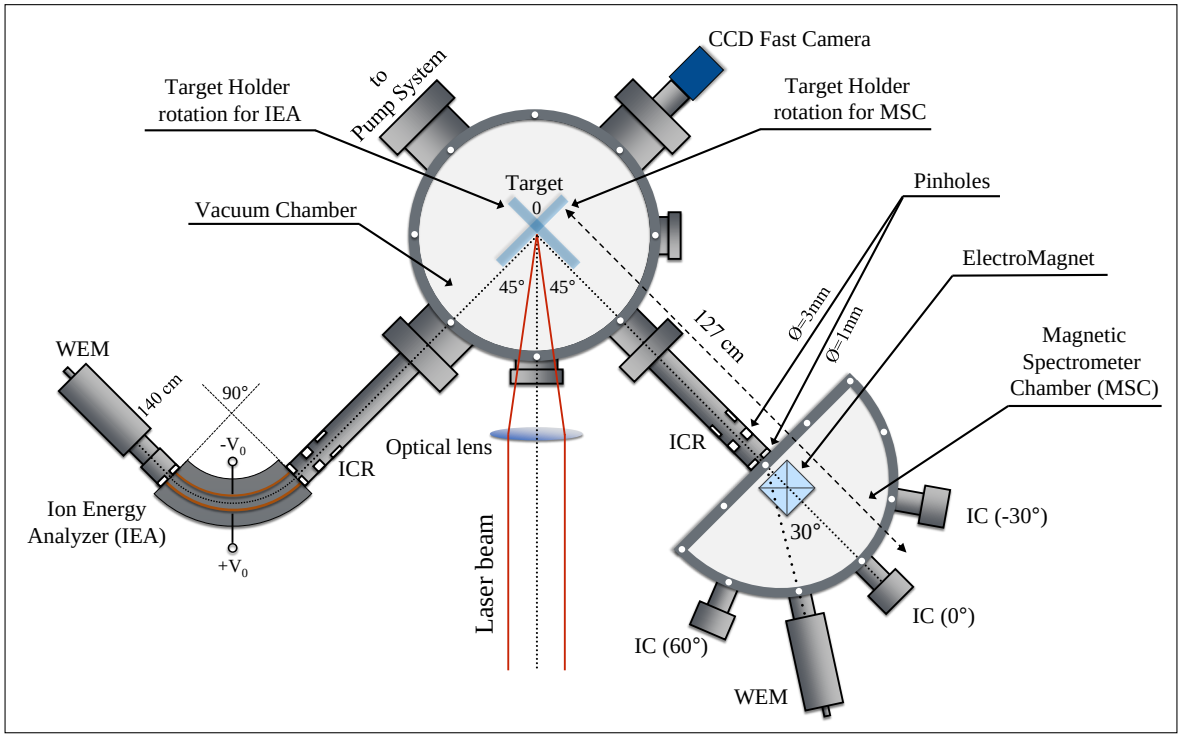

Figure 3.33: *Scheme of experimental setup, where a Nd:YAG laser at* 10^{10} $W\,cm^{-2}$ *was focused on a target placed in a vacuum chamber. The ion emitted by plasma are investigated by a magnetic (MSC) or electric deflector (IEA).*

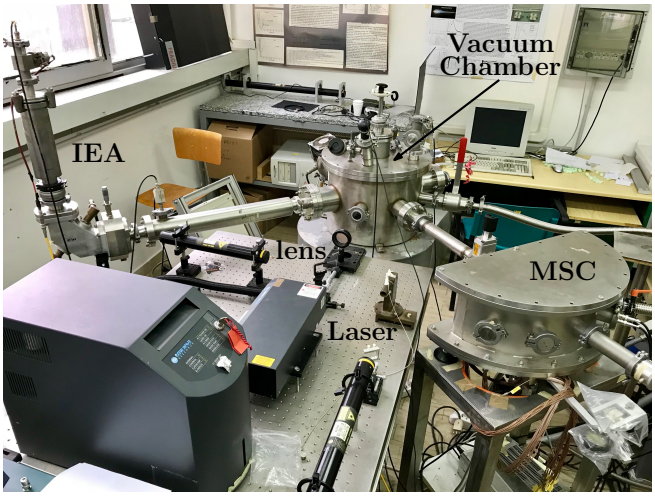

Figure 3.34: *Picture of experimental setup, where it is shown MSC and IEA spectrometer to analyse laser–generated plasmas.*

The Figure 3.34 shows a photo of the experimental apparatus, displaying the laser used for the measurements, the vacuum chamber, the magnetic (MSC) and electric (IEA) deflection system, for the non–equilibrium plasmas analysis.
The flight distance between target and detector for the IEA is 140 *cm* and the laser energy for these measurements is set to 300 *mJ*. In the case of the MSC, on the other hand, the flight distance of the ions is 127 *cm* and the laser pulse energy is 200 *mJ*. Finally, there are some detectors at fixed angles, and two ion collector rings located before their respective electric and magnetic deflectors.

For this measurements will be presented the spectra obtained by a Windowless Electron Multiplier (WEM) placed at 90° for the Ion Energy Analyzer, and at 30° for the Magnetic Spectrometer Chamber.
Figure 3.35 shows a WEM spectrum, obtained by irradiating copper target, through electric deflection by IEA (on the left) and magnetic deflection by the MSC (on the right).

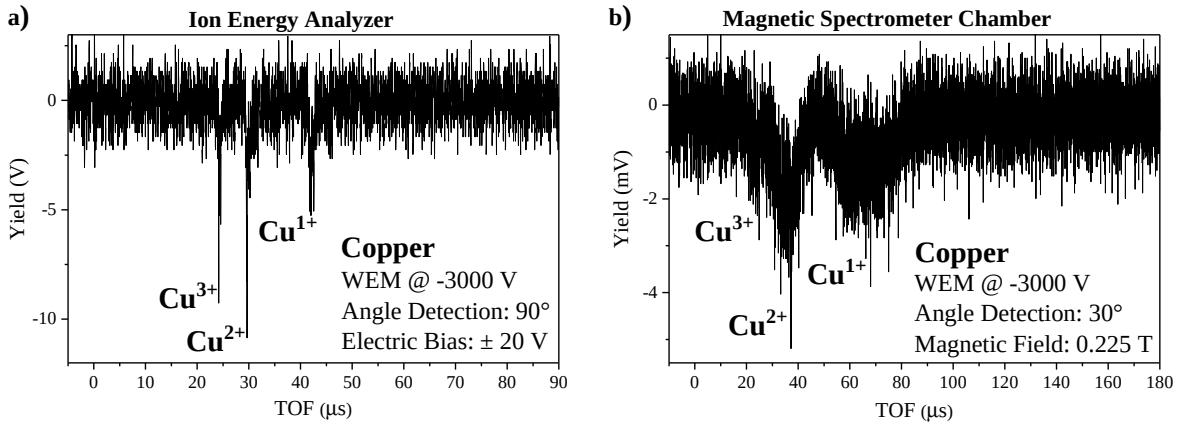

Figure 3.35: *WEM spectrum acquired by IEA with ±20 V per deflection plate (a), and by MSC with a magnetic field of 0.225 T (b).*

By varying the electrical potential for IEA electrodes, and the magnetic field for MSC electromagnet, a series of spectra are obtained such as those shown in Figure 3.35. Thus, evaluating the area of these peaks as function of energy or velocity of the ions, it is possible to obtain points that can be fit with Coulomb-Boltzmann energy or velocity Distributions (Equation 3.22 and Equation 1.71), as shown in Figure 3.36.

Figure 3.36a shows the fit of the energy distributions by CBS, obtained through the IEA, for the aluminium target. The average energy difference between the maximum of a distribution and the next is about $\Delta E = 184.1\ eV$. This means that experimentally the ions are accelerated to energies of $\sim 184.1\ eV$ per charge state.

On the other hand, the plasma temperature and potential estimated by the fit is 32.5 eV and 71.1 V respectively. Since, as mentioned above, the total energy acquired by the ions is the

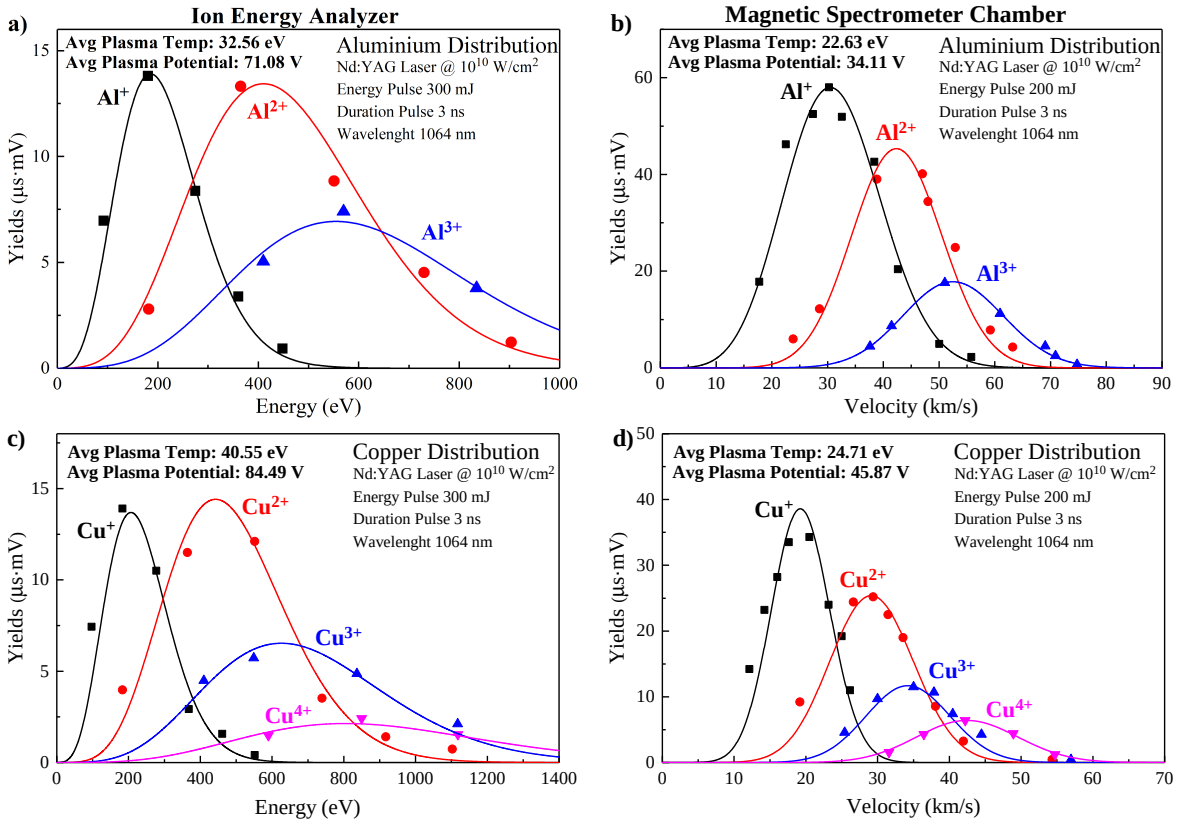

Figure 3.36: *Plot and fit of the WEM peak areas as function of the ions energy for aluminium (a) and copper (c) detected by electrical deflections through IEA. Plot and fit of the WEM peak areas as function of the ions velocity for aluminium (b) and copper (d) detected by magnetic deflections through MSC.*

sum of three contributions, the first thermal, the second adiabatic and the third coulombian, which are respectively:

$$E_T = \frac{3}{2}k_B T \cong 48.8\ eV; \qquad E_k = \frac{\gamma k_B T}{2} \cong 27.1\ eV; \qquad \frac{E_C}{z} = eV \cong 71.1\ eV$$

Summing them up will be about $E_{tot}/z = 147.0\ eV$. Thus, value obtained from the fit, $E_{tot}/z = 147.0\ eV$, is not so distant by that found experimentally, $\Delta E = 184.1\ eV$ per charge state.
Figure 3.36b shows the fit of the aluminium ion velocity distributions according to CBS. In this case the energy of the laser pulse is lower, so the plasma temperature and potential are smaller than in the previous case, i.e. 22.6 eV and 34.1 V respectively. The Al^+–ions plot has a maximum at around $\sim 30.5\ km/s$, which corresponds to an energy of 131.1 eV. The Al^{2+}–ions distribution, instead, has the maximum at around 42.4 km/s, which indicate an energy of 253.3 eV. Finally, the maximum of Al^{3+}–ions distribution is at 52.6 km/s, i.e. at an energy of about 389.8 eV. The distance between the maximums of the ions distributions produces an enlargement of approximately $\Delta E = 129.4\ eV$. As in the previous case, by means of the plasma temperature and potential, an $E_{tot}/z = 86.9\ eV$ is obtained. Also in this case the value obtained from the fit is not so far from the one experimentally expected.
Figure 3.36c shows the fit of the energy distributions by CBS, obtained through the IEA, for the copper target. The plasma temperature and potential estimated by the fit is 40.6 eV and 84.5 V respectively. Since the total energy acquired by the ions is the sum of three contributions, the first thermal, the second adiabatic and the third coulombian, which are respectively:

$$E_T = \frac{3}{2}k_B T \cong 60.9\ eV; \qquad E_k = \frac{\gamma k_B T}{2} \cong 33.9\ eV; \qquad \frac{E_C}{z} = eV \cong 84.5\ eV$$

Summing them up will be about $E_{tot}/z = 179.3\ eV$. On the other hand, the average energy difference between the maximum of a distribution and the next is about $\Delta E = 199.3\ eV$. This means that experimentally the ions are accelerated to energies of $\sim 199.3\ eV$ per charge state. Thus, the value obtained from the fit of $E_{tot}/z = 179.3\ eV$ is in very good agreement by that found experimentally, $\Delta E = 199.3\ eV$ per charge state.
Finally, Figure 3.36d shows the fit of the copper ion velocity distributions according to CBS. In this case the energy of the laser pulse is lower, so the plasma temperature and potential are smaller than in the previous case, i.e. 24.7 eV and 45.9 V respectively. The Cu^+–ions plot has a maximum at around $\sim 19.1\ km/s$, which corresponds to an energy of 121.0 eV. The Cu^{2+}–ions distribution, instead, has the maximum at around 29.2 km/s, which indicate an energy of 282.5 eV. The Cu^{3+}–ions plot has a maximum at around $\sim 34.3\ km/s$, which corresponds to an energy of 389.9 eV. Lastly, the maximum of Cu^{4+}–ions distribution is at 42.6 km/s, i.e. at an energy of about 601.4 eV. The distance between the maximums of the ions distributions produces an enlargement of approximately $\Delta E = 160.1\ eV$. As in the previous case, by means of the plasma temperature and potential, an $E_{tot}/z = 103.6\ eV$ is obtained. Also in this case the value obtained from the fit is not so far from the one experimentally expected.

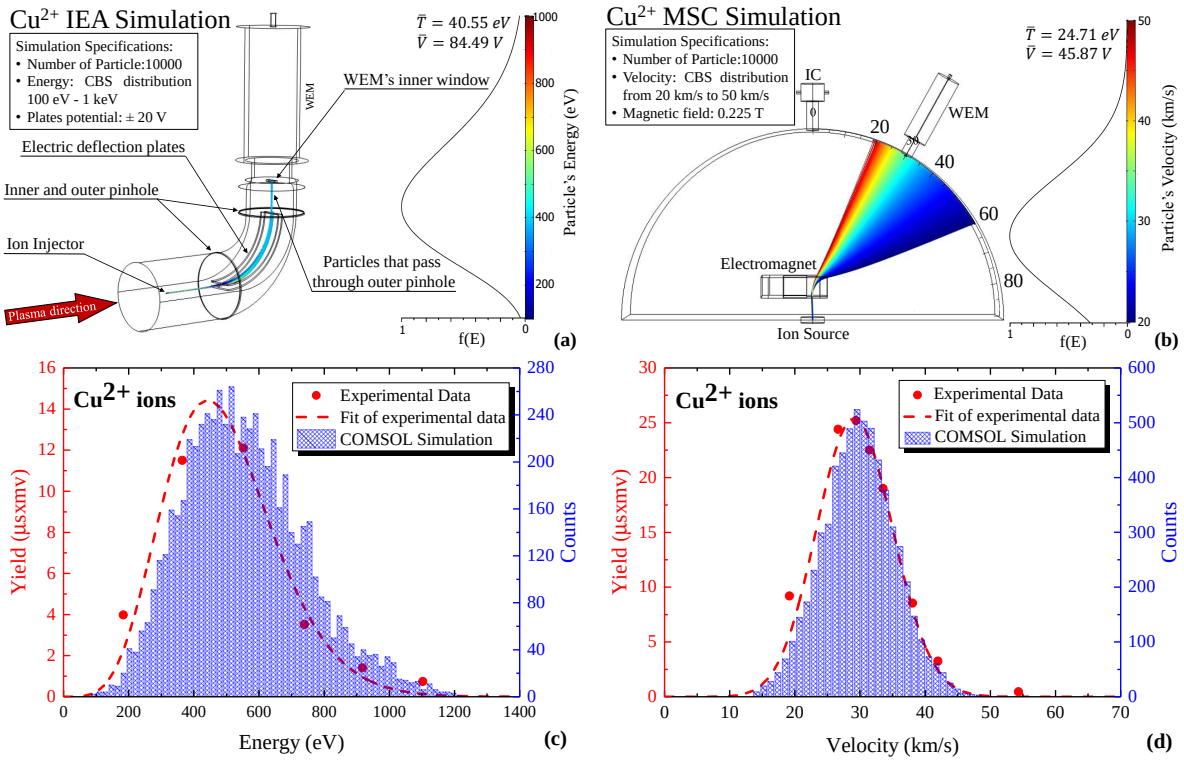

Figure 3.37: *COMSOL simulation for Cu^{2+} in IEA (a) and MSC (b) apparatus and their respective comparison with experimental data (c) and (d).*

The values obtained from the fit are almost comparable, within the limits of experimental errors (changes in the focal point, accuracy of the spectrometer, etc.). There is also an excellent agreement between the theoretical prediction, obtained by simulation with COMSOL Multiphysics software and the experimental data, as illustrated in Figure 3.37 for Cu^{2+}–ions. Thus, here it was presented the comparison between already well-known electric spectrometer (IEA) and a prototype of a new magnetic spectrometer. The values obtained are in good agreement with each other. The WEM spectra obtained in the two cases seem to be more accurate for the IEA, due to narrow input and output slit that increase the resolution. The strength of the MSC device lies in its ease of construction and assembly, which has allowed us to create a uniform magnetic field up to 0.35 T. Work is progress to try to increase the deflection magnetic field, use a more sensitive WEM, and insert multiple detectors at more deflection angles. However, rather than talking about comparison between these two devices, they can be considered as complementary because of the different quantities that can be obtained.

Chapter 4

Ion Acceleration and Diagnostics in TNSA Regime

Since the advent of pulse lasers with a duration shorter than picoseconds, that reach intensity value grater than 10^{16} Wcm^{-2}, a new frontier of ion acceleration is opened by the irradiation of thin foils. One of the most exciting experimental results is the acceleration of light ions, and in particular protons, which come from the rear, non–irradiated, target surface, reaching energies of the order of MeV or tens of MeV per charge state, high quality and with properties of an ion beam. This absolutely promising acceleration regime is called Target Normal Sheath Acceleration (TNSA). At these amounts of energy, the ions emitted by laser–generated plasma can be diagnostic by several techniques. Surely, the time–of–flight approach remains useful for the velocities and abundance characterization of ions accelerated in the TNSA regime. This can be done using Faraday Cups or semiconductor–based devices, such as Silicon Carbide (SiC) detector, which will be discussed. Rapid information on the maximum ions energy, on particles types according to their mass–to–charge ratio, and on their abundance, can be given by Thomson Parabola Spectrometer (TPS). This device deflects ions along the plane perpendicular to their trajectory, through a magnetic field and an electric field placed in sequence. Parabolas traced on a detector, which can be of different nature (MicroChannel Plate, track detector, GafChromic films, and others), can be reproduced with a computational calculation. The overlap between experimental and simulation data, will give the required information about the laser–generated plasmas.

4.1 TNSA mechanism: State of Art and Diagnostics

Energetic ion beams, with properties such as low emittance and high brilliance similar to those achieved by conventional accelerators, can be obtained by irradiating thin targets (thicknesses below tens of microns), with relativistically intense and ultra short laser pulses. As already discussed, the ionic beam acceleration technique from the rear surface of the target is called Target Normal Sheath Acceleration (TNSA). Although in principle any ion can be accelerated in TNSA regime, in many experiments a preferential acceleration has been observed for light ions, such as protons, up to carbon and oxygen.

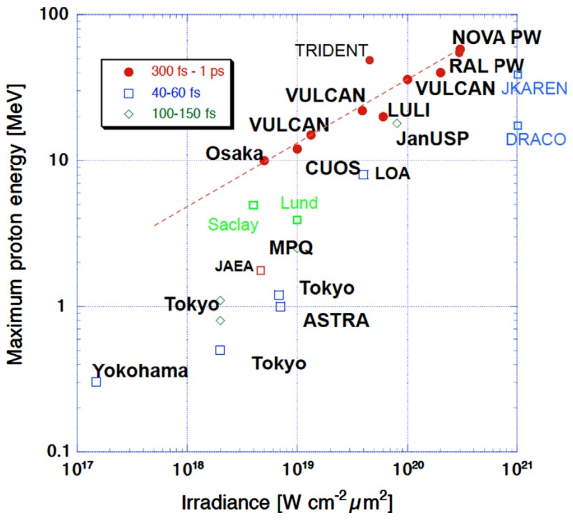

Figure 4.1: *Maximum proton energy versus laser irradiance obtain in various measurements of which the name is cited (image reprinted from the ref [97]).*

As discussed in Chapter 1, Section 1.3.2, current lasers intensity are not able to accelerate ions directly, but interact with electrons, heating up and pushing out them forward, as a result of the ponderomotive force and other mechanisms discussed in Chapter 1. For high laser intensity, electrons quickly become relativistic, reaching energies even in the order of hundreds of *MeV* order, so their collision range becomes much greater than the target's thickness, therefore they can propagate to the rear target's surface and expand in vacuum. In this way, a very intense electric field of the order of *TV/m* is generated between the electrons pushed forward and the rear surface of the target that has remained positively charged, which drives the light ion acceleration. The energy ion spectra has an exponential profile, with an high cut–off energy.

The conversion of laser energy into hot electron temperature is not perfect, in fact, if the model is isothermal and the hot electron temperature is assumed to be equal to the ponderomotive potential, only a fraction will be converted according to the relationship [91,94]:

$$\eta = 1.2 \times 10^{-15} \left(\frac{I_L}{W/cm^2} \right)^{0.74} \tag{4.1}$$

with a maximum value $\eta = 0.5$ for $I_L > I_L^* \approx 5.7 \times 10^{19}$ W/cm^2. For example a laser at intensity of 4×10^{18} W/cm^2 has a conversion of energy in hot electron temperature of about ~ 7 %.
Since parts of electrons are accelerated to relativistic energies, they approach the speed of light, and thus escape very quickly from the area where the longitudinal electric field of ion acceleration is active. The slower electrons are stopped and re–accelerated back into the target. The electric field thus generated is quasi–static, and lasts comparable to the acceleration time of the electrons. Therefore, ultra–short laser pulses, although providing the highest intensities, are not the optimum laser pulses for ion acceleration, but it's efficient for light particles like protons.
In Figure 4.1 are reported the maximum proton energy, observed in a large number of experiments (labelled by name), versus the laser irradiance. The laser beam irradiance conversion efficiency into high proton energy changes from about 1% for short laser pulses, up to about 10% for longer pulses and PetaWatt laser [95]. The highest energy reported in Figure 4.1 is about 60 *MeV*, obtained with large PetaWatt system. The proton beam emitted by rear

target surface can reach 10^{11}–10^{13} particle per laser shot, which corresponds to a current of *kA* order, if the co–moving electrons are removed from the beam. However, only 10^{7}–10^{8} *protons/MeV/sr* could be accelerated at high–energy value of the spectrum [159].
However, more recent experiments than those shown in Figure 4.1, report a proton acceleration approaching 100 MeV, with the Vulcan laser at the *Rutherford Appleton Laboratory* (UK), operating at an intensity of about $(3 \pm 2) \times 10^{20}$ W/cm^2 [104].
In TNSA regime, light ions in the order of tens *MeV* and relativistic electrons around hundreds of *MeV* are emitted by the plasma; however even neutral particles, such as photons ranging from visible to X–rays, are ejected at large angles. In the pulsed laser–generated plasmas the emission of high energy photons, such as X–rays in order of hundreds of *keV*, is due to three fundamental process which involving electrons: free–free, free–bound and bound–bound electrons transitions. In the first case, there is the interaction of free electrons with the Coulombian potential of an ions, the electrons are deflected and lose energy by emission of electromagnetic radiation. The energy spectrum produced is continuous, and the phenomenon is also called *bremsstrahlung effect*. The second process is due to a passage of an electron between a free state and a bound state. Again, the emission spectrum is continuous, and the phenomenon is called *recombination effect*. The bound–bound electronic transition is due to transitions between discrete energy levels of an atom; this produces spectral emission lines due to the energy difference between the levels [160, 161].
The phenomena of Bremsstrahlung and recombination are strongly influenced by the atomic number of ions that constitute the plasma and by the electronic temperature. In particular, the ratio between the intensities of the X–rays emitted by recombination (w_r) and by the bremsstrahlung effect (w_b) follows the relationship [162]:

$$\frac{w_r}{w_b} = 2.4 \frac{Z^2 E_H}{k_B T} \tag{4.2}$$

where $E_H = 13.6$ eV is the Hydrogen ionization energy, Z is the atomic number and $k_B T$ is the electron temperature. Thus, from the Equation 4.2, if we consider a carbon ion plasma ($Z = 6$), whose electronic temperature is $k_B T = 10$ keV, the ratio between the intensities of X–rays emitted in the two processes will be 0.11. If the temperature increases by an order of magnitude, this ratio will be equal to 0.01. Therefore, for low Z and/or high temperature plasmas, the Bremsstrahlung emission overcomes the recombination emission.
According to the energy, and consequently to the wavelength, it is possible to distinguish between the hard X–rays (with energies above a few units of *keV* and wavelengths lower than units of Angstrom) and the soft X–rays (with energies lower and wavelengths higher than the previous case). It should be noted that in plasma not only hot electrons can lead to X–ray production, but even cold electrons population.
Afterwards a brief discussion is given to some of the techniques most frequently used in plasmas diagnostics generated by short laser pulses [163]. Later the attention will be mainly focused on charged particles detections by different devices such as Thomson Parabola Spectrometer, Gafchromic film, track detector and detector based on Silicon Carbide.

4.1.1 Plasma Diagnostics Techniques

Since the advent of short or ultra–short pulses lasers, which reach high intensities between $10^{16} \div 10^{20}$ W/cm^2 order, the plasmas generated have become new sources rich in new phenomena, such as particles acceleration at high energy (approaching hundreds of MeVs), nuclear reactions induced by lasers, coherent radiation generation and more. The diagnostics of ultra–short pulsed laser–generated plasmas is a rapidly evolving field involving different complementary investigation techniques. The following paragraphs will introduce the main techniques of analysis used that are currently used.

Optical Measurements

In the laser–matter interaction, it is important to know the basic parameters of the irradiated target, such as the roughness, the surface composition, the quantity of impurities present, the type of sample used and so on. The main problem is related to the lack of knowledge on the initial target state to which the main pulse is interacting. Often, due to the pre–pulse, the interaction takes place between a under–critical density gas and the main peak of the laser [164]. One technique to characterize the target before the main pulse interacts with it, is the *interferometry*.

Laser interferometry is used to understanding temporal and spatial density profile, which are crucial parameters to model the laser–plasma interaction. In this technique, a laser beam is divided into two parts, the first part travels unperturbed (reference beam), while the second is passed through the plasma (probe beam). Since the laser beam of the probe cannot propagate in an over–critical plasma, being the critical density defined by the probe's laser beam wavelength, this imposes a theoretical limit for this method, which is generally $10^{21} \div 10^{22}$ cm^{-3}. However, often the maximum densities that can be detected are also two orders of magnitude lower due to refractive effects and opacity [165].

The probe beam is then magnified at the point where the entire experiment is detected, and the reference beam is reconnected with the probe beam. The plasma along the path of the probe beam causes a phase shift that generates an interference pattern on the detector. If the plasma can be considered as having a cylindrical symmetry and its size is smaller than the beams overlap area, the electronic density can be calculated by integrating the phase shift, $\Delta\Phi(x,r)$, in the interference pattern using the method known as *Abel inversion* [165]:

$$n_e(x,r) = n_{cr} \cdot \left[1 - \left(\frac{\lambda}{2\pi^2} \cdot \int_r^R \frac{\partial \Delta\Phi(x,y)}{\partial y} \frac{dy}{\sqrt{r^2 - y^2}}\right)^2\right] \tag{4.3}$$

where λ is the laser wavelength. A typical image detected by interferometry technique is show in Figure 4.2, that report also two dimensional electron density distribution calculated using the Abel inversion method, reported in Equation 4.3.

Another technique based on interferometry is the so–called VISAR (*Velocity Interferometer System for Any Reflector*), which is a diagnostic for measuring the shock wave velocity prop-

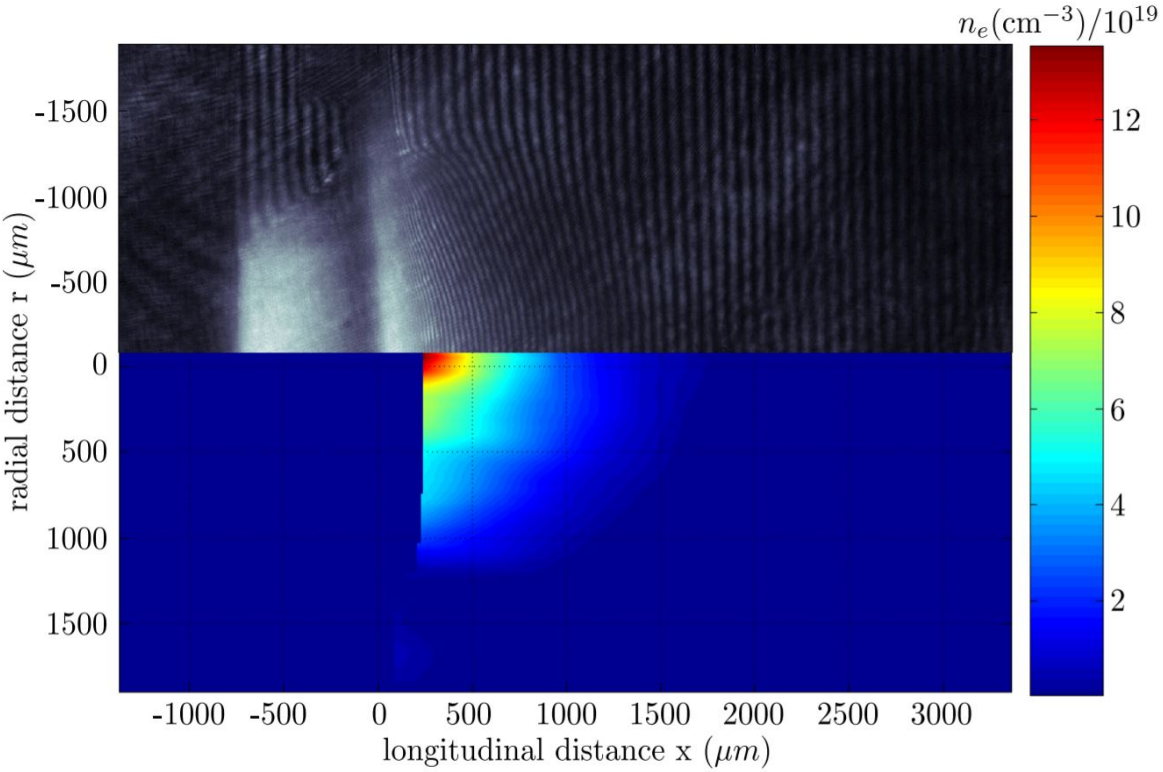

Figure 4.2: *Typical interferometry image on top, with the computed electron density distribution on bottom. In the interferometry image are present the free electrons both the front and the rear side, although only the front side can be analysed. The image was obtain by using a 355 nm probe beam wavelength with a pulse length of 500 ps, (image reprinted from ref [165]).*

agating in materials subject to laser–generated plasma. It is based on the measurement of the Doppler effect induced by the movement of a reflective surface using a probe beam that illuminates this moving surface. This device is based on the Mach–Zehnder interferometer in which it is introduced an etalon (typically a piece of glass with anti–reflection coating) and as a detector uses a streak camera to obtain time–resolved measurements. The fringe shift is related to the reflective surface speed from the [166, 167]:

$$F(t) = \frac{\Delta\phi(t)}{2\pi} = \frac{2\tau_0(1+\delta)}{\lambda} v(t) \tag{4.4}$$

where $\phi(t)$ is the phase of the fringe, τ_0 is the initial delay and δ is the corrective term associated with the spectral dispersion of the etalon. The final purpose of this diagnostic technique is to produce graphs of velocity as a function of time. The velocity allows to calculate internal pressures as a result of the induced shock [166].

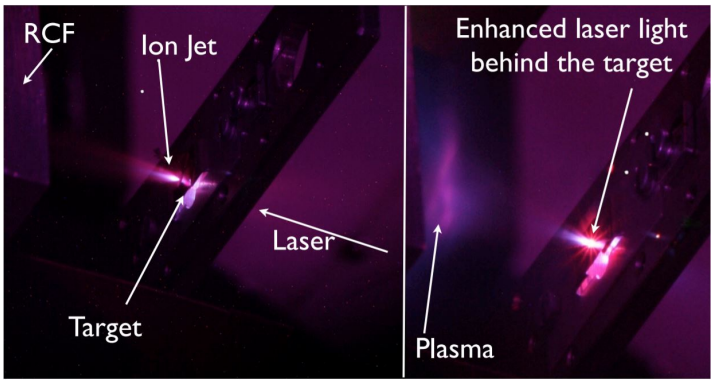

Figure 4.3: *A typical optical image of a short laser pulse at PHELIX facility in Germany. The bright spot of the laser interaction and the ions expansion is portrayed on the left. On the right is reported an experiment with enhanced the pre–pulse level (image reprinted from ref [165]).*

Anyway, the streak camera is not only used as a final detector, but sometimes it is employed as an additional diagnostic. As well as fascinating pictures of the experiment, the images captured with these devices of the expanding plasma can reveal interesting information about the dynamics of laser–matter interaction. These devices in fact offer high spatial and temporal resolutions and give the possibility to be triggered by the laser pulse. A typical measurement is reported in Figure 4.3. In this, the expansion of the plasma behind the target is portrayed. In addition, without the ion signal it was possible to observe the level of the pre–pulse, which destroyed the foil before the arrival of the main pulse.
Other optical measurements are carried out, for example, to investigate the evolution of the magnetic field in the generated plasma. The magnetic field has the same importance as the electric one; it can influence the energy flux from the interaction zone to the deepest layers of the target, the transport of electrons, and influence the instabilities. The initial measurements of the magnetic field involved a method of contact, for example with coils in front of the plasma, but these could only obtain field values in the less dense areas of the plasma. The introduction of the optical method has increased diagnostic capabilities. These techniques are based on the *Faraday rotation*, i.e. the measurement of the polarization rotation of a linearly polarized radiation that propagates through a magnetized plasma, or the *Zeeman effect*, i.e. the splitting measurement of the spectral lines emitted by the plasma. The first method has two disadvantages, which the first consists that the electronic density must be known, since the rotation of the angle of polarization is proportional to $\int n_e B dl$, and the second is that the beam which propagates through the plasma undergoes refraction, birefringence and depolarization. Using the Zeeman splitting does not incur these problems, however at high densities and temperatures it becomes complicated to observe the Zeeman effect because of the Stark and Doppler shift of the spectral lines. The highest magnetic field value measured with this technique is 0.5 *MG* [168]. More recent techniques for the measurement of magnetic fields are the *cut–off method*, where the p–component of self–generated harmonics decreases with increasing magnetic field, and the method that uses the *Cotton–Mouton effect*, which is used when there are no observable cut–offs of self–generated harmonics. The highest recorded magnetic fields were measured with these techniques [169, 170].

X–rays diagnostic

Like already mentioned, X–rays are produced by processes involving free–free, free–bound and bound–bound electron transitions. One of the most used diagnostics is the K_α fluorescence radiation, emitted by the ionization of the inner shells of an atom due to the fast electrons and the subsequent decay.

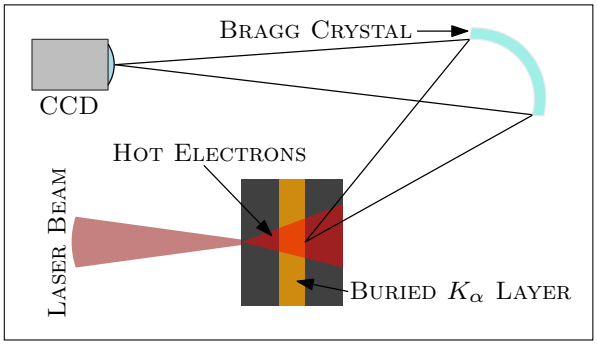

Figure 4.4: *Schematic measurement of K_α fluorescence diagnostic. A CCD camera detector uses a Bragg crystal mirror to image copper or titanium fluorescence layer embedded in a low Z material.*

Penumbral images of K_α fluorescence are used to measure the size of the K_α source both in pure targets and with layers buried in a low atomic number matrix. A 2D X–ray imaging technique was employed to record the origin of K_α fluorescence created by copper or titanium buried layers in aluminium or plastic targets [171]. The schematic experimental setup is shown in Figure 4.4. In this case, the photons are enough energy to escape from the surrounding target material and it is possible to observe the transverse electrons distribution at a resolution of about 12 μm.

However, there are many general problems related to the use of this technique, such as the low collision rate of the relativistic hot electrons with respect to the cold electrons of the return current, the introduction of the buried material may change the conductivity of the irradiated foil, and others [165].
A widely used and versatile technique for fully describing the plasma in its whole volume is the X–ray scattering, due to their very high penetration power. During the scattering process, X-ray transfers the moment $\hbar\boldsymbol{k}$ and an energy equal to $E = \hbar(\omega_0 - \omega_s) = \hbar\omega$ to the electron, being ω_0 and ω_s the frequency of incident and scattered photon. The cross section of the process for a single electron is called Thomson cross section; but in scattering diagnostics the measurement of the signal is the superimposition of many photon scatterings. Thus, the total cross section will depend on the structure of the plasma through the dynamic structure factor $S(\boldsymbol{k},\omega)$, defined as the time and space Fourier transform of the time–dependent electron density pair correlation function [165]. The structure factor is directly related to the electronic temperature via the equation:

$$\frac{S(\boldsymbol{k},\omega)}{S(-\boldsymbol{k},-\omega)} = \exp\left(-\frac{\hbar\omega}{k_B T_e}\right) \tag{4.5}$$

with $\omega = \omega_s - \omega_0$ and $\boldsymbol{k} = \boldsymbol{k}_s - \boldsymbol{k}_0$. Therefore with this principle it is possible to investigate the electronic temperature of the plasma [165].

Nuclear diagnostics of Laser–generated Plasmas

When an ultra short pulse interacts with a thin target the temperatures reached are enormous and correspond to electron velocity widely in the relativistic regime. The interaction of the latter with the nuclei, generates a bremsstrahlung radiation, whose most energetic component exceeds the nuclear reactions threshold induced by photons. According to the yield of hot electrons generated by the laser–matter interaction, the photo–neutron disintegration reactions become accessible. The diagnostics of plasmas generated by high–intensity lasers can be conducted using nuclear reactions induced by high–energy bremsstrahlung radiation. Modern diagnostics using such techniques, consist in evaluating combination of different produced isotopes, each of them with its own neutron separation threshold. Choosing the right isotope results in a high reaction yield for a wide range of photon energy in terms of the desired (γ,xn)–reaction. After the reactions have been performed, the isotopes activated in the target are measured with gamma spectroscopy to determine the absolute yield of the (γ,xn)–reaction products. Usually the analysis involves starting from a known cross–section spectrum by a database and consequently the energy derivation, which is related to the electronic distribution function [165].
More powerful laser pulses produce more energetic electrons and ions, and traditional detectors often fail to detect them. Nuclear activation technique can be used to help in the diagnostics of very energetic particles. A specific technique that has been very successful is the activation of nuclear reactions in Copper due to protons.

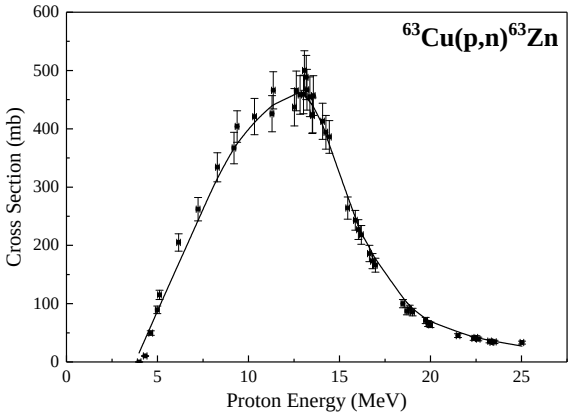

Figure 4.5: *Experimental nuclear reaction Cross Section for transmutation $^{63}Cu(p,n)^{63}Zn$, data from ref [173, 174].*

Energy protons above the neutron separation threshold of 4 *MeV* cause Copper to be transmuted into Zinc ^{63}Cu(p,n)^{63}Zn [172]. This unstable isotope rapidly decays back into Copper, with a half–life of 38 minutes, emitting positrons that can be easily detected. The cross section of the reaction has a peak at about $10 \div 12$ *MeV* protons and then decreases rapidly, as shown in Figure 4.5. A simply method to detect protons consists of to use a series of copper foils stacked one above the other, and exposed to the proton beam emitted by the plasma generated by the ultra–short pulse.

Each of these foils will degrade the energy of the beam according to the stopping power, and the last layer activated by the nuclear reaction (taking into account the threshold of 4 *MeV*) will be related to the maximum energy of the beam, according to the SRIM code [175]. This technique is called *Nuclear Activation Imaging Spectroscopy* (NAIS) [165].

Charged Particle diagnostics

Generally, during the interaction between a very high intensity laser pulse, greater than 10^{18} W/cm^2, electrons are pushed forward by the ponderomotive force, acquiring energies ranging from hundreds of keV to hundreds of MeV. Depending on the acceleration mechanism, such as Wakefield acceleration, they can also reach energies of several GeVs. Secondary processes see the acceleration of protons and heavy ions to energies of the order of hundreds of MeVs, but also the production of X–rays to energies of the MeVs–order, positrons for the pair production effect, and finally neutrons for nuclear reactions [165]. In the following paragraph it will be described some of the techniques most commonly used in the diagnosis of charged particles emitted by plasmas generated by ultra–short laser pulses.
Electron diagnostics is very important for the characterization of laser–generated plasmas, because it is a direct consequence of the absorption of laser beam. There are several ways to study the electronic population of plasma. As these particles are charged, one study passes through deflection by electric and/or magnetic fields and their revelation by a final detector. Often as a detector is used an image plates, i.e. a device based on the luminescent excitation of the material that constitutes it, which when subjected to the radiation of electrons transits in a metastable state emitting photons in the visible spectrum. An example of such spectrometers will be discussed in the Section 4.3.4.
Moreover, important information about the relativistic plasmas can be given by the positron detection. However, as a result of the small flow due to the rarity of events, the positron signal is often confused with the background. One possibility is to use compact permanent magnets with a nuclear emulsion track detectors (which will be discussed in more detail in the Section 4.1.4), to allow the separation of positrons from electrons and the ion component according to the applied field [176].

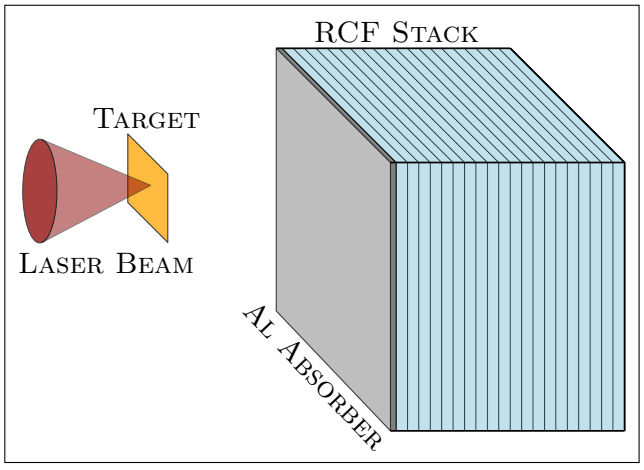

Figure 4.6: *Representation of experiments with RCF stack to light ions detection.*

Energetic protons may emerge from any type of material; they are always present as impurities in the targets' surface layers in contact with the ambient air. A very current and efficient technique is *Radiochromic film Imaging Spcetroscopy* (RIS). It can completely characterize the beam of protons, not only resolved in energy but also spatially resolved. Thus, three–dimensional distributions of protons can be obtained (x, y, E). The detectors used are *Radiochromic Film* (RCF), and the most common used are Grafchromic (of which more details will be given in the Section 4.1.3).

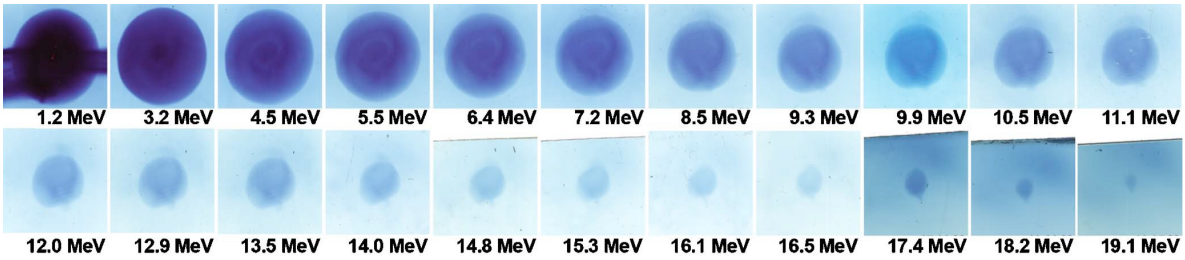

Figure 4.7: *RCF stack for proton detection at TRIDENT laser facility in New Mexico. Here, 19 films of HD–810 and 3 films of MD–55 type are exposed to the proton beam obtain from a gold foil irradiated by intensity laser of* 2×10^{19} *W/cm*^{2}*, (image reprinted from ref [178]).*

Using RCFs in stack configurations, as shown in the Figure 4.6, resolved energy measurements are possible. In this way, protons with lower energy will be stopped in the beginning layers, while protons with more energy will pass through these layers and will be stopped in the deeper RCFs, according to the stopping power of the particles [177]. Thus, each RCF can be attributed to an energy bin corresponding to an average proton energy, as in a histogram. The fraction of energy deposited by high energy protons in the first layers is small compared to the Bragg peak, but must be taken into account when calculating the number of protons for each film. An example of the proton signal in an RCF stack is shown in the Figure 4.7, obtain at TRIDENT laser facility in New Mexico [178].
The optical density is read out from a photodensimeter and it is correlate to the ions' energy released into the detector. Sometimes track detectors can be used instead of RCF, but this is not convenient due to high reading times (a few hours for each film), the limited detectable energy (protons above 10 *MeV* cause too little damage into device) and others [165].
Finally, the ions are also accelerated by the longitudinal electric field developed after the separation of charges between hot electrons and positive target surface layers (usually only the lightest ions). These can be detected by magnetic and/or electrical deflection devices, such as the Thomson Parabola Spectrometer (TPS, presented in the Section 4.1.2), Gafchromic films (discussed in the Section 4.1.3), track detectors (Section 4.1.4), and also by flight time measurements using Ion Collector or silicon carbide based devices (Section 4.1.5). In the following paragraphs, these devices are explained in detail; then their application to laser–generated plasmas is reported and discussed.

4.1.2 The Thomson Parabola Spectrometer

High-intensity lasers are able to accelerate protons and light ions up to tens of *MeV*, as already discussed. The ions of plasma are accelerated simultaneously, originating not only from the material that composes the target, but also from contaminants within it, such as hydrogen, absorbed in each material. Therefore such ion sources are typically multi–species,

and the question that arises to the spectrometers is the discrimination and separation between the various charged species. A useful device employed for this purpose is the *Thomson Parabola Spectrometer* (TPS), able to separate the ions according to their mass–to–charge ratio, and also have information on the energies of the charged particle beams that escape from the target, as a result of interaction with the high–intensity laser ($> 10^{16}$ W/cm^2).

In Figure 4.8 is reported a TPS schematization for a plasma analysis in TNSA regime. In sequence, right after the target, a collimation system is placed, consisting of two or more pinholes (to collimate the particle beam and increase the resolution, but at the expense of a decrease in signal intensity); the central part of the TPS are the magnetic and electric fields, able to deflect the ion beam just collimated, which moves along the *z–axis*. Finally, there is a detector after the fields, for images display, which can be of various nature as we will see, for example a MicroChannel Plate (MCP) coupled with a phosphor screen, Gafchromic film, track detectors and others. The images may not be latent, depending on the detector employed, as well as image storage system is used a normal camera, or even more complex systems of image acquisition.

Let's take into account a positively charged particle, with mass indicated by m and charge by $q = Ze$, which moves along the *z–axis*, with the velocity v_z. The deflections due to the magnetic field, indicated with B, and to the electric field, indicated with ξ, occur in the plane z–x and z–y respectively, as you can see in Figure 4.8. In other words, the ions are deflected in the horizontal plane by the magnetic field and in the vertical plane by the electric field.

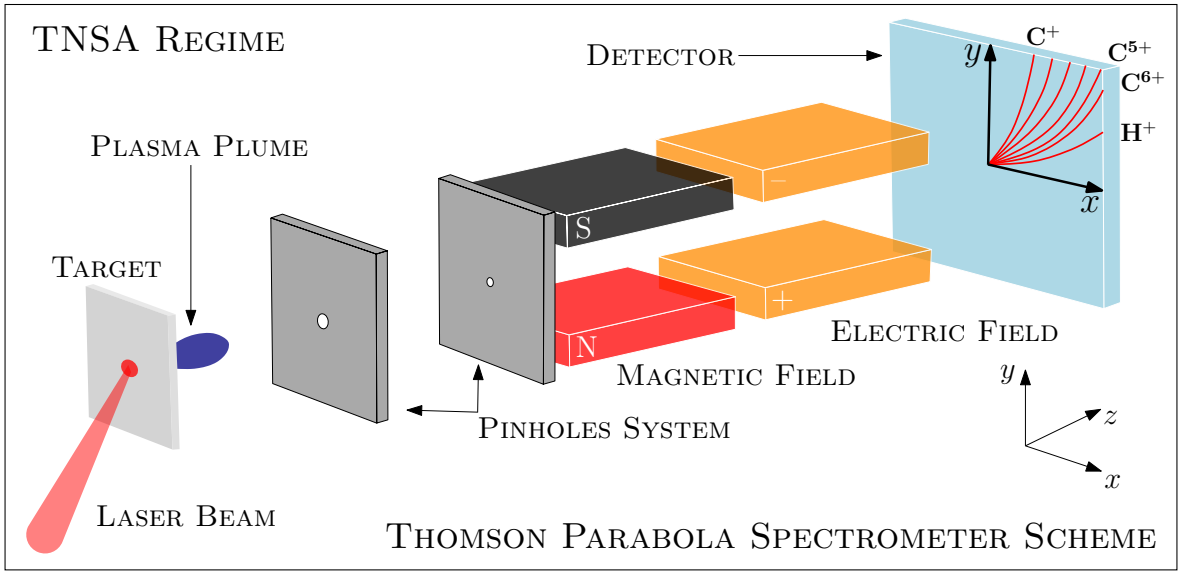

Figure 4.8: *Schematic diagram of a Thomson Parabola Spectrometer for the diagnostics of pulsed lasers–generated plasmas by irradiating thin carbon and hydrogen foil.*

By indicating with ℓ_B and ℓ_ξ the length of the two fields (magnetic and electric) in the *z–axis* direction respectively, and taking into account the distance between the magnetic or electric field and the detector, d_B or d_ξ respectively, the laws of deflection along the x and y directions will be the following:

$$x = \frac{qB\ell_B}{mv_z}\left(\frac{1}{2}\ell_B + d_B\right) \tag{4.6a}$$

$$y = \frac{q\xi\ell_\xi}{mv_z^2}\left(\frac{1}{2}\ell_\xi + d_\xi\right) \tag{4.6b}$$

In truth, the motion along *z–axis* is not really uniform, since the particle velocity changes due to the rotation induced by the magnetic field: for the development of this treatment we are therefore assuming that the displacement is small. By making explicit y as a function of x through the particle velocity v_z^{-1}, this is obtained:

$$y = \frac{m}{q}\frac{\xi}{B^2}\frac{\ell_\xi}{\ell_B^2}\left(\frac{1}{2}\ell_B + d_B\right)^{-2}\left(\frac{1}{2}\ell_\xi + d_\xi\right)x^2 \tag{4.7}$$

Therefore, the points' location where ions, with the same mass–to–charge ratio, impact by detector is a parabola, as observed by the Equation 4.7. As the mass or charge varies, a series of parabolas will be observed, which are shifted according to Equation 4.7. Knowing the coordinates x and y of a point in the parabola, with respect to the center of the ion source, it is possible to determine the particle energy value of the point pair considered (proportional to the velocity v_z), by means of Equation 4.6a and Equation 4.6b. In particular, if the x and y coordinates used to solve the problem are those of the parabola starting point, we will have information on the maximum velocity, and of course energy, of the ions deflected by the magnetic and electric fields [179].

Spatial Resolution

The collimator system plays a fundamental role in terms of the TPS spatial resolution. Usually these devices use a two pinholes system, where the second is placed downstream of the fields, which leads to a simplification in the treatment of the TPS spectrograms.
The main aim of a TPS is to separate the ions of a beam according to their mass–to–charge ratio. However, the ability to discriminate the charged species that are part of a plasma depends on the thickness of the parabola recorded on the detector. In practice, unfortunately, it is not possible to produce infinitely narrow parabolas because of the collimation procedure that uses holes with a finite diameter. The width of a parabola, on the reading device, can be estimated through a geometric procedure. By indicating with D_1 and D_2 the diameter of the first and second pinhole respectively, with L_1 and L_2 the distance between first and second pinhole and between second pinhole and detector respectively, as shown in the Figure 4.9,

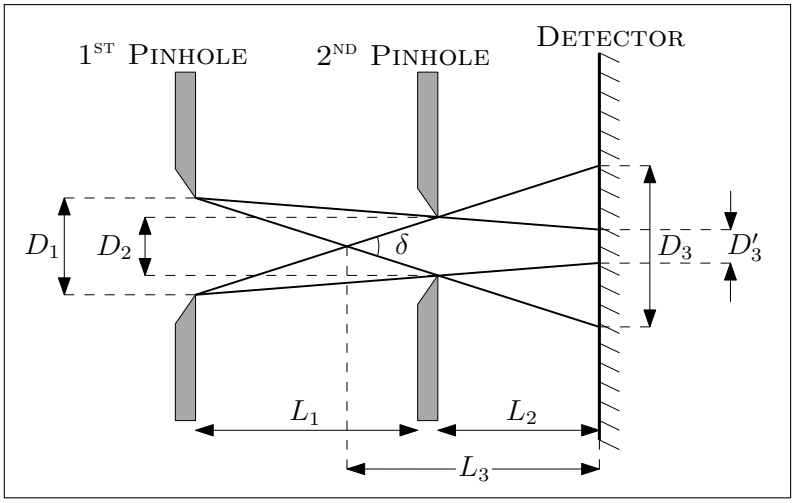

Figure 4.9: *Geometric representation of the beam collimation through a system of two pinholes, and image formation on a detector; where D_3 and D'_3 represent the diameter of the beam spot and of the peak intensity spot, respectively.*

the width of the parabola on the detector can be explained as follows [180]:

$$D_3 = D_2\left(1 + \frac{L_2}{L_1}\right) + D_1\frac{L_2}{L_1} \tag{4.8}$$

The width of the parabola D_3 corresponds to a subtended angle, δ, calculated by the following relation:

$$\delta = \frac{D_3}{L_3} \tag{4.9}$$

where L_3 is the distance at which the beams reaching the end of the spot D_3 intercept each other, as shown in Figure 4.9. It is therefore clear, that if the angle of deflection of two ion beams is less than the angle δ, the parabolas cannot be separated at the detector plane. Thus, δ is namely as *collimation resolution angle*.
The equations introduced up to now only take into account geometric considerations due to the two pinholes system. To analyze the charge resolution, let's consider a ion beam made up of a single species, having different charge states. Two parabolas on the TPS spectrogram, will be said to be resolved when the separation between the centers of them is greater than their width along that line, as shown in Figure 4.10a. In mathematical terms, what has just been said, means the following formulation [181]:

$$\Delta\theta_B > \delta\left(1 + \frac{\theta_B^2}{4\theta_\xi^2}\right)^{1/2} \qquad \& \qquad \Delta\theta_\xi = 0 \tag{4.10}$$

By indicating with θ_B and θ_ξ and the magnetic and electric deflection angles respectively,

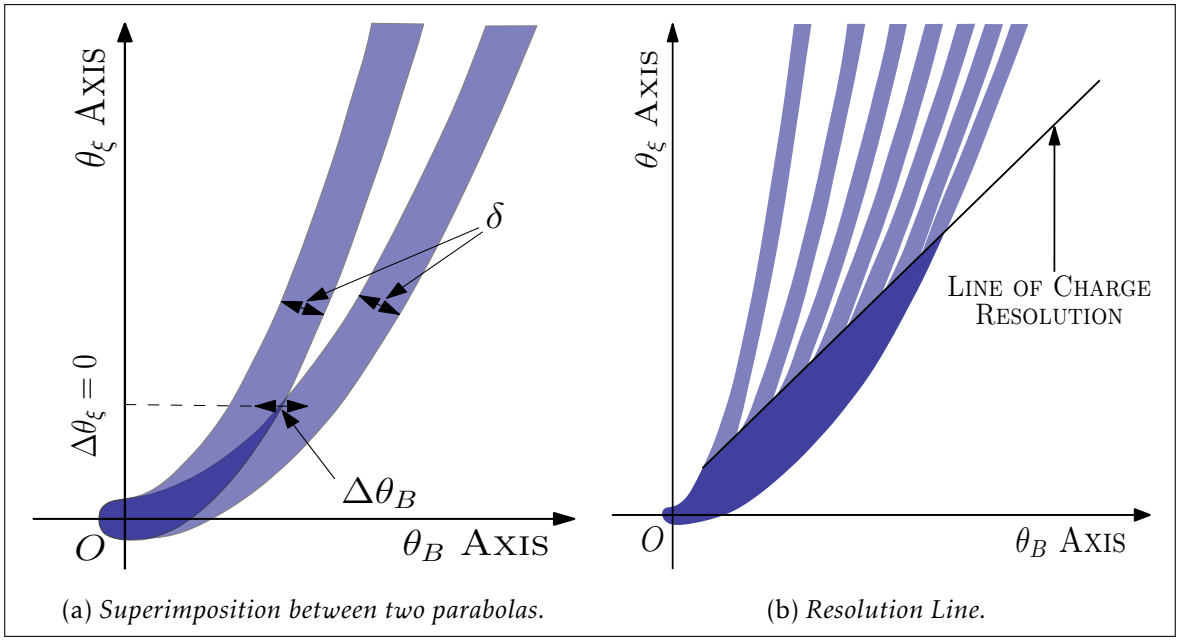

(a) *Superimposition between two parabolas.* (b) *Resolution Line.*

Figure 4.10: *Qualitative illustration of charge resolution, at TPS detector plane, for an ion species with different charge states.*

also given by the following equations [181]:

$$\theta_B = \frac{q \int B \, d\ell}{p} \tag{4.11a}$$

$$\theta_\xi = \frac{q \int \xi \, d\ell}{2E} \tag{4.11b}$$

where q represents the charge of the considered ion, B and ξ are the magnetic and electric fields, p and E are the momentum and energy of the particles respectively. The magnetic and electric fields are integrated along the ion path length. Through mathematical observations, the equation of the line below which the parables are no resolved will be as follows [181]:

$$\theta_\xi = \left\{ \left[4 + \left(\frac{k}{\delta} \right)^2 \right]^{1/2} - 2 \right\}^{-1/2} \theta_B \tag{4.12}$$

where k is worth:

$$k = \frac{q}{m} \frac{\left(\int B \, d\ell \right)^2}{\int \xi \, d\ell} \tag{4.13}$$

The straight line introduced in the Equation 4.12, is illustrated in Figure 4.10b. As can be seen from the example, above this line the parables are separated from each other, while on the contrary, below them they are not resolved; for this reason this line is called *line of charge resolution* [181].

TPS Spectrogram

Collimated ion beam, after passing through the pinholes system, reaches the region where the magnetic field is located, orthogonal to its motion, which deflects it along the *x–direction* (*x–z plane*). Following the magnetic field, there is the region where the electric field is active, also orthogonal to the beam motion, which deflects the charged particles in the *y–direction* (*y-z plane*). After this, ions travel through a free flight space, and then impact on the detector forming different parabolas according to their mass–to–charge ratio. Parabola equation is given by the composition of the motion along the x and y directions (*x–y plane*, shown in Equation 4.7), as reported in the Figure 4.11a.
The Figure 4.11a shows a typical theoretical spectrum obtained from a carbon and hydrogen ion beam deflected by a TPS. From mathematical analysis of the magnetic and electric deflection laws, it can be deduced that a TPS spectrogram has the following peculiarities:

- the position of points intersecting the line parallel to the magnetic deflection axis, have a constant value of energy–to–charge state ratio;
- the place of points intersecting the line parallel to the electrical deflection axis, have a constant value of momentum–to–charge state ratio;
- the place of points intersecting the line which have an angular coefficient other than zero and that passes through the origin, are characterized by the same ions velocity.

It is clear that the origin of the reference system must always be placed in the region where the neutral particles impact on the detector; these form a halo, more or less large, depending on the collimation system chosen. The distance between the beginning of a parabola and the point where photons or neutral particles hit the detector, is indicative of the maximum energy possessed by the ion.
The Figure 4.11b shows an experimental spectrogram [182], obtained at the *Prague Asterix Laser System* (PALS) laboratory in Prague, using a laser of intensity $\sim 10^{16}\ W/cm^2$ to irradiate a target of deuterated polyethylene (–CD_2–), in the TNSA regime. The laser has a fundamental wavelength of 1.315 μm, a maximum pulse energy of 500 J and a duration of 300 ps; this hits the target with a spot of 80 μm in diameter, forming an angle of 0° with respect its normal. The ions emitted by the plasma are analyzed by a TPS and other kinds of detectors placed at various angles [182].
The TPS for the spectrogram acquisition consists of two pinhole for input ion collimation; the first has an aperture of 1 mm in diameter, and the second, 10 cm away from it, has a diameter of 100 μm. At a distance of 5 mm from the latter there are the magnetic plates, 8 cm long. The magnetic field applied can vary from 0.01 p to 1 T. The electric plates, placed in

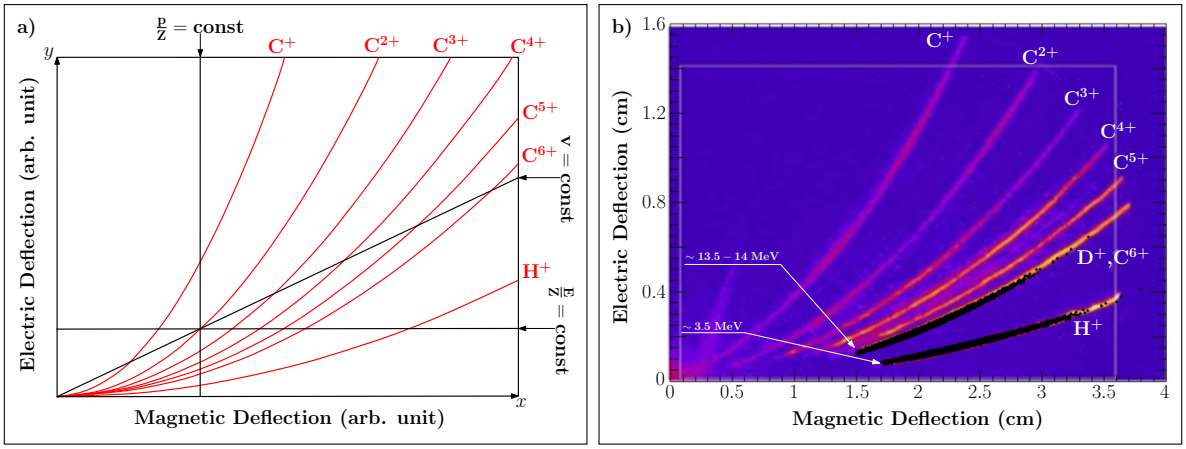

Figure 4.11: *Illustration of a typical TPS spectrogram obtained from a beam of carbon and hydrogen ions (a). TPS experimental spectrogram obtained at PALS laboratories in Prague, irradiating a target of deuterated polyethylene by a laser at 10^{16} W/cm^2 intensity order (image from the ref [182]); the overlap of the experimental spectrum and the simulation is performed by COMSOL software for protons and C^{6+}–ions (b).*

succession to the magnetic ones, have an extension of 8 *cm* and the value of the electric field can be varied between 1 *kV/cm* and 3 *kV/cm* by changing the potential of the electrodes. Finally, the detector is placed at a distance of 16.5 *cm* from the electric plates.

The simulation of the ion trajectory in the system of interest, carried out with COMSOL software, allowed to reconstruct the parabolas formed by the proton the 6+ carbon charge state on the detector (superimposed on the deuterium because of the same mass–to–charge ratio). The overlap between the parabolas obtained experimentally and those through simulation has permitted to recognize the ions that constituted the plasma and to have information about the maximum energies of these. For protons a maximum energy of about 3.5 *MeV* has been estimated, while for C^{6+}–ions the maximum energy was around 13.5–14 *MeV*.

As shown in this example, the TPS can be a very powerful tool and gives very fast information, both on the ions that compose a plasma and on their energies. The starting point for a good interpretation of a spectrum is always the parabola due to hydrogen ions, always present in any material, even as an impurity. In fact, protons are the least deflected on the electrical deflection axis because of its lower mass–to–charge ratio.

A limitation of this device can be better used for deflection of ions having energies higher than 500 *keV* per charge state, because at lower values the fields to be applied would be really too low. To have a more efficient collection of the less energetic ions, often the plates of the electric field are not perfectly parallel, but the negative one is placed at a certain angle, different from zero, with respect to the beam direction, to avoid as much as possible that the less energetic particles impact on it; for a more extensive treatment look at ref [183].

Detector for images display

Various kinds of detectors can be employed for the ion display after they have been deflected by the magnetic and electric fields. The most commonly used is the *Microchannel Plate* (MCP), because increasing current advantage, which is often very small due to the collimation system, and the possibility of real–time reading. Other detectors can also be used, such as GafChromics films, track detectors and others, but often require high doses and the reading of the device is done posteriorly.
The MCP is an assembly of many secondary electron multiplier miniature (like that treated in section 3.1.3), oriented parallel to each other. The typical diameters of the channels are in the range between 10 and 100 μm and have length–to–diameter ratios between 40 and 100. The channel axes generally form a small angle ($\sim 8°$) with respect to the input surface. The matrix of the channels is generally made up of lead glass, treated in such a way as to optimize the emission of secondary electrons, to make the walls of the channel semiconductor so as to allow charging by an external voltage source. Thus each channel acts as a dynode and the electrical contacts are provided by the deposition of a coating metal [184].
Figure 4.12a shows the simple mechanism of electrons multiplier. The kinematics is that κ^2 secondary electrons will be produced at second step, κ^3 at the third, and so on; overall the gain G will simply be $G = \kappa^n$. The secondary electron emission coefficient, κ , for leaded glasses reaches a value of about 2 for 300 eV incident electron energy. Clearly, if the trajectories of the electrons are almost parallel to the channels axes, there is a high probability that they will penetrate thoroughly before the primary interaction; this produces small gains. Positive ions have detection efficiencies similar to electrons [184]. The MCP is followed by a phosphor screen, as shown in Figure 4.12b, to display the ion traces. The resultant image is not latent and it is captured with an image acquisition system (e.g. a camera, or others).

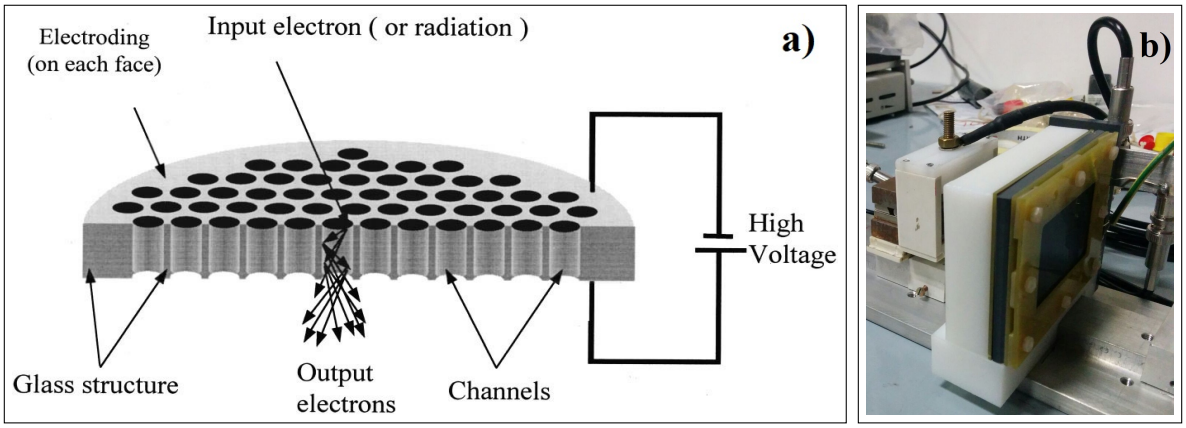

Figure 4.12: *Schematic of the electrons multiplication process in an MCP (a) (image from ref [185]); and photo of the MCP followed by a phosphor screen (b).*

4.1.3 Gafchromic film detector

GAFCHROMIC® films are radiochromic devices consisting of a thin active layer (varying from a few micron up to 30–40 μm), onto a polyester layer, typically Mylar, of thickness up to 100 μm. The active layer consists of a disubstituted di–acetylene emulsion (R–C≡C–C≡C–R', where R and R' are monovalent organic substitutes), which are a class of colorless monomer, above which is deposited a thin sheet of variable thickness ranging from a few hundred nanometers to several microns, which has the task of protecting the active layer below [186–188]. The layer structures for HD–810, MD–55–2 and EBT Gafchromics detector are shown in the Figure 4.13, while in Table 4.1 there are reported their material composition.

Table 4.1: *Composition of Gafchromics Detector Materials (from ref [189]).*

Material	Density (g/cm^3)	Effective Z	Element Composition (percentage by mass)				
			H	C	N	O	Other
Active Layer Emulsion (HD–810 & MD–55–2)	1.08	6.27	9.3	56.6	15.7	18.4	
Active Layer Emulsion (EBT)	1.1	7.05	9.4	57.4	13.2	16.4	0.8 Li; 2.9 Cl
Surface Layer	~ 1.2	9.90	6.5	32.3	21.6	20.5	2.3 Li; 16.8 Cl
Clear Polyester	1.35	6.64	4.2	62.5		33.3	
Adhesive	~ 1.2	6.26	9.4	65.6		24.9	3.5 S; 15.1 Ba

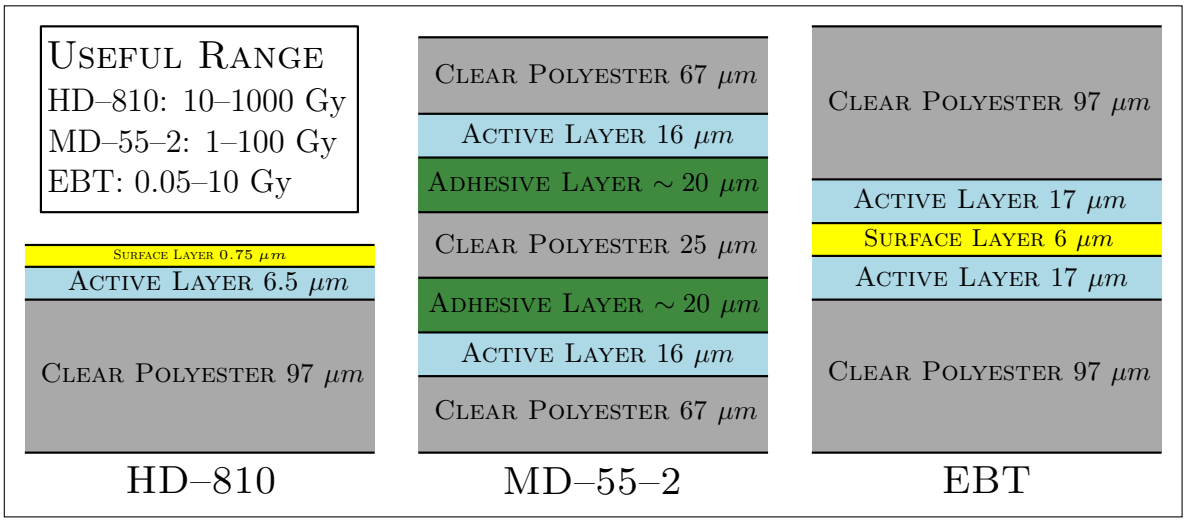

Figure 4.13: *Structures and useful ranges of HD–810, MD–55–2 and EBT Gafchromics films models; (values from ref [189]).*

The emulsion of the active layer, initially colorless, undergoes a polymerization process that induces a stable color, in blue shades, when an ionizing radiation[1] passes through the device. From the color intensity it is possible to determine the absorbed dose[2] of the device, therefore the energy of the incident radiation, since the quantity of produced polymers is proportional to the released energy.
The signal information obtained from an irradiated Gafchromic film is extrapolated through light transmission measurements. The transmission of light through a device is usually calculated as a fraction of the light intensity passing through the body, I_t, over the total light intensity sent on the body, I_0. However, the relationship between transmission and absorbed dose is inversely proportional and non-linear for many readout systems. Thus, it is preferable to use absorbance, or optical density (OD), defined as the ten-base logarithm of the inverse transmission:

$$OD = \log_{10}\left(\frac{I_0}{I_t}\right) \tag{4.14}$$

where the optical density is expressed in absorption units (AU). Thus, for example an optical density of 1 AU corresponds to a 10% of light transmission, an $OD = 2$ AU corresponds to a 1% of light transmission, and so on. However, it should be noted that the optical density depends on the wavelength at which it has been sampled; that is, as the light wavelength used by the readout instrument varies, different values of transmission, and therefore of absorbance, can be obtained. This means that the optical density measured for a irradiated radiochromic film is unique only if the sampling is done by a known wavelength or if the spectrophotometer[3] uses a monochromatic light source [189].
There are different kinds of Gafchromic that change in composition and internal structure, and in dose range where they can be used. In this discussion three examples of radiochromic devices are reported, namely HD–810, MD–55–2 and EBT Gafchromic film, whose layer structure and composition is shown in the Figure 4.13 and Table 4.1. In particular, the attention is focused more on the HD–810 because of their wide dose range in which they are available, Figure 4.13, which make them suitable to others when dealing with high energy particles emitted by plasmas in TNSA regime.
Gafchromic HD–810 was the first product introduced for dosimetric purposes. They consist of an active emulsion layer of the nominal thickness of 6.5 μm coated onto a polyester base of the nominal thickness of 97 μm. Above the active layer a protective material is inserted with a nominal thickness of approximately 0.75 μm. HD–810 films can be used in dose ranges from 10 to 1000 Gy. The emulsion of this Gafchromic film exhibits two main absorption

[1] This is an electrons, ions or electromagnetic radiation that carries enough energy to detach electrons from atoms or molecules, thereby ionizing them.
[2] The absorbed dose is a measure of the energy deposited by a ionizing radiation into a irradiated medium per unit of mass. The International System unit of measure is the Gray (Gy), defined as $J{\cdot}kg^{-1}$.
[3] It is a device that can measure the light beam intensity transmitted as a function of the wavelength sent on the sample. The most important features of spectrophotometers are spectral bandwidth, the percentage of transmitted light, the absorption, and sometimes a percentage of reflected light.

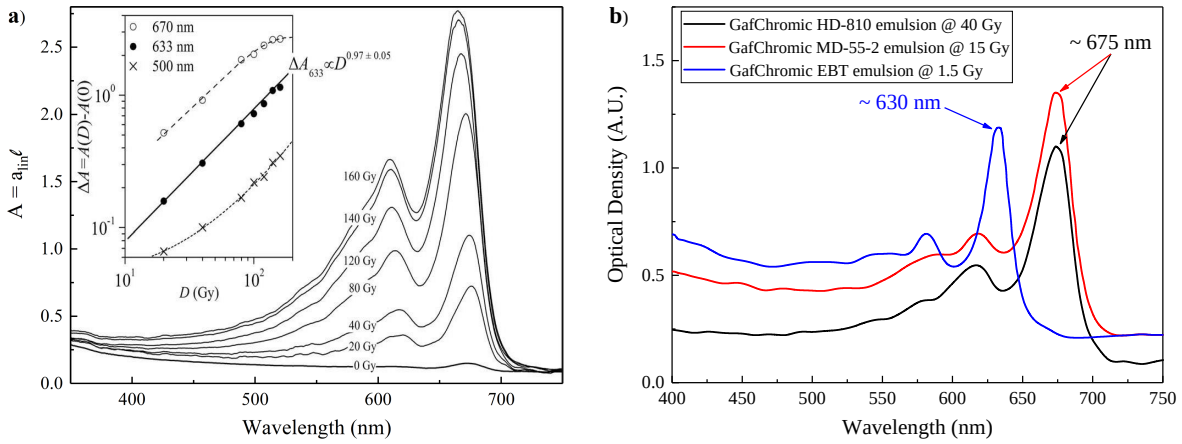

Figure 4.14: *Linear absorbance at room temperature $A = a_{lin}\ell$ (where a_{lin} is the linear absorption coefficient and ℓ the length of the absorbing medium) for Gafchromics HD–810 films at various doses D. The inset shows the dose dependences dependence of the linear absorbance difference, $\Delta A = A(D) - A(D = 0)$, at 500, 633 and 670 nm wavelength (a) (image from ref [188]). Typical absorbance spectra for HD–810, MD–55–2 and EBT Gafchromic films at different dose values (spectra from ref [188, 189]).*

bands in the spectrum around 615 *nm* and 675 *nm* as shown in the Figure 4.14a. The exact location depends on a number of factors, such as the amount of absorbed dose, the type of radiation and irradiation, storage and temperature reading that affects the crystalline structure. When using a light wavelength close to the absorption band to read the device, such as a He/Ne–laser (633 *nm*) or a diode laser (650–670 *nm*), the relationship between absorbance and absorbed dose remains fairly linear up to high doses (hundreds of Gray), as shown in inset of Figure 4.14a [188, 189].

On the other hand, MD–55–2 detectors consist of two 16 *μm* thick emulsion layers, sandwiched between 67 *μm* thick polyester and separated by a nominal thickness of about ~ 20 *μm* of adhesive material and a single 25 *μm* thick nominal centered polyester layer. The dosimetric range of applicability of the latter ranges from 1 to 100 *Gy*. The main advantage of this film compared to the HD–810 model, in addition to the sensitivity, is the ability to use the film immersed in water. Finally, EBT Gafchromic films consist of two layers of EBT–emulsions (different from the one used for HD–810 or MD–55–2), each about 17 *μm* thick, sandwiched between 97 *μm* thick polyester layers and separated by a nominal 6 *μm* surface layer. The emulsion used for these devices produces an increase in sensitivity of an order of magnitude. EBT detectors can be used in dose ranges from 0.05 to 10 *Gy*.

Finally the Figure 4.14b shows the comparison between HD–810, MD–55–2 and EBT films, irradiated with different dose amounts. The EBT Gafchromic emulsion shows an absorbance peak at lower wavelengths than those of the red spectrum region, in contrast to HD–810 or

MD–55–2. The main band in this case exhibits a peak around $\sim 630\ nm$, also in this case depends on a number of factors [188, 189].
The main advantages of using radiochromic films are the possibility of having a high spatial resolution, wide dynamic range (depending on the device used), relatively low spectral variations in sensitivity and no need for chemical processing. These factors make them suitable for the study of high energy particles emitted by short laser pulses–generated plasmas.

4.1.4 Track Detector

Laser–generated plasmas in the TNSA regime can be investigated using devices that record the high–energy particle trace, which can be placed for example after a deflection system such as the TPS. A high–energy ion is able to ionize the medium through which it is passing, transferring energy to the electrons and damaging the molecules along its path. The devices, which through a chemical etching process in a strong acid or base solution, are called *Track detectors*. The advantage of these devices is their simplicity of use and low cost [190].
It should be noted that these detectors have an intrinsic threshold, since for each particle there is a minimum value of the specific energy loss[4] before the damage is enough to cause an etchable trace. This fact determines a specific energy interval for each ions, as shown in

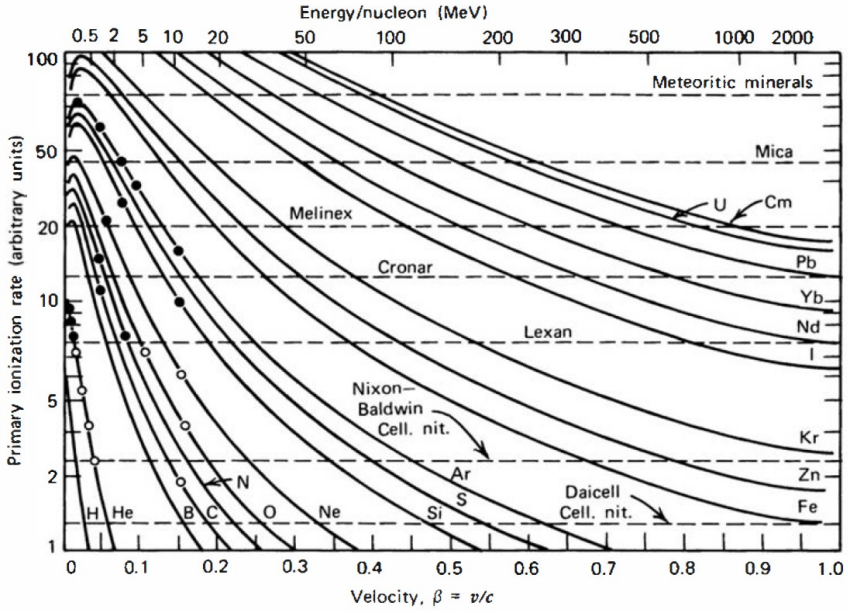

Figure 4.15: *Relative ionization rate as a function of ion energy per nucleon or velocity for lighter and heavier species. Horizontal dashed line indicate the minimum damage for 100% of tracks recording in various kind of track detectors; CR–39 dashed line is below that of Daicell, cellulose and nitrate (image reprinted from ref. [190]).*

[4]Specific Energy Loss refers to the charged particle's energy lost per unit of path by collision and radiative processes when it passes through a medium. In mathematical terms the specific energy loss or Stopping Power S, for an energy ion E that travels a path x within a medium will be: $S = -dE/dx$. Stopping power is given in J/m or in $keV/\mu m$. For a more exhaustive discussion see ref [177].

Figure 4.15; this reports the relative ionization rate as a function of ion energy per nucleon or velocity and the dashed line indicate the minimum damage for 100% of tracks recording in various kind of track detectors. Two of the most used track detectors are CR–39 and PM–355, which are both based on polyallyldiglycol carbonate (PADC), i.e. a plastic material.

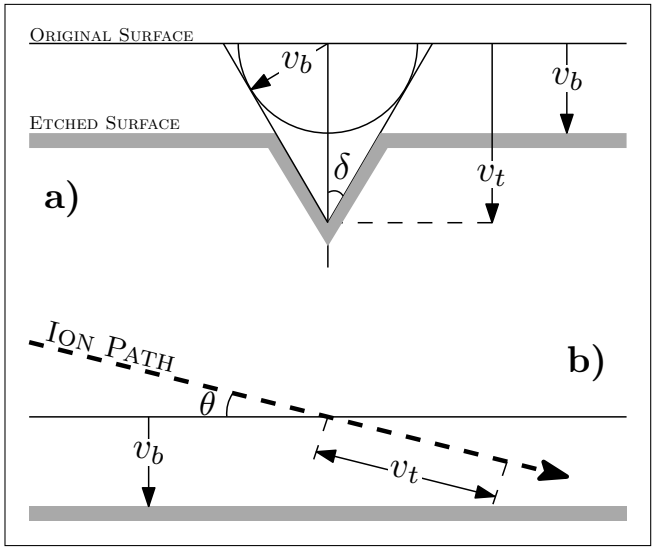

Figure 4.16: *Scheme of the chemical etching of a track detector, in which the normal surface is removed at a velocity v_b and the damaged track at a velocity v_t (a), and not revealed track due to particle angle incidence less than critical angle (b).*

A simplified model to explain the erosion behaviour of a track detector due to etching processes is shown in the Figure 4.16a. Let's assume, first of all, that the ion has created its track by normal incidence to the target surface, and the etching velocity is constant in that direction, indicated with v_b. We can also assume that the erosion velocity along the track, indicated with v_t is greater than v_b. In these conditions, a cone-shaped pit is formed, with the axis along the damaged track. In a more complete and exhaustive model it is necessary to take into account several important aspects, such as the change of the etching rate due to the depletion of the etching solution, or the degree of damage to the track, and so on [190].

The development of the track is governed by the law v_b/v_t; its formation is possible only if this ratio is less or equal to 1. It is possible to demonstrate that the ions incidence angle must exceed a critical angle, δ_c, in order to avoid its disappearance as a result of the etching process, as shown in Figure 4.16b. From geometrical consideration, the critical angle is:

$$\delta_c = \arcsin\left(\frac{v_b}{v_t}\right) \tag{4.15}$$

For example, in polyester materials, the critical angle track detection is about 5–15° [190]. Due to the variability of the etching rate and the energy loss threshold of the incident ions, the etching behaviour must be demonstrated in advance of any measurement, using a calibrated source of the same type and energy of particles involved in the measurement.
Several factors can change the etching rate of a track detector. For example, in Figure 4.17a is reported the calculation of the thickness reduction as a result of etching a CR–39 with sodium hydroxide (NaOH) at different temperatures, ranging from 50°C to 80°C [191]. The

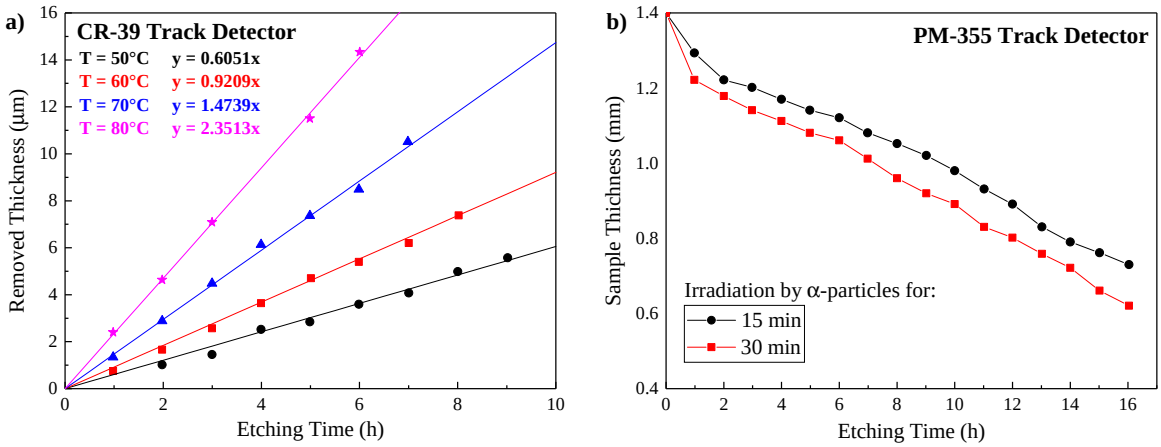

Figure 4.17: *CR–39 track detector removed thickness as function of etching time at different temperature, ranging between* $50 \div 80°C$ *(a) (image from ref [191]). PM–355 track detector thickness decrease as function of etching time at different dose irradiation (b) (image from ref [192]).*

etching rate, which is represented by the slope of the lines in the figure, varies from ~ 0.6 to ~ 2.4 $\mu m/h$. In other words, heating the etching solvent results in the fastest thinning of the detector. There is also a dependence of the etching rate on the dose absorbed by the detector. Figure 4.17b shows the study of a PM–355 exposed to different doses of alpha–radiation [192]. It is noted that the etching rate is faster in the case of higher absorbed radiation doses (the thickness of the track detector is more reduced at the same etching time when the absorbed dose by device is higher).

However, when dealing with the detection of several ion species with the same device, the so–called *depth dependence* must be taken into account. This indicates the different depths in the detector at which charged particles are stopped. This type of effect is most evident when light and heavy charged particles are detected with the same device [193–195].

4.1.5 Silicon Carbide Detector in TOF approach

In the last decade, *Silicon Carbide* (SiC) detectors have been increasingly used in diagnosing plasmas generated by long or short laser pulses. These devices are used in TOF–technique approach, to obtain information on the emitted plasma ions, but also on X–rays and fast electrons (typically in the picoseconds–nanoseconds scale). The really attractive aspect of SiC is that they are not sensitive to the visible or infrared light component. This aspect is due to the large band–gap, which is 3.26 eV for the 4H–SiC (where 4H identifies the hexagonal type crystalline structure). To form an electron-hole pair, a particle that interacts with the detector must spend 7.78 eV of its energy; this process generates a voltage signal that appears on electrodes, which is related to the energy released by the incident radiation.

Table 4.2: *Main SiC property at room temperature (from ref [196]).*

Property	4H–SiC	3C–SiC	6H–SiC
Crystal Strucure	Hexagonal	Zinc-blende	Hexagonal
Band Structure	Indirect	Indirect	Indirect
Energy Gap (eV)	3.26	2.20	2.86–3.03
Electron Mobility ($cm^2/V\ s$)	800–1000	1000	370–600
Hole Mobility ($cm^2/V\ s$)	100–115	50	50
Breakdown Electric field (MV/cm)	2.2–4.0	1.2	2.4–3.8
Thermal conductivity ($W/cm°C$)	3.0–5.0	3.0–5.0	3.0–5.0
Saturation velocity ($\times 10^7 cm/s$)	0.8–2.2	2.0–2.7	2.0
Relative dielectric constant	9.7	9.7	9.7
Max working temperature ($°C$)	1240	1240	1240
Melting point ($°C$)	1800	1800	1800
Electron–hole pair Energy (eV)	7.78		
Hole lifetime (s)	6×10^{-7}		
Density (g/cm^3)	3.21	3.21	3.24
Physical stability	Excellent	Excellent	Excellent
Atomic weight	44	76	46
Lattice constant (Å)	$a = 3.07\ c = 10.05$	4.36	$a = 3.07\ c = 15.12$
Electron affinity (V)	3.08	3.83	3.34

In Table 4.2 there are shown some of the most significant values of the SiC detectors that can be used to diagnose laser–generated plasmas analysis [196].

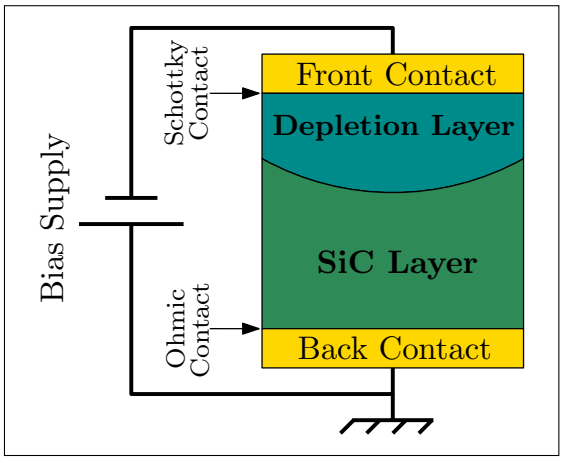

Figure 4.18: *Representation of a Silicon Carbide Detector structure.*

The structure of a SiC detector is shown in Figure 4.18. A lightly doped n^- layer of silicon carbide (with a doping concentration of $\sim 10^{14}\ cm^{-3}$) is grown epitaxially onto an n^+ 4H–SiC doped substrate (with a doping concentration of $\sim 10^{18}\ cm^{-3}$). A metallization coating (ranging from 20 to 200 *nm*) is created over the n^- SiC doped layer, in order to form a metal–to–semiconductor junction. This junction forms an electron potential barrier, called *Schottky barrier* [197], which has rectifying characteristics and is suitable for use as a diode. Finally an ohmic contact is formed backside to the substrate n^+ SiC, in order to connect the device to ground [198].

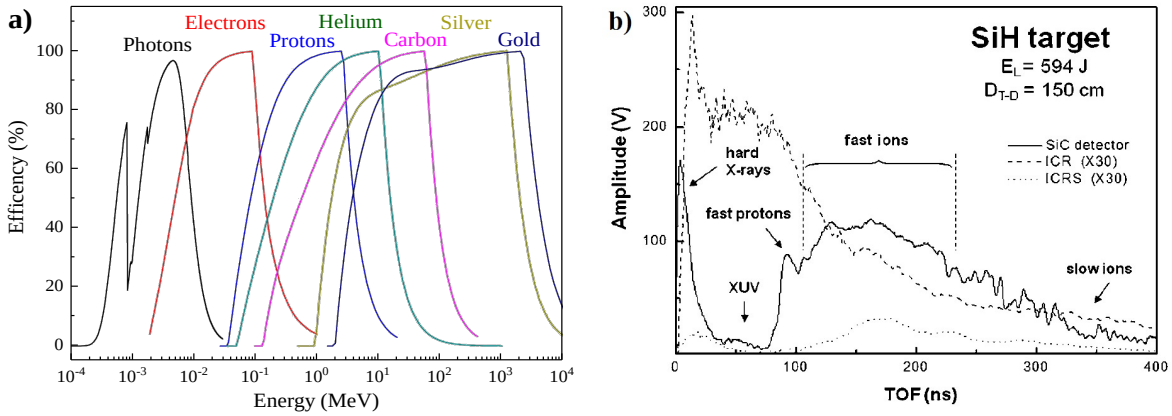

Figure 4.19: *SiC detection efficiency as function of photons, electrons and different ions energy (a) (image from ref [199]); comparison of TOF spectra of SiC detector, ICR unshielded and ICRS shielded detectors obtained by laser–irradiating SiH target (b) (image from ref [200]).*

SiC detectors work in reverse bias voltage in order to reduce the dark current, and increasing the depletion region that extends within the n^- type doped layer. The latter can be controlled by changing the applied reverse bias; it ranging from 10 μm up to 80 μm when the voltage is about 600 V [199]. The thickness of the metallization and the width of the depletion layer are two key parameters to define the window of detectable energies for incident particles. In fact, if not properly set, particles could be stopped in the metallization (without producing any electron–hole pair), or they could pass through the depletion layer, stopping outside it. SiC Schottky diode may provide an efficiency of 100% for charge collection as shown in Figure 4.19a. Here, the detection efficiency for the radiation energy of photons, electron and different ions, is calculated for a SiC detectors with a Schottky contact 200 nm thick, made of Ni_2Si obtained by sputtering and a thermal process, grown onto a 4H–SiC epitaxial layer 80 μm thick with 10^{14} cm^{-3} dopant concentration. The substrate is a n–type highly doped 4H–SiC, covered on the back side with a 200 nm thick Ni_2Si film, in order to create a ohmic contact. The voltage is set to -200 V in order to have a reverse current of 80 pA [199].
Figure 4.19b [200] shows a comparison of a TOF measurement by SiC or IC detectors. ICR detector have a poor discrimination of the different ion contributions, due to its response to the XUV component of the plasma. When a thin aluminium absorber is placed in front of detector (ICRS), TOF spectrum shows a reduction of the XUV peak, better ions discrimination, but low intensity. SiC detector allows a high attenuation of the plasma–emitted UV and soft X-ray radiation (XUV) due to its wide band–gap.
Silicon Carbide detectors have desirable characteristics such as radiation hardness, application at high temperature, fast signal collection time, room temperature work with low dark current, high signal–to–noise ratio, very high detection efficiency, high energy gap, and controllable depletion layer thickness [196, 201].

4.2 Ion energy enhancement in TNSA regime

Published Paper[2019]

Protons accelerated in the Target Normal Sheath Acceleration regime by a femtosecond laser

L. Torrisi[1], M. Cutroneo[2], A. Torrisi[2], L. Silipigni[1], G. Costa[1], M. Rosinski[3], J. Badziak[3], J. Wołowski[3], A. Zaraś–Szydłowska[3] and P. Parys[3]

[1]*Dipartimento di Scienze Fisiche, MIFT, Università di Messina, V.le F.S. D'Alcontres 31, 98166 S. Agata, Messina, Italy*
[2]*Nuclear Physics, Institute, CAS 25086, Řež, Czech Republic*
[3]*Institute of Plasma Physics and Laser Microfusion (IPPLM), Warsaw, Poland*

Published as: L. Torrisi, M. Cutroneo, A. Torrisi, L. Silipigni, G. Costa, M. Rosinski, J. Badziak, J. Wołowski, A. Zaraś–Szydłowska and P. Parys: "Protons accelerated in the Target Normal Sheath Acceleration regime by a femtosecond laser", *Physical Review Accelerators and Beams*, Volume: 22(2), Pages: 021302(1–7) (2019)

Available from: 10.1103/PhysRevAccelBeams.22.021302

Publication Date: Received 15 November 2018; Published 8 February 2019

There are many aspects involved in the acceleration of high–energy ions from laser–generated plasmas. In fact, this process depends not only on the intensity and wavelength of the laser employed, but also on the irradiation conditions, such as the distance of the laser beam's focal point from the target surface or the pulse shape, and on the composition and characteristics of the irradiated target [202, 203].
Advanced target can be employed for the enhance of the ions' energy [204]. As already seen in Section 1.3.2, energetic ions emitted from plasma are accelerated not directly by the laser fields, but by the longitudinal electric field due to hot electrons, heated by laser pulse. The longitudinal quasistatic electric field varies on a timescale comparable to the laser pulse duration and could be in similar magnitude comparable to fast oscillating laser fields, giving the ions significantly longer time to accelerate. From the equation of the maximum electric ions' acceleration field, given by Equation 1.75, it can be observed that electron density and plasma temperature play an important role in the determination of the maximum electric field driving the ion acceleration. The electron density may be increased by use of metallic heavy elements placed at the target surface, such as gold or tantalum, from which electrons can be accelerated by the laser electromagnetic pulse to relativistic velocity along forward direction. Thus, in this section, we take into account advanced targets based on thin films of graphene oxide covered by metallic layers have been irradiated at high laser intensity to investigate the forward ion acceleration in TNSA regime. In this way, it is expected an increase in the hot electron density, in the rear side of the foil, and a consequent increase in the driving electric field of ion acceleration, as it will be presented and discussed observing the experimental measurements [**205**].

4.2.1 Materials and Methods

A femtosecond Ti–Sapphire laser system (PULSAR) was employed for this experiment at IPPLM laboratory of Warsaw. It operates at 800 *nm* wavelength, 40 *fs* pulse duration, 300 *mJ* maximum pulse energy, p–polarized radiation, up to 10^{19} W/cm^2 intensity, with a minimum focal diameter of 10 microns. The focal position may be moved from −500 microns (in front of the target surface) to 0 μm (at the target surface), and up to +500 microns (inside the target surface) using a micrometric step motor controllable in high vacuum (10^{-6} *mbar*). The pulse contrast, i.e. prepulses and amplified spontaneous emission (ASE), was 10^{-8}. The laser was employed to study the TNSA forward ion acceleration at high intensity laser when thin foils are irradiated in normal incidence. Figure 4.20 shows a scheme and a picture (in the inset) of the experimental setup.

Foils of reduced Graphene Oxide (rGO), 7 μm thick, were employed due to its following

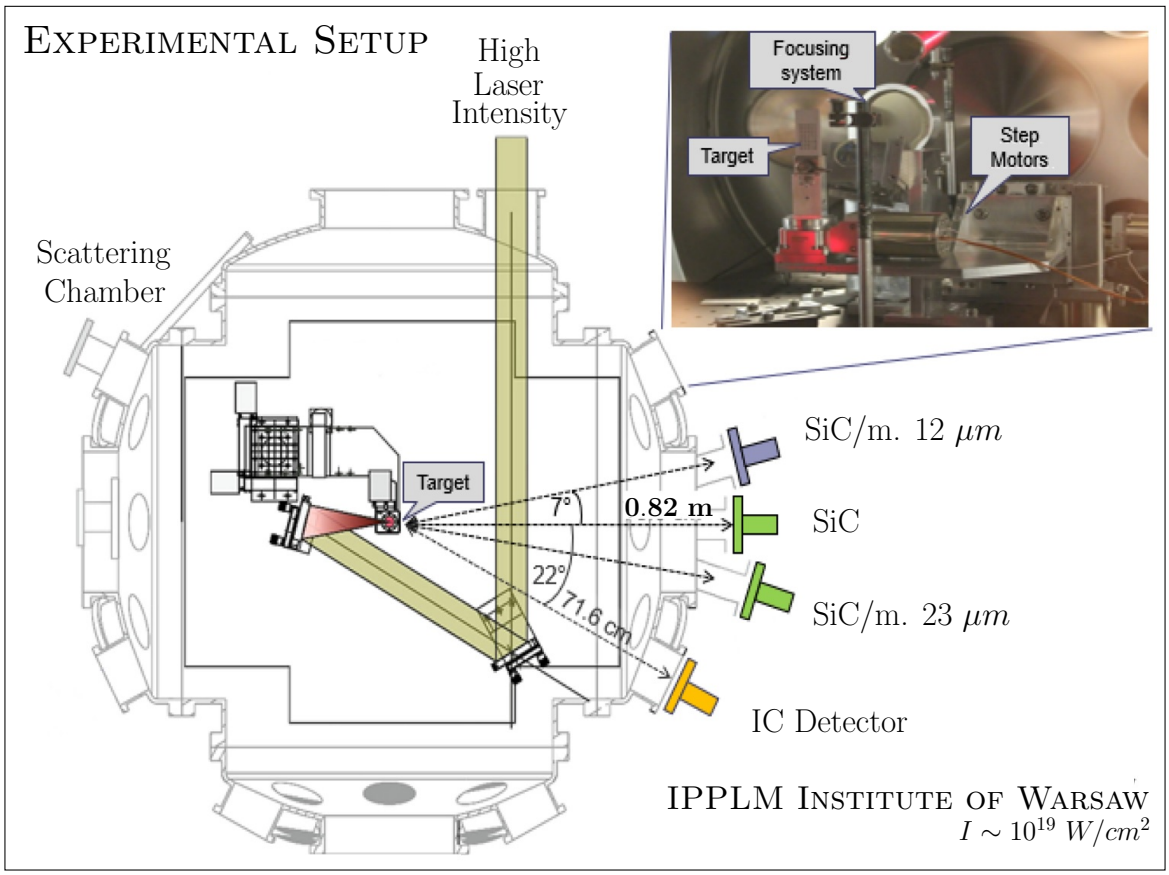

Figure 4.20: *Scheme and picture (inset) of the experimental setup.*

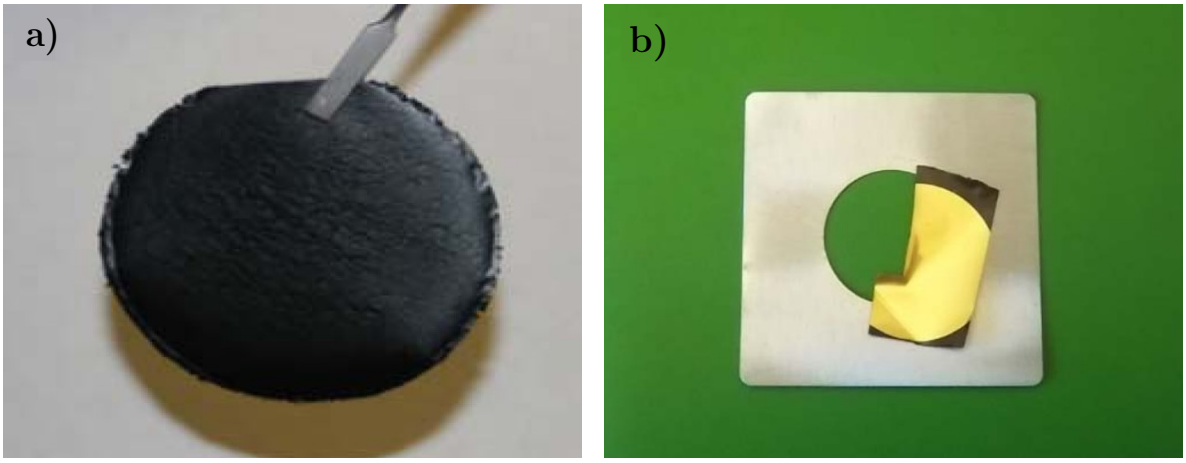

Figure 4.21: *Picture of graphene oxide foil (a) and GO foil covered by gold 200 nm thick film (b).*

ten advantages [206]: (i) high mechanical resistance of the foil; (ii) high IR laser light transmission; (iii) high electrical conductivity of the foil; (iv) high effect of electron channelling though GO; (v) high hydrogen concentration absorbed by GO; (vi) low laser reflection in GO; (vii) low foil density (1.45 g/cm^3); (viii) low electron stopping power in GO; (ix) low electron scattering in GO; (x) control of the electron plasma density by metals films (Al, Cu, and Au). The rGO foil was covered by 200 nm of metallic layer, in order to increase the number of electrons accelerated by the laser pulse. In Figure 4.21a is shown a picture of a rGO target used for the measurements. On the other hand, in Figure 4.21b is shown a GO foil covered by gold layer 200 *nm* thick. The laser focusing on the target is accomplished by an optical microscope showing the minimum spot (10 microns in diameter) at high magnification on an LCD screen.

SiC semiconductor detectors and ion collectors (IC) were employed for the fast on–line plasma diagnostics in TOF technique approach. The SiC detectors have an active depth zone of 80 microns, an active area of 4 mm^2 and a surface metallization constituted by 200 *nm* of Ni_2Si. As we already see, the detection efficiency depends on the surface metallization thickness and active depth region. Figure 4.22a shows typical curves of detection efficiency versus the energy for photons, electrons, protons and gold ions.

Three SiC detectors were placed at 0°, 7° and −7° in the forward direction to a distance of 82 *cm* from the target. The central one (SiC1) was employed without absorber and the other two use a Mylar absorber 12 μm (SiC2) and 23 μm (SiC3) in thickness, respectively. The Mylar absorber thicknesses correspond to 700 and 1080 *keV* proton range, respectively. The ion stopping powers and range in the absorbers were calculated using SRIM code [175]. The IC detectors were also used in the TOF approach, in the forward direction at +4° at a distance of 36 *cm*. SiC and IC detectors are connected to a fast storage oscilloscope (500 *MHz*, 2.5 *GS/s*) and are triggered by the photopeak of one SiC detector.

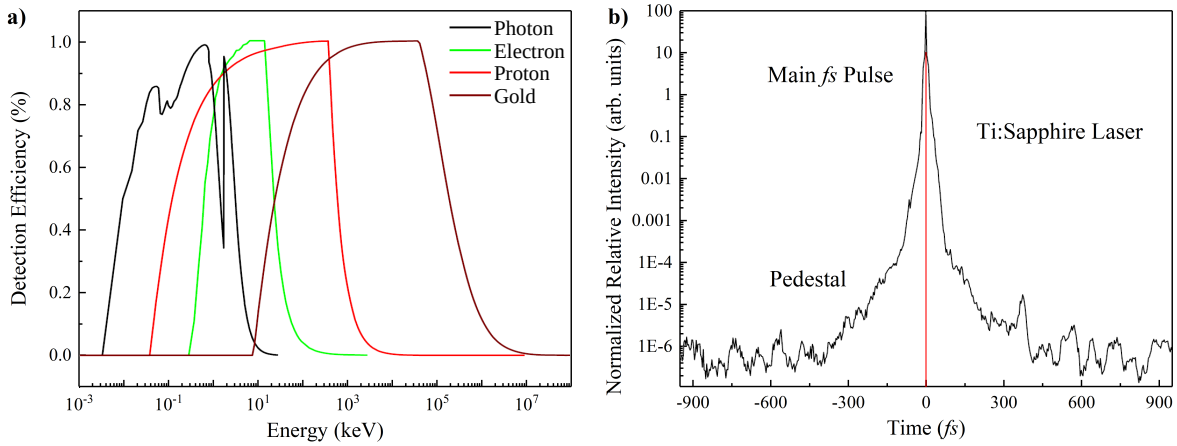

Figure 4.22: *Detection efficiency as function of the various kind of radiation energy (a), and shape of the fs laser pulse vs time (b).*

The experiment was conducted using a *fs* laser pulse at high contrast ($\sim 10^{-8}$) whose shape and relative intensity as function of time are reported in Figure 4.22b. The spectrum shows a pedestal with a duration of about 0.4 *ps*, and a mean relative intensity, with respect to the main peak assumed 100, of about 10^{-5}. The main pulse have a duration (FWHM) of about 40 *fs* and a relative intensity of 100. The laser peak and pedestal shape, duration and relative intensity, is very important in in the context of the maximum achievable ion energy. In this case, prepulse (pedestal) is many orders of magnitude lower than the main pulse and cannot generate significant preplasma before the arrival of the main pulse on the target.

4.2.2 Ion acceleration from Advanced Targets

Let's consider a study of how the acceleration of ions emitted by the plasma changes when targets to achieve higher energies are used, known as advanced targets.
SiC–TOF spectrum obtained by irradiating GO foil, 7 μm in thickness, covered by 200 *nm* of gold film (Au), employed for maximize the conditions of ion acceleration, is shown in Figure 4.23a. The irradiation was done through minimum focal spot size, chosen a flat and at less roughness surface, by using a laser pulse energy of 351 *mJ*, 40 *fs* pulse duration, p–polarized radiation, and laser beam focal position FP = +340 μm, i.e. the laser focus is inside the target and far beyond the thickness of the foil. In such conditions, the spectrum shows a high photopeak due to the detection of X–rays and relativistic electrons, followed by a wide peak due to the ions detection. The starting point of the ion signal correspond to the faster protons arrival time on the detector, which are detected at a TOF of 35 *ns*, i.e. they have a velocity of 2.34×10^7 *m/s* and a kinetic energy of 2.85 *MeV*. The TOF–spectra also indicates the presence of ions, detected at longer times and therefore at lower velocities.

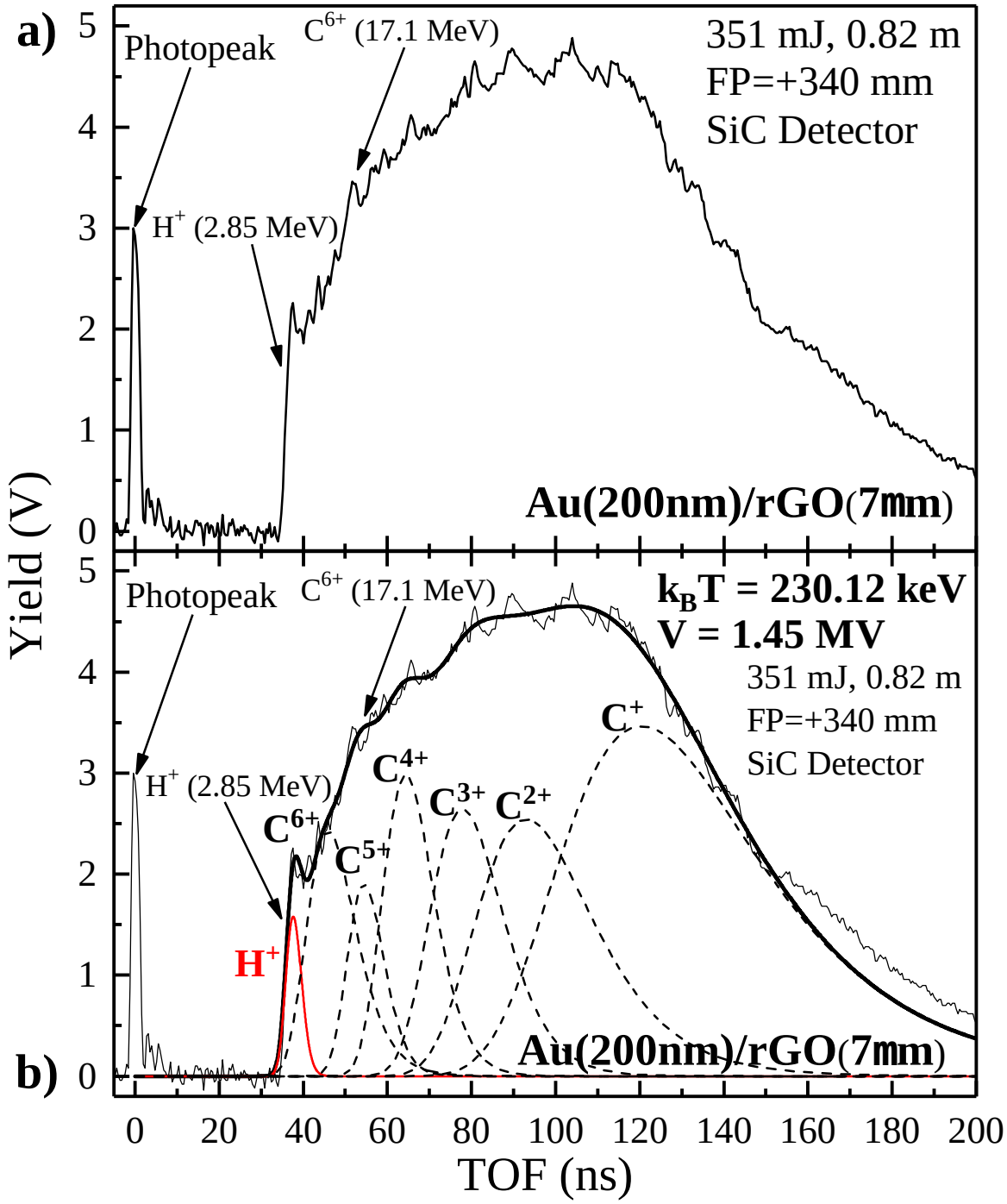

Figure 4.23: *Experimental SiC–TOF obtained by irradiating Au(200nm)/rGO(7μm) (a) and peak deconvolution for protons and carbons ions through using the CBS distribution function (b).*

Examining the signal obtained in Figure 4.23a, it is clear that the spectrum can not be due only to protons with Boltzmann velocity distributions, because the tail of the peak would indicate proton energies too low, not comparable with the TNSA regime, and also the peak structure would not be explained by the detection of a single ion type. To this, the CBS distribution (Equation 2.30) was considered to fit experimental data, assuming that the accelerated ions are protons, as foil impurities, and as carbon due to bulk composition. Oxygen ions could also be present but their concentration would be negligible compared to that of carbon ions, thus they were neglected in the ion peak deconvolution.

Assuming that the maximum proton energy is 2.85 MeV, and that it is indicative of the maximum acceleration voltage, which is worth 2.85 MV/z (being z the charge state), the energy of C^{6+}–ions is up to $2.85 \times 6 = 17.1$ MeV, while that of C^{+}–ions is up to 2.85 MeV. In Figure 4.23b the deconvolution of experimental data is reported. The TOF shifts of the six carbon charge states indicates an average voltage potential of 1.45 MV. The average plasma temperature obtained from the proton–carbon ions fit is worth about 230 keV. This temperature value is in agreement with the theoretical predictions for hot electron temperature estimation, introduced in Equation 1.22. Because the intensity and wavelength of the laser were about 3×10^{18} W/cm^2 and 0.8 μm respectively, the theoretical evaluation given by Equation 1.22 corresponds to ~ 270 keV. A similar proton energy was obtained by the IC collector, although the spectrum was more disturbed by electromagnetic noise, and was not reported in this work.

From spectra reported in Figure 4.23 it is possible to evaluate the ion current due to protons and carbon ions. Although the SiC detector solid angle detection is very small, which corresponds to 6 μstr, the electrical signal acquired in the TOF–signal was about 2 V with 10 ns duration. Knowing that the input oscilloscope resistance was 50 Ω, it corresponds to a charge detection of 4×10^{-10} C, which is due to the electrons collection generated in SiC by about 2 MeV protons. Thus, by considering the SiC gap energy of 3.3 eV, the number of protons producing the TOF signal should be about 8.3×10^3 $protons/6\mu str$. Now, due to the high directivity of the accelerated ions, assuming that the proton emission occurs on a solid angle of about $\pi/2$ str, it means that the total proton emission should correspond to about 2.2×10^9 $protons/pulse$. From this, the total energy transported by the protons is abut 0.7 mJ, that corresponding to a conversion efficiency of the laser in proton energy of about 0.2%.

The carbon current emission is higher than protons one. By the carbon yield areas, it is possible to evaluate, as a first approximation, that the total carbon emission should be 20 times higher than that of protons, i.e. of about 4.4×10^{10} $carbon–ions/pulse$.

When SiC detector is covered by Mylar absorbers, TOF–spectra changes due to ions' range lower than the absorber thickness, that doesn't allow you to detect them. The spectra detected using a Mylar foil of 12 μm (SiC2) and 23 μm (SiC3), compared to that without absorber and placed at 0° angle (SiC1), are reported in Figure 4.24a. Spectra show that the proton peak is always present, in fact, the range for 2.85 MeV protons in Mylar is 105 μm, higher than the thickness of both absorbers. The protons travel for the 0.82 m flight path and

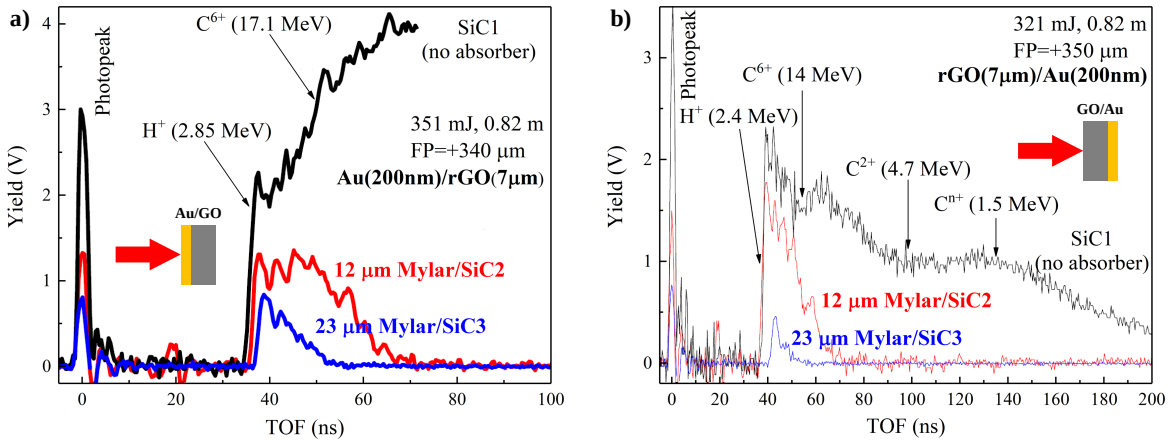

Figure 4.24: *Comparison of SiC–TOF spectra with different thickness of Mylar absorbers, obtained by irradiating Graphene 7 µm thick covered by* 200 *nm of gold in front (a) or in the rear side (b).*

are transmitted by the filter, thus they are not shifted in timescale. The 17.1 *MeV* carbon ions have a range in Mylar of 19 *µm*, thus they are detected by the SiC2, that using 12 *µm* thickness, and not by the SiC3, that using 23 *µm* absorber thickness, confirming the presence of carbon ions in the spectrum. The signal obtained using 23 *µm* Mylar thickness as absorber indicates that the minimum proton energy is of about 1.4 *MeV*; which energy corresponds to a range in Mylar of 33 *µm*. Thus, this analysis indicates that accelerated protons have a near monochromatic energy ranging between 2.85 and 1.4 *MeV*.

Figure 4.24b reports the comparison of SiC–TOF spectra with different thickness of Mylar

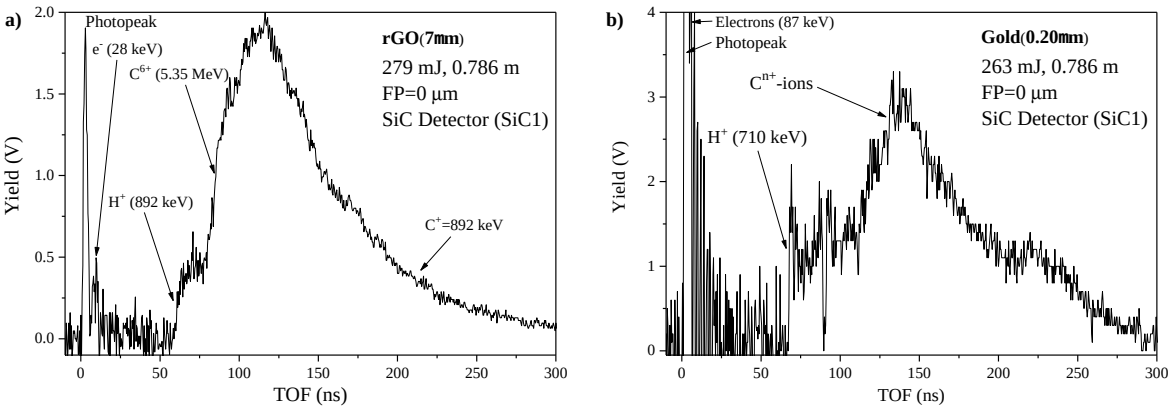

Figure 4.25: *SiC spectra obtained irradiating the sample made by only 7 µm rGO foil without Au (a)* 200 *nm of gold without rGO (b).*

absorbers, by foil irradiation from the graphene oxide surface toward the gold film, unlike the previous case. It is possible to observe that in this condition the proton acceleration decreases to 2.4 *MeV*. By irradiating only the 7 *μm* rGO without gold coverage the maximum proton energy decreases to about 900 *keV*, as shown in Figure 4.25a. By irradiating only Au thin film (200 *nm* thickness) the maximum proton acceleration decreases to 700 *keV*, as shown in Figure 4.25b. Thus, the proton acceleration of 2.85 *MeV*, obtained in the first case, is the better result for the prepared thin foils. This target, in fact, increases the plasma density, by the use of the gold surface thin film placed on a suitable thickness of carbon foil with a very low density to enhance the transport of electrons in the rear side of the target, and thanks to high electrical and thermal conductivity of the rGO foil.

4.2.3 Dependence on the Focal Position

An important feature to obtain high proton acceleration is where the laser beam focal position (FP) lies. In our measurements, the optimal conditions were found for FP = +340 *μm*. By changing the FP, proton acceleration decreases. Measurements were performed in the range between 400 *μm* (in front of the target surface), to 0 *μm* (at the gold layer target surface), and up to +400 *μm* (inside the target), confirming that the maximum acceleration occurs near +340 *μm*. Figure 4.26 reports two SiC spectra of the Au/GO foil obtained using a FP = 0 *μm* and FP = −100 *μm*, which show a maximum proton energy of 1.4 *MeV* and 760 *keV*, respectively.
The maximum proton energies obtained by changing the focal position are shown in the

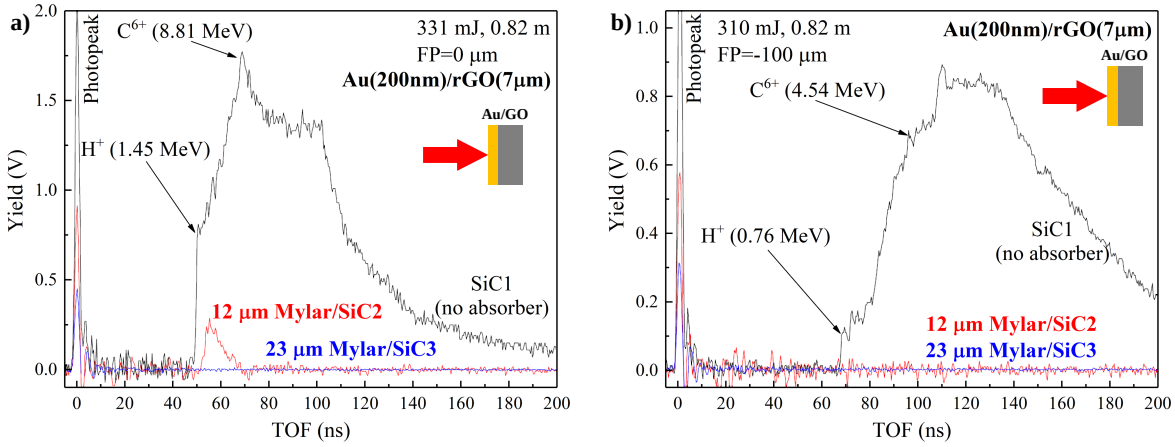

Figure 4.26: *SiC TOF–spectra obtained by irradiating a target of reduced Graphene oxide, 7 μm of thickness, covered by 200 nm of gold on the hit surface, using a laser focal position of 0 μm (a) and of −100 μm (b). The proton energy change from 1.45 MeV for* FP = 0 *μm to 0.76 MeV for* FP = −100 *μm.*

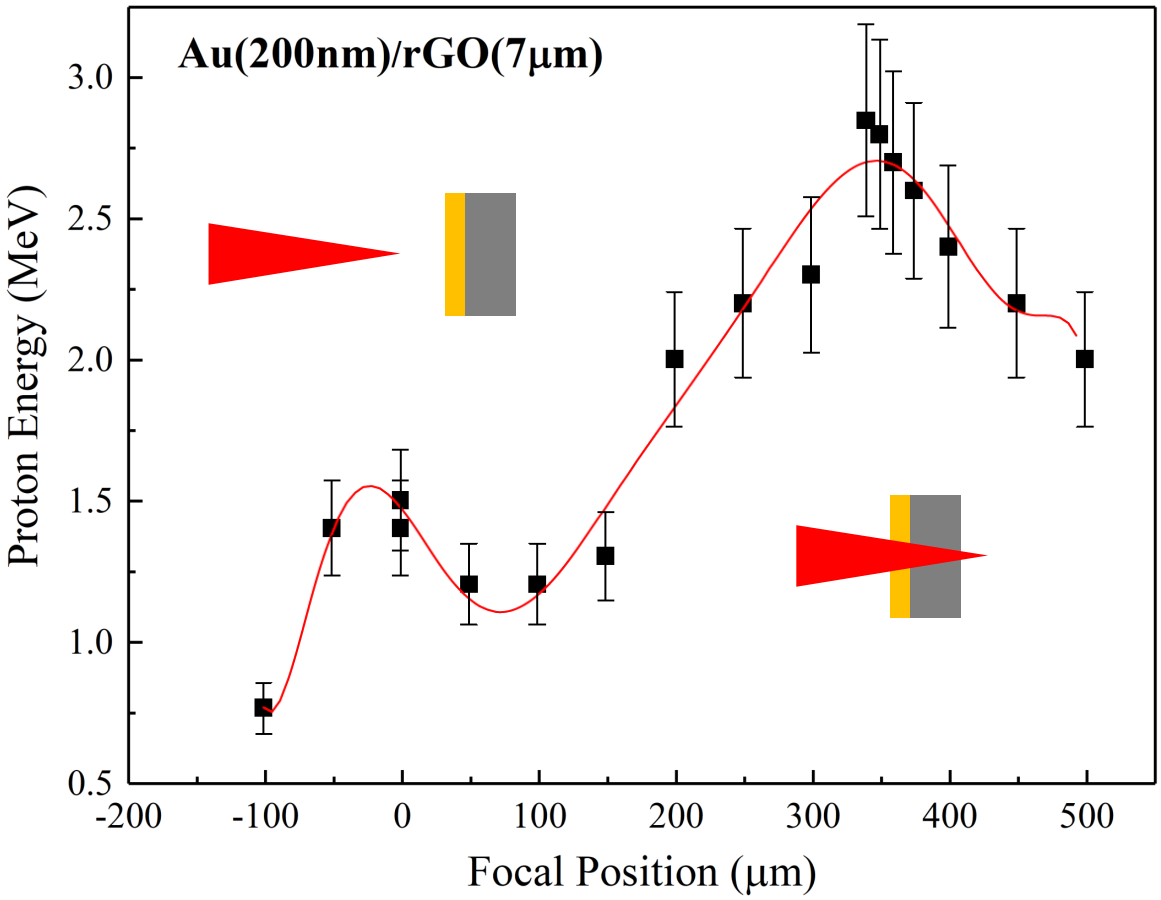

Figure 4.27: *Experimental maximum proton energy, detected by irradiating a target of reduced Graphene oxide, 7 μm of thickness, covered by 200 nm of gold on the hit surface, as a function of the laser focal position. Two peaks are observed in the energy of the protons obtained: the first, at about* FP = −25 *μm, probably due to a self–focusing effect of the incident laser beam that propagates inside the preplasma. The second peak, more marked at* FP = +340 *μm, due to an optimal laser spot size on the target that increases the electrons number heated by the external field, producing a longitudinal acceleration field more intense, which drives protons to higher energies.*

plot of Figure 4.27. The error on the proton energy measurement is of about 12%, while the focal position error is of about ±1 *μm*. This plot demonstrates that in general, the proton energy increases when the focal position is localize inside the target. This effect increases the spot area and, consequently, the number of electrons that are accelerated forward by the incident laser pulse. Thus, accelerated electron density increases and, of course, the longitudinal electric acceleration field becomes more strong, improving the proton maximum

energy reached. It is possible to note that two peaks occur Figure 4.27. One less marked occurs at about −25 μm, probably due to the self–focusing effect due to preplasma in front of the target, and another, more pronounced, occurs to +340 μm at which the electron density and plasma temperature have a maximum value. FP higher than the +340 μm decreases the ion acceleration effect because the laser intensity goes down, due to increase of laser spot on the target; thus the electron pushed out to the rear side of the foil decreases, and consequently the acceleration as well.

4.2.4 Section Conclusions

The relatively high proton energy obtained in this experiment is attributed to the special properties of GO foil, which has the advantages are reported in Section 4.2.1. The low GO density and low atomic number permit to transmit high relativistic electron density in the rear side of the foil enhancing the longitudinal electric field responsible for the ion acceleration. For the GO employed in these measurements, the graphene platelets forming the GO foil, 7 μm in thickness, are randomly oriented, thus the real effect of electron channeling is minimum. In future analysis, it is interesting to improve the properties of GO using oriented platelets permitting higher electron channeling and low electron scattering so that we expect higher ion acceleration for these advanced targets to be demonstrated.

In any case, the use of these foils has permitted to generate high proton acceleration with significant yield and near–monochromatic energy, approximately within 2.85 and 1.4 MeV. Also carbon ions are accelerated at kinetic energy of about 2.8 MeV/z, and with charge state from 1+ up to 6+. The presence of carbon ions in the signal recorded by SiC1 (at an angle of 0°) is highlighted by SiC2 and SiC3, where the Mylar absorber shields the ions detection.

Measurements performed on pure GO, 7 μm in thickness, or pure Au, 200 nm in thickness, have demonstrated that the proton acceleration is lower, thus the presence of both foils means that the target enhances the ion acceleration process, injecting electrons from the gold surface through the GO up to the rear side of the target. Similarly the change of the laser focal position at +340 μm demonstrates the increment of the acceleration process, while other FP distances decrease it.

Although the obtained results are satisfactory, still much can be achieved both to increase the process of ion acceleration and that of the emitted ion stream, and of the energy conversion efficiency of the laser pulse into electron and ion energy, which in these experiments generally is in the order of 10%. Different improvements can be sought by using more suitable experimental conditions, such as to enhance the proton emission current enhancing a GO foil richer in absorbed hydrogen. The GO film thickness and the Au film thickness could be optimized to enhance the electron field acceleration, as reported in the literature. The structure of the GO could be used with higher crystallinity using oriented platelets to enhance the electron transmission of the foil.

4.3 High Energy Ion diagnostics by TPS

Published Paper[2019]

Compact Thomson Parabola Spectrometer for fast diagnostics of different intensity Laser–generated Plasmas

L. Torrisi and G. Costa
Dipartimento di Scienze Fisiche, MIFT, Università di Messina, V.le F.S. D'Alcontres 31, 98166 S. Agata, Messina, Italy

Published as: L. Torrisi and G. Costa: "Compact Thomson Parabola Spectrometer for fast diagnostics of different intensity Laser–generated Plasmas", *Physical Review Accelerators and Beams*, Volume: 22(4), Pages: 042902(1–9) (2019)
Available from: 10.1103/PhysRevAccelBeams.22.042902
Publication Date: Received 21 November 2018; Published 25 April 2019

Ion streams generated by laser induced plasmas, with an energy of the order of *keV–MeV*, can be detected using different devices such as Faraday cups, semiconductor detectors, Gafchromic films, track detectors, and others. High ions energy can be obtained using *ns–fs* laser pulse durations and intensities up to 10^{12} W/cm^2.
With the aim to characterize the laser–produced plasma, many types of spectrometers can be employed for the its diagnostics, such as optical measurements in visible (VIS), UV and X-ray wavelength regions to determine the temperature and electron plasma density. Fast streak cameras permit to measure the plasma expansion velocity and the temperature gradients during the expansion. Langmuir probes are employed to evaluate the plasma potential, temperature and density. The charged particles detection using fast semiconductors is a valid method to determine the ion and electron energy distributions. Mass spectrometers used for the particle mass emission evaluations permit to determine the ablation yield. The Thomson parabola spectrometer (TPS) appears the most appropriated between other techniques thanks to its possibility to distinguish the ion mass, charge state and energy with high resolution. The TPS diagnostics permit to solve the recognition problems of the ion species (charge state and mass) and of energetic electrons. The device gives the possibility to evaluate quickly some parameters, such as the maximum energy of protons and ions, the amount of ion charge states for each species in the plasma, the type of different ions accelerated by laser–induced plasma, and the measure of medium and maximum electron energy, according to their magnetic and electric deflection, as we already see in Section 4.1.2. Moreover, by the signal intensity of the parabolas signal, it is possible to evaluate the particle energy distribution for each ion species and their charge state distribution. In addition, the use of TPS for electrons permits to have direct information on the energy of hot and cold electrons emitted from the non–equilibrium plasma.
The modern TPS, generally, has high sensitivity and precision but large dimensions (1–2 meters). The cost of these devices is high due to the use of expensive electromagnets that

absorb high currents, to the high vacuum technology and to the use of microchannel plate (MCP) detectors coupled to phosphorous screen and fast CCD cameras [207].
Now, let's take into account high intensity laser–generated plasmas diagnostics using a compact (low volume), cheap and simple TPS. The volume compactness of this spectrometer is given in respect to the larger ones present at INFN-LNS in Catania [207], Prague Asterix Laser System (PALS) Laboratory in Prague [208] and other big facilities such as the Queen's University in Belfast [209]. Before the alignment pinholes, this TPS has a ring ion collector in input to control the flux of ions arriving in the direction of the TPS along *z–axis* [**210**].
Of course, this simple spectrometer is less accurate in sensitivity and precision than those mentioned above because it does not use the MCP system but it is very useful for a very fast first diagnostic and for its transportability in each laboratory. The compact TPS has dimensions about a factor 2–5 times lower and a cost up to a factor 10 lower. It can be used for plasma analysis produced by low and high laser intensity, by regulating the magnetic and electric fields properly.

4.3.1 Compact Thomson Parabola Spectrometer

The measurements presented, were obtained in three different laboratories using the same compact TPS instrument. A schematization of the three experimental setups is reported in Figure 4.28a, while a picture of this is shown in Figure 4.28b. The laser pulse interacts with a solid target with an incidence angle of 45° placed in a high vacuum chamber. The produced plasma, developed along the normal to the target surface (*z–direction*), is directed towards an electromagnetic TPS spectrometer analysing the mass–to–charge ratio. For TNSA accelerations the foil is very thin (microns), the laser arrives from the back of the target and the plasma is produced in the forward direction. For backward plasma acceleration (BPA) the laser incidence occurs on the surface from which will be emitted the plasma and the target generally is thick ($\sim 1\ mm$).
A first experiment has been performed at INFN–LNS (South National Laboratories) in Catania, in collaboration with the MIFT Department of the Messina University, using a thick target in BPA regime, which can be positively polarized to induce Coulomb repulsion and post ion acceleration in the backward direction, as reported in the literature [211]. For this measurement, an Nd:YAG laser, with a fundamental wavelength of 1064 nm, a maximum pulse duration of 9 ns, and variable energy between 1 and 900 mJ, is focused on a target, consisting of titanium oxide, through an optical lens of focal length 50 cm. The irradiation occurs in high vacuum at 10^{-7} $mbar$. The generated plasma emits ions with low energy (of 200 eV per charge state), which is not enough for an optimal TPS deflection, so ions are submitted to a post–acceleration system to be further accelerated.
Post–acceleration system is shown in Figure 4.28c, while its schematization is reported in Figure 4.28d. A lateral window allows the laser beam to enter into the system, where it is located the target. The target and the plasma expansion chamber are insulated from the ground. They are electrically connected, and a potential between 0 and 60 kV can be applied

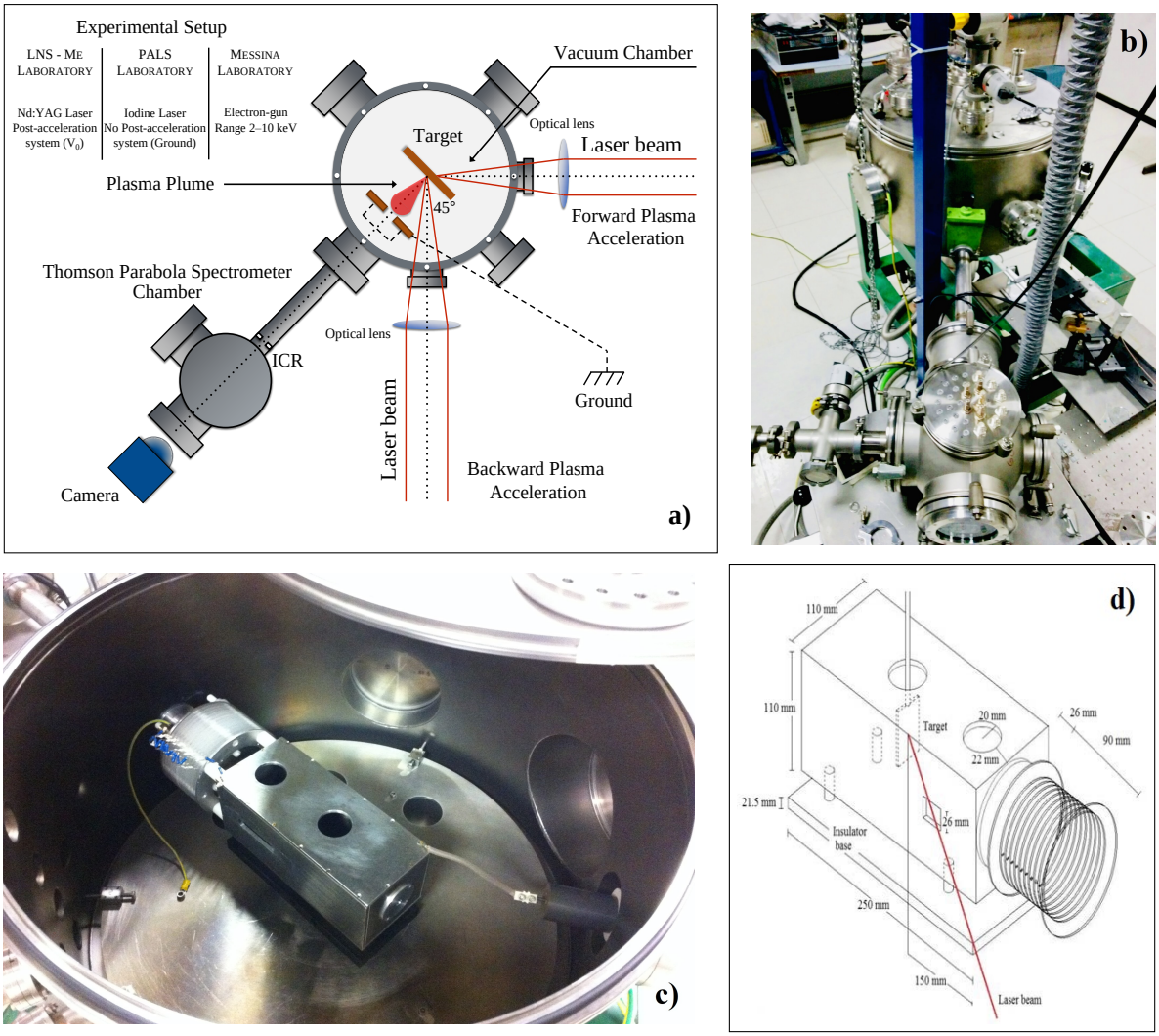

Figure 4.28: *Experimental setup using for laser–target interactions in TNSA and BPA regimes and plasma production directed towards the TPS spectrometer (a), photos of the external camera (top view) (b). Picture of the post–acceleration system (c) and representation of it (d).*

to them. The extraction of the ions occurs along the normal through a circular window 12 *mm* in diameter, and 15 *cm* distant from the target. After the extraction, 12 metal discs, 2 *mm* thick and 10 *cm* in diameter, separated 5 *mm* from each other, are connected to the high voltage (HV) and to the ground, through a resistive circuit with 1 $M\Omega$ resistances. This generates a voltage drop to the ground, which allows the extraction of positive ions through an 8 *mm* wide output window.

Laser–generated plasma is previously analyzed by an ICR (ion collector ring), with and without post–acceleration, using a time–of–flight (TOF) technique. In addition, the produced ion beam is collimated by two aligned pinholes along the *z–axis* of the TPS to be analyzed in detail.
The ICR, placed in front of TPS input pinholes, consists in an annular Faraday cup with a secondary electron suppression polarized to –100 *V*, whose collector is coupled to a fast storage oscilloscope through a small capacitor, as reported in the scheme of Figure 4.29. Both ICR and TPS are aligned along the *z–axis* and are assembled in a vacuum chamber whose photo is reported in Figure 4.28b.

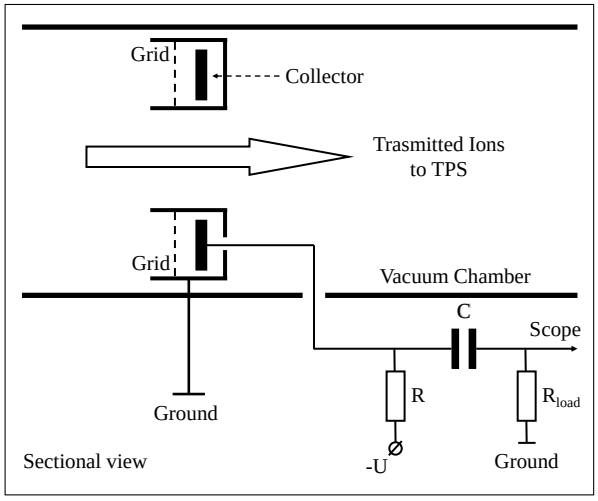

Figure 4.29: *Schematization of Ion Collector Ring (ICR) for for preliminary diagnostics.*

A second experiment has been performed at PALS Laboratory in Prague using a thin foil irradiated in TNSA regime to induce forward ion acceleration. In this case, an iodine laser was employed to irradiate a polyethylene foil. The laser has a fundamental wavelength of 1315 *nm*, a maximum pulse duration of 300 *ps*, pulse energy up to 700 *J* and a focal spot diameter of 70 μm. In this case, the plasma ion stream is produced at high kinetic energy, of the order of some *MeV* per charge state. The plasma was analyzed both with ICR–TOF and with TPS spectrometers.
A third experiment was performed at Messina Laboratory, using a setup similar to that reported in Figure 4.28a, but with an electron gun placed in the vacuum chamber, which emits electrons along the *z–axis* and directed towards the ICR and TPS spectrometer. Electrons have high current (μA), and kinetic energy ranging between 2 and 10 *keV*.
The compact TPS used for these three measurements is the same, and it is reported in the schematization of Figure 4.30a, of which a picture is reported in Figure 4.30b. It is constituted by two input pinholes, to guarantee the directivity of the incident ions, distant from each other 100 *mm*, and with holes of 1 *mm* (input) and 100 μm (output) in diameter respectively (Figure 4.30c). Immediately afterwards, there is a magnetic and an electric deflection field, both 25 *mm* long , shown in details in Figure 4.30d–e. The fields are directed parallel to each other, and orthogonal to the direction of motion of the incident particles. Finally, at a distance of 150 *mm* from the electric field, there is a planar detector, which can employ different recording methods. The TPS system is placed in a high vacuum at 10^{-7} *mbar*.
The magnetic and electric fields used for the experimental setups, prepared at INFN-LNS Catania Laboratory and at PALS in Prague have the same module and geometrical features,

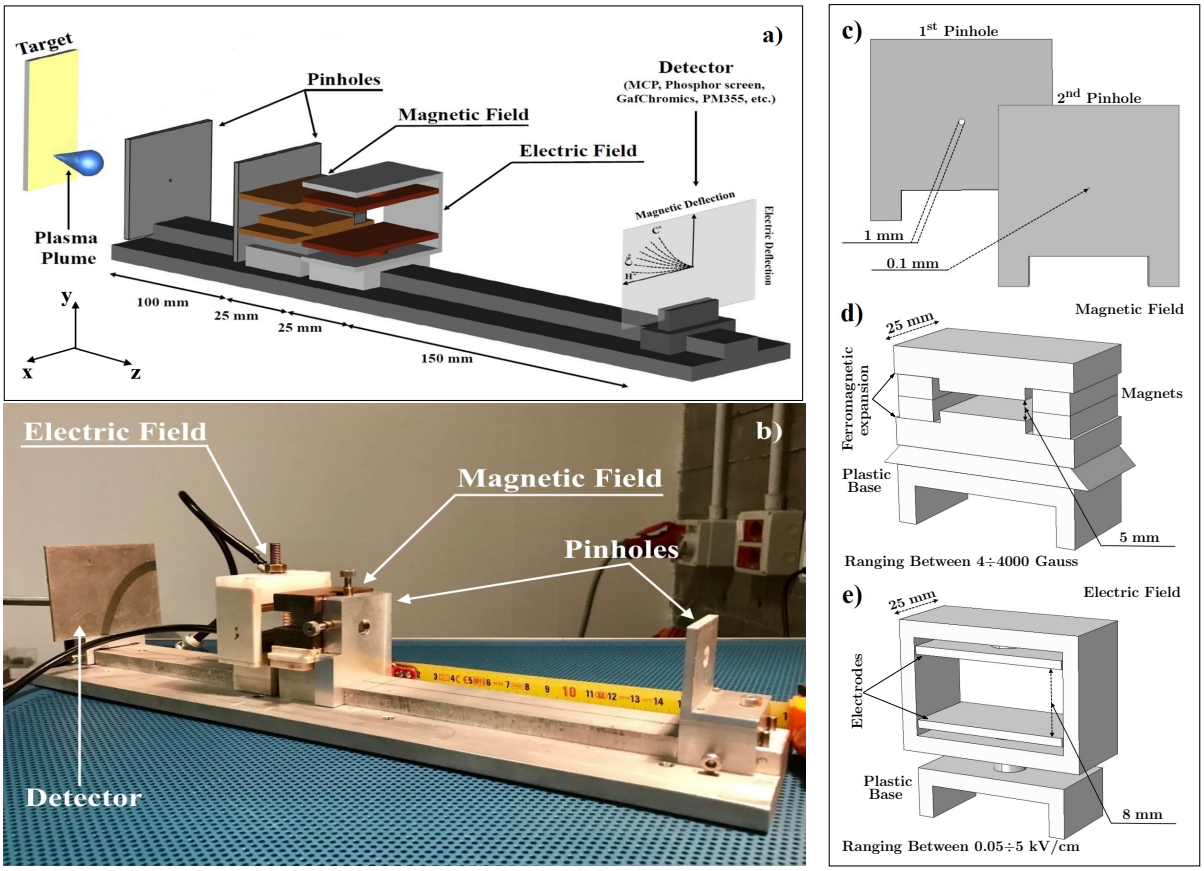

Figure 4.30: *Representation (a) and picture (b) of the compact TPS used for the measurements. In details, illustration of pinholes collimation system (c), magnetic (d) and electric (e) fields.*

which correspond to 2500 *Gauss* and 0.67 *kV/cm*, respectively. In such experiments,t he detector used for TPS was a HD–810 Gafchromic film and a PM–355 track detector, previously mentioned. We already see that the track detector need to chemical etched to be read. According to etching solution concentration, temperature and time, it is possible to reveal the most superficial heavy ion tracks or the deepest tracks due to energetic protons.

The measurements performed at Messina Laboratory (University of Messina) are conduct by the same TPS with a magnetic and electric field of 7.5 *Gauss* and 0.1 *kV/cm* respectively. In such a case, the TPS detector was a luminescent phosphor screen.

COMSOL Multiphysics software was employed to perform simulations of ions trajectories emitted from the plasma source, which moving into magnetic and electric fields. Trajectories computation facilitates all steps in the modelling process defining the geometry, meshing, specifying the involved physics mechanisms, solving, and then visualizing the results.

4.3.2 Post–accelerated ions measurements

By irradiating a titanium oxide target with the Nd:YAG laser of the INFN–LNS Laboratory in Catania, two ICR time–of–flight spectra were obtained, when the post–acceleration potential is turned off (0 V) and when it is set on 30 kV; these results are reported in Figure 4.31 [211]. The IC spectra are triggered with the laser shot at TOF= 0 time. The TOF spectrum obtained without the post–acceleration system (Figure 4.31a) represents the convolution of all detected ion species, and indicates that the faster ions (protons) are positioned at a time of 7 μs (protons as impurities are not very evident on the scale of Figure 4.31a). Since the target distance from the ICR is 100 cm, these will have a maximum kinetic energy of about 106 eV. The oxygen ions have a minimum TOF of about 13 μs, corresponding to a maximum energy of about 492 eV and the titanium ion contribution is detected at a TOF of about 22

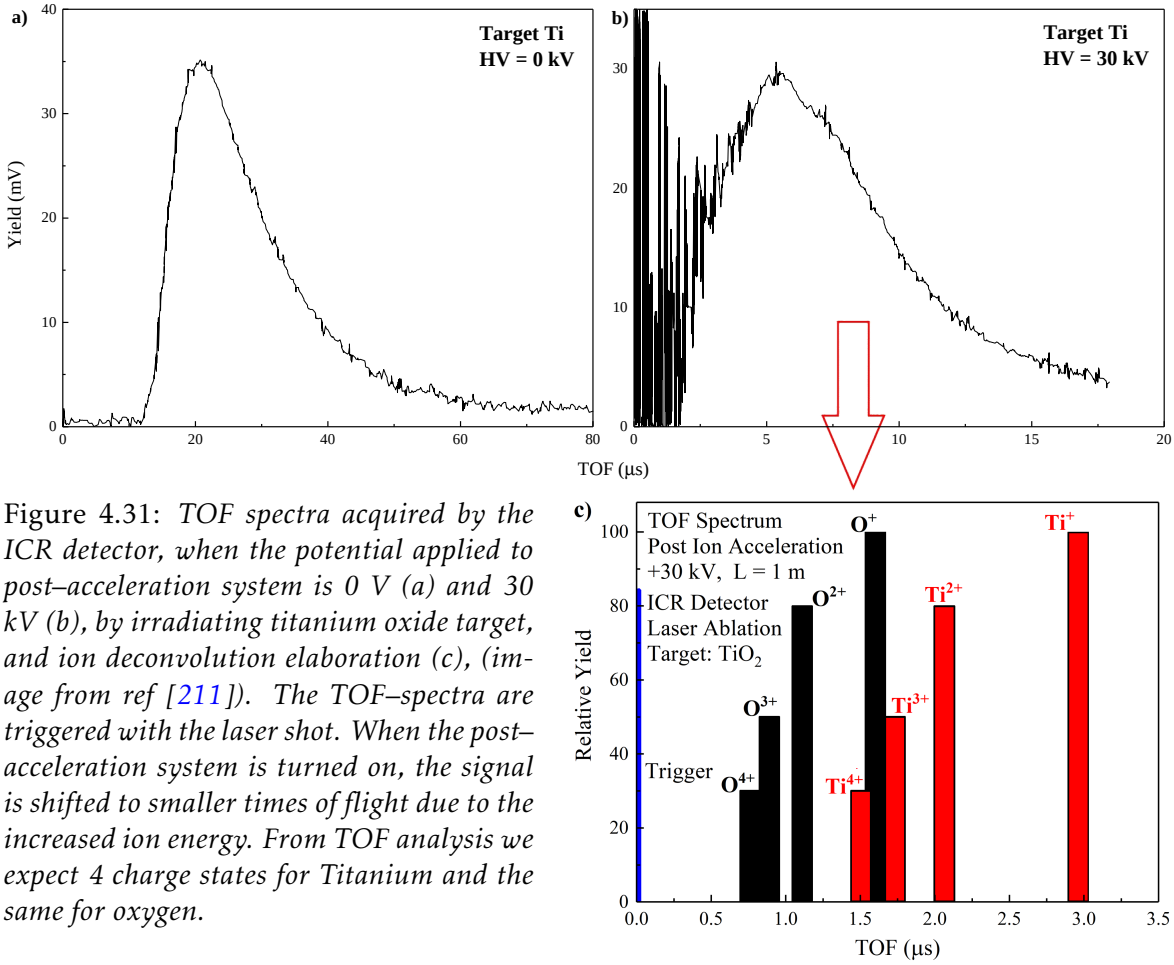

Figure 4.31: *TOF spectra acquired by the ICR detector, when the potential applied to post–acceleration system is 0 V (a) and 30 kV (b), by irradiating titanium oxide target, and ion deconvolution elaboration (c), (image from ref [211]). The TOF–spectra are triggered with the laser shot. When the post–acceleration system is turned on, the signal is shifted to smaller times of flight due to the increased ion energy. From TOF analysis we expect 4 charge states for Titanium and the same for oxygen.*

μs, corresponding to a maximum kinetic energy of about 516 eV. These results indicate that the plasma ion acceleration is of about 106 eV per charge state; thus, the maximum charge states of the oxygen and titanium ions are 4+. The ionization potentials of O^{4+} and Ti^{4+} ions are 77.4 and 43.3 eV, thus the maximum electron energy, comparable to the plasma temperature, should be lower than 100 eV.

When a post–accelerative potential of 30 kV is applied between target and ground, the obtained TOF–spectrum is that shown in Figure 4.31b. In this case, the arrival time of the ions

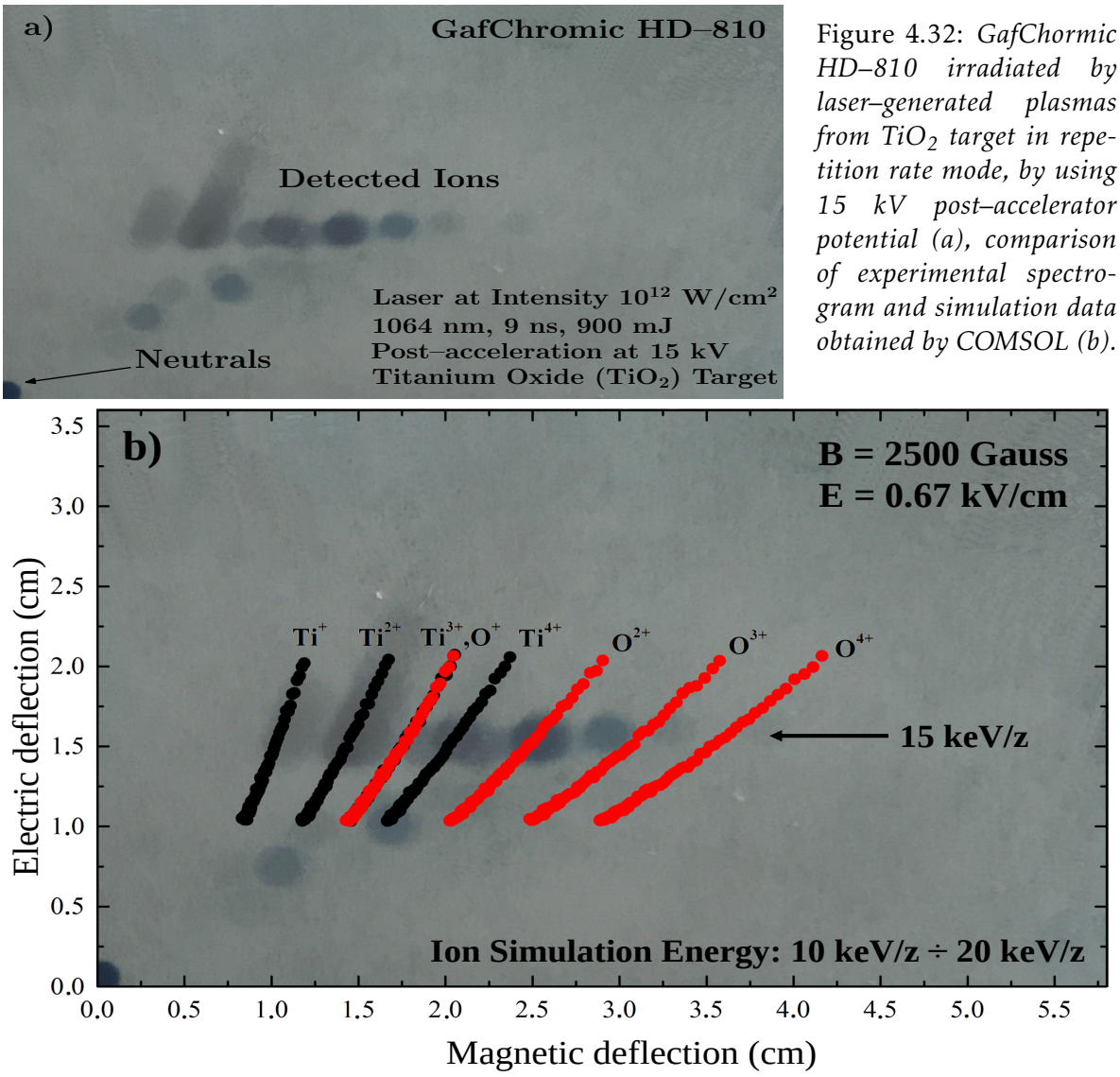

Figure 4.32: *GafChormic HD–810 irradiated by laser–generated plasmas from TiO_2 target in repetition rate mode, by using 15 kV post–accelerator potential (a), comparison of experimental spectrogram and simulation data obtained by COMSOL (b).*

decreases significantly because ions are post–accelerated to 30 *keV* per charge state. The TOF peaks of oxygen ions are placed at 1.67, 1.18, 0.96, and 0.83 μs, for O^{+}, O^{2+}, O^{3+}, and O^{4+}, respectively. The TOF peaks of titanium ions are placed at 2.9, 2.0, 1.67, and 1.44 μs, for Ti^{+}, Ti^{2+}, Ti^{3+}, and Ti^{4+}, respectively, as reported in the ion deconvolution elaboration of the IC spectrum of Figure 4.31c.
Results confirm the expected values of 30 *keV* for both main ions. Less evident by ICR but more evident using the TPS spectrometer, it is possible to distinguish the energies of 30, 60, 90 and 120 *keV*, due to the acceleration of the charge states 1+, 2+, 3+ and 4+, respectively.
After the preliminary analysis performed using the ICR detector, the post–accelerated ions are analysed with a TPS deflection system. The presented measurements were performed using a post–acceleration potential settled to 15 *kV*, so the ions acquire 15 *keV* per charge state. Figure 4.32a shows the spectrogram acquired using the gafchromic film (HD–810 dosimeter) as a detector placed in the TPS and a laser operating at 1 *Hz* repetition rate mode. In this experiment, the electric and magnetic field were of 0.67 *kV/cm* and 2500 *Gauss*, respectively. Through the comparison of experimental parabolas and the simulation data calculated by COMSOL Multiphysics software (shown in Figure 4.33), which is able to reconstruct the trajectory of the ions in the system of interest, it is possible to recognize the energies and charge states of each charged species in the plasma. Ion beams with energies between 10 and 20 *keV* per charge state were simulated.

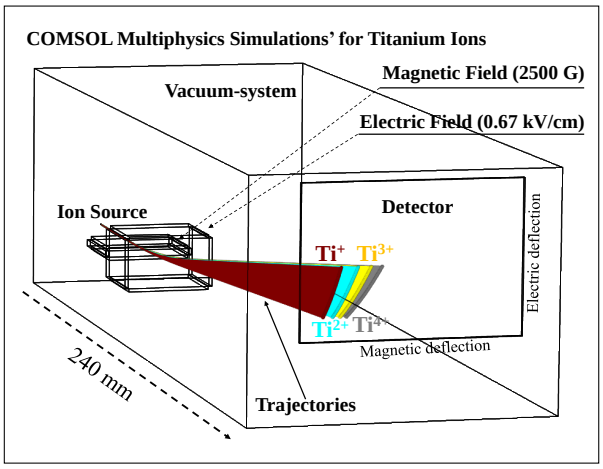

Figure 4.33: *COMSOL Multiphysics simulation for titanium ions with charge state from* 1+ *up to* 4+ *in the system of interest. The deflection by magnetic and electric field produce different parabolas on the detector according to ions mass–to–charge ratio.*

The overlapping of the experimental and simulation data reported in Figure 4.32b showed an excellent agreement. In this particular case, the energy is fixed due to the post–acceleration system, the comparison between the experimental and simulation data makes it possible to identify the species that make up the analysed plasma.
Results confirm the four charge states for titanium and for oxygen ions, as expected. Because of the low dose provided by the protons, present only as an impurity in the target, it is not possible to impress them on the device. In fact, due to heating effects on the target, and removal of material from it, after the first two–three laser shots the protons can no longer be observed appreciably.

4.3.3 MeV–ions from laser–generated plasmas detected by TPS

Another application of this compact TPS was performed to analyze the ions produced by a plasma generated irradiating a polyethylene (PE) thin target in the TNSA regime at 10^{16} W/cm^2 intensity at PALS Laboratory in Prague. Figure 4.34a reports the ICR spectrum at 80 *cm* distance from the irradiated PE target. The spectrum shows a high photopeak due to the detection of X–rays on the collector, a little peak at 50 *ns* due to fast protons at a kinetic energy of 1.3 *MeV* and a large and intense peak due to the different contribution of carbon peak, from C^+ (slower) up to C^{6+} (faster). Moreover, a long tail demonstrates that also slowly ions are detected, due detection of C_xH_y molecular groups, according to the literature [212]. In Figure 4.34b is shown the deconvolution of hydrogen and carbon ion peaks are obtained on the base of the Coulomb–Boltzmann shifted distribution function (Equation 2.30), assuming the proton energy as representative of the value of the light ion acceleration per charge state. It means that the C^+ has the same energy of the protons and that the C^{6+} ion energy is about $1.3 \times 6 = 7.8$ *MeV*, evaluated in correspondence of the peak. The ion energy distributions are Boltzmann curves shifted proportionally to the ion charge state. The theoretical approach permits to evaluate plasma temperature and acceleration potential, which are about 211 *keV* and 583 *kV*, respectively.

In Figure 4.35a is shown experimental data obtained by irradiating the polyethylene foil in TNSA regime; while Figure 4.35b shows the overlap between the experimental TPS spectrum and the simulation of the ionic traces, obtained with COMSOL Multiphysics. In this case, the ions are recorded using a PM–355 track detector and by electric and magnetic field module as the same of the previous experiment (0.67 *kV/cm* and 2500 *Gauss*). To read these track

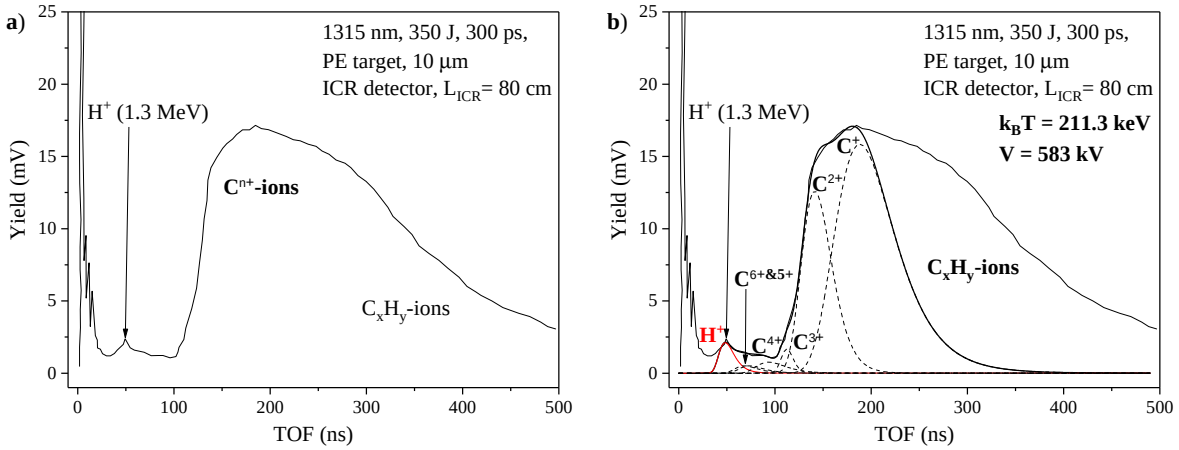

Figure 4.34: *ICR TOF–spectra obtained by polyethylene irradiation at 10^{16} W/cm^2 in TNSA regime at PALS laboratory in Prague (a) and its deconvolution by Coulomb–Boltzmann distribution for each ions charge state (b).*

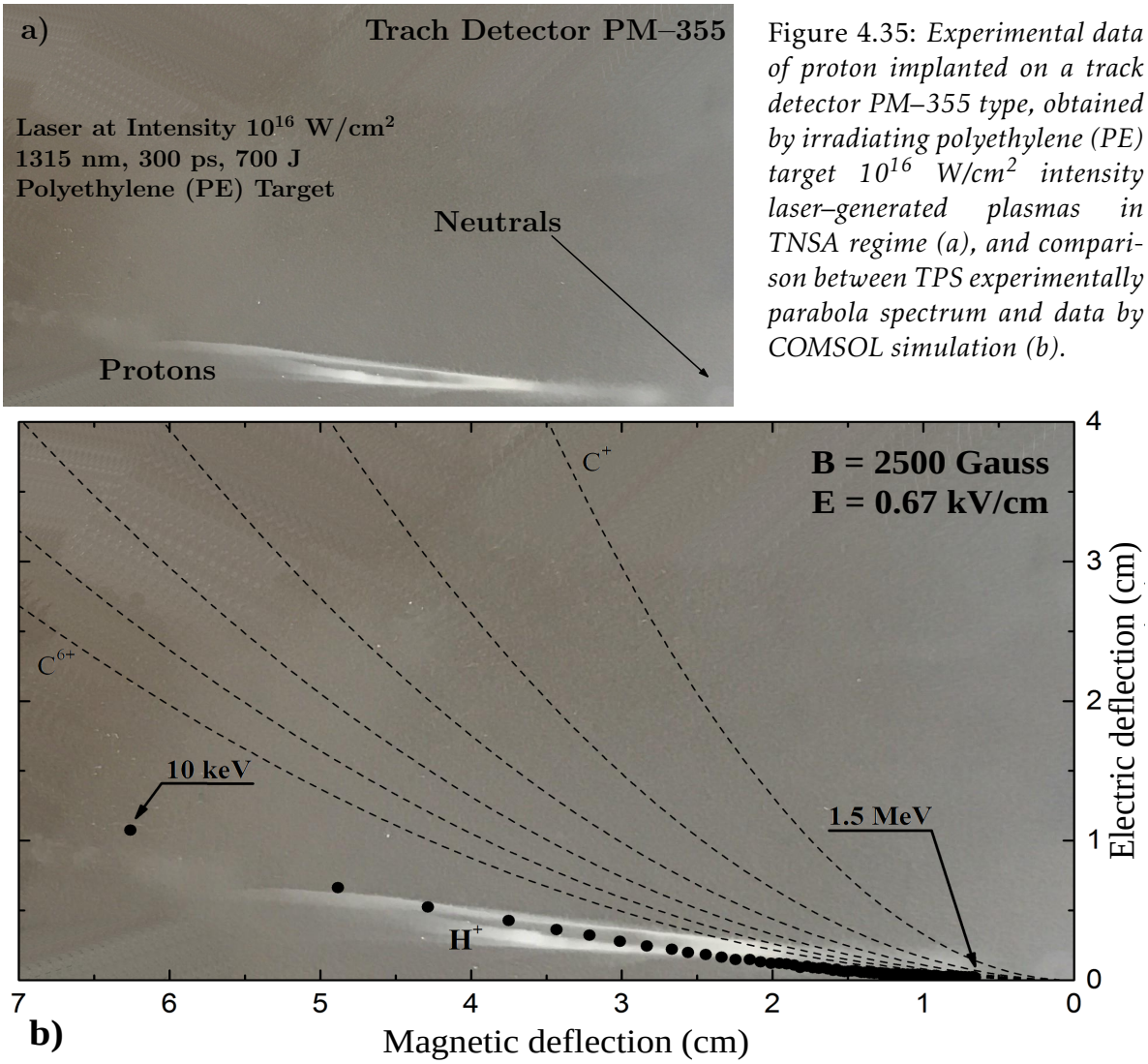

Figure 4.35: *Experimental data of proton implanted on a track detector PM–355 type, obtained by irradiating polyethylene (PE) target 10^{16} W/cm^2 intensity laser–generated plasmas in TNSA regime (a), and comparison between TPS experimentally parabola spectrum and data by COMSOL simulation (b).*

films it is necessary to perform a suitable chemical etching controlling solution (NaOH) concentration, time duration and etching temperature. Depending on the duration of the processing, it is possible to observe only the superficial traces of the carbon ions or protons at greater depth. The 1 *MeV* protons, in fact, are implanted in the plastic detector at greater depths (25 μm); on the other hand, 1 and 6 *MeV* carbon ions are implanted in the plastic detector at 2.5 and 8.5 μm, respectively, as calculated from SRIM code. Thus, when etching is obtained for quite long times the traces of carbon ions are erased, while only those of the protons emerge. Conversely, for a short time, the traces of carbon ions are visualized, while

those of the protons remain hidden. In the presented data reported in Figure 4.35a the traces of only protons are reported. Thus, the superficial etching has removed immediately the carbon ion tracks leaving the traces of the protons in the polymeric detector avoidable. The data allows observing a great agreement between the experimental data and those obtained by simulations, as shown in Figure 4.35b. In this case, we were able to obtain the maximum value of energy observed for the protons by measuring the minimum distance between the zero deflection and the proton parabola points, which is near to 1.5 *MeV*, also confirmed by complementary measures. The carbon ion curves obtained by a theoretical calculation are shown in Figure 4.35b.

Figure 4.36a reports the TPS spectrum obtained using an MCP detector coupled with a red phosphorus screen and a CCD camera, irradiating at PALS a thin polyethylene foil (5 μm in thickness) in the TNSA regime using 606 *J* laser pulse energy. In this case, the TPS sensitivity is very high and the six states of charge of the carbon and the protons emitted by the plasma can be well separated. The maximum proton energy corresponds to 1.5 *MeV*.

The Figure 4.36b shows the overlap between the data obtained experimentally at the PALS laboratory with laser energy of about 600 *J* and focal position of −100 μm, by irradiating deuterated polyethylene (–CD_2–), and the parabolas obtained by computational calculation with COMSOL. Deuterium ions are indistinguishable from C^{6+} ions due to the same mass–to–charge ratio. In this case the evaluated energy was of about 3 *MeV* per charge state, thus the maximum kinetic energy was ∼ 18 *MeV* for C^{6+}–ions and ∼ 3 *MeV* for protons. The increase in energy compared to the previous case is due to the D–D nuclear reactions that occur in the deuterium ion–rich plasma. In fact, this nuclear reaction can lead to the formation of $T(1.01\ MeV) + H^+(3.02\ MeV)$ or $^3He(0.82\ MeV) + n(2.45\ MeV)$, with the same probability, in accordance with the literature [213].

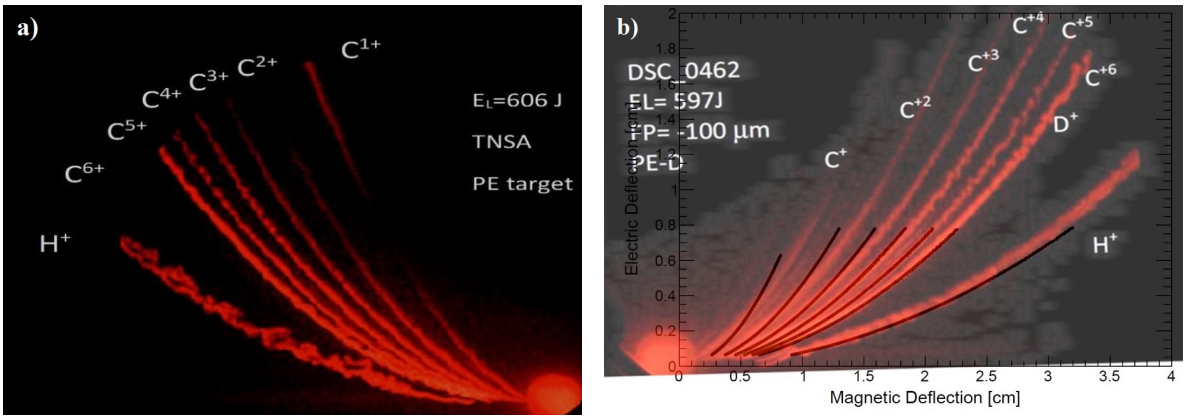

Figure 4.36: *TPS spectrogram obtained with 10^{16} W/cm^2 intensity at PALS Laboratory in Prague using an MCP detector, by irradiating a target of polyethylene (–CH_2–) (a) [**210**], and deuterated polyethylene (–CD_2–) with simulation by COMSOL software comparison (b) [**154**].*

4.3.4 TPS calibration for Electron diagnostics

Finally, this compact TPS has been calibrated, at the Messina MIFT Laboratory (University of Messina), by detection electrons in *keV* range, with the experimental setup shown in Figure 4.37a. Figure 4.37b–c shows the picture of the spectrogram for electrons obtained experimentally with its zoom; the overlap between COMSOL simulation data and experimental electron parabola is reported in Figure 4.37d.

The electrons detection is not very simple because of their small mass. In addition, due to their low energy of emission from the used electron gun, and for their very small mass, the magnetic and electric fields are significantly reduced with respect to previous cases, which are 7.5 *Gauss* and 0.1 *kV/cm*, respectively. Electron energy, however, is correlated to the

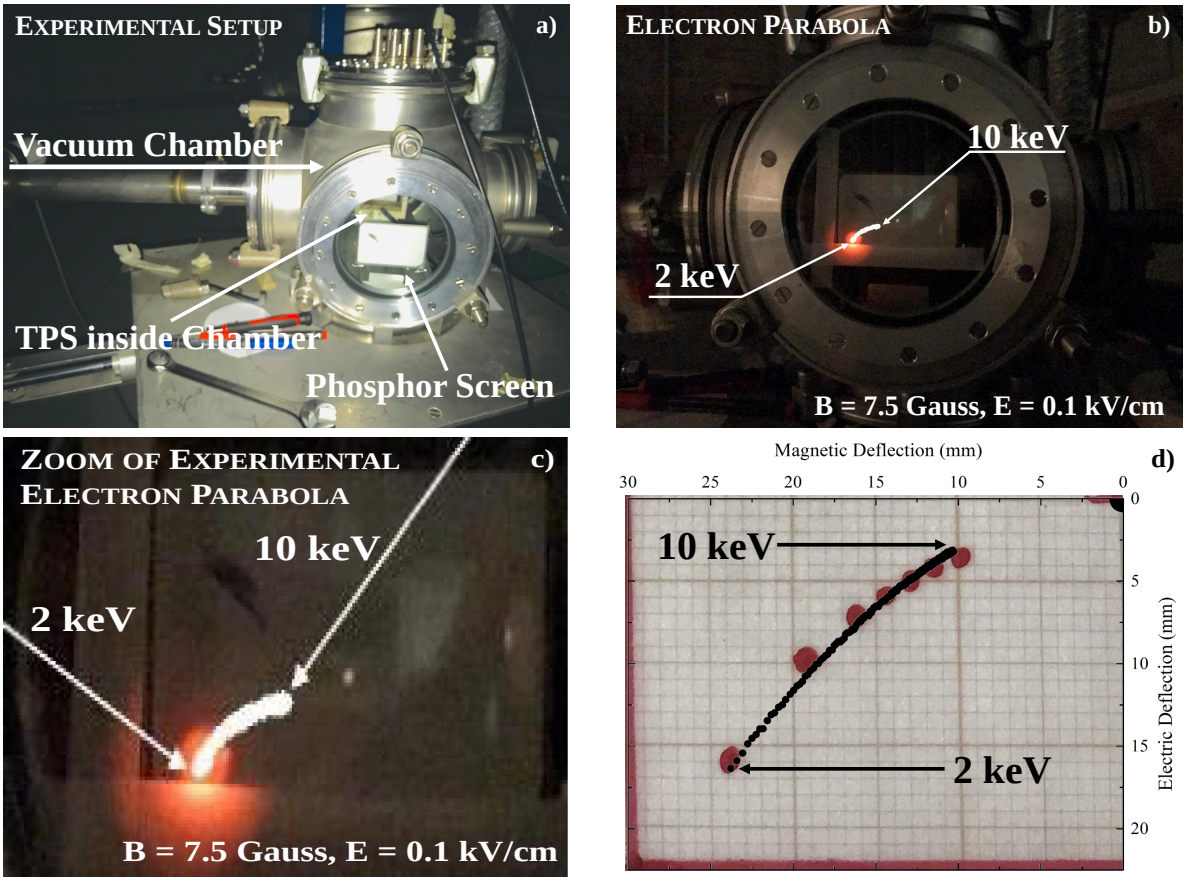

Figure 4.37: *Picture of the experimental setup (a), and of the spectrogram obtained experimentally at the Messina Laboratories, using an electron gun (b), with electrons parabola zoom (c), and overlapping with the simulation data obtained by COMSOL (d).*

plasma temperature and to the ion acceleration process in the TNSA regime. The experimental electrons parabola is reported digitally through the use of a phosphor screen, and superimposed on the curve obtained from the electrons simulation in the system of interest, performed by COMSOL software. The overlap between the experimental and simulative data shows a great agreement. This study has permitted the TPS calibration for electron beams with energies going from about 0.5 to 10 keV, representing a useful method to evaluate the electron plasma temperature of hot ionized gases.

4.3.5 Section Conclusions

The TPS is a device very versatile and easy to read when applied to plasmas generated by high laser intensities both for backward BPA and forward TNSA regimes. As we just see, the TPS gives a rapid response on the properties and species that make up a plasma characterized by energies of the order of tens of MeV per charge state or higher.
The compact TPS presented here, has the advantages to be a portable device, low volume, cheap and simple to be built, using permanent magnets and implemented with an ICR diagnostics for preliminary measurements in TOF approach, very useful for laser–generated plasma characterization. The main advantages with respect to more expensive and larger TPS of big facilities, consist of the simple construction, absence of high–current generators for electromagnets and expensive MCPs. A significant improvement can be obtained using a suitable MCP coupled to a phosphorous screen with a CCD camera, in order to obtain high spatial resolution parabola images using low and high ion energies, as that used at PALS Laboratory in the past years, of which one is reported in Figure 4.35.
It permits to evaluate the mass–to–charge ratio of the particles analyzed. Knowing the mass of the ion, it is possible to have informations about ionization degree of a plasma generated by laser pulses. In addition, the intensity of the parabolas impressed on the detector can give information on the abundance of ions in the plasma, and therefore on the energy distributions of these. The presented TPS is a very compact device (length of about 30 cm and weight less than 5 kg) that can be easily transported and that can be used both for cold and hot plasmas, generated by low and high laser intensities.
However, the compactness volume reduces the performance of the TPS due to magnetic and electrical deflection limitation do not permit a better separation between many parabolas in complex plasmas, and to measure very well high energetic particles, of the order of 10 MeV per charge state. Moreover, another defect in TPS could be that of failing to detect low–energy particles, such as those produced by medium–low intensity lasers ($< 10^{14}\ W/cm^2$) accelerating ions at low energies of the order of 1 keV per charge state or less. In addition, the accuracy of the measure is affected by more errors, of the order of 15%, due to the use of the less spatial resolution of Gafchromic images with respect to the MCP equipment.
Work is in progress to try to improve the applicability of this device to a higher range of energy values of the particles to be analyzed and to carry out measurements in other laboratories with different lasers at different intensities and wavelengths.

Chapter 5

Particle–in–Cell method to model the Laser–Plasma interaction

The Particle–In–Cell (PIC) method has a long history in the study of laser–plasma interaction. In the last few decades, however, the PIC method has become increasingly popular due to its analogy with actual plasmas. The latter are, in fact, a set of charged particles, i.e. electrons, protons, ions, which interact with each other through self–consistently generated fields. PIC codes are based on this assumption: a set of real particles is represented by a significantly lower number of macro–particles. Each of these macro–particles could be thought of as a cloud of real particles, which occupy a volume of finite space and all move at the same velocity. The fields of interaction are calculated by numeric solving of Maxwell's equations on fixed points of a suitably chosen spatial grid, and these are used to compute the Lorentz force acting on the particles, so as to update their positions and velocities. This generates a cycle that repeats itself in time intervals defined as time–step, and it is the core of every PIC code. In this chapter are introduced the principles of computational approach by particle–in–cell codes, and some of the most known artefacts related to it, such as self–heating. Subsequently, the fully relativistic EPOCH code, developed at the University of Warwick, will be introduced. The discussion will then focus on the input and output parameters of the EPOCH code, and on the optimal parameters to choose for a simulation. Finally, a study of a plasma generated by an fs laser pulse, with an intensity of the order of 10^{18} W/cm^2 through the 2D–EPOCH code is presented and discussed.

5.1 Understanding Particle–in–Cell approach

The *Particle–in–cell* (PIC) method refers to a technique used for the solving of specific differential equations on fixed points. The first computation PIC method dates back to 1955. However, although these models had the property of conserving exactly the total momentum, it did not conserve the total energy of the system. In fact, the total energy of the system, according to the type of time–differentiation used to solve the differential equations, increased or decreased as a result of numerical heating or numerical cooling, respectively [214]. We

have to wait until the early seventies, when *Langdon* [215] proposes a method for energy conservation based on Lagrangian formalism.
At present, PIC codes to simulate the collisionless plasma kinetics are among the most commonly used in plasma physics. The core of PIC algorithms has been extensively discussed, demonstrating its accuracy and stability in detail [216, 217]. This section will provide an overview of how PIC algorithms calculate the dynamics of interaction between electromagnetic waves and plasmas.

5.1.1 Overview on Numerical Calculation

There are three approaches for computation of plasma evolution by numerical calculation; they are the *hydrodynamics model*, the *Maxwell–Vlasov model* and *quasi–particles PIC method*. The hydrodynamic model is more suitable for plasmas generated by long pulses, in the order of nanoseconds, in which electrons heat the plasma through collisional effects and the condition of Local Thermodynamic Equilibrium (LTE) is assumed. For ultra–short pulses, electrons do not heat the plasma by collisional effects, so the plasma is out of the LTE condition and only the Maxwell–Vlasov or quasi–particle approach can be applied.
In the context of the computation of plasmas generated by femtosecond pulses, the Maxwell–Vlasov code offers the possibility of producing smooth results, handling a distribution function that returns the probability of finding a plasma particle in the phase space. On the other hand, this approach is very expensive from the point of view of computing resources; in fact, the distribution function must be solved in the six dimensions of the phase space, which may require supercomputers. Instead, the grid defined in the quasi–particle PIC model, which may also require the use of large amounts of computing resources, has half of the dimensions compared to that used in the Maxwell–Vlasov approach (only three spatial coordinates, against three spatial plus three momentum coordinates). Thus, the PIC method is certainly the most convenient for the calculation. The basic aspects of the three models are considered and discussed below [218, 219].

Hydrodynamics Model

In the hydrodynamic model the conservation equations of mass, moment and energy are coupled with the Maxwell equations. Moreover, for a fluid model, the assumption of local thermodynamic equilibrium LTE is introduced, so the knowledge of the equations of state of the system, such as the relation between temperature, pressure and so on, is mandatory for the resolution of the computational calculation. Assumption of LTE means that all species in the plasma have Mexwellian velocity distribution everywhere. This model represents a good approximation for plasmas generated by relatively low laser intensities, of the order of 10^{12} W/cm^2, and relatively long pulses, in the nanosecond regime. The interaction between ultrashort pulses and plasma cannot be adequately simulated with this technique because it cannot be described by fluid equations [220, 221].

Maxwell–Vlasov Model

The Maxwell–Vlasov model refers to a kinetic description of a collisionless plasma, in which the different species that constitute the plasma are described by a macroscopic distribution functions, $f_s(\boldsymbol{x},\boldsymbol{p},t)$, where s denotes a given species consisting of particles with charge q_s and mass m_s. Each particle has its own position in the phase space $(\boldsymbol{x},\boldsymbol{p})$ at the time t, where $\boldsymbol{x}$ represents the spatial coordinate for the degree of freedom and $\boldsymbol{p}$ is the momentum components. To describe the evolution of the distribution function $f_s(\boldsymbol{x},\boldsymbol{p},t)$, let's introduce the Vlasov equation for each species of particles [222]:

$$\left(\partial_t + \frac{\boldsymbol{p}}{m_s\gamma}\cdot\boldsymbol{\nabla} + \boldsymbol{F}_L\cdot\boldsymbol{\nabla}_{\boldsymbol{p}}\right) f_s = 0 \tag{5.1}$$

where γ is the relativistic Lorentz factor, and $\boldsymbol{F}_L$ is the Lorentz force, introduced in Equation 1.17. Lorentz's strength is due to the existence of collective magnetic, $\boldsymbol{B}(\boldsymbol{x},t)$, and electric, $\boldsymbol{\xi}(\boldsymbol{x},t)$, fields in the plasma, which must satisfy the *Maxwell equations*:

$$\boldsymbol{\nabla}\cdot\boldsymbol{B} = 0 \tag{5.2a}$$
$$\boldsymbol{\nabla}\cdot\boldsymbol{\xi} = \rho/\epsilon_0 \tag{5.2b}$$
$$\boldsymbol{\nabla}\times\boldsymbol{B} = \mu_0\boldsymbol{J} + \mu_0\epsilon_0\partial_t\boldsymbol{\xi} \tag{5.2c}$$
$$\boldsymbol{\nabla}\times\boldsymbol{\xi} = -\partial_t\boldsymbol{B} \tag{5.2d}$$

where ρ is the total electric charge density, ϵ_0 and μ_0 are the vacuum permittivity and permeability, respectively. The set of Maxwell's equations (Equation 5.2) and Equation 5.1, together with Lorentz's force, represent the self–consistent dynamics of the plasma, in which the particles in turn modify the magnetic and electric fields through their charge and current densities. This is a good approximation only if the collective effect are much higher than collision with nearby particles; thus, for this reason Equation 5.1 is considered collsionless. On the other hand, if collision is not negligible, a term for taking it into account is added on the right side of Vlasov equation.

Quasi–Particles approach (PIC Model)

Laser–generated plasmas are constituted by a large number of particles, including ions and electrons. For practical and computational reasons, the number of particles introduced into the simulation is lower than that actually present in a real plasma. Each of the simulated particles, called *quasi–particles* or *macro–particles*, represents a large number of real particles, through a multiplicative factor called weight, indicated by w_p. When the density changes, for a given number of simulated macro–particles, the weight changes in order to reproduce the real structure density. However, it is obvious that a reduction in the number of macro–particles in the simulation produces an increase in noise.

The quasi–particle method, or PIC, derives its name from the discretization of the distribution function f_s, reported in Equation 5.1, as the sum of N_s quasi–particles [222]:

$$f_s(\boldsymbol{x},\boldsymbol{p},t) = \sum_{p=0}^{N_s} w_p S\left[\boldsymbol{x}-\boldsymbol{x}_p(t)\right]\delta\left[\boldsymbol{p}-\boldsymbol{p}_p(t)\right] \tag{5.3}$$

where w_p is the numerical weight of the particle, $\boldsymbol{x}_p$ and $\boldsymbol{p}_p$ are the particle position and momentum respectively, δ is the Dirac delta function, and S is a shape function of position. Of course, the choice of shape function have an important impact on the numerical properties of the algorithm.
In one dimension, the spatial shape functions S must to be non–negative symmetric functions, which satisfy $\int S(\boldsymbol{x})d\boldsymbol{x} = 1$. The spatial shape function should also allow for interpolation of fields and currents at low computational impact. These properties are all satisfied by a class of functions called b-splines, which at zero order have the following form [222]:

$$S^{(0)}(x) = \Delta x\ \delta x \tag{5.4}$$

where Δx is the grid increment or spatial–step. The zero order b–splines represents the delta Dirac function. However, the zero order is never used because it leads to non–physical solutions; at *n–th* order (see Paragraph 5.1.3), b–spline class functions is recursive using convolution, and have the following form:

$$S^{(n)}(\boldsymbol{x}) = S^{(n-1)}(\boldsymbol{x}) * S^{(0)}(\boldsymbol{x}) \tag{5.5}$$

More generally, in three dimension the shape function can be write $S_n(\boldsymbol{x},\boldsymbol{y},\boldsymbol{z}) = S_n(\boldsymbol{x})\cdot S_n(\boldsymbol{y})\cdot S_n(\boldsymbol{z})$. The order of the interpolation is related to the resulting density smoothness. The interpolation error within a cell is smoother with higher order weighting scheme [223].

5.1.2 Core of PIC Algorithm

The cyclical operations that a standard PIC code performs during a single time-step can be summarized in the Figure 5.1. The initial position and velocity of the particles are used to calculate the current and charge densities on the grid positions, through the numerical weight, by the Equation 5.3, ($x_p, v_p \longrightarrow \rho_g, J_g$, where the particle properties are indicated with the subscript p while the grid properties with g). These are used to calculate the fields, using the Maxwell Equations 5.2 ($\rho_g, J_g \longrightarrow \xi_g, B_g$), and the new fields are used to calculate the Lorentz force acting on the particles ($\xi_g, B_g \longrightarrow F_p$). From this force are calculated the new particle positions and velocities ($F_p \longrightarrow x_p, v_p$), starting again the cycle.
Simply, the core of PIC solver can be distinguished in two coupled solvers: the first one is the *Field Solver*, which calculates Maxwell's equations for Electromagnetic (EM) field on a fixed spatial grid subject to the currents calculated by particle motions. The second is the *Particle Pusher*, which moves particles in the space under the influence of EM fields and calculates the currents due to particles motion. By these two solvers, the collisionless interaction of a kinetic plasma can be take into account.

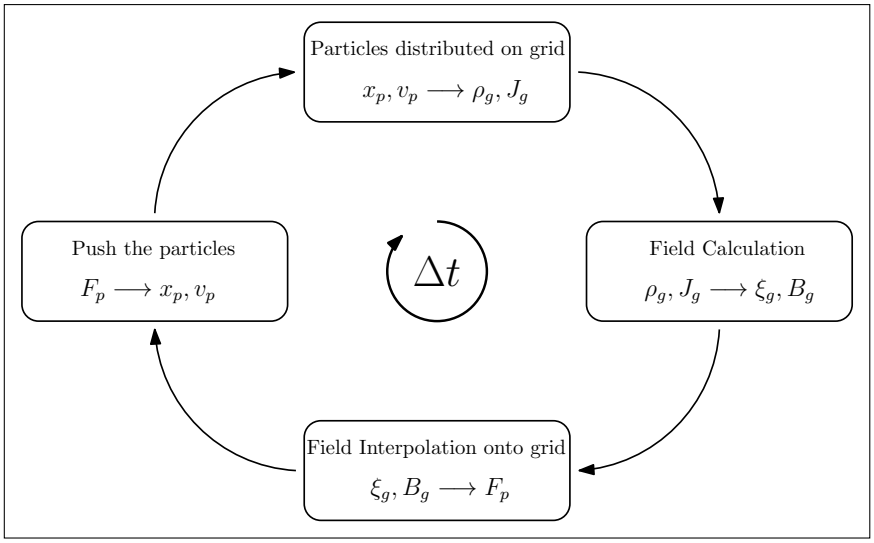

Figure 5.1: *General PIC code in a single time–step; the particles properties are indicated with the subscript "p" while the grid properties are indicated with the subscript "g".*

The Field Solver

Many PIC simulation codes use the *Finite–Difference Time–Domain* (FDTD) method as numerical solver of Maxwell's equations. The components of the magnetic and electric fields are defined on the Yee staggered grid [224], shown in the Figure 5.2. Here, electric field components are calculated in the middle of the edges and in the center of the square cell in the two-dimensional case, or in the middle of the cubic cell faces in the three-dimensional case; while magnetic field components are calculated in the middle of the edges and on the vertex of the square cell in the two-dimensional case, or in the middle of the edges of the cubic cell in the three-dimensional case. The grid staggering thus defined implies that the second order derivatives are easily implemented [225].

The FDTD implemented in many PIC codes uses the standard or modified leapfrog method [226], in which the electric and magnetic fields are updated both at half time–step and at full time–step. In a simple FDTD scheme, first the electric and magnetic fields, $\boldsymbol{\xi}$ and $\boldsymbol{B}$ respectively, are advanced on half time–step, from n to $n + 1/2$, using the current density calculated at n step:

$$\boldsymbol{\xi}^{n+\frac{1}{2}} = \boldsymbol{\xi}^{n} + \frac{\Delta t}{2}\left(c^2 \boldsymbol{\nabla} \times \boldsymbol{B}^{n} - \frac{\boldsymbol{J}^{n}}{\epsilon_0}\right) \tag{5.6a}$$

$$\boldsymbol{B}^{n+\frac{1}{2}} = \boldsymbol{B}^{n} - \frac{\Delta t}{2}\left(\boldsymbol{\nabla} \times \boldsymbol{\xi}^{n+\frac{1}{2}}\right) \tag{5.6b}$$

where Δt is the time–step, c is the speed of light and ϵ_0 is the vacuum permittivity. Now, the current density is update to $\boldsymbol{J}^{n+1}$ from the particle pusher (described in the following

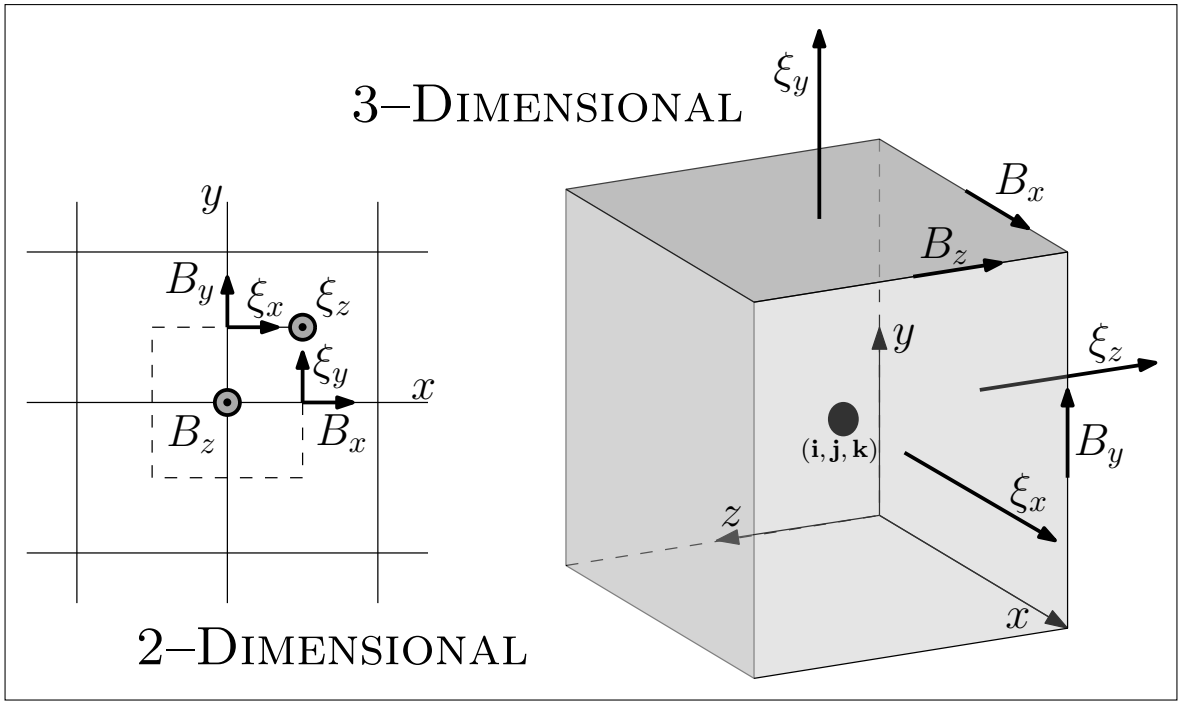

Figure 5.2: *Yee staggered grid used for the electric and magnetic fields solver in 2D and 3D simulation cell, (image inspired from ref [227]).*

paragraph), and so the field are updated from $n+1/2$ to $n+1$ to complete the step:

$$\boldsymbol{B}^{n+1} = \boldsymbol{B}^{n+\frac{1}{2}} - \frac{\Delta t}{2}\left(\boldsymbol{\nabla}\times\boldsymbol{\xi}^{n+\frac{1}{2}}\right) \tag{5.7a}$$

$$\boldsymbol{\xi}^{n+1} = \boldsymbol{\xi}^{n+\frac{1}{2}} + \frac{\Delta t}{2}\left(c^2\boldsymbol{\nabla}\times\boldsymbol{B}^{n+1} - \frac{\boldsymbol{J}^{n+1}}{\epsilon_0}\right) \tag{5.7b}$$

Note that the FDTD solvers are subject to a Courant–Friedrich–Lewy (CFL) condition. For the standard solver, the CFL condition requires the time–step to be smaller than:

$$\Delta t < \frac{1}{c\sqrt{\Delta x^{-2} + \Delta y^{-2} + \Delta z^{-2}}} \tag{5.8}$$

where Δx, Δy and Δz are the spacing of the grid along x, y and z direction, respectively. This modified leapfrog approach means that all fields can be defined at the same time and allows to calculate the half–step values required for particle push. This also makes the inclusion of additional physical packages, which often require EM fields either full or half–step values, easier [227].

The Particle Pusher

The particle pusher step calculates the relativistic motion equation for each particles in the simulation, under the influence of Lorentz Force. In order to calculate the trajectories with second order accuracy, electric and magnetic fields are used at half time-step, i.e. in the first half of the Field Solver [227]:

$$\boldsymbol{p}_\alpha^{n+1} = \boldsymbol{p}_\alpha^n + q_\alpha \Delta t \left[\boldsymbol{\xi}^{n+\frac{1}{2}} \left(\boldsymbol{x}_\alpha^{n+\frac{1}{2}} \right) + \boldsymbol{v}_\alpha^{n+\frac{1}{2}} \times \boldsymbol{B}^{n+\frac{1}{2}} \left(\boldsymbol{x}_\alpha^{n+\frac{1}{2}} \right) \right] \tag{5.9}$$

where $\boldsymbol{p}_\alpha$ is the momentum of the particle α, defined as $\boldsymbol{p}_\alpha = \gamma_\alpha m_\alpha \boldsymbol{v}_\alpha$, in which m_α and $\boldsymbol{v}_\alpha$ are the particle's mass and velocity respectively, and γ_α is the relativistic Lorentz factor. In Equation 5.9 above, q_α is the particle's charge and $\boldsymbol{x}_\alpha$ is its position in the space. Finally, $\boldsymbol{\xi}^{n+1/2}(\boldsymbol{x}_\alpha^{n+1/2})$ and $\boldsymbol{B}^{n+1/2}(\boldsymbol{x}_\alpha^{n+1/2})$ are the electric and magnetic field calculated at half time–step in the $\boldsymbol{x}_\alpha^{n+1/2}$ particle position. Thus, current due to particle motion is updated from $\boldsymbol{J}^n$ to $\boldsymbol{J}^{n+1}$, and the fields are updated from $n+1/2$ to $n+1$ to complete a step, as described in the previous paragraph.
The Equation 5.9 may be split into two parts: a first part responsible for the acceleration due to the electric field, and a second due to the rotation of charged particles into magnetic field; this approach is called Boris rotation algorithm [228], and is used in many PIC codes.
Through the Lorentz equation written above (Equation 5.9), the particles are pushed, and their positions and velocities are then updated. The current that is generated by them, used for the resolutions of the Maxwell equations, can be calculated using different approaches [229–231]. These methods of charge conservation ensure that the divergence of the electric field, Equation 5.2b, is always satisfied without solving it.

5.1.3 Numerical Stability and Accuracy

The Particle–in–Cell approach is very useful for studying the kinetic behaviour of plasma, due to its first principles treatment of the particle and field dynamics, and self–consistent solution. As already discussed, a problem related to PIC simulations are the so–called phenomena of numerical instability, which often lead to self–heating, resulting in a dramatic energy increase in the system. However, sometimes even though they conserve energy, the numerical values obtained are not physically correct. To avoid effects related to the instability of the simulation, or the accuracy of the calculations, the parameters of the simulations must be chosen appropriately. The most important parameters that characterize a simulation are the time–step to complete cycle (Δt), the spatial–step (Δx, in one dimension) also refereed to as cell width or as cell size to the simulation box, the number of particles introduced into each plasma–cell, the shape function (S–function, introduced in Equation 5.3), the current smoothing algorithms (if applicable) and the boundary conditions of the simulation box. Some tips to improve numerical stability and to ensure the accuracy of the calculations are presented and discussed below.

Choice of appropriate Numerical Parameters

We have already seen in the field solver case, that the time–step between one cycle and the next must satisfy the CFL condition, Equation 5.8. This is a fundamental requirement for a stable propagation of the electromagnetic wave in the simulation box [216]. Moreover, this condition ensures that the macroparticles, do not move more than one cell per time–step, so as to avoid inaccuracies in the current computation. In the case of 3-dimensional PIC codes, for the CFL condition, the time–step is sets as follows:

$$\Delta t = \frac{K}{c\sqrt{\Delta x^{-2} + \Delta y^{-2} + \Delta z^{-2}}} \tag{5.10}$$

where K is a constant value between 0 and 1 ($0 < K < 1$), generally sets close to 1, in order to satisfy the CFL condition in Equation 5.8. For example, if the spatial–step is chosen to 10 nm in each direction and $K = 0.95$, from Equation 5.10 the time–step will be ~ 0.02 fs; in order to perform a simulation 500 fs long, the PIC code will run about ~ 25000 iterations.
A further condition that the time–step has to satisfy is to ensure the propagation of the electron plasma waves, which must be able to oscillate at the electronic frequency of the plasma, ω_{pe}, [232]:

$$\omega_{pe}\Delta t \leq 2 \tag{5.11}$$

Even if this condition is fulfilled, plasma waves may often be distorted. Therefore, it is generally preferable to set the time–step, in order that its product for the plasma frequency is less or equal to 0.2 [232].
Let's now consider the spatial–step; this must be small enough to resolve the physical phenomena investigated, and also to minimize as much as possible the phenomenon of self–heating. In order to resolve the physical phenomena at plasma–vacuum boundary, the spatial–step in the direction of the large density gradient (e.g. in the *x–direction*), may be lower than the plasma skin depth:

$$\Delta x \leq \frac{c}{\omega_{pe}} \tag{5.12}$$

For example, if the electron density of the simulated plasma was 2×10^{29} el/m^{-3}, it means that the electron plasma frequency was about $\sim 2.5 \times 10^{16}$ Hz, thus the spatial–step must be less than ~ 12 nm. However, numerical heating may emerge due to the effects of aliasing plasma waves. Aliasing occurs when the waves of the highest frequencies cannot be represented on a discrete grid, and are then combined with the waves of the lowest frequencies. In order to reduce the numerical heating the cell say may satisfy an additional requirement:

$$\Delta x \leq \pi\lambda_D \tag{5.13}$$

where λ_D is the Debye length. However, by using shape functions of a higher order than the top–hat ones and smoothing current algorithm [223, 227], the condition introduced in the Equation 5.13 is not so relevant, due to the strong reduction of the aliasing effect.

Lastly, a very important parameter is the particle number of each species introduced per cell that constitutes the plasma. This value strongly depends on the phenomena in the plasma studied, on the density of particles entered and on the type of shape function chosen. The appropriate choice of this parameter depends on the experience of the PIC code user.

The Shape function

In order to calculate the forces acting on the particles, it is necessary to know the value of the electric and magnetic fields at each point of the grid where the particles are located. On the other hand, from the position of the particles, the currents must be calculated in order to update the electric field. Since, as already described, each macro–particles represents a number of real particles, it is necessary to choose spatial distribution of particle weighting throughout the volume occupied by the simulated particle [227].
The simplest and fastest method, from a computational point of view, is to distribute the particles throughout the cell volume ($\Delta x \times \Delta y \times \Delta z$), although it introduces a lot of noise into the simulation results. This is commonly called *top–hat* function, and represents the first–order of the b–splines class function shown in the Figure 5.3:

$$S^{(1)}(\boldsymbol{x}) = \begin{cases} 1 & \text{if} \quad \boldsymbol{x} \leq \frac{\Delta x}{2} \\ 0 & \text{otherwise} \end{cases} \tag{5.14}$$

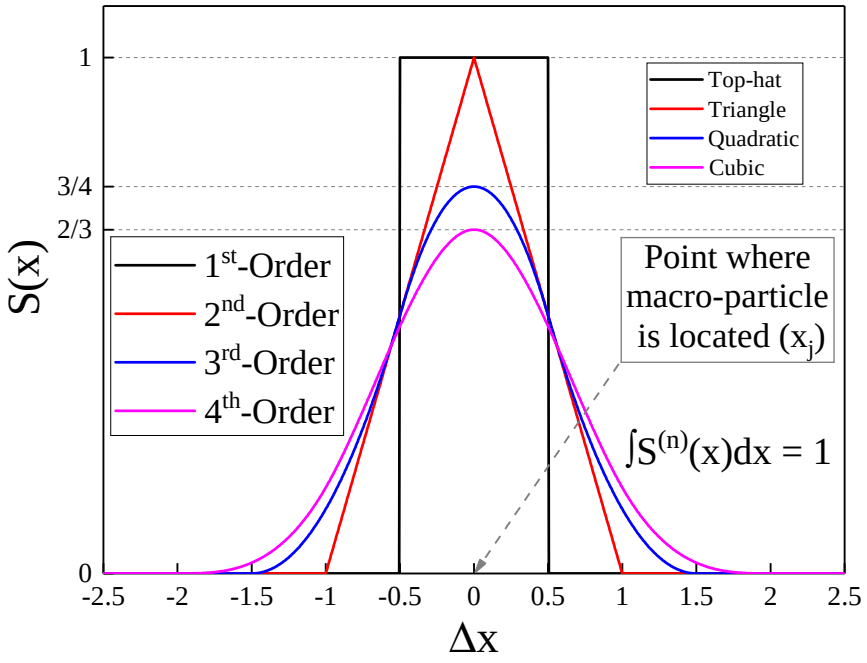

Figure 5.3: *First, second, third and fourth order particle shape function implemented in several PIC code. These are the b–splines class functions, which are used to describe the distribution assumed by the real particles that constitute a macro–particle. The lowest order is the simplest and quickest but produces very noisy solutions.*

Since functions must have unitary integral, another way to represent the distribution of real particles is to consider a triangular shape, as the second–order of the b–splines function class. This approach is based on the assumption that the macro–particle is located at the peak position of the triangular shape function, which has a width of $2\Delta x$ (in one dimension, $2\Delta x \times 2\Delta y \times 2\Delta z$ in three dimension, of course), as shown in the Figure 5.3. In mathematical terms it can be written as follows [217]:

$$S^{(2)}(\boldsymbol{x}) = \begin{cases} 1 - \frac{|x_j - \boldsymbol{x}|}{\Delta x} & \text{if} \quad |x_j - \boldsymbol{x}| < \Delta x \\ 0 & \text{otherwise} \end{cases} \tag{5.15}$$

where x_j is the spatial point where the macro–particle is located. Equation 5.15 is called *triangle* function. This is the most used in several PIC codes as standard approach, because it is certainly a good compromise between results accuracy and calculation speed.
However, sometimes it is possible to deal with cases in which the plasma density is high; this implies that the Debye length is decreased, and the spatial–step may not satisfy the Equation 5.13, which may lead to numerical heating. By increasing the order of the shape function to the third, shown in Figure 5.3 the undesirable effects of non–physical heating are suppressed. In this case the function is called *quadratic*, and it is written:

$$S^{(3)}(\boldsymbol{x}) = \begin{cases} \frac{3}{4} - \left(\frac{x_j - \boldsymbol{x}}{\Delta x}\right)^2 & \text{if} \quad |x_j - \boldsymbol{x}| \leq \frac{\Delta x}{2} \\ \frac{1}{2}\left(\frac{3}{2} - \frac{|x_j - \boldsymbol{x}|}{\Delta x}\right)^2 & \text{if} \quad \frac{\Delta x}{2} < |x_j - \boldsymbol{x}| \leq \frac{3\Delta x}{2} \\ 0 & \text{otherwise} \end{cases} \tag{5.16}$$

The result of Equation 5.16 is plotted in the Figure 5.3, which shows that the quadric shape function, whose peak is taken at the position where the macro–particle is placed, has a width of $3\Delta x$, in one dimension ($3\Delta x \times 3\Delta y \times 3\Delta z$ in three dimension). The use of this distribution function increases the required calculation time; however, the simulations has more stability even with far fewer simulated macro–particles. The results obtained are obviously more accurate. However, the quadratic function over three cells is not used as the one sided nature requires the same computational effort as that over four cells for less accuracy [227]. Thus the fourth order of the b–splines function is the following [222]:

$$S^{(4)}(\boldsymbol{x}) = \begin{cases} \frac{2}{3} - \left(\frac{x_j - \boldsymbol{x}}{\Delta x}\right)^2 + \frac{1}{2}\left|\frac{x_j - \boldsymbol{x}}{\Delta x}\right|^3 & \text{if} \quad |x_j - \boldsymbol{x}| \leq \Delta x \\ \frac{4}{3}\left(1 - \frac{1}{2}\frac{|x_j - \boldsymbol{x}|}{\Delta x}\right)^3 & \text{if} \quad \Delta x < |x_j - \boldsymbol{x}| \leq 2\Delta x \\ 0 & \text{otherwise} \end{cases} \tag{5.17}$$

The Equation 5.17 is called *cubic* function; it is centered where the macro–particle is located, as it can be seen from plot in Figure 5.3. Equation 5.17 is defined between $\pm 2\Delta x$, thus it has a width of $4\Delta x$ in one dimension, and $4\Delta x \times 4\Delta y \times 4\Delta z$ in three dimensions.

Higher orders of the b–spline function classes are rarely used due to high computational costs, although the simulations would be increasingly stable. However, the order can be increased through the convolution of the functions again and again. It is clear that top–hat shape function should never be used for laser–solid simulations [227].
Another way to limit the non–physical effect of self–heating is to use smoothed currents, combined with higher–order shape functions. Several PIC codes provide for the use of both options. A simple way to achieve this is to weigh the currents over neighbouring cells, such that the total current sum over all cells is preserved [233].

Boundary Conditions

Once each time–loop has been completed, the boundary conditions are applied to particles and fields in the simulation box. The boundary conditions are artificial conditions which allow to keep a finite dimension in the simulation domain. Boundary conditions have a strong impact on the numerical calculation stability and on the results physical accuracy.

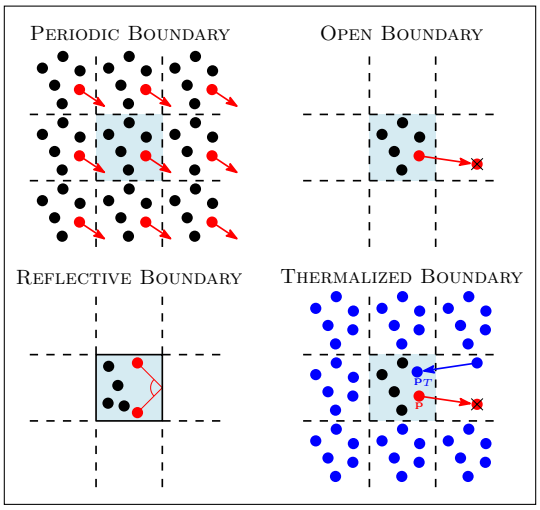

Figure 5.4: *Representation of particle's boundary condition in particle–in–cell code.*

The macro–particles that reach the edge of the simulation box can be wrapped round to the opposite boundary (*periodic–boundary*), can be stopped (momentum set to zero), removed from the simulation (*open–boundary*), reflected in the opposite direction (*reflective–boundary*, where momentum and position follow specular reflection rules) or could be thermalized (*thermalized–boundary*), as shown in Figure 5.4. The latter case means the using of "thermal bath" of particles at the boundary; i.e. a macro–particle that leave the simulation box are replicated by a new macro–particles, whose new momentum is randomly sampled in a Maxwell velocity distribution given by a temperature corresponding to that of the initial conditions.

Similar conditions may apply to electromagnetic waves reaching the edge of the simulation box. The periodic condition assumes that the EM waves impacting on one edge of the simulation box are replaced from the opposite border. The open condition, on the other hand, indicates that the EM wave is transmitted through the simulation box border with the lowest reflection; in order to further reflection minimize of EM waves from the boundary, it is possible to use the so–called perfectly matched layer boundary conditions, alternatively called *absorbing–boundaries* [234]. Thus, there are various boundary conditions for field and particles. Their choice mostly depends both on the phenomenon studied and user's experience.

5.1.4 Further advanced PIC code aspects

The core of the PIC codes described up to now models ideal collsionless plasma without taking into account ionization processes, radiation losses or quantum phenomena. Ionization processes are very significant due to the macroscopic consequences in laser–plasma interaction, such as laser defocusing, electron injection in specific plasma areas, and fast shuttering, which is the process whereby a critical reflective surface is formed in the plasma mirror. The effects of quantum electrodynamics (QED) emission processes must also be addressed in the new generation of 10PW–Lasers [227]. The QED model includes the pair production, synchrotron emission and radiation reactions.
In order to take into account these physical phenomena, many PIC codes use optional modules that adopt a semi–classical approach to calculate the radiation losses of electrons, or the Monte Carlo method [235] to calculate ionization or quantum phenomena [227].
There are currently many PIC codes used for model laser–plasma interaction, some of the most common are shown in the table. The symbols RZ and RZ$^+$ represent the codes that use axisymmetric coordinates instead of Cartesian ones; sometimes it is possible to obtain advantages in terms of computational cost from the use of these [236]. In the following sections the fully relativistic 3D PIC–EPOCH code will be discussed in its basic aspects and implemented for comparison with experimental measurements.

Table 5.1: *Most common PIC codes updated to 2019 (from ref [236]).*

Code Name	Type	Availability/License	Website/References
ALaDyn	EM–PIC 3D	Open/GPLv3+	https://aladyn.github.io/ALaDyn
Architet	EM–PIC RZ	Open/GPL	https://github.com/albz/Architect
EPOCH	EM–PIC 3D	Collaborators/GPL	https://cfsa-pmw.warwick.ac.uk/EPOCH/epoch
FBPIC	EM–PIC RZ$^+$	Open/modified BSD	https://fbpic.github.io
LSP	EM–PIC 3D/RZ	Commercial/Proprietary	http://www.northropgrumman.com
MAGIC	EM–PIC 3D	Commercial/Proprietary	http://www.northropgrumman.com
OSIRIS	EM–PIC RZ$^+$	Collaborators/Proprietary	https://picksc.idre.ucla.edu/software/software-production-codes/osiris
PICCANTE	EM–PIC 3D	Open/GPLv3+	http://aladyn.github.io/piccante
PIConGPU	EM–PIC 3D	Open/GPLv3+	https://www.hzdr.de
SMILEI	EM–PIC 3D	Open/CeCILL	http://www.maisondelasimulation.fr/projects/Smilei/html/licence.html
VSim (Vorpal)	EM–PIC 3D	Commercial/Proprietary	https://www.txcorp.com/vsim
WARP	EM–PIC 3D/RZ$^+$	Open/modified BSD	http://warp.lbl.gov

EM = electromagnetic; PIC = Particle-in-Cell; 3D = three–dimensional; RZ = axisymmetric; RZ$^+$ = axisymmetric with azimuthal Fourier decomposition.

5.2 PIC EPOCH Code

The *Extendible PIC Open Collaboration* (EPOCH) code is a plasma physics simulation code which uses the Particle–in–Cell method, developed by University of Warwick (UK). The code runs in agreement with the method outlined in section 5.1 of this chapter.
The structure of EPOCH is composed of three source codes, the first for simulation in one dimension, the second for simulations in two dimensions, and the third for full three–dimensional simulations. In this document it will take into account only one–dimensional or two–dimensional simulations, due to the limited computing power, (three–dimensional simulations require the use of so–called High Performance Computers, HPC). Since the code is designed for the widest and most different users, the entire code is written in International System (SI) Units; although some parts of the code, for convenience, use other units (where specified). The user does not interact directly with the code, but defines the initial conditions and simulation parameters by means of a text file called "*input.deck*". The EPOCH User's Manual [237] contains all the complete details to correctly set the parameters in the input.dek, but here the most relevant to this topic will be discussed.
The input deck has a blocks structure, in which several parameters are provided, depending on the block of pertinence. Each block starts with "begin:*block*" and ends with "end:*block*" (for the block named *block*). There are currently fourteen different blocks that can be loaded into the EPOCH code input deck [237]. Anyway, the ones most relevant to this discussion (some of which are mandatory) are the following:

- *control* – Contains information about the general code setup.
- *boundaries* – Contains information about the boundary conditions.
- *constant* – Contains information about user defined constants and expressions.
- *laser* – Contains information about laser parameter.
- *species* – Contains information about the particles' species which are used in the code.
- *output* – Contains information about the outputs' type and when/how to dump them.

Other blocks, that will not be discussed for the speech linearity, are for example: *fields*, which contain information on the EM fields specified at the beginning of the simulation; *window*, which contains information on how to move the simulation box if used (often used to speed up calculations); *collisions*, which contains information on plasma particle collisions in the simulation box; *qed*, which contains information about quantum electrodynamics pairs production; and still described in the reference [237].
Since the input deck is read in two steps from the code, the blocks can be entered in any order. The first step is to read which blocks are present, and whether all mandatory ones have been defined; EPOCH then allocates memory for the grid and particles. In the second step the initial conditions are read, if they are valid and there aren't syntax errors the code starts to run. EPOCH is an excellent choice for the study of collisionless plasma kinetics, where collections of physical particles are represented by a smaller number of macro–particles.

5.2.1 Initial Conditions

The initial conditions must be defined in an input deck obligatorily, and are used to set the basic parameters of the simulation box. Following are described some of the fundamental parameters used in the numerical computation that will follow in this chapter. The first block to be taken into account is the control block. In this block are defined all the parameters of the grid, the dimensions of the simulation box, the ending time of the simulation, the type of initial conditions to use, and more. The control block is mandatory in EPOCH.

```
begin:control
    # Global number of Gridpoints
    nx = 6000
    ny = 3000

    # Size Domain
    x_min = -30.0 * micron
    x_max = 30.0 * micron
    y_min = -15.0 * micron
    y_max = 15.0 * micron

    # Final time of Simulation
    t_end = 500 * femto

    particle_tstart = 50 * femto

    smooth_currents = T

    dt_multiplier = 0.95

    dlb_threshold = 0.5

    stdout_frequency = 10
end:control
```

Input.deck 5.1: *Example of 2D control block.*

Input.deck 5.1 shows an example of a control block. Note that the "#" symbol is treated as a comment character, i.e. the code will ignore everything that is written to follow it, on the line where it is inserted. Thus, the parameters nx and ny represent the number of points into which the grid is divided in the x and y directions, respectively (if the simulation should be performed in three dimensions, it is necessary to introduce also nz, obviously). The dimensions of the simulation box are set by the parameters x_min and x_max in the *x–direction*, and y_min and y_max in the *y–direction*; if there is a third dimension, it is introduced through the definitions of z_min and z_max. The example shown in the Input.deck 5.1, indicates that the simulation box will be 60 μm long in the *x–direction* and 30 μm wide in the *y–direction*. Since the number of grid points along x is 6000 and the number of grid points along y is 3000, the simulation box will be composed by cells of 10×10 nm size. The final simulation time is indicated by t_end; this value is given in seconds, so it must be multiplied by the appropriate scaling factor.

The parameters inserted below the final simulation time in the Input.deck 5.1 are not mandatory, but are inserted in the example because they are used in the simulations that will be presented later. To specify when starting to push the particles it is used the command particle_tstart; the particles pusher solver has a big computational impact, and sometimes it is preferred to inactivate it until the electromagnetic wave is nearby to the plasma particles. The smooth_currents is a logical command, and is followed by "T", which means true, or

"F", meaning false. When activated, a smoothing function is applied to the currents that are generated during the particles pusher; this reduces the noise and self–heating of the system, as already explained. The `dt_multiplier` corresponds to the K value of the Equation 5.10, in order to satisfy the time CFL condition; smaller is this value and smaller will be the time–step. Finally, `dlb_threshold` and `stdout_frequency` are two commands which are used first to balance the processors at code start–up, and second to print a status message line after every given number of time–steps, respectively. Many other parameters can be entered in the command block, as it can see from reference [237].

```
begin:boundaries
    bc_x_min = simple_laser
    bc_x_max = simple_outflow
    bc_y_min_particle = thermal
    bc_y_max_particle = thermal
    bc_y_min_field = simple_outflow
    bc_y_max_field = simple_outflow
end:boundaries
```

Input.deck 5.2: *Typical 2D boundaries block.*

The boundaries block sets the boundary conditions of each boundary of the domain; a two dimensional example is shown in Input.deck 5.2. The boundary conditions at the edges of the *x–direction* can be attached using `bc_x_min` and `bc_x_max`; the same is true in the *y–direction* (and also in the *z–direction*, if the simulation is done in 3D). Any boundary condition can be specified if valid for field (laser) or particle.

An electromagnetic wave can be introduced into the domain using the `simple_laser` boundary condition. This indicates that the electromagnetic wave impinging on the input edge is transmitted with as little reflection as possible. The particles, on the other hand, are totally transmitted. The `simple_outflow` boundary condition is a simplified version of the first one, which has the same transmission properties as the incident wave and particles, but which cannot have EM wave sources attached to it. The `thermal` boundary condition, instead, has the properties already described in the Paragraph 5.1.3; meaning that a particle which leaves the domain from this boundary is replaced with a particle having randomly selected velocity according to a Maxwellian distribution given by a temperature set by the user. Other boundary conditions, such as `periodic`, `open`, `reflect`, and others, already described in the Paragraph 5.1.3, can be introduced depending on the computation model to be performed.

The constant block is used to define parameters or mathematical expressions that can then be used by name later in the code, even in other blocks; it makes the input deck more flexible and maintainable, but it is not mandatory. In the example shown in the Input.deck 5.3 several pre-defined constants have been used (like `pi` and `c`) and also many functions can be used (`critical`, `sqrt`, `gauss`, and others) [237].

```
begin:constant
    plasma_thick = 13.0 * micron
    cell_xsize = (x_max - x_min) / nx
    nx_foil = plasma_thick / cell_xsize
    las_lambda0 = 800 * nano
    omega0 = 2.0 * pi * c / las_lambda0
    n_crit = critical(omega0)
end:constant
```

Input.deck 5.3: *Typical 2D constant block.*

5.2.2 Sets Laser Parameters

Once the simulation box has been created and all its main properties have been defined, the laser beam can be introduced inside it. The EM wave is attached to the boundary where `simple_laser` has been set, in the boundary block.

```
begin:laser
    boundary = x_min
    intensity_w_cm2 = 4.0e18
    lambda = 800 * nano
    pol_angle = 0.0
    phase = 0.0
    t_profile = gauss(time,45*femto,27*femto)
    t_start = 0.0 * femto
    t_end = 90.0 * femto
end:laser
```

Input.deck 5.4: *Example of 2D laser block.*

In the Input.deck 5.4 is shown an example of a laser block, where a few, but not all, features of the laser beam are reported. As already explained, it is necessary to indicate from which edge the laser enters the box, which must be in agreement with the boundaries conditions; this is defined by the `boundary` command, as shown in the Input.deck 5.4. In this example the laser is attached by `x_min`, and moves to `x_max` direction.

The variables used in the laser block are clearly self–explanatory. Anyway, `intensity_w_cm2` is used to define the intensity of the laser beam in W/cm^2, instead of `intensity` which defines the intensity in W/m^2. There are many other parameters that can be defined in the laser block, for a more complete description it is suggested to see the reference [237].
One variable on which more notice is needed is the time profile of the laser, indicated by `t_profile`. This parameter is used to define the time profile for the laser field amplitude. The laser field is multiplied by this variable, reason why it is generally desirable to use values between 0 and 1, so as not to cause increases in laser intensity. The function used in the example in the Input.deck 5.4 is a Gaussian function:

$$f(x) = \exp\left[-\left(\frac{x - x_0}{w_0}\right)^2\right] \tag{5.18}$$

where x represents the independent variable, which in this case is `time`, x_0 is the center of the distribution and w_0 is the characteristic width. Thus, the Full Width at Half Maximum (FWHM) is defined as follows:

$$\text{FWHM} = 2w_0\sqrt{\ln 2} \tag{5.19}$$

For the function introduced in the example in Input.deck 5.4, the FWHM is about 45 *fs*. When the `t_profile` variable is not included in the input deck, the laser field is multiplied by 1. The difference between a constant pulse and a Gaussian time pulse is shown in the Figure 5.5, obtained by EPOCH code. It should be noted that, more clearly in Figure 5.5a, the core of the FDTD solver for the electromagnetic field can introduce spurious solutions if the laser field changes suddenly. Using the variables `t_start` and `t_end`, which define the

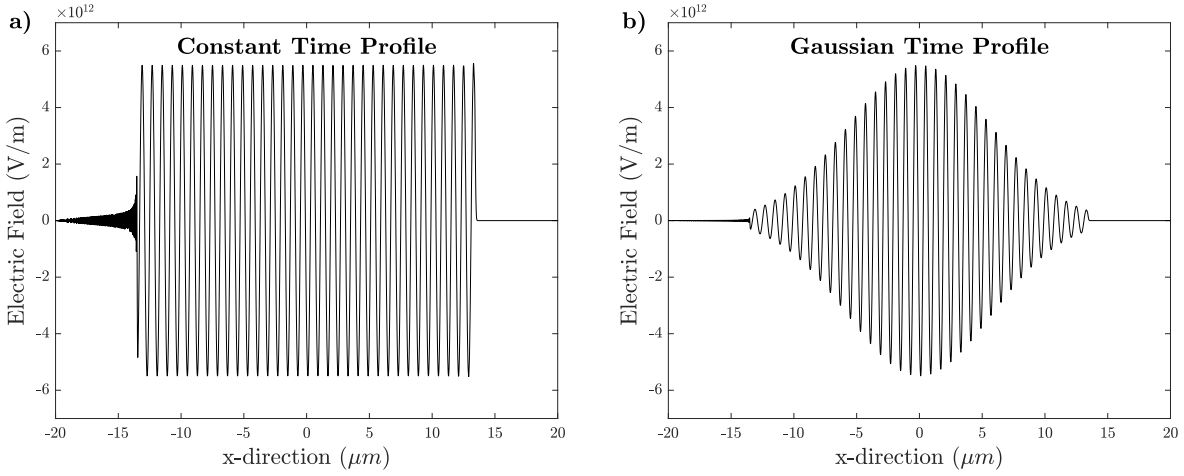

Figure 5.5: *Simulated laser pulse with a length of 90 fs and constant time profile (a) or Gaussian time profile (b); obtained by EPOCH code.*

start and end time of the laser pulse in seconds, respectively, the laser pulse is hard cutoff. Since the final time was not an exact multiple of the period, in Figure 5.5a, the result is the introduction of spurious oscillations behind the pulse. Depending on the phase of the laser pulse defined by the user, if its amplitude does not start from zero, a similar result can be produced at the beginning of the field [237].

Focusing a Laser Beam

In the input deck shown in the Input.deck 5.4, there is no mention about the spatial profile of the laser beam. In many laser applications, the beam is considered to be Gaussian shaped; the amplitude profile of the electric and magnetic field are modulated by a Gaussian function, as well as the intensity of the beam. The electric and magnetic field amplitude along any point on the beam's propagation axis (for a given wavelength and polarization) are determined by the waist w_0, which represents the focus.

To correctly focus a laser beam in a PIC simulation, some parameters need to be defined; one of these is the *Rayleigh length* or *Rayleigh range*, which represents the distance along the direction of propagation of a beam from the waist to the point where the spot area is doubled, as shown in Figure 5.6:

$$z_R = \frac{\pi w_0^2}{\lambda} \tag{5.20}$$

where λ is the wavelength. At a position x, from the focal point, along the beam axis, the

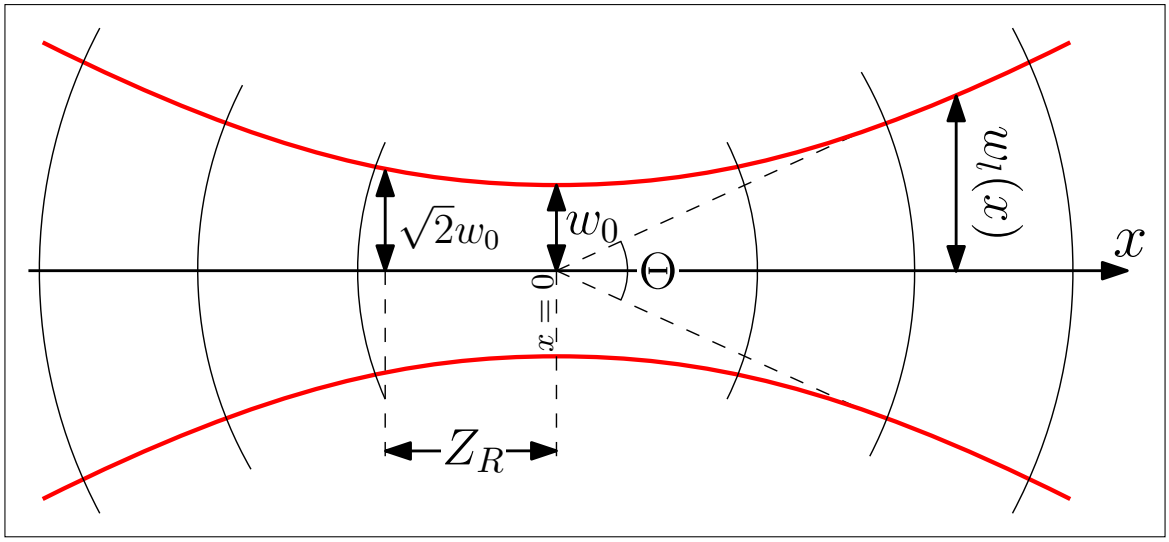

Figure 5.6: *Gaussian beam profile as a function of the axial distance x.*

spot size parameter $w_l(x)$ is given by [238]:

$$w_l(x) = w_0\sqrt{1+\left(\frac{x}{z_R}\right)^2} \tag{5.21}$$

From its definition, the minimum value of w_l corresponds to w_0 when $x = 0$, of course, instead when $x = z_R$ thus $w_l = \sqrt{2}w_0$.
Another parameter to consider is the curvature of the wavefront. At $x = 0$ the curvature approaches zero. The radius of curvature of the wavefront is given by the formula:

$$R(x) = x\left[1+\left(\frac{z_R}{x}\right)^2\right] \tag{5.22}$$

Thus the radius of curvature is infinite at the beam waist. The curvature radius is important to describe the phase of the incident EM wave.
Finally, in order to correctly scale the intensity of the beam, when the focal position does not match to the target surface, let's introduce a geometric factor that takes this effect into account:

$$F_I^{2D} = \left[1+\left(\frac{x}{z_R}\right)^2\right]^{-1/2} \tag{5.23}$$

defined in two dimensional scheme. Thus for example, if we have to simulate a laser with a wavelength of 0.8 μm and the waist was $w_0 = 8.5$ μm, the Rayleigh range from Equation 5.20 will be $z_R \backsimeq 141.3$ μm. At a distance of 50 μm from the focal position, the intensity factor in

2D will be about $F_I^{2D} \backsimeq 0.94$; so the laser intensity reaching the target surface will be reduced of about 6%, due to the increase in the size of the laser spot.

```
begin:constant
    las_lambda0 = 800 * nano
    wt = 75.0*femto/(2.0*sqrt(loge(2.0)))
    w0 = 10.0*micro/(2.0*sqrt(loge(2.0)))
    FP = 0.0 * micro
    zR = pi * w0^2 / las_lambda0
    wl = w0 * sqrt(1.0+(FP^2)/(zR^2))
    f2D = 1.0 / sqrt(1.0+FP^2/zR^2)
end:constant

begin:laser
    boundary = x_min
    intensity_w_cm2 = 4.0e18 * f2D
    lambda = las_lambda0
    profile = gauss(y,0.0,wl)
    t_profile = gauss(time,45*femto,wt)
    t_start = 0.0 * femto
    t_end = 90.0 * femto
end:laser
```

Input.deck 5.5: *Gaussian Space–time profile.*

To scale the spatial profile according to the focal position, the just mentioned parameters are defined in the constants block. The spatial profile of the laser is taken into account with the `profile` variable, to be inserted in the laser block, as shown in the Input.deck 5.5. With this command, the laser field is multiplied by the defined function, in this case Gaussian. The product of the field for the chosen function is evaluated at the boundary, where it is attached. It is advisable that the function has values between 0 and 1, so as not to increase the field introduced by the user. The Figure 5.7 shows a 2D plot of a laser beam with a Gaussian spatial profile, and a unitary time profile (Figure 5.7a) or a Gaussian time profile also (Figure 5.7b), obtained by means of the parameters shown in Input.deck 5.5.

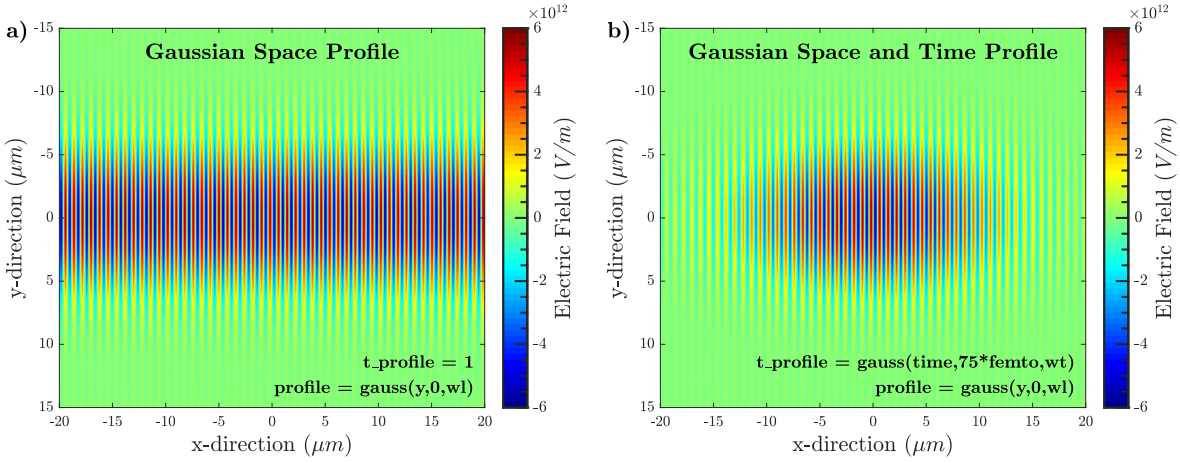

Figure 5.7: *Laser pulse with Gaussian spatial profile and constant time profile (*`t_profile=1`*) (a) or Gaussian time profile (b); obtained by EPOCH, using the input deck of the Input.deck 5.5.*

5.2.3 Introducing Particles in Simulation

Now the simulation box can be populated by the particles of the plasma that we want to simulate, such as electrons, protons, and others. In the input deck the particles are taken into account through the *species block*.

```
begin:species
    name = electron
    charge = -1.0
    mass = 1.0
    npart_per_cell = 100
    density = 3.4e29
    temp_ev = 1000
end:species
```

Input.deck 5.6: *Example of 2D species block.*

The Input.deck 5.6 shows an example of a species block for the electron definition in the input deck. Each particle species in the plasma is defined in electronic charge units and masses. In this way, for example, protons will be defined by `charge = 1.0` and `mass = 1836.0`. The `name` is a mandatory parameter, and it is used to identify the specie in any consequent input block and for labelling species data in output dumps.

In this input block we can specify the number of particles per cell, for the defined species, using the command `npart_per_cell`; this must be an integer value. However, often, when the plasma does not completely fill the simulation box, but is defined only in a range of lengths, such as when a solid target has to be simulated, and when multiple species with different number densities are introduced; in these conditions it is preferable to use the parameter `npart`. This simply defines the number of total macro–particles that have to be loaded at the beginning of the simulation. In order to take into consideration the number of cells in which the macro–particles will be inserted effectively, in the definition of the *constants block* in Input.deck 5.3, the parameter `nx_foil` entered took into account the number of cells constituted the simulated plasma; in a similar way we can define `ny_foil` or `nz_foil`, in y and z direction respectively. Therefore, in this way, if one wants to simulate 100 macro–particles per cell that composes the foil, the parameter to be introduced in two dimension will be: `npart = 100 * nx_foil * ny_foil`.
Finally, the particle density of the plasma is introduced with the `density` parameter, and it is set in m^{-3} units. By using the variable `mass_density` the density value introduced is set in kg/m^3. If the density is defined as shown in the input deck in the Input.deck 5.6, the particles density will fill the entire simulation box. In order to set an isotropic temperature distribution for the particles, in eV, it possible to use `temp_ev` parameter. More other optionals parameters could be add at this block [237].
However, as often occurs, the target does not fill the entire simulation box, but is restricted to a certain domain along one or more dimensions, depending on the thickness and size of the plasma foil that must be investigated. Sometimes, it can also happen to have to simulate complex structures, with density parameters that change domain by domain. In order to take into account all these phenomena, a conditional instruction can be used to appropriately define the simulation model.

For example, let's suppose that we have to simulate a target 13 μm thick at constant electronic density of 3.4×10^{29} m^{-3}, and that this is positioned in the simulation box starting from position $x = 0$; the condition that has to be written in the species block will be the following:

```
begin:species
    name = electron
    charge = -1.0
    mass = 1.0
    npart = 10000 * nx_foil
    density = if((x lt 13 * micro) and (x gt 0), 3.4e29, 0.0)
    temp_ev = 1000
end:species
```

Input.deck 5.7: *Example of 1D species block for electrons with density distributed between 0 and 13 µm. The parameter* `nx_foil` *is defined in Input.deck 5.3.*

In the Input.deck 5.7, the definition of density means: "if the *x–dimension* is less than 13 μm and the *x–dimension* is greater than 0 μm, then the density is 3.4×10^{29} m^{-3}, otherwise it will be 0.0". The number of particles introduced is multiplied by the number of cells that constitute the plasma, defined in the Input.deck 5.3.
However, sometimes it happens that the density structure that has to be reproduced is not constant in a given direction. For this purpose, to the constant density between 0 and 13 μm of the previous case, we add two electronic densities with increasing and decreasing exponential shape, before and after the foil with constant structure.

```
begin:species
    name = electron
    charge = -1.0
    mass = 1.0
    npart = 10000 * (nx_preplasma + nx_foil + nx_postplasma)
    density = if((x lt 0.0) and (x gt (-15*micro)), 1.7e27*exp(x/(7.5*micro)), 0.0)
    density = if((x lt 13*micro) and (x gt 0), 3.4e29, density(electron))
    density = if((x lt 20*micro) and (x gt 13*micro), 1.7e27*exp(-( x-13*micro )/
    /( 3.5*micro )), density(electron))
    temp_ev = 1000
end:species
```

Input.deck 5.8: *Example of 1D species block for electrons with increasing exponential shape density between -15 and 0 µm, constant density distributed between 0 and 13 µm and decreasing exponential shape density between 13 and 20 µm. The parameter* `nx_preplasma` *and* `nx_postplasma` *is defined in the same way of* `nx_foil` *in Input.deck 5.3.*

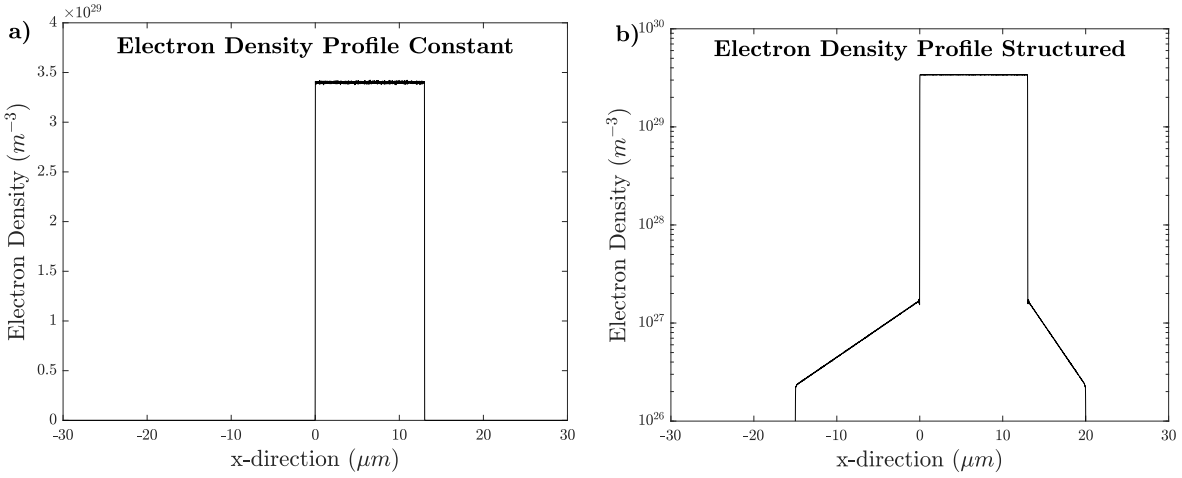

Figure 5.8: *Electron density profile as function of x–direction, defined constant between 0 and 13 μm (a), and same profile but structured as exponential shape between both -15 and 0 μm, and 13 and 20 μm (b).*

In the example in Input.deck 5.8, before the constant electronic density range, for x ranging from -15 μm to 0 μm, the electronic density takes on the value of $1.7 \times 10^{27} \exp(x/7.5\mu m)$, i.e. an increasing exponential profile, where at 0 μm it reaches its maximum value of 1.7×10^{27}. Between 13 μm and 20 μm, instead, a decreasing exponential profile has been assumed, according to the relation$1.7 \times 10^{27} \exp[-(x - 13\mu m)/3.5\mu m]$.
The examples for the species block shown in Input.deck 5.7 and the one in Input.deck 5.8, are reported graphically in Figure 5.8(a-b), respectively. The electronic density profiles were obtained with EPOCH-1D. If we consider a Ti:Sapphire laser with a wavelength of 800 nm, the critical density will be about 1.7×10^{27} m^{-3}. Thus, the Figure 5.8a show a constant density profile at about $200n_{cr}$, and Figure 5.8b report a profile in which the target at $200n_{cr}$ is preceded by a pre–plasma of increasing exponential shape from 0 to critical density, and a post–plasma profile with decreasing exponential shape from n_{cr} to zero.

5.2.4 Output Parameters

The final block that remains to be dealt with among those mainly of relevance in this discussion is the *output block*. In such block all the parameters of interest are defined. The outputs are divided into two categories: those related to the grid, ie the grid's physical geometry, electric and magnetic fields, current densities; and those related to particles, such as momentum, number densities, charge densities, temperature, and so on. As we have seen the total run time is indicated in the *control block*; in the *output block* the user can define how to cut this time in order to extrapolate the simulation data for each established period.

```
begin:output
    name = outputs
    file_prefix = o

    dt_snapshot = 20 * femto

    # Properties on grid
    grid = always + single
    ex = always + single
    ey = always + single
    ez = always + single
    bx = always + single
    by = always + single
    bz = always + single
    jx = never
    jy = never
    jz = never

    # Properties at particle positions
    particle_grid = always + species + single
    particle_weight = always + species
    px = always + species + single
    py = always + species + single
    pz = always + species + single
    number_density = always + species +
    single + no_sum
    mass_density = never
    charge_density = always + species
    ekbar = never
    temperature = always + species + single
end:output
```

Input.deck 5.9: *Example of output block.*

The Input.deck 5.9 report an example of *output block*, in which the mainly important variables are reported. The `file_prefix` directive defines a prefix to be placed in front of every output's file that the *output block* generates. It is generally more used when multiple *output blocks* are defined, so as not to override the files. In order to set the interval between output dumps in simulation, it is possible to use `dt_snapshot`. This value is given in seconds, thus it must be multiply for the appropriate scale factor. The code does not guarantee that the outputs will be written exactly to `dt_snapshot`, but it does guarantee that they will be produced at the first iteration corresponding to the time greater or equal than `dt_snapshot`. However, each of the variables present in the *output block*, shown in the Input.deck 5.9, can be switched on with the command `always`, or switched off with the command `never`; when using `never`, the variable is not written in the results at any dumps. Exclusively for the properties related to the particles in the simulation, it is possible to apply also other directives, such us `species`, `single`, `no_sum` and others, like shown in Input.deck 5.9.

Therefore, `species` is used to subdivide the derived output in species by species (if the plasma is formed by different particles such us electrons, protons, and so on), `single`, is introduced to write the variable in single precision, `no_sum`, is take into account in order for not sum over all species, and other parameters [237].

Some of the properties that are defined on the regular Cartesian mesh are: the `grid`, which defines the location of the grid variables, the electric field (`ex`, `ey`, `ez`), the magnetic field (`bx`,

by, bz) and the current density (jx, jy, jz) in the three directions. For particle, the properties to be accounted, will be: particle_grid, which defines the physical grid where the particles are positioned, particle_weight, which takes into account the weighting function which describes how many real particles the macro–particles represent, the momenta (px, py, pz) in the three directions, the number density of the particles on the grid (number_density), the temperature of the particles on the grid (temperature), and more. For a more detailed description see reference [237].

5.2.5 Parameters choice to reduce Self–Heating

When performing a PIC–coded simulation, it is important to ensure that the conditions set, are optimal enough to minimize numerical heating. The chosen parameters vary from case to case, and it is always better to check that there are no temperature increases due to non–physical phenomena in the system.
To verify the stability of the simulations carried out with PIC-EPOCH in two dimensions (version 4.9.0), some tests are presented in which the macro–particles are always initialized at a temperature of 1 *keV*. The Figure 5.9a shows the trend of the numerical self–heating as a function of time. The simulation was performed for a box of 100×100 cells, whose boundary conditions are periodic. Each square cell has a size of 10 *nm*. The density set for electrons is $1.7 \times 10^{29}\ m^{-3}$. The decrease in the number of macro–particles per cell causes a drastic increase in temperature for non–physical effects. For a number of macro–particles between 100 and 500, temperature increases from 1 *keV* to less than 2.5 *keV* in 500 *fs*. The

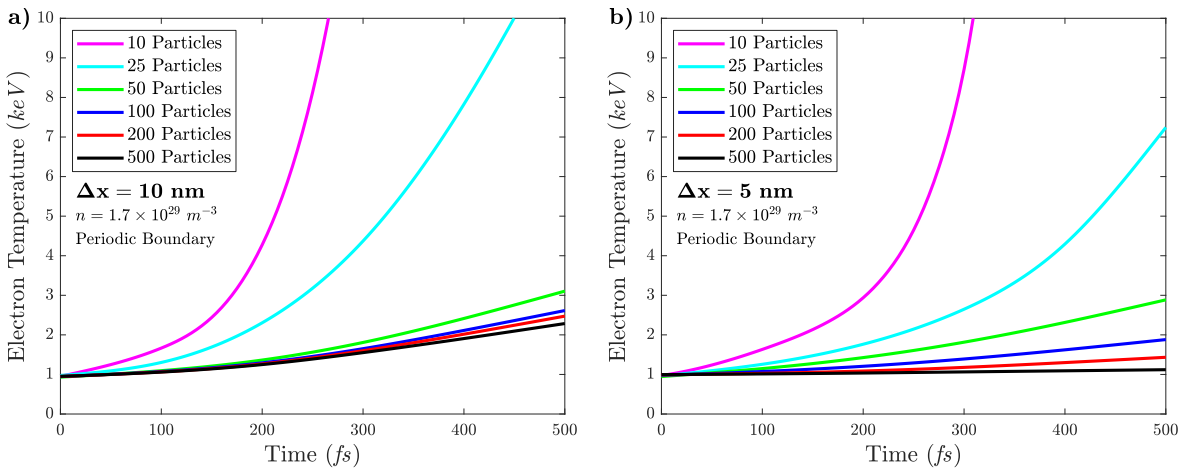

Figure 5.9: *Temperature increase due to self–heating as a function of time, for different macro–particles numbers per cell, electronic density of* $1.7 \times 10^{29}\ m^{-3}$*, periodic boundary conditions, and with a space–step of 10 nm (a) or 5 nm (b) in both x and y directions.*

effect is more severe with a much lower number of macro–particles, as in the case of 10 and 25 electrons per cell, where the temperature exceeds 10 *keV* in about 250 and 450 *fs*.

By decreasing the spatial–step, however, the effect of numerical heating goes down, as shown in Figure 5.9b. The reduction in cell size, obviously, produces greater stability in the simulation. The computations shown in Figure 5.9b are calculated in the same condition as the previously case, but with a spatial–step of 5 *nm* in each directions. For the simulation with 10 macro–particles, at 300 *fs*, there is a decrease of 80.4% of the numerical heating, even though the value remains high. For 25 micro–particles the decrease at 400 *fs* is 97.2%. The stability of the simulation grows as the number of macro–particles increases; for 500 macro–particles per cell, under the simulation conditions shown in Figure 5.9b, the electronic temperature remains almost constant in 500 *fs* time simulation. As one might expect, decreasing the spatial–step, that also means decreasing the time–step in accordance with the Equation 5.10, results in a higher accuracy of the data obtained, especially when high densities have to be simulated.

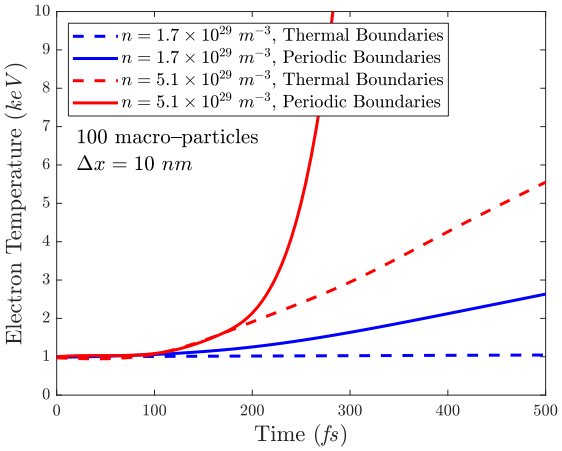

Figure 5.10: *Electron temperature trend as a function of time at densities of* 1.7×10^{29} m^{-3} *and* 5.1×10^{29} m^{-3}, *blue and red curves respectively. The thermal or periodic boundaries conditions, dashed or continuous curve respectively, affect the numerical self–heating. The simulations are performed for 100 macro–particles and spatial–step of 10 nm.*

For very high densities, the undesirable effects of numerical heating tend to increase. The Figure 5.10 shows two trends at different densities, respectively of 1.7×10^{29} m^{-3} and 5.1×10^{29} m^{-3} (blue and red lines). Simulations are performed for 100 macro–particles per cell, with 10 *nm* spatial–step. The choice of appropriate boundary conditions reduces the effects of non–physical self–heating of the system, as discussed in Section 5.1.3. In fact, here thermal or periodic boundary conditions are used (dotted or continuous lines respectively). The thermal conditions are largely stable for the simulated system. However, the really excessive density for the red line (5.1×10^{29} m^{-3}), requires further improvements of the simulation techniques, which can also lead to a substantial increase of the calculation time, such as the use of a greater order shape function, higher number of macro–particles, smaller spatial–size, and more.

Note that the self–heating tends to increase with time, hence, longer simulations may increase non–physical heating effects. The input parameters are correlated to each other in order to resolve the laser–plasma interaction; it's a user's task to find a compromise that does not overburden the calculation and, at same time, minimizes effect of numerical heating.

5.3 Plasma study using PIC–EPOCH code

Submitted Paper[2019]

Ion acceleration by *fs* laser in TNSA regime and comparison of TOF spectra with PIC simulations

L. Torrisi and G. Costa
Dipartimento di Scienze Fisiche, MIFT, Università di Messina, V.le F.S. D'Alcontres 31, 98166 S. Agata, Messina, Italy

Submitted as: L. Torrisi and G. Costa: "Ion acceleration by *fs* laser in TNSA regime and comparison of TOF spectra with PIC simulations", *Physical Review Accelerators and Beams*, (2019)
Available from: Not Available Yet
Publication Date: Received 19 April 2019

In this section is presented a study comparing data obtained experimentally and the PIC simulation with the EPOCH code in two dimensions. The ion acceleration though an *fs* laser irradiating a graphene oxide foil in TNSA regime is investigated using a SiC detector connected in Time–Of–Flight configuration. The experimental data indicated a maximum proton energy of 1.8 *MeV* and a large amount of carbon ions accelerated at different energies depending on their charge state. PIC simulations applied to the studied target given the electron density as a function of the space and of the time and permits to evaluate the electrical field developed in the rear side of the foil driving the forward ion acceleration. The simulation indicates that the carbon ions are subjected to a lower acceleration with respect to protons, due to their slow velocity, depending on the charge–to–mass ratio. The latter does not permit carbon ions to be affected by the maximum electric field but to a lower intensity due to the time decay of the electric field. Considering the angular emission of protons and the six carbon ions, the charge particles' Boltzmann energy distributions, with fixed cut–off at high energy, are in agreement with the experimental measurements of energy. This work represents an innovative comparison of experimental and simulation data for high intensity laser–generated plasmas, because literature does not report such an approach starting from spectra acquired using semiconductor detectors. In fact, for the first time, are reported the comparison between experimental ion measurements using TOF technique performed by a SiC detector and PIC simulation results, for TNSA regime experiments, by using an *fs* laser at 4×10^{18} W/cm^2 intensity [239].

5.3.1 Experimental Setup and Method

The experiments were performed at the *Institute of Plasma Physics and Laser Microfusion* (IPPLM) of Warsaw (Poland) using a Ti–Sapphire laser operating at 800 *nm* wavelength, with 313 *mJ* pulse energy, 45 *fs* pulse duration, 10^9 contrasts, focused to 10 μm spot diameter, with an intensity of about 8×10^{18} W/cm^2 and in single shot.

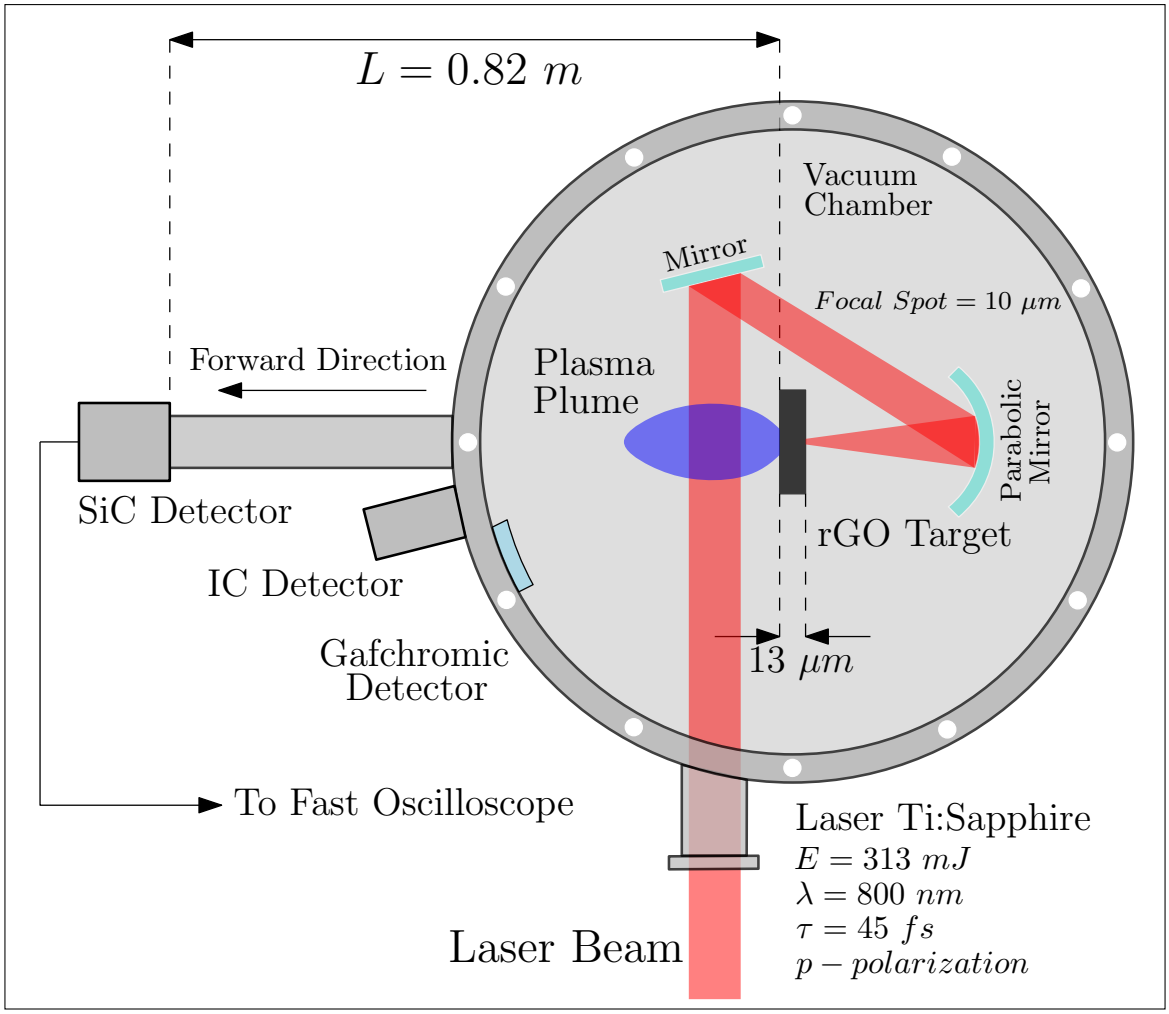

Figure 5.11: *Schematic representation of the experimental setup.*

The solid target consists in graphene oxide (GO) foil, 13 μm in thickness, irradiated at an incidence angle of 3°. Such target was chosen for the interest towards an innovative foil containing high carbon and hydrogen concentration, mechanically high resistant, ready to become reduced and highly conductive just irradiated by the laser pulse, in accordance with the literature [240]. The target preparation method is described in previous paper [241].

The plasma diagnostics use a SiC detector, having 4 mm^2 active surface area and 80 μm active depth, placed at a known distance from the target (82 cm), along the normal to the target surface for TOF measurements of photons, electrons, and ions. The solid angle of the SiC detector, very high accurate detector in this experiment, is very low and corresponds

to 6 μsr. SiC detector also allows to detect X–rays, electrons, and ions in the same TOF spectrum. Moreover, due to its energy gap of 3.3 eV it is blind to visible radiation and does not reveal the intense emission due to visible light coming out from the plasma. In addition, its leakage current at room temperature is more than two orders of magnitude lower with respect to silicon detector, permitting to have high sensitivity. More details on SiC detectors have been discussed in chapter 4 of this book, in Section 4.1.5.
An ion collector (Faraday Cup) was also employed operating in TOF connection (70 cm from the target) placed in forward at 3° angle with respect to the normal to the surface. Gafchromic films (HD–V2) were employed to evince the presence of high energetic protons filtered by suitable Aluminium (Al) absorbers. Being the proton range in Al of 14.4 μm and 41.6 μm for 1 MeV and 2 MeV, an Al absorber of 15 μm and another of 42 μm were employed to cover the Gafchromic detector to reveal protons higher than 1 MeV and 2 MeV, respectively. Ion stopping powers, energy loss, and ranges were calculated using SRIM code [175]. Figure 5.11 reports the schematization of the experimental setup just described.
We compare the experimental results with 2D–Particle in Cell simulation by the use of EPOCH code [237], (version 4.9.0). The cell box is set to dimension of $50\mu m \times 30\mu m$ (x–*direction* × y–*direction*), from -20 μm to 30 μm in the x–*direction* and between ±15 μm in the y–*direction*. The box contains square cells with a size of 10 nm, in order to have simulation stability, due to the high electron density of the solid, to resolve the plasma skin depth.

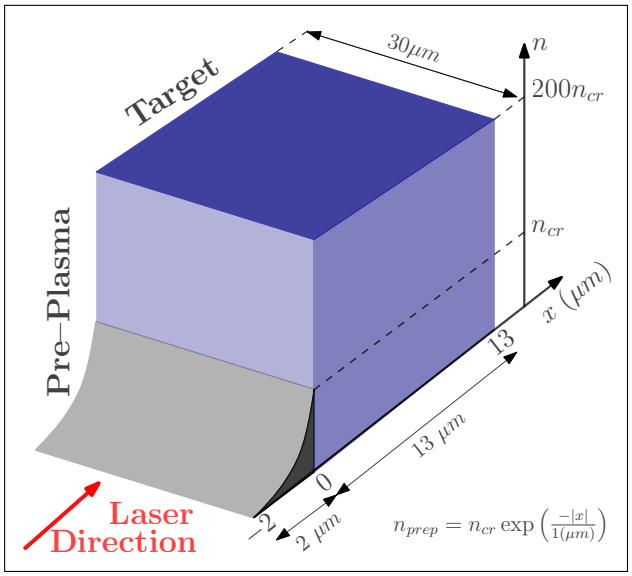

Figure 5.12: *Illustration of the electron density in the simulation.*

The target density is that of the graphene oxide, i.e. 1.7 g/cm^3. Here we assume that the carbon atoms of the bulk are in the fourth ionization state, then the electron density set in the simulated plasma is 3.4×10^{23} $electrons/cm^3$. Thus, because critical density depends on the laser wavelength and it is 1.7×10^{21} $electrons/cm^3$ from Equation 1.39, the target electron density corresponds to $200 \times n_{cr}$, which is defined between 0 and 13 μm, according to target length. In addition, boundary conditions are chosen as thermal along the edges of the y–*direction*, and simple laser or simple outflow along the x–*direction*, in order to reduce the self–heating.

In order to take into account pre–plasma formation, due to pre–pulse interaction with the target, we introduce an increasing exponential shape for electrons density, namely n_{prep}, up

to critical density, n_{cr}, defined between -2 μm and 0 μm in x backward direction [242], which has the following form:

$$n_{prep} = n_{cr} \exp\left(-\frac{|x|}{1\ \mu m}\right) \tag{5.24}$$

Thus, the pre–plasma has a short range of 2 μm, and decreases its value at $0.37 n_{cr}$ at 1 μm from the target surface. In Figure 5.12 shows schematically the electrons profile density introduced in the simulation box; at the beginning the laser interacts with a under–critical plasma, because of the increasing exponential shape of the pre–plasma, and then it hits the over–critical plasma.
It was introduced 90 electrons per cell in the entire plasma size; in the bulk, we introduce 50 macro–particles of carbon 6+ per cell, at densities of $50 n_{cr}$ (i.e. $1/4 n_e$). Finally, 20 nm of rear surface thickness, with respect to the laser pulse direction, contains 2000 particles per cell for each carbon charge state and for protons. The shape function is the default EPOCH function, i.e. second order triangular shape. For the fields we use the standard second order Yee scheme for solving Maxwell's equations.
The laser pulse enters in the simulation box from $x = -20\ \mu m$, and reaches the target at the time referred to as $t = 0$. Is assumed a laser pulse intensity of $4 \times 10^{18}\ W/cm^2$ with normal incidence on the target, and p–polarized. The decrease in intensity compared to the experimental case is justifiable because the energy of the ions tends to be exaggerated in 2D simulations, because of the reduced degrees of freedom. The pulse has a Gaussian temporal profile, with an FWHM of 45 fs. The full pulse duration is chosen to 90 fs. The PIC–simulation code returns the output value of interest every 20 fs, as defined by the user.

5.3.2 Comparison between Experimental and Simulation Results

The SiC–TOF spectrum acquired by irradiating the GO foil using a single laser shot is reported in Figure 5.13. The spectrum reports a photopeak due to the detection of X–rays and relativistic electrons emitted from the plasma, followed by a large, structured and intense ion signal, in agreement with similar experiments using SiC–TOF technique [212]. The faster–detected ions are protons, due to hydrogen presents in the sample as water, C–O–H functional groups chemically bonded to C atomic structure, and absorbed as gas in the GO foil. The minimum flight time of the proton signal is measured at 44 ns, corresponding to a velocity of $1.87 \times 10^7\ m/s$ and to kinetic energy of 1.8 MeV. Protons are followed, at higher TOF values, by an intense and structured peak due to the main elements composing the target, i.e. to the accelerated carbon ions, with a velocity lower than protons. The net and high discontinuity of the ion spectrum between the little proton peak and the bigger ion peak occurs at a TOF of about 83 ns, corresponding to the detection of carbon ions at a kinetic energy of 6 MeV.
The maximum proton energy was also measured through the IC detector but its signal was very disturbed by the high electromagnetic noise produced during the laser pulse emission.

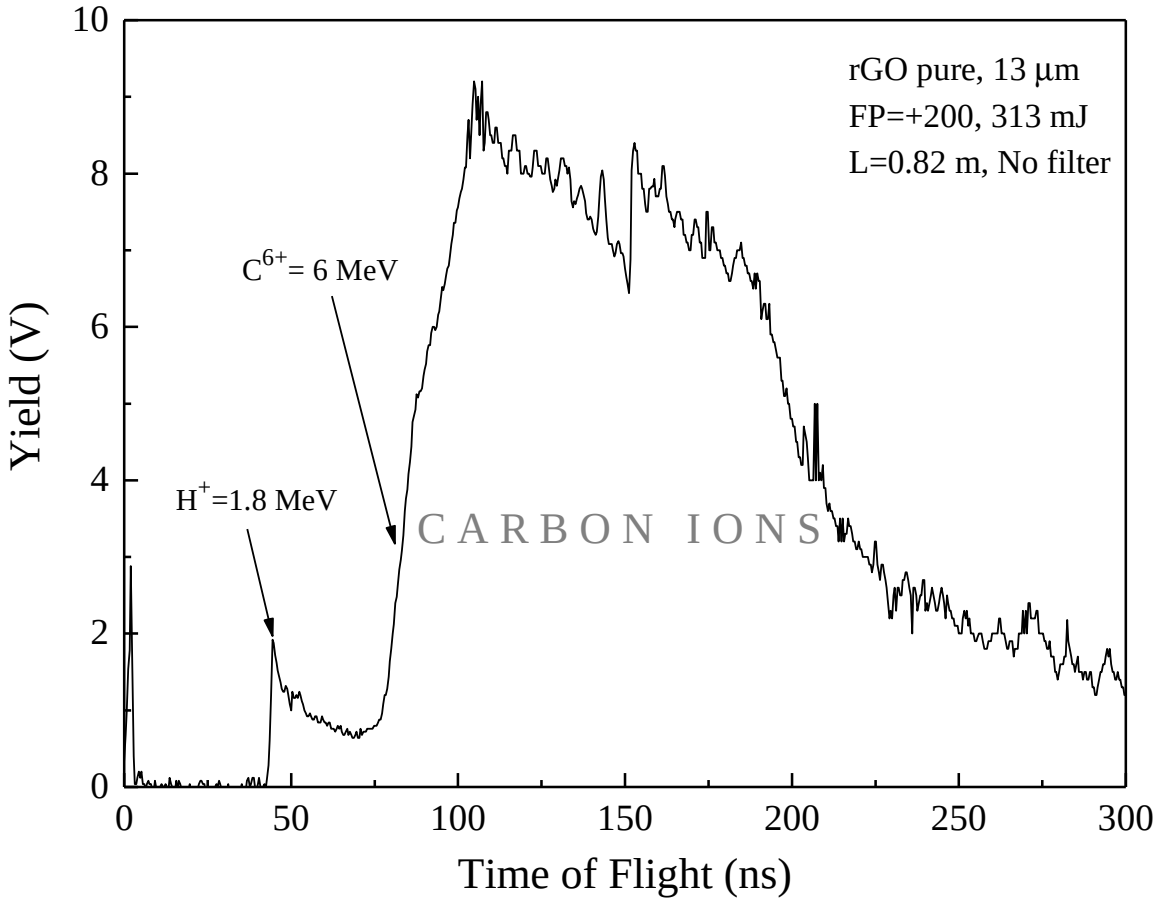

Figure 5.13: *SiC–TOF spectrum obtained irradiating a Graphene Oxide foil, 13 µm thick, by 313 mJ pulse using a TOF distance of 0.82 m.*

In addition, the maximum proton energy of 1.8 *MeV* was also confirmed by the Gafchromic detectors employed with Al absorbers, in facts, the Gafchromic have shown the typical dark color of ion dose when the absorber was 15 microns and not when it was increased to 42 microns, in agreement with the literature [243].

In order to deconvolve the ion peak show in Figure 5.13, separating the contribution of the protons from that of carbon ions, and separating the different detected carbon ion charge states, a PIC simulation was performed; thus, a comparison between the computational data and the experimental spectrum is achievable. Figure 5.14 shows a 2D–PIC spatial map for emitted electrons density profile in the simulation box reporting this at different times, starting with the laser interaction, chosen at 0 *fs*, up to a time of 200 *fs*. At 0 fs, the laser reaches the target, thick 13 *µm* with the density of about 3.4×10^{23} *electrons/cm*^{3}. Of course, the emis-

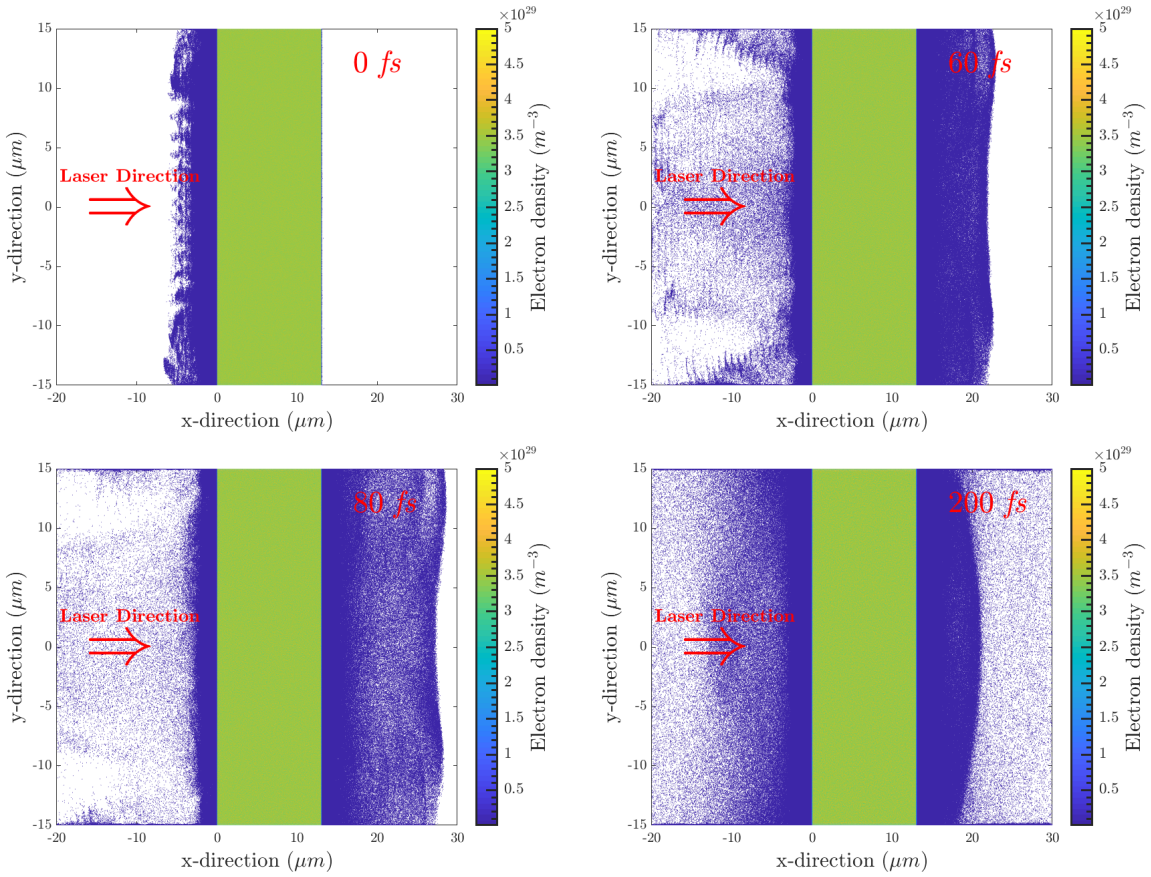

Figure 5.14: *2D–PIC spatial map for emitted electrons density profile near to the target at different times starting with the laser interaction: 0 fs, 60 fs, 80 fs and 200 fs.*

sion of electrons starts in backward direction. Subsequently, the laser guides the electrons in the forward direction, which between 60 and 80 *fs* are responsible for the main peak in the longitudinal electric field (there is a large number of electrons closely to target surface). Within about 100 *fs*, the fastest electrons left the simulation box. The frame at 200 *fs* shows an increase in the number of electrons near to the surface of the target that will be responsible for a further peak, with lower intensity, in the longitudinal electric field driving the ion acceleration.

The electron density emergent from the back of the irradiated target, in TNSA regime, can be plotted as a function of the target distance in forward direction, for the different times after the laser shot. Figure 5.15a indicates that the emitted electron density decreases exponentially from the rear target surface and reduces to about one order of magnitude at about 0.1 *μm*from the rear target surface, at 100 *fs*, while a significant increment in the value occurs

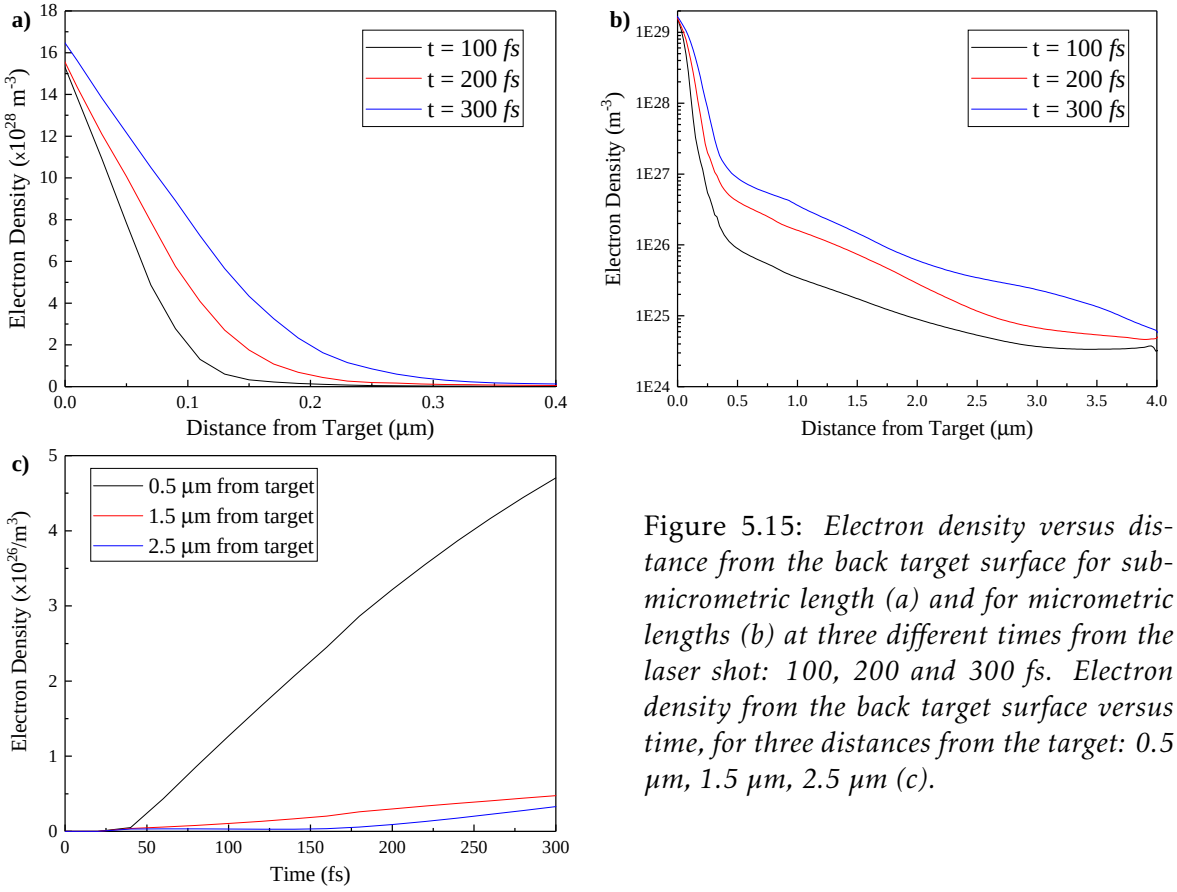

Figure 5.15: *Electron density versus distance from the back target surface for submicrometric length (a) and for micrometric lengths (b) at three different times from the laser shot: 100, 200 and 300 fs. Electron density from the back target surface versus time, for three distances from the target: 0.5 µm, 1.5 µm, 2.5 µm (c).*

for a time of about 300 *fs*. More details of the forward emitted electron density versus target distance, for the lower levels of electron density, as calculated by the PIC simulation, are reported in the plot of Figure 5.15b. The electron density from the rear target surface can be plotted as a function of the time from the laser shot for a fixed distance, as reported in Figure 5.15c. This plot shows as the density decrease strongly with the time, as observable at times higher than 100 *fs* from the laser shot.

The forward emission of electrons generates an electric field between the electron cloud and the positive target, which is responsible for the TNSA ion acceleration, according to Equation 1.75. This electric field is characterized by the electron density and plasma temperature kinetics and is developed as a function of the time and of the space as reported in Figure 5.16. In particular, Figure 5.16a shows the longitudinal electric field, in *x–forward direction*, as a function of the distance from the target surface, indicating a peak value of about 1.75×10^{12} *V/m* at about 60 *fs* from the laser shot and positioned at about 14 *µm*. This means that the peak is placed at about 1 *µm* from the rear target surface and that the acceleration voltage

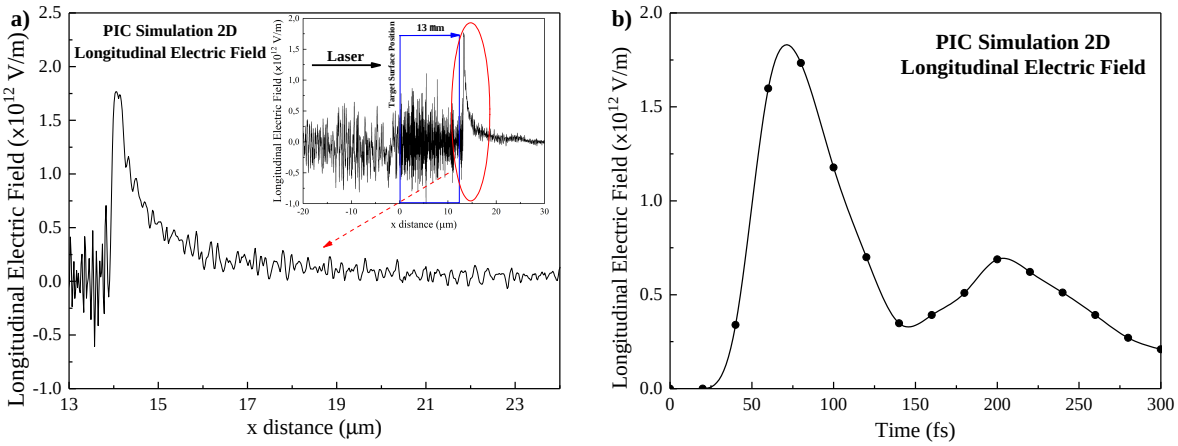

Figure 5.16: *Longitudinal electric field versus distance from the target surface, evaluated from PIC code as zoom and un–zoomed figure (inset) (a) and as a function of the time at the position of maximum value (14 μm) (b).*

corresponds to 1.75 *MV*. Thus, for the fast accelerated protons is expected an acceleration up to an energy of about 1.75 *MeV*, in good agreement with the measurements of 1.8 *MeV*. The electric field peak has a spatial width (FWHM) of about 0.5 *μm*.

Figure 5.16b reports the longitudinal electric field as a function of the time by fixing the distance from the front target surface at 14 *μm*. It is possible to observe that two peaks occur in the time due to the return of emitted electrons towards the target, of which the first is the more intense with a duration of about 50 *fs* (FWHM) and it is responsible for the higher forward proton acceleration. The second peak is about one third less intense and has a double duration.

The electrical field developed on the rear side of the target changes with the time. Protons, which are very light, are accelerated by the maximum value of the electric field, but the successive carbon ions, having an higher mass and minor velocity, do not receive the maximum acceleration value of the electric field since it decreases during their acceleration motion.

In addition, PIC–EPOCH simulation code has permitted to evaluate the equivalent plasma temperature by the electron energy distributions. Assuming a Boltzmann energy distribution, with a cut–off at about 4.4 *MeV* electron energy, Figure 5.17a shows the evaluated electron temperature of the plasma, $k_B T$, corresponding to about 302.3 *keV*. This result is in agreement with the theoretical evaluation of the temperature, calculated using the Equation 1.22, which is worth about 354 *keV*, thus in good agreement with the value determined by PIC simulation.

In Figure 5.17b are reported the carbon ion energy obtained by PIC simulation, in which is possible to observe that ions follows Boltzmann distributions with a cut–off proportional to the charge state and ranging within 0.8 *MeV* for C^{1+} and 6.8 *MeV* for C^{6+}. Similarly,

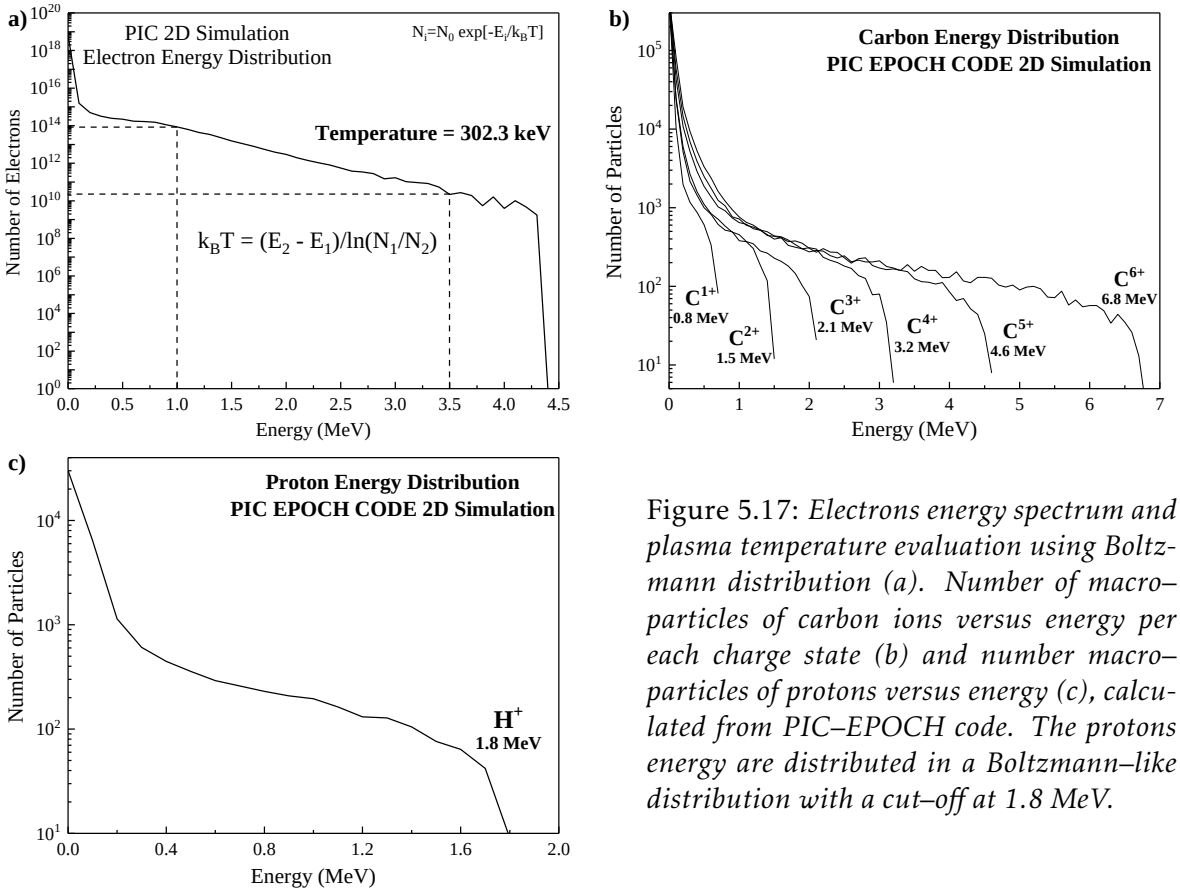

Figure 5.17: *Electrons energy spectrum and plasma temperature evaluation using Boltzmann distribution (a). Number of macro–particles of carbon ions versus energy per each charge state (b) and number macro–particles of protons versus energy (c), calculated from PIC–EPOCH code. The protons energy are distributed in a Boltzmann–like distribution with a cut–off at 1.8 MeV.*

Figure 5.17c shown the proton energy by the computational approach. These are distributed in a Boltzmann–like distribution with a cut–off energy, which is calculated at 1.8 *MeV*.

On the base of the results obtained by the experimental measurements of TOF ion spectra and of the PIC theoretical simulations above reported, it is possible to find an important data agreement. It permits to correlate the ion acceleration effect with the detected spectra separating the contribution to the acceleration of each ion species depending on its mass to charge ratio. Protons are the faster ions, followed by the carbon ions of which the faster is the more charged C^{6+} and the slower the fewer charge C^{1+}. The TOF spectra acquired using a SiC detector with an active area of only 4 mm^2, placed at 0°, along the axis of maximum emission yield and energy, shows profiles in energy decreasing with the time and not as expected in a Boltzmann distribution. This effect is due to the less energetic ions mainly emitted at large angles and not detected if not as a background signal compared with the minimum detection limit. Thus, the TOF spectra and the ion energy distributions, which can be derived, not show a Boltzmann distribution but peaks quickly damped.

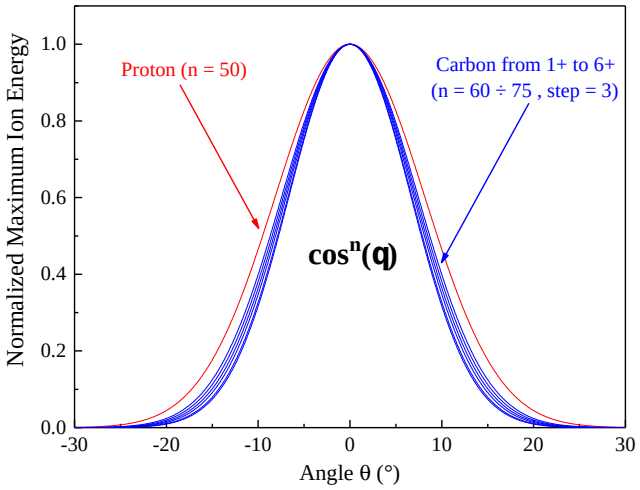

Figure 5.18: *Behaviour of the experimental maximum ion energy angular distribution around to the normal of the target surface.*

By rotating the SiC detector in forward direction around to the normal to the target surface, was recorded the angular ion emission and was observed that it decreases in energy and yield, assuming the maximum value at 0° angle, as expected. The high proton and carbon energy is maintained high near to 0° (±2°) while its yield remains significant approximately within ±25° and ±20°, respectively. According to the literature [244, 245], the higher carbon charge states are more directive of the lower and protons have a larger angular distribution due to their small mass.

Thus, the angular emission, indicated by θ, is a function of the ion yield, indicated by $Y(\theta)$, can be written as follows:

$$Y(\theta) \propto \cos^n(\theta)$$

being the exponent $n = 50$ for protons and $n = 60$ to 75 for carbon–ions from C^{1+} up to C^{6+}, respectively. As reported in the angular distribution of Figure 5.18, for each plasma charge species the ion emission has high directivity, which is higher for the C^{6+} ions with respect to the C^{1+} ions and with respect to the larger emitted protons.
Correlating the PIC ion energy distributions, shown in Figure 5.17, with the angular distribution of the accelerated particles, reported in Figure 5.18, it is possible to deconvolve the TOF ion spectrum in the different ion contributions as reported in the plot of Figure 5.19. The deconvolution reports the proton contribution and that of the six carbon charge states. From such ion peaks it is possible to evaluate their maximum energy, which corresponds to 1.8, 6.8, 4.6, 3.2, 2.1, 1.5 and 0.8 *MeV* for H^+, C^{6+}, C^{5+}, C^{4+}, C^{3+}, C^{2+}, and C^+, respectively. By comparing the ion yield, in terms of peak areas, it is possible to observe that the maximum contributions are due to higher ionized states of carbon ions, due to their angular distribution more peaked with respect to the lower charge states and to the protons.
The ion energy distributions, obtained by PIC simulations, fit very well the experimental TOF spectrum. They indicate that the protons have a maximum ion acceleration per charge state (1.8 *MeV/z*) while the carbon ions have a lower acceleration due to their higher mass, having a maximum value for C^{6+} (1.13 *MeV/z*) and a minor value for C^{1+} (0.8 *MeV/z*). This result confirms that the faster protons reach the spatial position where the electrical field of

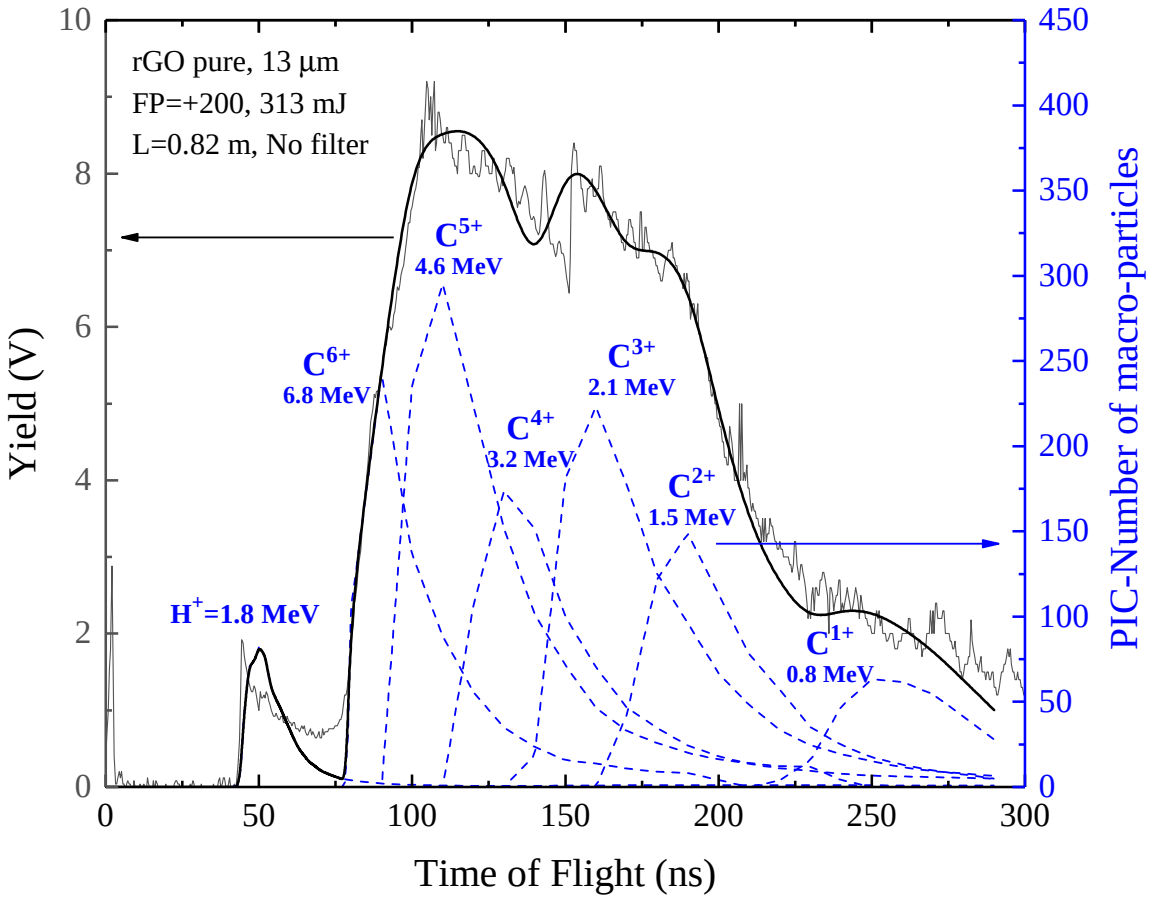

Figure 5.19: *SiC–TOF spectrum and deconvolution peaks of protons and carbon ions, with their maximum energy, as evaluated from PIC–EPOCH code.*

acceleration is maximum, while the carbon ions, having an higher mass and lower velocity, are subjected to a lower average electric field which is reduced during their forward motion. Figure 5.20 reports the ion energy as a function of the ion charge state as obtained by PIC code and by applying the *Torrisi*'s CBS (Coulomb–Boltzmann–Shifted) theory [149]. In the first case, it is possible to observe that the maximum carbon ion energy, E_M, increases with a law proportional to the square of the charge state z, due to the higher mass of the carbon ions with respect to protons. The fit of the PIC data gives:

$$E_M(C^{z+})\,[MeV] = 0.19z^2 - 0.18z + 0.91$$

In the second case, the acceleration is assumed to be of 1.8 MeV per charge state both for protons and per carbon ions ($E_M(H^+)\,[MeV] = 1.8z$), thus the C^{6+} ions should have an energy of

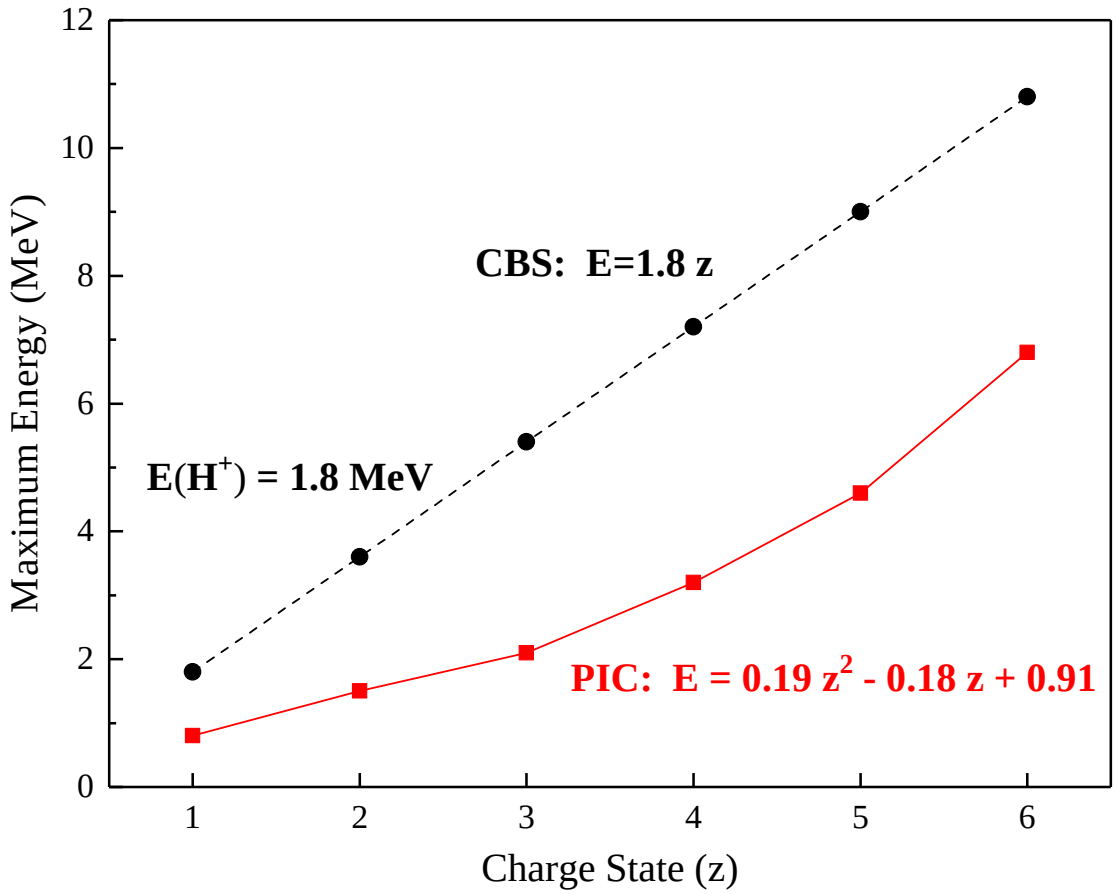

Figure 5.20: *Comparison between maximum ions energy versus charge state calculated by PIC–EPOCH code and by using the CBS approach.*

10.8 *MeV*. Experimental data agree with the PIC model instead with the CBS approach. This last case, in fact, is applicable to lower laser intensities and to higher laser pulse durations, as reported in the literature, and demonstrates that its application for intensities above 10^{18} W/cm^2 can be only approximated [149, 246].

5.3.3 Conclusions and Future Perspectives

This article shows innovative results of comparison between Time of Flight ion spectra and Particle–in–Cell simulation data for ions accelerated from TNSA regime using *fs* laser at 8×10^{18} W/cm^2 intensity. The comparison, in fact, is not simply between the two different approaches, experimental and theoretical of course, and the literature does not report previous studies to this correlation.

The spectrum here reported for proton and carbon acceleration from reduced Graphene Oxide target was obtained using a SiC detector placed at a known flight distance from the target and triggered by the laser shot. It was extracted from a campaign of experiments at IPPLM laboratory (Poland) [**205**, 247]. Originally, the spectrum was interpreted using the Coulomb–Boltzmann–Shifted theory presented in literature, affirming that the ions are subject contemporary to an acceleration of the electrical field developed in the rear side of the target. This theory, useful and confirmed for lower laser intensity and for laser pulse duration between *ns* and hundred *ps* order, is not valid for an high laser intensity of the order of 10^{18} W/cm^2 or more and for laser pulses of tens *fs* duration. Experiments performed irradiating gold targets with *fs* laser, in fact, have not permitted to detect the high energy of the high charge states of the gold ions [247]. The results presented in this paper confirm, in fact, that protons can be accelerated at high kinetic energy because they are effectively subjected to the maximum electric field developed in the non–equilibrium plasma. However, heavy ions are not accelerated or are only weakly accelerated because they do not arrive in synchronism with the maximum electric field, which decays exponentially in times of the order of one hundred femtosecond. Just light ions, such as carbons may be accelerated, but less with respect to protons, especially if they have lower charge; heavier ions like gold ions are not accelerated due to their too high mass and too much low velocity [248].
PIC simulations correlated to the experimental measurements has permitted to plot the different ion contributions to the TOF spectrum, taking into account their angular emission distribution and their detection through the small active surface of the SiC detector placed along the normal to the target surface direction. PIC–EPOCH simulation code determinates a longitudinal electrical field that drives the ion acceleration at about 1.75 *MeV*, in good agreement with the 1.8 *MeV* obtained by TOF measurement. This result confirms that the electron density time and space evolution predicted by PIC–EPOCH code can be correct and that the high electric field duration is of about 100 *fs* and acts on about 1 μm length. Carbon ions instead, due to their lower velocity with respect to protons, find a lower electric field value and thus are less accelerated, proportionally to their charge state.
PIC has permitted also to determine the plasma temperature of about 300 *keV*, in good agreement with theoretical previsions, and has proposed a Boltzmann electron and ion energy distributions with a cut–off at the maximum electric field of their acceleration.
Actually, works are in progress for other types of targets to compare again TOF spectra with PIC simulations to test the time and spatial kinetics of collisionless plasma for other types generated by *fs* laser at high intensity and high contrast [**249**].

Conclusions

The interaction between a high power laser beam and a target generates a non–equilibrium plasma that expands rapidly in front of its surface. The plasmas generated by laser pulses consist mainly of photons, electrons, protons and heavier ions, and are characterized by high temperatures, densities and specific ionization distributions. In this concluding part, a brief summary showing the main data obtained in the field of laser–plasma interaction, and their main applications, is given below.

Summary

In this PhD thesis the research activity is mostly focused on the ionic component of the plasma, generated by long pulses (*ns*–class laser) or by short and ultra–short pulses (*ps–fs* class laser). In Chapter 1 the main phenomena responsible of ionisation as a result of irradiation are presented and discussed. The laser intensities reached to date, below 10^{21} W/cm^2, are not yet able to directly accelerate the ions of the target due to their large mass. However, the energy of the incident electromagnetic wave is partially absorbed by the electrons, which mediate between the laser field and ions through a longitudinal electric field that drives ions' acceleration due to charge separation (which could reach TV/m order). Three acceleration regimes are considered, based on laser intensity and target characteristics. The first is the Backward Plasma Acceleration (BPA), related to the interaction of long pulses with thick targets; the plasma expands in the opposite direction with respect to the laser pulse and ions are expelled with Boltzmann energy distributions. The second is the Target Normal Sheath Acceleration (TNSA), due to the interaction of short and ultra–short pulses with thin targets (less than tens of μm), which produces particle beams with low emittance and Boltzmann energy distributions with a cut–off that could reaches hundreds of MeVs. The third acceleration regime is the Radiation Pressure Acceleration (RPA), where ultra–short pulses interact with thin targets producing beams with low angular spread and very high energy.
Chapter 2 is dedicated to the transport and focusing of ion beams emitted by plasmas. Here, the basic notions on the main particle beam features are outlined, to which it is necessary to refer for an adequate beam modelling. Experimental measurements conducted at the University of Messina are presented, using a laser of an intensity of the order of 10^{10} W/cm^2.

The application of magnetic fields with cylindrical symmetry to the generated plasma, which have magnetic axes parallel to the target normal surface, generates a focusing effect for the charged particle beams, analogous to an optical lens with light. By using the geometry presented in the work, properly studied, an increase in ion current up to 6.6 times has been obtained. In addition, the magnets trap the electronic cloud in front of them, because of their small mass, for hundreds of nanoseconds. The localized electron density generates an increase in the longitudinal electric field that further drives the ion acceleration to higher energies, in agreement with the electronic density of the target. The energy increase for plasma protons has been estimated to be about 2 times higher. The experimental measurements were conformed by simulation using the COMSOL Multiphysics software.
The non–equilibrium plasmas diagnostics depend strongly on the laser intensities used. In fact, low laser intensities, less than 10^{16} W/cm^2, generated by long pulses, generate particles with energy less than hundreds of keV per charge state, contrarily to short pulses. In this context, ions can be characterized using magnetic or electrical spectrometers only. In Chapter 3, a magnetic deflection spectrometer, called Magnetic Spectrometer Chamber (MSC), and an electric deflection spectrometer, called Ion Energy Analyzer (IEA), are presented and described. Both are used with the Time–of–Flight (TOF) technique. The detector used for the measurements depends on the ion current to be detected; when it is high enough (> 10 μA), simple Ion Collectors (ICs) can be used; when it is low, devices able to amplify the signal such as Secondary Electron Multipliers (SEMs) are generally employed. MSC and IEA spectrometers allow to obtain the distribution of the velocities or energy of the single species that constitute the plasma, respectively. The comparison of temperature and potential inside the plasma obtained by the distribution fit (temperatures of the order of tens of eV, and potentials below hundreds of V) obtained through measurements with the two devices is in good agreement, also confirmed by simulation with COMSOL Multiphysics software. However, rather than talking about comparison between these two devices, they can be considered as complementary because of the different quantities that can be obtained.
Since the advent of short and ultra–short pulses, less than hundreds of ps, a new and exciting frontier of ion acceleration via laser pulse is open. In fact, for lasers with an intensity greater than 10^{16} W/cm^2, interacting with thin targets, protons and light ions are accelerated from the rear target surface by an electric field generated between them and the cloud of hot electrons that quickly moves away from the target. With this mechanism, higher energies of protons obtained to date approach the hundreds of MeVs, as described in the text. Chapter 4 of this thesis examines the diagnostics of high energy particles, greater than the units of MeV per charge state. The techniques most used for this purpose are presented and discussed. The time-of-flight technique remains valid for efficient analysis of hot plasma. This chapter presents measurements using the TOF technique, with semiconductor detection devices, based on Silicon Carbide. The experiment was conducted by irradiating advanced targets of pure GO (7 μm thickness), or coated with 200 nm of gold. The use of these foils has allowed to generate high accelerations of protons with near–monochromatic energies, approximately

between 2.85 and 1.4 *MeV*. Another device, widely used for the characterization of plasmas generated by short pulses, is the Thomson Parabola Spectrometer (TPS). This device uses a magnetic field and an electric field in series, orthogonal to the direction of the ion beam, in order to deflect the charged particles. These can be revealed by various detectors presented in the text. The strength of the device presented is its compactness and versatility (about 30 *cm* long for a weight of less than 5 *kg*), which allows to be easily transported to different laboratories. This compact TPS can also be used for both cold and hot plasmas as reported in the measures presented. Comparison with the simulation of ion trajectories using COMSOL Multiphysics software allows to identify the charged species in the plasma, evaluating the mass–to–charge ratio and their maximum energies as reported.
Finally, an overview of the Particle–in–Cell (PIC) method used to model laser–plasma interaction is described in Chapter 5. The PIC method was developed more than 60 years ago, and today is the most commonly used code to simulate collionless plasma kinetics, due to its demonstrated accuracy and stability. The method refers to a technique used for solving Maxwell's equations on fixed points of a simulation grid. The calculated fields are then used to update velocity and position of the quasi–particles under the action of the Lorentz force. Each quasi–particles represents a large number of real particles, distributed through a properly weight function. More details are of course given in the text. In order to understand the dynamics of laser–plasma interaction we have compared an experimental spectrum (obtained by irradiating rGO with a thickness of 13 μm by a laser with an intensity of 8×10^{18} W/cm^2) with a simulation by the PIC method through the full relativistic 2D–EPOCH code. Through EPOCH code the electronic density profile was evaluated, and the longitudinal electric field, which drives ions' acceleration, was estimated at 1.75 *TV/m* peak. This accelerates protons with Boltzmann distributions having an energy cut–off at about 1.75 *MeV*, in good agreement with the experimental data (1.8 *MeV*). Further analysis allowed to estimate the electrons' temperature by EPOCH, which is worth about 300 *keV*; even this value is in good agreement with the theoretical predictions. This work shows an innovative result between the comparison of a TOF spectrum and the PIC method, in TNSA regime by using an *fs*–laser. The comparison, done taking into account the angular distribution of the emitted ions from the target, in fact, is not at all simple, and there are no works in the literature that report previous studies of this correlation.

Laser–generated Plasma Application Fields

Ion acceleration driven by laser pulses has always attracted an impressive and constantly growing research effort due to the many applications that derive from it. Depending on the laser used, on the parameters of the plasma produced (such as density and temperature), on the energy of the particles emitted by the plasma, there are different fields of application concerning the laser–matter interaction. Some words are to be spent for these, among which the most important are for example the Laser Ion Source (LIS), Laser Ion Implatation

(LII), Laser induces Nuclear Reactions, Laser Plasma Accelerator, Proton or Hadrontherapy by laser. Other interesting applications of high–energy ions produced by intense pulsed laser–generated plasmas range from astrophysics to microelectronics, and from the chemical industry to the environment. Below, only the main are briefly reported.

Laser Ion Source

The Laser Ion Source (LIS) refers to the technique employed to produce ions from plasma, which are used to be injected into large particle accelerators. The first application of LIS for ion injections into a high–energy synchrotron was made at the 10–GeV synchrotron at the Joint Institute for Nuclear Research (JINR), Dubna, Russia, in 1977, using light and medium ions mass, up to 13 times ionized chromium [250]. The ions emitted by the plasma must be picked up with an appropriate extraction system. This is usually a device based on the application of an electric field between the target and the extraction window, which is generated by a potential of the order of tens of kV. The current density is proportional to the extraction potential. Magnetic selectors located below the extractor allow to select one state of charge of the produced ion rather than another. Long laser pulses are generally used in LIS, since short laser pulses sometimes do not completely accelerate very massive ions. The greatest advantage of using LIS is that it is possible to inject any type of material into the accelerators, even those with a high melting point, which is more difficult to obtain with traditional techniques. For example, in ECLISSE experiment performed at INFN–LNS in Catania, Tantalum ions (melting point 3017°C) produced by intensity laser of $5{\times}10^{10}$ W/cm^2, are injected into the Superconducting Cyclotron [251]. Anyway, it may also be possible to accelerate ions of radioactive species.

Laser Ion Implantation

The Laser Ion Implatation (LII) technique consists of implanting the ions emitted by a pulsed laser–generated plasma into a substrate. The LII can be performed by direct implantation or driven by an accelerating potential. In summary, there are two techniques used to perform LII, shown in the Figure C.1. The first is through the deposition of laser pulses on a substrate placed in front of the target; while in the second case the substrate is placed laterally to the target [252]. In the latter case, only the positive ions (roughly) will penetrate the target, while the neutrals and electrons will not. The positive potential accelerates the ions to a certain energy, which will be stopped at a given depth in the substrate in accordance with the SRIM code [175].

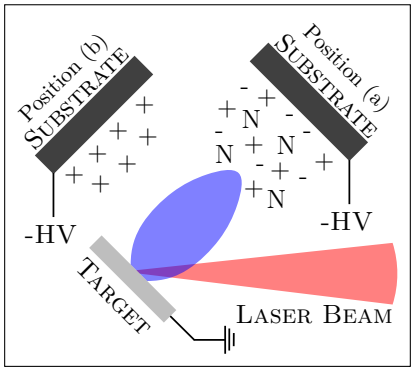

Figure C.1: *LII representation: target in front to substrate (a) and target lateral to substrate (b).*

Through LII it is possible to modify the superficial properties of the substrate, to increase its hardness and resistance to oxidation, corrosion, and so on; but also to improve the superficial mechanical resistance. It is also possible to develop innovative materials with special electrical, optical and chemical properties. This is a technique widely used in industry and beyond [253].

Laser induces Nuclear Reactions

In recent decades, the intensities of laser fields in the beam focal spot have reached values ranging from 10^{16} to 10^{20} W/cm^2. It is well know that intensities above 10^{18} W/cm^2 produce relativistic plasmas. These plasmas are sources of very energetic particles, such as highly relativistic electrons, hard bremsstrahlung, protons with energies of hundreds of MeV, and more. Because of the high energies within a plasma, nuclear reactions could occur, such as fusion, neutron generation, neutron capture, photo–fission and others [254].

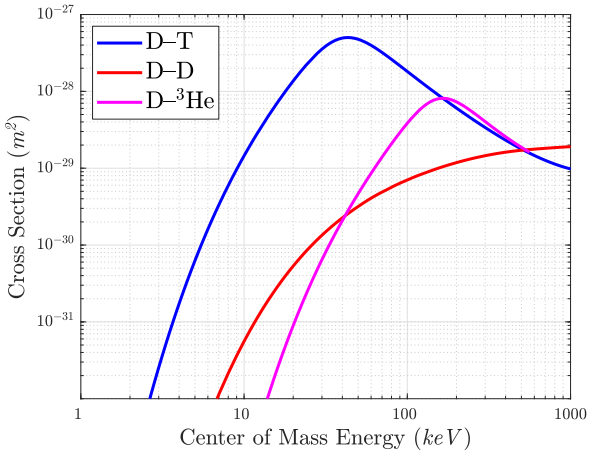

Figure C.2: *Fusion cross section for D–T, D–D and D–^{3}He; data from ref [173].*

When materials rich in deuterium are irradiated with high intensity lasers, such as deuterated plastics, the ejection of electrons causes a Coulomb explosion, pushing the D^+ ions outwards. If enough of these ions reach the energy of hundreds of keV, they will begin to induce nuclear fusion reactions with nearby stationeries, as shown in the total cross section in Figure C.2. The D–D fusion reaction has two channels that occur with the same probability:

$$\text{D–D} \longrightarrow \text{T}(1.01\ MeV)+\text{p}(3.02\ MeV)$$
$$\text{D–D} \longrightarrow {}^3\text{He}(0.82\ MeV)+\text{n}(2.45\ MeV)$$

In some materials, the fusion reaction between deuterium and nearby clusters may take place, and lead to reactions D–T producing α–particles of 3.5 MeV and neutrons of 14.1 MeV, or to reactions D–^{3}He producing α–particles of 3.6 MeV and neutrons of 14.7 MeV, according to the cross sections shown in the Figure C.2. The characteristic energy carried by the neutrons can be measured with the TOF technique.
It has also been demonstrated the possibility of inducing nuclear fission in heavy elements, such as ^{238}U and ^{232}Th, through high–energy photons generated by bremsstrahlung of hot electron. Fission processes have many reaction channels, which lead to a different decay products, that can be identified by their own γ–ray emission lines. Finally, in many experiments were observed nuclear transmutation reactions by effect of high–energy photons [2].

Laser Plasma Accelerators

Conventional accelerators, such as synchrotrons and LINACs, operate with limited electric field gradients, around 100 MV/m; a plasma, differently, since already ionized, is immune to electric breackdown, and can tolerate fields of the order of TV/m or higher. Such fields are involved into acceleration of protons and light ions, whereas the electric fields supported by the creation of electron plasma waves can be related to acceleration processes of lighter particles such as electrons and positrons.
In laser–plasma interaction, electrons are pushed forward by the ponderomotive force, proportional to the gradient of the laser intensity. The electrons transit quickly in relativistic regime approaching the speed of light. Through different mechanisms, such as laser Wakefield acceleration, modern lasers are able to accelerate electrons up to a few GeVs in a few centimetres distance. The electron beam produced can reach current peaks of the order of kA units, with low energy spread values, less than 5%, low emittance and high quality [255,256].
Unlike electrons, protons and light ions are not accelerated directly by the laser, but through the electric field due to charge separation between them and the accelerated electrons. Recent measurements have shown the acceleration of protons to 94 MeV energy by irradiating thin plastic targets with thicknesses between 10 nm and 1.5 μm. The experiment was conducted with the PW laser Vulcan at the Rutherford Appleton Laboratory in the UK [104].
There are many advantages that would result from the use of laser–generated plasmas in substitution of conventional accelerators, such as the reduction of operating and building costs, the significant reduction in the size of these, the possibility of generating very intense electric fields, and more. The work done in the last decade for the actuation of laser plasma accelerators has gone from successes and failures; thanks to all these pioneering works we are leading towards a future where the acceleration from laser plasmas becomes a reality.

Medical treatments by Laser–generated Plasmas

High–energy radiation to cancer treatment, known as radiotherapy, plays an important role since it not only provides local control of the tumour, but also improves the patient's quality of life compared to other treatments. Today, the most commonly used radiotherapy, uses X–rays with the energies of some MeV, produced by bremsstrahlung radiation of electrons accelerated by linear accelerators. The electrons are accelerated to energies of the order of MeV, up to 20 MeV, values widely achievable through modern ultra–short pulses laser–generated plasmas, which could provide the required dose of a few minutes.
Although there are advanced techniques in photon beam radiotherapy, such as Intensity Modulated RadioTherapy (IMRT) [257] or Stereotactic RadioSurgery (SRS, using CyberKnife or Gamma–Knife) [258], which allow improvements in the dose distribution between healthy and diseased tissues, ion beams have physical advantages over photons. In fact, as shown in the Figure C.3, ions deposit most of their energy at the end of their path, in the so–called Bragg peak, which depends on medium crossed, the ion beam energy and its nature.

By degrading the most energetic ion beam through an absorber (Spread Out Bragg Peak, SOBP), it is possible to irradiate uniformly the diseased tissue, as shown in the Figure C.3. Conventional accelerators for proton beams, such as cyclotrons, have a diameter of 4 m and a weight of 200 t. This is reduced to 2 m and 50 t using superconducting magnets that require cooling systems at temperatures of 4 K [259]. In recent years, following advances in the physics of laser generated plasmas, several projects have emerged with the aim of performing proton–therapy by laser, such as ELIMED project [260]. Among the numbers advantages would be a drastic reduction in costs for the infrastructure (from about 100 $M€$ to 10 $M€$), reduction in the size and weight of the systems.

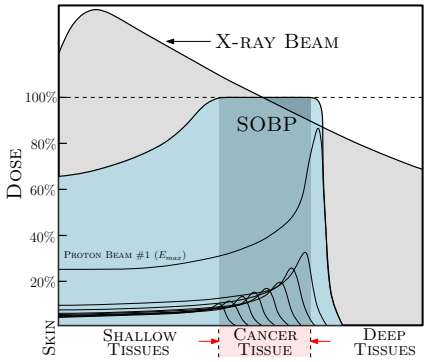

Figure C.3: *Behaviour of the relative dose released in a tissue by photons and a protons beam.*

However, before proton–therapy by laser becomes a reality, it is necessary to achieve energies for protons of 200 MeV, to have sufficient protons at that energy to treat the patient for sessions of a few minutes (high repetition rates are required, greater than 10 Hz), and to have a reliable and stable laser pulse [255]. Although actually these goals have not been fully achieved yet the path is mapped out for implementation in the near future.

Conclusions and Future Perspectives

In this PhD thesis we have discovered the very attractive and promising field of particle acceleration from plasmas generated by laser pulses with a scale duration from nanosecond to femtosecond. The fascination in this fundamental science, which involves large research groups all over the world, is mainly due to the wide range of applications arising from it. These cover from long laser pulses, which accelerate ions using the BPA scheme, to short and ultra–short pulses, with protons energies in the hundreds of MeVs using the already affirmed TNSA and the promising RPA scheme. The applications already consolidated, those under definition and those still far from being implemented have produced, and still produce, a huge research effort, with many experimental, theoretical and simulation results, which have allowed a better understanding of the relevant phenomena in the laser–generated plasma.
The work presented in this text should not be considered as conclusive, but on the contrary must motivate research in this constantly evolving field. In fact, the development of laser ion acceleration has always had an high scientific, industrial and social impact. Thus, it is necessary to look to the future, through the study of the most advanced acceleration regimes, the optimization of systems, the design of advanced targets, in order that the most suggestive applications become topical.

Bibliography

[1] P. Mulser and D. Bauer: "High power laser–matter interaction". Springer, **238**, (2010).

[2] P. Gibbon: "Short Pulse Laser Interactions With Matter: An Introduction". Imperial College Press, (2005).

[3] S. Gammino, G. Ciavola, L. Torrisi, et al.: "Preliminary tests for the electron cyclotron resonance ion source coupled to a laser ion source for charge state enhancement experiment". *Review of Scientific Instruments*, **71**(2), 1119–1121 (2000).

[4] S. Lanzafame, A.M. Mezzasalma, G. Mondio, T. Serafino, F. Barreca, L. Torrisi and G. Bruno: "Structural, electronic, and optical properties of ITO thin films prepared at room temperature by pulsed laser deposition". *Radiation Effects and Defects in Solids: Incorporating Plasma Science and Plasma Technology*, **165**(6–10), 592–600 (2010).

[5] M. Cutroneo, A. Mackova, L. Torrisi and V. Lavrentiev: "Laser ion implantation of Ge in SiO_2 using a post-ion acceleration system". *Laser and Particle Beams*, **35**(1), 72–80 (2017).

[6] J. Braenzel, A.A. Andreev, K. Platonov, M. Klingsporn, L. Ehrentraut, W. Sandner and M. Schnürer: "Coulomb–driven energy boost of heavy ions for laser–plasma acceleration". *Physical review letters*, **114**(12), 124801 (2015).

[7] L. Torrisi, A. Borrielli, D. Margarone: "Study on the ablation threshold induced by pulsed lasers at different wavelengths". *Nuclear Instruments and Methods in Physics Research Section B: Beam Interactions with Materials and Atoms*, **255**(2), 373–379 (2007).

[8] G. Cristoforetti, G. Lorenzetti, P.A. Benedetti, E. Tognoni, S. Legnaioli and V. Palleschi: "Effect of laser parameters on plasma shielding in single and double pulse configurations during the ablation of an aluminium target". *Journal of Physics D: Applied Physics*, **42**(22), 225207 (2009).

[9] P. Drude: "Zur elektronentheorie der metalle; II. Teil. galvanomagnetische und thermomagnetische effecte". *Annalen der Physik*, **308**(11), 369–402 (1900).

[10] M. Von Allmen and A. Blatter: "Laser–Beam Interactions with Materials". *Springer*, 5–40 (1995).

[11] M. Fox: "Optical properties of solids". *Oxford University Press*, (2010).

[12] D. Bäuerle: "Laser Processing and Chemistry: Fourth Edition". *Springer*, (2011).

[13] J. Ihlemann, A. Scholl, H. Schmidt and B. Wolff-Rottke: "Nanosecond and femtosecond excimer–laser ablation of oxide ceramics". *Applied Physics A*, **60**(4), 411–417 (1995).

[14] W. Kautek and J. Krüger: "Femtosecond pulse laser ablation of metallic, semiconducting, ceramic, and biological materials". *Laser materials processing: industrial and microelectronics applications*, 2207, 600–612 (1994).

[15] B.N. Chichkov, C. Momma, S. Nolte, F. Von Alvensleben and A. Tünnermann: "Femtosecond, picosecond and nanosecond laser ablation of solids". *Applied Physics A*, **63**(2), 109–115 (1996).

[16] R.E. Russo, X.L. Mao, C. Liu and J. Gonzalez: "Laser assisted plasma spectrochemistry: laser ablation". *Journal of Analytical Atomic Spectrometry*, **19**(9), 1084–1089 (2004).

[17] L. Ji: "LIon acceleration and extreme light field generation based on ultra-short and ultra–intense lasers". *Springer Science & Business Media*, (2014).

[18] G.S. Voronov and B.N. Delone: "Ionization of the Xenon atom by the electric field of Ruby laser emission". *JETP letters*, **1**(2), 66–68 (1965).

[19] G.S. Voronov and B.N. Delone: "Free–free transitions following six–photon ionization of Xenon atoms". *Physical Review Letters*, **42**(17), 1127 (1979).

[20] L.V. Keldysh and others: "Ionization in the field of a strong electromagnetic wave". *Sov. Phys. JETP*, **20**(5), 1307–1314 (1965).

[21] P. Lambropoulos: "Mechanisms for multiple ionization of atoms by strong pulsed lasers". *Physical review letters*, **55**(20), 2141 (1985).

[22] C.Z. Bisgaard and L.B. Madsen: "Tunneling ionization of atoms". *American Journal of Physics*, **72**(2), 249–254 (2004).

[23] A.M. Perelomov, V.S. Popov and M.V. Terent'ev: "Ionization of atoms in an alternating electric field". *Sov. Phys. JETP*, **23**(5), 924–934 (1966).

[24] B.W. Boreham and B. Luther-Davies: "High–energy electron acceleration by ponderomotive forces in tenuous plasmas". *Journal of Applied Physics*, **50**(4), 2533–2538 (1979).

[25] P.H. Bucksbaum, M. Bashkansky and T.J. McIlrath: "Scattering of electrons by intense coherent light". *Physical review letters*, **58**(4), 349 (1987).

[26] A. Chao and W. Chou: "Reviews of accelerator science and technology". *World Scientific*, **1**, (2008).

[27] F. Brunel: "Not–so–resonant, resonant absorption". *Physical Review Letters*, **59**(1), 52 (1987).

[28] D. Bauer, P. Mulser and W-H. Steeb: "Relativistic ponderomotive force, uphill acceleration, and transition to chaos". *Physical review letters*, **75**(25), 4622 (1995).

[29] E.A. Startsev and C.J. McKinstrie: "Multiple scale derivation of the relativistic ponderomotive force". *Physical Review E*, **55**(6), 7527 (1997).

[30] S.C. Wilks and W.L. Kruer: "Absorption of ultrashort, ultra–intense laser light by solids and overdense plasmas". *IEEE Journal of Quantum Electronics*, **33**(11), 1954–1968 (1997).

[31] G. Malka J.L. and Miquel: "Experimental confirmation of ponderomotive–force electrons produced by an ultrarelativistic laser pulse on a solid target". *Physical Review Letters*, **77**(1), 75 (1996).

[32] C.I. Moore, J.P. Knauer and D.D. Meyerhofer: "Observation of the transition from Thomson to Compton scattering in multiphoton interactions with low–energy electrons". *Physical review letters*, **74**(13), 2439 (1995).

[33] R.O. Dendy: "Plasma physics: an introductory course". *Cambridge University Press*, (1995).

[34] G.J. Pert: "Inverse bremsstrahlung in strong radiation fields at low temperatures". *Physical Review E*, **51**(5), 4778 (1995).

[35] A.B. Langdon: "Nonlinear inverse bremsstrahlung and heated–electron distributions". *Physical Review Letters*, **44**(9), 575 (1980).

[36] W.L. Kruer: "The physics of laser plasma interactions". *Reading, MA (US); Addison-Wesley Publishing Co.*, (1988).

[37] R.J. Goldston and P.H. Rutherford: "Introduction to plasma physics". *CRC Press*, (1995).

[38] W. Rozmus, V.T. Tikhonchuk and R. Cauble: "A model of ultrashort laser pulse absorption in solid targets". *Physics of Plasmas*, **3**(1), 360–367 (1996).

[39] W. Rozmus and V.T. Tikhonchuk: "Skin effect and interaction of short laser pulses with dense plasmas". *Physical Review A*, **42**(12), 7401 (1990).

[40] D. Griffiths: "Introduction to electrodynamics". *AAPT*, (2005).

[41] R.W. Boyd: "Nonlinear optics". *Elsevier*, (2003).

[42] T. Tajima and J.M. Dawson: "Laser electron accelerator". *Physical Review Letters*, **43**(4), 267 (1979).

[43] D. Umstadter: "Review of physics and applications of relativistic plasmas driven by ultra–intense lasers". *Physics of Plasmas*, **8**(5), 1774–1785 (2001).

[44] A. Pukhov: "Strong field interaction of laser radiation". *Reports on progress in Physics*, **66**(1), 47 (2002).

[45] A. Macchi, F. Cattani, T.V. Liseykina and F. Cornolti: "Laser acceleration of ion bunches at the front surface of overdense plasmas". *Physical review letters*, **94**(16), 165003 (2005).

[46] E. Siminos, M. Grech, S. Skupin, T. Schlegel and V.T. Tikhonchuk: "Effect of electron heating on self–induced transparency in relativistic-intensity laser-plasma interactions". *Physical Review E*, **86**(5), 056404 (2012).

[47] D. Giulietti, L.A. Gizzi, A. Giulietti, A. Macchi, D. Teychenné, P. Chessa, A. Rousse, G. Cheriaux, J.P. Chambaret and G. Darpentigny: "Observation of solid–density laminar plasma transparency to intense 30 femtosecond laser pulses". *Physical review letters*, **79**(17), 3194 (1997).

[48] A.I. Akhiezer and R.V. Polovin: "Theory of wave motion of an electron plasma". *Soviet Phys. JETP*, **3**, (1956).

[49] J. Dawson: "One–dimensional plasma model". *The Physics of Fluids*, **5**(4), 445–459 (1962).

[50] T.P. Coffey: "Breaking of large amplitude plasma oscillations". *The Physics of Fluids*, **14**(7), 1402–1406 (1971).

[51] T. Katsouleas and W.B. Mori: "Wave–breaking amplitude of relativistic oscillations in a thermal plasma". *Physical review letters*, **61**(1), 90 (1988).

[52] K.A. Brueckner and S. Jorna: "Laser–driven fusion". *Reviews of modern physics*, **46**(2), 325 (1974).

[53] E. Esarey, C.B. Schroeder and W.P. Leemans: "Physics of laser–driven plasma–based electron accelerators". *Reviews of modern physics*, **81**(3), 1229 (2009).

[54] D.W. Forslund, J.M. Kindel and E.L. Lindman: "Nonlinear behavior of stimulated Brillouin and Raman scattering in laser–irradiated plasmas". *Physical Review Letters*, **30**(16), 729 (1973).

[55] P. Sprangle, E. Esarey and A. Ting: "Nonlinear theory of intense laser–plasma interactions". *Physical review letters*, **64**(17), 2011 (1990).

[56] A. Pukhov and J. Meyer–ter–Vehn: "Relativistic laser-plasma interaction by multi–dimensional particle–in–cell simulations". *Physics of Plasmas*, **5**(5), 1880–1886 (1998).

[57] E. Esarey, P. Sprangle, J. Krall and A, Ting: "Self–focusing and guiding of short laser pulses in ionizing gases and plasmas". *IEEE Journal of Quantum Electronics*, **33**(11), 1879–1914 (1997).

[58] Y. Nabekawa, A.A. Eilanlou, Y. Furukawa, K.L. Ishikawa, H. Takahashi and K. Midorikawa: "Multi–terawatt laser system generating 12–fs pulses at 100 Hz repetition rate". *Applied Physics B*, **101**(3), 523–534 (2010).

[59] U. Schramm, M. Bussmann, A. Irman, M. Siebold, K. Zeil, D. Albach, C. Bernert, S. Bock, F. Brack, J. Branco, et al.: "First results with the novel petawatt laser acceleration facility in Dresden". *Journal of Physics: Conference Series*, **874**(1), 012028 (2017).

[60] S.C. Rae: "Ionization-induced defocusing of intense laser pulses in high-pressure gases". *Optics communications*, **97**(1–2), 25–28 (1993).

[61] P. Gibbon, F. Jakober, P. Monot and T. Auguste: "Experimental study of relativistic self–focusing and self–channeling of an intense laser pulse in an underdense plasma". *IEEE Transactions on plasma science*, **24**(2), 343–350 (1996).

[62] M.I.K. Santala, M. Zepf, I. Watts, F.N. Beg, E. Clark, M. Tatarakis, K. Krushelnick, et al.: "Effect of the plasma density scale length on the direction of fast electrons in relativistic laser–solid interactions". *Physical Review Letters*, **84**(7), 1459 (2000).

[63] Y. Ping, R. Shepherd, B.F. Lasinski, M. Tabak, H. Chen, H.K. Chung, K.B. Fournier, et al.: "Absorption of short laser pulses on solid targets in the ultrarelativistic regime". *Physical review letters*, **100**(8), 085004 (2008).

[64] N.B. Zorov, A.A. Gorbatenko, T.A. Labutin and A.M Popov: "A review of normalization techniques in analytical atomic spectrometry with laser sampling: From single to multivariate correction". *Spectrochimica Acta Part B: Atomic Spectroscopy*, **65**(8), 642–657 (2010).

[65] Y.T. Lee: "A model for ionization balance and L–shell spectroscopy of non–LTE plasmas". *Journal of Quantitative Spectroscopy and Radiative Transfer*, **38**(2), 131–145 (1987).

[66] L.D. Landau and E.M. Lifshitz: "The Propagation of Electromagnetics Waves". *Electrodynamics of continuous media*, **3**, 290–330 (1986).

[67] I.P. Shkarofsky, T.W. Johnston and M.P. Bachynski: "The particle kinetics of plasmas". *Reading, Mass.: Addison-Wesley Publishing Company*, (1966).

[68] V.I. Kolobov and D.J. Economou: "The anomalous skin effect in gas discharge plasmas". *Plasma sources science and technology*, **6**(2), R1 (1997).

[69] N.G. Denisov: "On a singularity of the field of an electromagnetic wave propagated in an inhomogeneous plasma". *SOVIET PHYSICS JETP-USSR*, **4**(4), 544–553 (1957).

[70] C. Thaury and F. Quéré: "High–order harmonic and attosecond pulse generation on plasma mirrors: basic mechanisms". *Journal of Physics B: Atomic, Molecular and Optical Physics*, **43**(21), 213001 (2010).

[71] P. Gibbon: "Efficient production of fast electrons from femtosecond laser interaction with solid targets". *Physical review letters*, **73**(5), 664 (1994).

[72] W.L. Kruer and K. Estabrook: "J× B heating by very intense laser light". *The Physics of fluids*, **28**(1), 430–432 (1985).

[73] J. Guillory and G. Benford: "Estimates of dense plasma heating by stable intense electron beams". *Plasma Physics*, **14**(12), 1131 (1972).

[74] S.A. Gaillard, T. Kluge, K.A. Flippo, M. Bussmann, B. Gall, T. Lockard, M. Geissel, et al.: "Increased laser-accelerated proton energies via direct laser–light–pressure acceleration of electrons in microcone targets". *Physics of Plasmas*, **18**(5), 056710 (2011).

[75] C.M. Brenner, A.P.L. Robinson, K. Markey, R.H.H. Scott, R.J. Gray, M. Rosinski, et al.: "High energy conversion efficiency in laser-proton acceleration by controlling laser–energy deposition onto thin foil targets". *Applied Physics Letters*, **104**(8), 081123 (2014).

[76] G. Milluzzo, V. Scuderi, A.G. Amico, M. Borghesi, G.A.P Cirrone, G. Cuttone, et al.: "Laser–accelerated ion beam diagnostics with TOF detectors for the ELIMED beam line". *Journal of Instrumentation*, **12**(02), C02025 (2017).

[77] X. Zhao and Y.C. Shin: "Coulomb explosion and early plasma generation during femtosecond laser ablation of silicon at high laser fluence". *Journal of Physics D: Applied Physics*, **46**(33), 335501 (2013).

[78] I. Last and J. Jortner: "Dynamics of the Coulomb explosion of large clusters in a strong laser field". *Physical Review A*, **62**(1), 013201 (2000).

[79] Z.B. Seksembayev, O.S. Bayakhmetov and S.K. Sakhiyev: "Coulomb explosions in plasma". *Journal of Physics: Conference Series*, **907**(1), 012028 (2017).

[80] C. Phipps: "Laser ablation and its applications". *Springer*, **129**, (2007).

[81] S.J. Gitomer, R.D Jones, F. Begay, A.W. Ehler, J.F. Kephart and R. Kristal: "Fast ions and hot electrons in the laser–plasma interaction". *The Physics of fluids*, **29**(8), 2679–2688 (1986).

[82] J.P. Zheng, Z.Q. Huang, D.T. Shaw and H.S. Kwok: "Generation of high-energy atomic beams in laser–superconducting target interactions". *Applied Physics Letters*, **54**(3), 280–282 (1989).

[83] R. Kelly and R.W. Dreyfus: "On the effect of Knudsen–layer formation on studies of vaporization, sputtering, and desorption". *Surface science*, **198**(1–2), 263–276 (1988).

[84] R. Kelly: "Gas dynamics of the pulsed emission of a perfect gas with applications to laser sputtering and to nozzle expansion". *Physical Review A*, **46**(2), 860 (1992).

[85] L. Torrisi, S. Gammino, L. Andò and L. Laska: "Tantalum ions produced by 1064 nm pulsed laser irradiation". *Journal of applied physics*, **91**(7), 4685–4692 (2002).

[86] N.M. Bulgakova, A.V. Bulgakov and O.F. Bobrenok: "Double layer effects in laser–ablation plasma plumes". *Physical Review E*, **62**(4), 5624 (2000).

[87] M. Capitelli, A. Casavola, G. Colonna and A. De Giacomo: "Laser-induced plasma expansion: theoretical and experimental aspects". *Spectrochimica Acta Part B: Atomic Spectroscopy*, **59**(3), 271–289 (2004).

[88] L. Torrisi, F. Caridi, D. Margarone, A. Picciotto, A. Mangione and J.J. Beltrano: "Carbon–plasma produced in vacuum by 532 nm–3 ns laser pulses ablation". *Applied surface science*, **252**(18), 6383–6389 (2006).

[89] L. Torrisi, F. Caridi, D. Margarone and A. Borrielli: "Characterization of laser–generated silicon plasma". *Applied Surface Science*, **254**(7), 2090–2095 (2008).

[90] S.C. Wilks, A.B. Langdon, T.E. Cowan, M. Roth, M. Singh, S. Hatchett, M.H. Key, D. Pennington, A. MacKinnon and R.A. Snavely: "Energetic proton generation in ultra-intense laser–solid interactions". *Physics of plasmas*, **8**(2), 542–549 (2001).

[91] M. Roth and M. Schollmeier: "Ion acceleration–target normal sheath acceleration". *arXiv preprint arXiv:1705.10569*, (2017).

[92] S. Backus, C.G. Durfee III, M.M. Murnane and H.C. Kapteyn: "High power ultrafast lasers". *Review of scientific instruments*, **69**(3), 1207–1223 (1998).

[93] S. Keppler, A. Sävert, J. Körner, M. Hornung, H. Liebetrau, J. Hein and M.C. Kaluza: "The generation of amplified spontaneous emission in high–power CPA laser systems". *Laser & photonics reviews*, **10**(2), 264–277 (2016).

[94] H. Daido, M. Nishiuchi and A.S. Pirozhkov: "Review of laser–driven ion sources and their applications". *Reports on Progress in Physics*, **75**(5), 056401 (2012).

[95] M. Borghesi, A. Bigongiari, S. Kar, A. Macchi, L. Romagnani, P. Audebert, J. Fuchs, T. Toncian, O. Willi, S.V. Bulanov, et al.: "Laser–driven proton acceleration: source optimization and radiographic applications". *Plasma Physics and Controlled Fusion*, **50**(12), 124040 (2008).

[96] M. Passoni, L. Bertagna and A. Zani: "Target normal sheath acceleration: theory, comparison with experiments and future perspectives". *New Journal of Physics*, **12**(4), 045012 (2010).

[97] M. Borghesi: "Laser–driven ion acceleration: State of the art and emerging mechanisms". *Nuclear Instruments and Methods in Physics Research Section A: Accelerators, Spectrometers, Detectors and Associated Equipment*, **740**, 6–9 (2014).

[98] M. Passoni, V.T. Tikhonchuk, M. Lontano and V.Yu. Bychenkov: "Charge separation effects in solid targets and ion acceleration with a two–temperature electron distribution". *Physical Review E*, **69**(2), 026411 (2004).

[99] A. Macchi and C. Benedetti: "Ion acceleration by radiation pressure in thin and thick targets". *Nuclear Instruments and Methods in Physics Research Section A: Accelerators, Spectrometers, Detectors and Associated Equipment*, **620**(1), 41–45 (2010).

[100] S. Kar, K.F. Kakolee, M. Cerchez, D. Doria, A. Macchi, P. McKenna, D. Neely, et al.: "Experimental investigation of hole boring and light sail regimes of RPA by varying laser and target parameters". *Plasma Physics and Controlled Fusion*, **55**(12), 124030 (2013).

[101] B. Qiao, S. Kar, M. Geissler, P. Gibbon, M. Zepf and M. Borghesi: "Dominance of radiation pressure in ion acceleration with linearly polarized pulses at intensities of 10^{21} Wcm^{-2}". *Physical review letters*, **108**(11), 115002 (2012).

[102] A.P.L. Robinson, M. Zepf, S. Kar, R.G. Evans and C. Bellei: "Radiation pressure acceleration of thin foils with circularly polarized laser pulses". *New journal of Physics*, **10**(1), 013021 (2008).

[103] A.P.L. Robinson, P. Gibbon, M. Zepf, S. Kar, R.G. Evans and C. Bellei: "Relativistically correct hole–boring and ion acceleration by circularly polarized laser pulses". *Plasma Physics and Controlled Fusion*, **51**(2), 024004 (2009).

[104] A. Higginson, R.J. Gray, M. King, R.J. Dance, S.D.R. Williamson, N.M.H Butler, R. Wilson, R. Capdessus, et al.: "Near–100 MeV protons via a laser–driven transparency–enhanced hybrid acceleration scheme". *Nature communications*, **9**(1), 724 (2018).

[105] T. Esirkepov, M. Borghesi, S.V. Bulanov, G. Mourou and Tajima, T: "Highly efficient relativistic–ion generation in the laser–piston regime". *Physical review letters*, **92**(17), 175003 (2004).

[106] A. Macchi, S. Veghini, T.V. Liseykina and F. Pegoraro: "Radiation pressure acceleration of ultrathin foils". *New Journal of Physics*, **12**(4), 045013 (2010).

[107] S. Steinke, P. Hilz, M. Schnürer, G. Priebe, J. Bränzel, F. Abicht, D. Kiefer, C. Kreuzer, et al.: "Stable laser–ion acceleration in the light sail regime". *Physical Review Special Topics-Accelerators and Beams*, **16**(1), 011303 (2013).

[108] B. Qiao, M. Zepf, M. Borghesi and M. Geissler: "Stable GeV ion–beam acceleration from thin foils by circularly polarized laser pulses". *Physical review letters*, **102**(14), 145002 (2009).

[109] S.M. Weng, M. Liu, Z.M. Sheng, M. Murakami, M. Chen, L.L. Yu and J. Zhang: "Dense blocks of energetic ions driven by multi–petawatt lasers". *Scientific reports*, **6**, 22150 (2016).

[110] J. Buon: "Beam phase space and emittance". *Paris-11 Univ.*, (1992).

[111] K. Wille: "The physics of particle accelerators: an introduction". *Clarendon Press*, (2000).

[112] M. Rosenlicht: "Liouville's theorem on functions with elementary integrals". *Pacific Journal of Mathematics*, **24**(1), 153–161 (1968).

[113] M.P. Stockli, R.F. Welton and R. Keller: "Self-consistent, unbiased root–mean–square emittance analysis". *Review of scientific instruments*, **75**(5), 1646–1649 (2004).

[114] T. Kalvas: "Beam extraction and transport". *arXiv preprint arXiv:1401.3951*, (2014).

[115] D.C. Carey: "The optics of charged particle beams. Accelerators and Storage Rings". *Harwood academic publishers*, (1987).

[116] E.D. Donets: "Historical review of electron beam ion sources". *Review of Scientific Instruments*, **69**(2), 614–619 (1998).

[117] T.E. Cowan, J. Fuchs, H. Ruhl, A. Kemp, P. Audebert, M. Roth, R. Stephens, I. Barton, et al.: "Ultralow emittance, multi–MeV proton beams from a laser virtual-cathode plasma accelerator". *Physical review letters*, **92**(20), 204801 (2004).

[118] P. Dahl: "Introduction to electron and ion optics". *Elsevier*, (2012).

[119] E. Hecht: "Optics 2nd edition". *Optics 2nd edition by Eugene Hecht Reading, MA: Addison-Wesley Publishing Company*, **5**, 1–44 (1987).

[120] L.S. Pedrotti: "Basic geometrical optics". *Society of Photo-Optical Instrumentation Engineers, Bellingham, WA, accessed Dec*, **5**, 1–44 (2008).

[121] A. El–Kareh: "Electron beams, lenses, and optics". *Academic press*, (1970).

[122] R.F. Egerton: "Physical principles of electron microscopy". *Springer*, (2016).

[123] J. Rossbach and P. Schmueser: "Basic course on accelerator optics". *Conf. Proc.*, **9209071**, 17–88 (1992).

[124] A. Wolski: "Introduction to Beam Dynamics in High–energy Electron Storage Rings". *Morgan & Claypool Publishers*, (2018).

[125] R.J. Steinhagen: "Tune and chromaticity diagnostics". *CERN*, (2009).

[126] P.H. Dawson: "Quadrupole mass spectrometry and its applications". *Elsevier*, (2013).

[127] P.E. Miller and M.B. Denton: "The quadrupole mass filter: basic operating concepts". *Journal of chemical education*, **63**(7), 617 (1986).

[128] H. Liebl: "Applied charged particle optics". *Springer*, (2008).

[129] L. Reimer and H. Kohl: "Transmission electron microscopy: physics of image formation". *Springer*, (2008).

[130] V. Kumar: "Understanding the focusing of charged particle beams in a solenoid magnetic field". *American Journal of Physics*, **77**(8), 737–741 (2009).

[**131**] L. Torrisi and **G. Costa**: "Magnetic focusing of emitted ions from laser–generated plasma: enhancement of yield and energy". *Laser and particle Beams*, **35**(2), 202–209 (2017).

[132] W.B.J. Zimmerman: "Multiphysics modeling with finite element methods". *World Scientific Publishing Company*, **18**, (2006).

[133] COMSOL Multiphysics: "Introduction to COMSOL Multiphysics®". *COMSOL Multiphysics, Burlington, MA, accessed Feb*, **9**, (2018).

[134] COMSOL Multiphysics Version 5.1: *Actual Website* (2019): https://www.comsol.it/.

[135] L. Torrisi, S. Gammino, A.M. Mezzasalma, A.M. Visco, J. Badziak, P. Parys, J. Wołowski, E. Woryna, et al.: "Laser ablation of UHMWPE–polyethylene by 438 nm high energy pulsed laser". *Applied surface science*, **227**(1–4), 164–174 (2004).

[136] W. Lotz: "An empirical formula for the electron–impact ionization cross–section". *Zeitschrift für Physik*, **206**(2), 205–211 (1967).

[137] W. Lotz: "Electron–impact ionization cross-sections and ionization rate coefficients for atoms and ions from hydrogen to calcium". *Zeitschrift für Physik*, **216**(3), 241–247 (1968).

[138] W. Lotz: "Electron–impact ionization cross–sections for atoms up to Z = 108". *Zeitschrift für Physik A Hadrons and nuclei*, **232**(2), 101–107 (1970).

[139] NIST: Atomic Spectra Database Ionization Energies Form: *Actual Website* (2017): https://physics.nist.gov/PhysRefData/ASD/ionEnergy.html.

[140] L. Torrisi: "Laser–induced ablation: Physics and diagnostics of ion emission". *Nukleonika*, **56**, 113–117 (2011).

[141] S.N. Srivastava, B.K. Sinha and K.P. Rohr: "Ions and ion–energy spectra of a collisional laser plasma produced from multi–species targets of aluminium and titanium". *Journal of Physics B: Atomic, Molecular and Optical Physics*, **39**(14), 3073 (2006).

[142] L. Torrisi, D. Margarone, S. Gammino and L. Ando: "Ion energy increase in laser-generated plasma expanding through axial magnetic field trap". *Laser and Particle Beams*, **25**(3), 453–464 (2007).

[**143**] L. Torrisi and **G. Costa**: "Magnetic Field to focalize and Accelerate ions produced by *ns* Laser–generated plasmas". *Japanese Journal of Applied Physics*, Submitted, (2019).

[144] M. Zepf, E.L. Clark, K. Krushelnick, F.N. Beg, C. Escoda, A.E. Dangor, M.I.K. Santala, et al.: "Fast particle generation and energy transport in laser–solid interactions". *Physics of Plasmas*, **8**(5), 2323–2330 (2001).

[145] R.A. Snavely, M.H. Key, S.P. Hatchett, T.E. Cowan, M. Roth, T.W. Phillips, M.A. Stoyer, et al.: "Intense high–energy proton beams from petawatt–laser irradiation of solids". *Physical review letters*, **85**(14), 2945 (2000).

[146] M. Allen, P.K. Patel, A. Mackinnon, D. Price, S. Wilks and E. Morse: "Direct experimental evidence of back-surface ion acceleration from laser-irradiated gold foils". *Physical review letters*, **93**(26), 265004 (2004).

[**147**] **G. Costa** and L. Torrisi: "Design of an Electromagnet for Laser-generated Plasma diagnostics". *Activity Report del Dottorato di Ricerca in Fisica*, *Università degli Studi di Messina*, ISSN: 2038–5889 (2017).

[148] Y. Gao, B. Zhu, D. Liu and Z. Lin: "Propagation of flat–topped multi-Gaussian beams through a double–lens system with apertures". *Optics Express*, **17**(15), 12753–12766 (2009).

[149] L. Torrisi: "Coulomb–Boltzmann–Shifted distribution in laser–generated plasmas from 10^{10} up to 10^{19} W/cm^2 intensities". *Radiation Effects and Defects in Solids*, **171**(1–2), 34–44 (2016).

[150] E. Woryna, P. Parys, J. Wołowski and W. Mroz: "Corpuscular diagnostics and processing methods applied in investigations of laser–produced plasma as a source of highly ionized ions". *Laser and Particle beams*, **14**(3), 293–321 (1996).

[151] E. de Hoffmann and V. Stroobant: "Mass spectrometry: principles and applications". *Wiley*, (2207).

[152] M.P. Stöckli and D. Fry: "Analog gain of microchannel plates for 1.5–154 keV/q Ar^{q+} ($3 \leq q \leq 16$)". *Review of scientific instruments*, **68**(8), 3053–3060 (1997).

[153] J. Krása, E. Woryna, M.P. Stöckli, S. Winecki and B.P. Walch: "Gain of windowless electron multipliers 226EM and EMI 9643/2B for highly charged Ta ions". *Review of scientific instruments*, **69**(1), 95–100 (1998).

[**154**] **G. Costa** and L. Torrisi: "Diagnostics of Particles emitted from a Laser generated Plasma: Experimental Data and Simulations". *The European Physics Journal: Web of Conferences*, **167**, 04005(1–6) (2018).

[**155**] L. Torrisi and G. **Costa**: "Simple Magnetic Spectrometer for ions emitted from Laser–generated Plasma at 10^{10} W/cm^2 intensity". *Laser and Particle Beams*, **36**(2), 163–170 (2018).

[**156**] L. Torrisi, **G. Costa**, G. Ceccio, A. Cannavò, N. Restuccia and M. Cutroneo: "Magnetic and electric deflector spectrometers for ion emission analysis from laser generated plasma". *The European Physics Journal: Web of Conferences*, **167**, 03011(1–7) (2018).

[157] F. Caridi, L. Torrisi, D. Margarone and A. Borrielli: "Investigations on low temperature laser–generated plasmas". *Laser and Particle Beams*, **26**(2), 265–271 (2008).

[**158**] **G. Costa** and L. Torrisi: "Electrical and magnetic spectrometry of ions emitted from laser–generated plasma at 10^{10} W/cm^2 intensity". *45th EPS Conference on Plasma Physics (EPS2018)*, (2018).

[159] A. Macchi, A. Sgattoni, S. Sinigardi, M. Borghesi and M. Passoni: "Advanced strategies for ion acceleration using high-power lasers". *Plasma Physics and Controlled Fusion*, **55**(12), 124020 (2013).

[160] A. Cannavò, L. Torrisi, G. Ceccio, M. Cutroneo, L. Calcagno, A. Sciuto and M. Mazzillo: "Characterization of X–ray emission from laser generated plasma". *EPJ Web of Conferences*, **167**, 03004 (2018).

[161] K.A. Bhatti, R. Ahmed, M.I Khan, J.Z.A. Khan, A. Ali, G. Siddique and A. Latif: "Comparison of the laser–induced plasma of different metal targets as X–rays sources in vacuum". *Radiation Effects and Defects in Solids*, **173**(11–12), 921–928 (2018).

[162] D. Giulietti and L.A. Gizzi: "X–ray emission from laser–produced plasmas". *La Rivista del Nuovo Cimento*, **21**(10), 1–93 (1998).

[163] M. Rosinski, J. Badziak, P. Parys, A. Zaras-Szydłowska, L. Ryc, L. Torrisi, et al.: "Acceleration of protons in plasma produced from a thin plastic or aluminum target by a femtosecond laser". *Journal of Instrumentation*, **11**(05), C05017 (2016).

[164] A. Giulietti, P. Tomassini, M. Galimberti, D. Giulietti, L.A. Gizzi, P. Koester, L. Labate, et al.: "Prepulse effect on intense femtosecond laser pulse propagation in gas". *Physics of plasmas*, **13**(9), 093103 (2006).

[165] M. Roth: "The diagnostics of ultra-short pulse laser–produced plasma". *Journal of Instrumentation*, **6**(09), R09001 (2011).

[166] A. Hashim: "VISAR Analysis Theory and Mathematical Formalism". (2016).

[167] D. Batani, A. Morace, Y. Maheut, K. Jakubowska and L. Volpe: "Diagnostics of laser–produced plasmas". *Nukleonika*, **61**(4), 393–401 (2016).

[168] J. Briand, J.C. Kieffer, A. Gomes, C. Arnas, J.P. Dinguirard, Y. Quemener, L- Berge, M. El Tamer and M. Armengaud: "Measurements of magnetic fields using the Zeeman effect in laser–produced plasmas". *The Physics of fluids*, **30**(9), 2893–2897 (1987).

[169] M. Tatarakis, A. Gopal, I. Watts, F.N. Beg, A.E. Dangor, K. Krushelnick, U. Wagner, P.A. Norreys, et al.: "Measurements of ultrastrong magnetic fields during relativistic laser–plasma interactions". *Physics of Plasmas*, **9**(5), 2244–2250 (2002).

[170] M. Tatarakis, I. Watts, F.N. Beg, E.L. Clark, A.E. Dangor, A. Gopal, M.G. Haines, P.A. Norreys, et al.: "Laser technology: Measuring huge magnetic fields". *Nature*, **415**(6869), 280 (2002).

[171] R.B. Stephens, R.A. Snavely, Y. Aglitskiy, F. Amiranoff, C. Andersen, D. Batani, S.D. Baton, et al.: "K_α fluorescence measurement of relativistic electron transport in the context of fast ignition". *Physical Review E*, **69**(6), 066414 (2004).

[172] L. Robson, P.T. Simpson, R.J. Clarke, K.W.D. Ledingham, F. Lindau, O. Lundh, T. McCanny, et al.: "Scaling of proton acceleration driven by petawatt–laser–plasma interactions". *Nature physics*, **3**(1), 58 (2007).

[173] Experimental Nuclear Reaction Data (EXFOR): *Actual Website* (2019): https://www-nds.iaea.org/exfor/.

[174] R. Collé, R. Kishore and J.B. Cumming: "Excitation functions for (p,n) reactions to 25 MeV on ^{63}Cu, ^{65}Cu, and ^{107}Ag". *Physical Review C*, **9**(5), 1819 (1974).

[175] J.F. Ziegler, M.D. Ziegler and J.P. Biersack: "SRIM–The stopping and range of ions in matter (2010)". *Nuclear Instruments and Methods in Phys. Res. Sec. B*, **268**(11–12), 1818–1823 (2010).

[176] C. Gahn, G.D. Tsakiris, G. Pretzler, K.J. Witte, P. Thirolf, D. Habs, C. Delfin and C.G. Wahlström: "Generation of MeV electrons and positrons with femtosecond pulses from a table–top laser system". *Physics of plasmas*, **9**(3), 987–999 (2002).

[177] J.F. Ziegler: "Stopping of energetic light ions in elemental matter". *Journal of applied physics*, **85**(3), 1249–1272 (1999).

[178] F. Nürnberg, M. Schollmeier, E. Brambrink, A. Blažević, D.C. Carroll, K. Flippo, D.C. Gautier, et al.: "Radiochromic film imaging spectroscopy of laser–accelerated proton beams". *Review of scientific instruments*, **80**(3), 033301 (2009).

[179] A. Alejo, D. Gwynne, D. Doria, H. Ahmed, D.C. Carroll, R.J. Clarke, et al.: "Recent developments in the Thomson Parabola Spectrometer diagnostic for laser–driven multi–species ion sources". *Journal of Instrumentation*, **11**(10), C10005 (2016).

[180] M.J. Rhee: "Compact thomson spectrometer". *Review of scientific instruments*, **55**(8), 1229–1234 (1984).

[181] R.F. Schneider, C.M. Luo and M.J. Rhee: "Resolution of the Thomson spectrometer". *Journal of applied physics*, **57**(1), 1–5 (1985).

[182] L. Torrisi, S. Cavallaro, M. Cutroneo, L. Andò, L. Calcagno, G. Bertuccio, J. Ullschmied, J. Krása, D. Margarone, J. Wołowski and M. Rosinski: "Laser ion acceleration for nuclear applications (LIANA Project): State of art". *LNS Activity Report: Ion Sources and Accelerators*, 223–226 (2012).

[183] J.T. Morrison, C. Willis, R.R. Freeman and L. Van Woerkom: "Design of and data reduction from compact Thomson parabola spectrometers". *Review of Scientific Instruments*, **82**(3), 033506 (2011).

[184] J. L. Wiza, et al.: "Microchannel plate detectors". *Nuclear Instruments and Methods*, **162**(1–3), 587–601 (1979).

[185] W. Yi, T. Jeong, S. Jin, S.G. Yu, J. Lee, J. Heo, J. Yoo and J.M. Kim: "Characteristic features of new electron-multiplying channels in a field emission display". *Journal of Vacuum Science & Technology B*, **19**(6), 2247–2251 (2001).

[186] S. Devic, J. Seuntjens, W. Abdel–Rahman, M. Evans, M. Olivares, E.B. Podgorsak, T. Vuong and C.G. Soares: "Accurate skin dose measurements using radiochromic film in clinical applications". *Medical physics*, **33**(4), 1116–1124 (2006).

[187] F.M. Khan and J.P. Gibbons: "The Physics of Radiation Therapy". *Lippincott Williams & Wilkins*, (2014).

[188] A.D. Koulouklidis, S. Cohen and J. Kalef–Ezra: "Thermochromic phase-transitions of GafChromic films studied by z–scan and temperature–dependent absorbance measurements". *Medical physics*, **40**(11), 112701(1–12) (2013).

[189] C.G. Soares, S. Trichter and S. Devic: "Radiochromic film". *Clinical Dosimetry Measurements in Radiotherapy*, 759–813 (2009).

[190] G.F. Knoll: "Radiation Detection and Measurement". *John Wiley & Sons*, (2010).

[191] S.H.S. Al–Niaemi and A.K.M. Al–Ramadhni: "Bulk Etch Rate and the Activation Energy of the CR–39 Detector using Thickness Difference Method". *Kirkuk University Journal–Scientific Studies*, **13**(2), 114–126 (2018).

[192] T.M. Salman, A.Y. Al–Ahmad, H.A. Badran and C.A. Emshary: "Diffused transmission of laser beam and image processing tools for alpha–particle track–etch dosimetry in PM–355 SSNTDs". *Physica Scripta*, **90**(8), 085302 (2015).

[193] D. Nikezic and K.N. Yu: "Formation and growth of tracks in nuclear track materials". *Materials Science and Engineering: R: Reports*, **46**(3–5), 51–123 (2004).

[194] A. Malinowska, M. Jaskóła, A. Korman, A. Szydłowski and M. Kuk: "Characterization of solid state nuclear track detectors of the polyallyl–diglycol–carbonate (CR–39/PM–355) type for light charged particle spectroscopy". *Review of Scientific Instr.*, **85**(12), 123505 (2014).

[195] A. Cannavò, V. Lavrentiev, I. Lavrentieva, L. Torrisi, P. Horàk, G. Ceccio and j. Vacìk: "Characterization of ion tracks in CR39 polymer exposed to ^{241}Am α–particles". *Radiation Effects and Defects in Solids*, **173**(9–10), 807–817 (2018).

[196] L. Torrisi, G. Foti, L. Giuffrida, D. Puglisi, J. Wołowski, J. Badziak, O. Parys, M. Rosinski, et al.: "Single crystal silicon carbide detector of emitted ions and soft X rays from power laser–generated plasmas". *Journal of Applied Physics*, **105**(12), 123304 (2009).

[197] R.T. Tung: "The physics and chemistry of the Schottky barrier height". *Applied Physics Reviews*, **1**(1), 011304 (2014).

[198] F.H. Ruddy, J.G. Seidel, H. Chen, A.R. Dulloo and S.H. Ryu: "High-resolution alpha–particle spectrometry using 4H silicon carbide semiconductor detectors". *IEEE transactions on nuclear science*, **53**(3), 1713–1718 (2006).

[199] L. Torrisi, V. Havranek, M. Cutroneo, A. Mackova, L. Calcagno, A. Cannavò and A. Torrisi: "SiC detector for high helium energy spectroscopy". *Nuclear Instruments and Methods in Physics Research Section A*, **903**, (2018).

[200] M. Cutroneo, P. Musumeci, M. Zimbone, L. Torrisi, F. La Via, D. Margarone, A. Velyhan, J. Ullschmied and L. Calcagno: "High performance SiC detectors for MeV ion beams generated by intense pulsed laser plasmas". *Journal of Materials Research*, **28**(1), 87–93 (2013).

[201] L. Torrisi and A. Cannavò: "SiC detector damage and characterization for high intensity laser–plasma diagnostics". *Journal of Instrumentation*, **11**(05), P05009 (2016).

[202] L. Torrisi: "Ion energy enhancement from TNSA plasmas obtained from advanced targets". *Laser and Particle Beams*, **32**(3), 383–389 (2014).

[203] L. Torrisi: "Advanced polymer targets for TNSA regime producing 6 MeV protons at 10^{16} W/cm^2 laser intensity". *Physics of Plasmas*, **24**(2), 023111 (2017).

[204] J. Psikal, J. Grym, L. Stolcova and J. Proska: "Hollow target for efficient generation of fast ions by ultrashort laser pulses". *Physics of Plasmas*, **23**(12), 123121 (2016).

[**205**] L. Torrisi, M. Cutroneo, A. Torrisi, L. Silipigni, **G. Costa**, M. Rosinski, J. Badziak, J. Wołowski, A. Zaraś–Szydłowska and P. Parys: "Protons accelerated in the target normal sheath acceleration regime by a femtosecond laser". *Physical Review Accelerators and Beams*, **22**(2), 021302(1–7) (2019).

[206] M. Aliofkhazraei, N. Ali, W.I. Milne, C.S. Ozkan, S. Mitura and J.L. Gervasoni: "Graphene science handbook: electrical and optical properties". *CRC press*, (2016).

[207] G.A.P. Cirrone, A. Tramontana, G. Candiano, M. Carpinelli, S. Cavallaro, M. Cutroneo, et al.: "A new Thomson Spectrometer for high energy laser–driven beams diagnostic". *Journal of Instrumentation*, **9**(08), T08001 (2014).

[208] M. Cutroneo, L. Torrisi, S. Cavallaro, A. Velyhan, et al.: "Thomson parabola spectrometry of laser generated plasma at PALS laboratory". *Journal of Physics: Conference Series*, **508**(1), 012020 (2014).

[209] A. Alejo, S. Kar, A. Tebartz, H. Ahmed, S. Astbury, D.C. Carroll, J. Ding, D. Doria, et al.: "High resolution Thomson Parabola Spectrometer for full spectral capture of multi–species ion beams". *Review of Scientific Instruments*, **87**(8), 083304 (2016).

[**210**] L. Torrisi and **G. Costa**: "Compact Thomson Parabola Spectrometer for fast diagnostics of different intensity Laser–generated Plasmas". *Physical Review Accelerators and Beams*, **22**(4), 042902(1–9) (2019).

[211] L. Torrisi, L. Giuffrida, M. Rosinski and C. Schallhorn: "Ge and Ti post–ion acceleration from laser ion source". *Nuclear Instruments and Methods in Physics Research Section B*, **268**(17–18), 2808–2814 (2010).

[212] L. Torrisi, M. Cutroneo and J. Ullschmied: "TNSA and ponderomotive plasma production in enriched carbon polyethylene foils". *Physics of Plasmas*, **24**(4), 043112 (2017).

[213] L. Torrisi, M. Cutroneo, S. Cavallaro and J. Ullschmied: "D–D nuclear fusion processes induced in polyethylene foams by TW Laser–generated plasma". *EPJ Web of Conferences*, **96**, 01032 (2015).

[214] S. Markidis and G. Lapenta: "The energy conserving particle–in–cell method". *Journal of Computational Physics*, **230**(18), 7037–7052 (2011).

[215] A.B. Langdon: "Energy–conserving plasma simulation algorithms". *Journal of Computational Physics*, **12**(2), 247–268 (1973).

[216] C.K. Birdsall and A.B. Langdon: "Plasma physics via computer simulation". *CRC press*, (2004).

[217] R.W. Hockney and J.W. Eastwood: "Computer simulation using particles". *CRC press*, (1988).

[218] K. Eidmann, J. Meyer–ter–Vehn, T. Schlegel and S. Hüller: "Hydrodynamic simulation of subpicosecond laser interaction with solid–density matter". *Physical Review E*, **62**(1), 1202 (2000).

[219] P. Bertrand, M. Albrecht–Marc, T. Reveille and A. Ghizzo: "Vlasov Models for Laser-Plasma Interaction". *Transport Theory and Statistical Physics*, **34**(1–2), 103–126 (2005).

[220] J. Peebles, C. McGuffey, C.M. Krauland, L.C. Jarrott, A. Sorokovikova, M.S. Wei, et al.: "Impact of pre–plasma on fast electron generation and transport from short pulse, high intensity lasers". *Nuclear Fusion*, **56**(1), 016007 (2015).

[221] B.R.Mancinelli, F.O. Minotti and H. Kelly: "Numerical modelling of a cutting torch". *Journal of Physics: Conference Series*, **511**(1), 012071 (2014).

[222] J. Derouillat, A. Beck, F. Pérez, T. Vinci, M. Chiaramello, A. Grassi, et al.: "Smilei: a collaborative, open-source, multi–purpose particle–in–cell code for plasma simulation". *Computer Physics Communications*, **222**, 351–373 (2018).

[223] E. Cormier-Michel, B.A. Shadwick, C.G.R. Geddes, E. Esarey, C.B. Schroeder and W.P. Leemans: "Unphysical kinetic effects in particle–in–cell modeling of laser wakefield accelerators". *Physical Review E*, **78**(1–2), 016404(1–17) (2008).

[224] K. Yee: "Numerical solution of initial boundary value problems involving Maxwell's equations in isotropic media". *IEEE Transactions on antennas and propagation*, **14**(3), 302–307 (1966).

[225] R. Nuter, M. Grech, P.G. de Alaiza Martinez, G. Bonnaud and E. d'Humières: "Maxwell solvers for the simulations of the laser–matter interaction". *The European Physical Journal D*, **68**(6), 177 (2014).

[226] S.J. Cooke, M. Botton, T.M. Antonsen and B. Levush: "A leapfrog formulation of the 3D ADI–FDTD algorithm". *Workshop on Computational Electromagnetics in Time-Domain*, 1–4 (2007).

[227] T.D. Arber, K. Bennett, C.S. Brady, A. Lawrence–Douglas, M.G. Ramsay, N.J. Sircombe, P. Gillies, et al.: "Contemporary particle–in–cell approach to laser–plasma modelling". *Plasma Physics and Controlled Fusion*, **57**(11), 113001 (2015).

[228] S. Zenitani and T. Umeda: "On the Boris solver in particle–in–cell simulation". *Physics of Plasmas*, **25**(11), 112110 (2018).

[229] T.Z. Esirkepov: "Exact charge conservation scheme for particle–in–cell simulation with an arbitrary form–factor". *Computer Physics Communications*, **135**(2), 144–153 (2001).

[230] J. Villasenor and O. Buneman: "Rigorous charge conservation for local electromagnetic field solvers". *Computer Physics Communications*, **69**(2–3), 306–316 (1992).

[231] T. Umeda, Y. Omura, T. Tominaga and H Matsumoto: "A new charge conservation method in electromagnetic particle–in–cell simulations". *Computer Physics Communications*, **156**(1), 73–85 (2003).

[232] D. Tskhakaya, K. Matyash, R. Schneider and F. Taccogna: "The Particle–In–Cell Method". *Contributions to Plasma Physics*, **47**(8–9), 563–594 (2007).

[233] O. Buneman, H. Matsumoto and Y. Omura: "Computer Space Plasma Physics, Simulation Techniques and Softwares". *Terra Scientific, Tokyo*, 67–84 (1993).

[234] T. Umeda, Y. Omura and H Matsumoto: "An improved masking method for absorbing boundaries in electromagnetic particle simulations". *Computer Physics Communications*, **137**(2), 286–299 (2001).

[235] R.Y. Rubinstein and D.P. Kroese: "Simulation and the Monte Carlo method". *John Wiley & Sons*, **10**, (2006).

[236] J. Vay and R. Lehe: "Simulations for plasma and laser acceleration". *Reviews of Accelerator Science and Technology*, **9**, 165–186 (2016).

[237] K. Bennett, C. Brady, H. Schmitz, C. Ridgers, T. Arber, R. Evans and T. Bell: "Users Manual for the EPOCH PIC codes". *University of Warwick*, (2017).

[238] O. Svelto: "Principles of Lasers". *Springer*, (2010).

[**239**] L. Torrisi and **G. Costa**: "Ion acceleration by *fs* laser in TNSA regime and comparison of TOF spectra with PIC simulations". *Physical Review Accelerators and Beams*, Submitted, (2019).

[240] L. Torrisi, L. Silipigni and M. Cutroneo: "Radiation effects of IR laser on graphene oxide irradiated in vacuum and in air". *Vacuum*, **153**, 122–131 (2018).

[241] L. Torrisi, M. Cutroneo, V. Havranek, L. Silipigni, B. Fazio, M. Fazio, G. Di Marco, A. Stassi and A. Torrisi: "Self–supporting graphene oxide films preparation and characterization methods". *Vacuum*, **160**, 1–11 (2019).

[242] J. Psikal and M. Matys: "Dominance of hole–boring radiation pressure acceleration regime with thin ribbon of ionized solid hydrogen". *Plasma Physics and Controlled Fusion*, **60**(4), 044003 (2018).

[243] L. Torrisi, M. Cutroneo, A. Torrisi, M. Rosinski, A. Zaraś–Szydłowska and P. Parys: "Investigation of the effect of plasma waves excitation on target normal sheath ion acceleration using fs laser–irradiating hydrogenated structures". *Contributions to Plasma Physics*, e201900029 (2019).

[244] L. Laska, K. Jungwirth, J. Krasa, E. Krouskỳ, M. Pfeifer, K. Rohlena, A. Velyhan, et al.: "Angular distributions of ions emitted from laser plasma produced at various irradiation angles and laser intensities". *Laser and Particle Beams*, **26**(4), 555–565 (2008).

[245] M. Roth and M. Schollmeier: "Ion acceleration–target normal sheath acceleration". *CERN Yellow Reports*, **1**, 231 (2016).

[246] L. Torrisi: "Large–scale studies of ion acceleration in laser–generated plasma at intensities from 10^{10} W/cm^2 to 10^{19} W/cm^2". *Optics & Laser Technology*, **99**, 7–14 (2018).

[247] L. Torrisi, M. Cutroneo, M. Rosinski, J. Badziak, P. Parys, J. Wołowski, A. Zaraś–Szydłowska and A. Torrisi: "Near–3–MeV protons from Target–Normal–Sheath–Acceleration femtosecond laser irradiating advanced targets". *Contributions to Plasma Physics*, e201800127(1-14) (2019).

[248] J. Psikal, J. Limpouch, S. Kawata and A.A. Andreev: "PIC simulations of femtosecond interactions with mass–limited targets". *Czechoslovak Journal of Physics*, **56**(2), B515–B521 (2006).

[**249**] **G. Costa** and L. Torrisi: "Particle–in–Cell simulation for experimental ion acceleration by *fs* laser–generated plasma". *Radiation Effects and Defects in Solids*, Submitted, (2019).

[250] B. Sharkov and R. Scrivens: "Laser ion sources". *IEEE Transactions on plasma science*, **33**(6), 1778–1785 (2005).

[251] S. Gammino, L. Torrisi, F. Consoli, D. Margarone, L. Celona and G. Ciavola: "Perspectives for the ECLISSE method with third generation ECRIS". *Radiation Effects & Defects in Solids*, **163**(4–6), 277–286 (2008).

[252] B. Qi, R.M. Gilgenbach, M.C. Jones, M.D. Johnston, Y.Y. Lau, L.M. Wang, j. Lian, G.L. Doll and A. Lazarides: "Diagnostic characterization of ablation plasma ion implantation". *Journal of applied physics*, **93**(11), 8876–8883 (2003).

[253] M. Rosinski, P. Gasior, E. Fazio, L. Ando, L. Giuffrida, L. Torrisi, P. Parys, A.M. Mezzasalma and J. Wołowski: "Laser generated Ge ions accelerated by additional electrostatic field for implantation technology". *Applied Surface Science*, **272**, 109–113 (2013).

[254] F. Krausz, G. Korn, P. Corkum and I.A. Walmsley: "Ultrafast Optics IV: Springer Series in OPTICAL SCIENCES". *Springer*, **95**, 489–495 (2004).

[255] V. Malka, J. Faure, Y.A. Gauduel, E. Lefebvre, A. Rousse and K.T. Phuoc: "Principles and applications of compact laser–plasma accelerators". *Nature physics*, **4**(6), 447 (2008).

[256] O. Lundh, J. Lim, C. Rechatin, L. Ammoura, A. Ben-Ismaïl, X. Davoine, G. Gallot, et al.: "Few femtosecond, few kiloampere electron bunch produced by a laser–plasma accelerator". *Nature Physics*, **7**(3), 219 (2011).

[257] A. Taylor and M.E.B Powell: "Intensity–modulated radiotherapy–what is it?". *Cancer Imaging*, **4**(2), 68 (2004).

[258] W. Kilby, J.R. Dooley, G. Kuduvalli, S. Sayeh and C.R. Maurer Jr: "The CyberKnife® robotic radiosurgery system in 2010". *Technology in cancer research & treatment*, **9**(5), 433–452 (2010).

[259] L. Karsch, E. Beyreuther, W. Enghardt, M. Gotz, U. Masood, U. Schramm, K. Zeil and J. Pawelke: "Towards ion beam therapy based on laser plasma accelerators". *Acta Oncologica*, **56**(11), 1359–1366 (2017).

[260] G.A.P. Cirrone, M. Carpinelli, G. Cuttone, S. Gammino, S.B. Jia, G. Korn, et al.: "ELIMED, future hadrontherapy applications of laser–accelerated beams". *Nuclear Instr. and Meth. in Phys. Res. Sec. A*, **730**, 174–1776 (2013).